STRONGLY CORRELATED PHOTONIC MATERIALS: PARAMETRIC INTERACTIONS AND ULTRASTRONG COUPLING IN CIRCUIT QED

MARIUS ANDREI VRAJITOAREA

A DISSERTATION
PRESENTED TO THE FACULTY
OF PRINCETON UNIVERSITY
IN CANDIDACY FOR THE DEGREE
OF DOCTOR OF PHILOSOPHY

RECOMMENDED FOR ACCEPTANCE
BY THE DEPARTMENT OF
ELECTRICAL ENGINEERING
ADVISER: ANDREW A. HOUCK

SEPTEMBER 2020

Abstract

In recent years, superconducting circuits have become a promising architecture for quantum computing and quantum simulation. This advancing technology offers excellent scalability, long coherence times, and large photon nonlinearities, making it a versatile platform for studying non-equilibrium condensed matter physics with light. This thesis covers a series of experiments and theoretical developments aimed at probing strongly correlated states of interacting photons. Building upon previous efforts on nonlinear superconducting lattices, this work focuses on establishing new platforms for generating interactions between microwave photons in multi-mode circuits.

The first experiment presents a new paradigm in exploiting the nonlinearity of a Josephson junction to tailor the Hilbert space of harmonic oscillators using a dynamical three-wave mixing process. This allows a single microwave resonator to be addressed as a two-level system, offering a promising pathway to long-lived qubits. A theoretical proposal is outlined for building a field-programmable quantum simulator, harnessing this dynamical nonlinearity for stimulating strong photon-photon interactions. The system consists of a lattice of harmonic modes in synthetic dimensions, where particle hopping and on-site interactions can be independently controlled via frequency-selective flux modulation. Numerical studies show that for strong interactions the driven-dissipative steady-state develops a crystalline phase for photons.

The second experiment explores the physics of quantum impurities, where a single well-controlled qubit is coupled to the many modes of a photonic crystal waveguide. The light-matter coupling strength is pushed into the ultrastrong coupling regime, where the qubit is simultaneously hybridized with many modes and the total number of excitations is not conserved. Probing transport through the waveguide reveals that the propagation of a single photon becomes a many-body problem as multi-photon bound states participate in the scattering dynamics. Furthermore, the effective photon interactions induced by just this single impurity leads to interesting inelastic emission of photons. Probing correlations in the field emission reveals signatures of multi-mode entanglement.

This work presents opportunities for exploring large-scale lattices with strongly interacting photons. These platforms are compatible with well-established techniques for generating artificial magnetic fields and stabilizing many-body states through reservoir engineering, complementing growing efforts in the quest for building synthetic quantum materials with light.

Acknowledgements

This thesis wouldn't have been possible without the incredible support of my mentors, family, friends and coworkers. While I cannot list everyone here, I would like to express my sincere gratitude to all of you!

First and foremost, I would like to thank my adviser Prof. Andrew Houck for his guidance and support in research and beyond. Andrew's enthusiasm for science and optimistic personality is contagious, and his talent for problem solving is invaluable when facing difficulties in research. His insightful suggestions and willingness to let me independently explore physics at my own pace have been instrumental in helping me grow as a scientist. Andrew, thank you for believing in me, it has been my great privilege having you as an adviser and as a mentor.

I would like to thank Prof. Claire Gmachl and Prof. Alejandro Rodriguez for acting as readers of this thesis and providing valuable feedback. I would also like to thank Prof. Steve Lyon and Prof. Jeff Thompson for their valuable guidance over the years and for serving in my FPO committee.

Special thanks to the Houck lab members for shaping my research experience into an enjoyable journey full or bumper hockey and lab war stories. When I joined the group I had the privilege of being mentored by the senior members James Raftery, Yanbing Liu, Gengyan Zhang and Neereja Sundaresan, who trained me in the fine art of fabrication, cryogenics, performing measurements and lab maintenance. James helped me measure my first qubit and introduced me to bumper hockey. Yanbing reminded me of how little physics I know and how I should keep high standards as a researcher. Gengyan started the lab hardware-agnostic code base and was instrumental in the initial T_1 crisis period. Neereja taught me how to be patient when debugging a problem and careful when designing an experiment. Mattias Fitzpatrick is very passionate about teaching and I am thankful for the time we worked together as AI instructors. Tom Hazzard, I enjoyed our chats full of random science ideas and

I appreciate your help in indulging my bumper hockey cravings in the mornings, and afternoons. I am grateful for the opportunity to have worked with András Gyenis on measuring the first iterations of the zero-pi qubit and I have learned a lot from our discussions. Many thanks to Alicia Kollár for the valuable help debugging lab equipment and dealing with fridge fiascoes, as well as for sharing insights and knowledge from her AMO background. Thank you Zhaoqi Leng for the very useful discussions and assistance in the lab. It was my pleasure to share my experience and provide guidance to the next generation of lab members, Pranav Mundada, Basil Smitham, Anjali Premkumar, Alex Place, Jake Bryon and Sara Sussman. I am thankful for their hard work improving the lab and wish them all the best for the future. Pranav, I have enjoyed our tennis matches and I appreciate your efforts in trying to guess if I am making a joke or if I am being serious. Let me know what you think of this thesis. Basil, you have now gained the title of lab member with the quirkiest sense of humor and I am certain you will not disappoint. Anjali, I appreciate your efforts in improving the social climate in the department. Alex, your capacity for fabricating new devices should inspire the new lab members. Many thanks to Christie Chiu for the very insightful discussions and for giving great feedback on the thesis.

The optimal path to success is to surround yourself with people who are smarter than you. With that in mind, I would like to acknowledge theory collaborators which have provided enormous support for the work presented in this thesis. Many thanks to Ziwen Huang, Peter Groszkowski and Jens Koch for their valuable contribution to the Kapatron project, helping me search through the vast parameter space until we got the right device implementation. I would also like to acknowledge Andy Li for our many discussions on the nonlinear synthetic lattice. Many thanks to Ron Belyansky, Rex Lundgren, Seth Whitsitt and Alexey Gorshkov for their valued contribution on the quantum impurity project. With their help we explored the many ways in which this experiment could have been implemented and measured, and I am very happy we reached a favorable outcome.

The broader community in our department has been extremely helpful. I would like to thank Bert Harrop, Joe Palmer and other MNFL staff for their valuable support in the cleanroom. Sincere thanks to Barbara Fruhling, Lidia Stokman, Colleen Conrad and other administrative staff, for all their help and support during my program.

This thesis would not have been possible without my amazing wife Fang, who encouraged me to come to Princeton for graduate school. Your love and unwavering support helped me navigate through the difficult times and I appreciate your patience and the sacrifices you made. You are truly an amazing and caring person. Sharing this journey with you has been my great privilege.

And finally, I sincerely thank my Mom, who raised me to become the person I am today and encouraged my career choices. One day I will repay the favor and explain what these qubits are used for.

To my family.

Contents

List of Tables

List of Figures

Chapter 1

Introduction

1.1 Quantum simulation

Since the early 1980s, it was recognized that understanding quantum mechanical phenomena in complex physical systems is a challenging problem, beyond the reach of classical computers [1]. For example, in order to describe the quantum state of N spin-1/2 particles, one needs to store 2^N complex coefficients, which grows exponentially with the system size. Not only is calculating the ground state and expectation values difficult, the number of matrix operations required to simulate the dynamics also scales exponentially with the system size. Performing this task on a classical computer would be impossible for $N \geq 50$, which is an infinitesimal number compared to the number of electrons in a material $N \approx 10^{23}$. Understanding these problems will have numerous applications in diverse scientific areas, such as condensed matter physics, high-energy physics, cosmology, chemistry or nuclear physics [2].

Realizing this obstacle, Richard Feynman proposed the concept of a *quantum simulator* [1]. This idea involves understanding complex quantum systems using quantum mechanics itself. In essence, a quantum simulator is a machine described by a well-understood quantum system consisting of many interacting quantum particles which can be individually controlled. In the decades to follow, it became clear that such a quantum machine has enormous impact to computational algorithms, due to its potential for storing information which scales exponentially with the physical resources and for processing it efficiently using quantum parallelism and interference [3].

In a general quantum simulation problem, one is interested in finding the state of the quantum system $|\Psi(t)\rangle$ at any point in time t and evaluating useful physical quantities. The time evolution of the quantum state $|\Psi(t)\rangle = \mathbf{U}(t)|\Psi(0)\rangle$ is described by the unitary transformation $\mathbf{U}(t) = \exp\left[-i\mathbf{H}_{\text{sys}}t\right]$, dictated by the Hamiltonian of the target system $\mathbf{H}_{\text{sys}}$. A quantum simulator is a well controlled quantum system, described by the Hamiltonian $\mathbf{H}_{\text{sim}}$, used for emulating the quantum system of interest $\mathbf{H}_{\text{sys}}$. The idea is to prepare the simulator in a known initial state $|\phi(0)\rangle$, let it evolve under the unitary $\mathbf{U}'(t) = \exp\left[-i\mathbf{H}_{\text{sim}}t\right]$, and measure the final state $|\phi(t)\rangle$. The simulation is meaningful provided there is a state mapping $\phi \longleftrightarrow \Psi$ between the simulator and target system. Furthermore, the validity of a simulator platform is verified by a set of conditions outlined by Cirac and Zoller [4]. In short, the simulator needs to consist of many quantum quantum degrees of freedom, the initial state $|\phi(0)\rangle$ must be known, the Hamiltonian $\mathbf{H}_{\text{sim}}$ is fine-tunable, and finally information about the system can be extracted in order to benchmark the result to problems with known solutions and provide answers to problems that cannot be verified classically.

There are two approaches for performing quantum simulation. What Feynman originally envisioned was in fact a *digital quantum simulator* - "a quantum machine that could imitate any quantum system, including the physical world" [1]. This idea was later formalized by Seth Lloyd [5] who proved that a quantum computer can be used as a universal quantum simulator. A quantum computer is a collection of two-level quantum systems (qubits) that can be individually initialized, measured and manipulated using a universal set of quantum gates [3]. The basic concept is to consider the evolution of the target system in small time steps $\mathbf{U}(\Delta t)$ and approximate

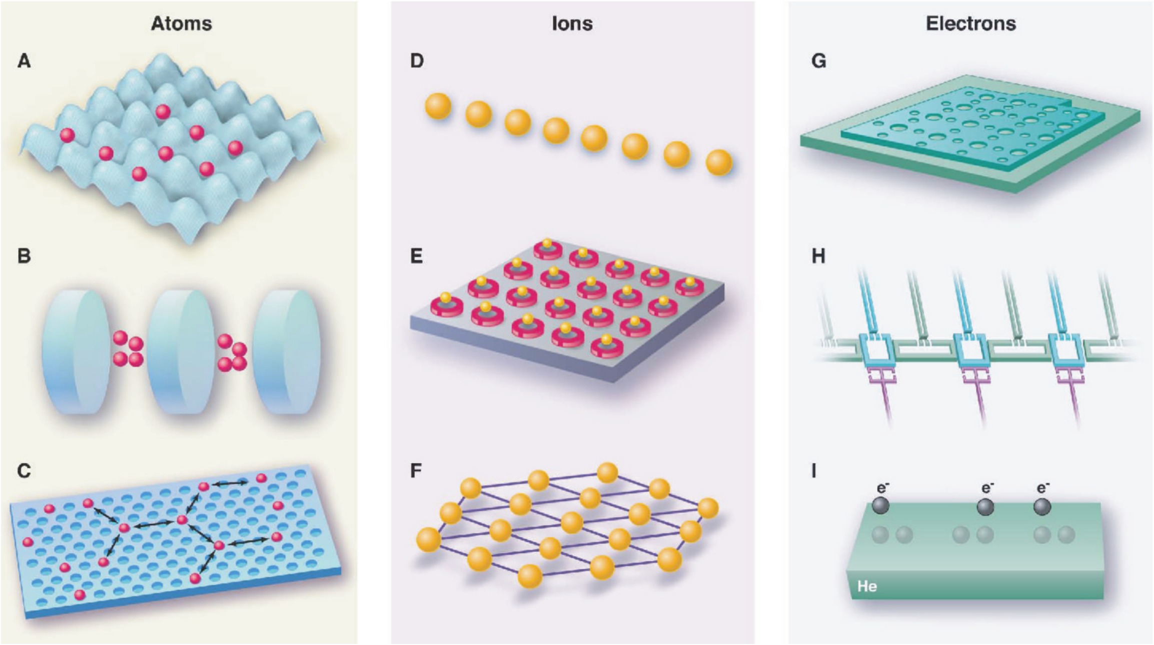

Figure 1.1: **Quantum simulators.** Platforms used for simulating condensed matter models involve manipulating atoms in **a** optical lattices, cavity arrays in **b** one or **c** two dimensions; ions in **d** linear chains, **e** two dimensional traps or **f** Coulomb crystals; electrons in **g** arrays of quantum dots, **h** arrays of superconducting circuits or **i** confined on the surface of liquid helium. Figure adapted from Ref [2].

each discrete evolution by a sequence of one- and two-qubit gates, using what is called a Trotter decomposition. This allows the simulation of any many-body Hamiltonian in a time interval that scales polynomially with the number of particles. Nevertheless, mapping many-body interactions to a sequence of two-qubit gates is challenging and the Trotter approximation is very susceptible to errors in your gates [2].

Building a quantum computer is a very challenging, yet intellectually stimulating, task as it involves finding the right balance between isolating your system from the environment to protect quantum coherence and achieving full control over the multi-qubit system with exceptional precision. There have been impressive advancements in developing controllable quantum systems in a variety of platforms, including trapped ions [6, 7, 8], ultracold atoms [9, 10], spin qubits [11, 12], photonics [13], and superconducting circuits [14, 15, 16, 17] - the focus of this thesis. Current machines are still far from the goal of achieving fault-tolerant large scale quantum processors. However, recent promising work has achieved the 'break-even' point [18] where a single logical qubit lifetime surpassed the lifetime of its constituent physical qubits.

The other approach for simulating quantum physics is *analog quantum simulation*. It involves directly mapping the Hamiltonian of the system you want to study to a reasonably well-controlled quantum system $\mathbf{H}_{\text{sys}} \sim \mathbf{H}_{\text{sim}}$ which exactly mimics the exact continuous evolution. This modest approach is designed to target only specific classes of many-body models and is not as versatile as a universal simulator. Nevertheless, it holds great promise for performing important simulations even with the current noisy quantum hardware. Since it does not involve the Trotter expansion, this scheme is less prone to errors. In fact, error correction is not required as the Hamiltonian mapping is directly implemented on the noisy physical qubits. Moreover, these simulations are less demanding, in cases where we are not interested in the precise reconstruction of the many-body wavefunction, but rather the focus is on specific observables, such as densities, magnetization or correlations, needed to map out a phase diagram [4]. Analog simulators are implemented in various physical platforms, all with their unique capabilities suited for targeting specific scientific problems. Some of these platforms are displayed in Fig. 1.1 and outlined in Ref [2].

It is an exciting time for experimental quantum simulation. Recent growing interest has been fueled not only by the large number of applications in physics and chemistry, but also by the technological advancements in coherently controlling small quantum systems. This monumental progress allows for practical quantum simulation in the near future, and the knowledge gained from validating these simulators will no doubt benefit the ongoing efforts for building a universal quantum computer.

1.2 Interacting photons in nonlinear media

In recent years, quantum simulation with interacting photons has emerged as an excellent platform for studying many-body physics. Since photonic systems are inherently dissipative and can be driven with external fields, it makes this platform particularly suitable for exploring condensed matter with light in a non-equilibrium setting. Reviews outlining the latest experiments and promising ideas in this direction can be found in these references [16, 19, 20, 21, 22, 23]

This concept of building synthetic materials with photons started with the development of quantum fluids of light in nonlinear optical systems [24]. Confining photons in a nonlinear medium, they inherit an effective mass and they collide with one another, and this enables a many-photon ensemble to collectively behave as a quantum fluid. The notion of interacting photons can be very confusing at first, since photons only interact with charged particles and when confined in vacuum they ignore each other. This justifies the necessity for guiding light to propagate through a material. As the material becomes polarized, the elementary excitations are now described by polaritons, hybridized states of photons and matter excitations. In other words, photons start to develop matter-like properties. If the medium has a nonlinear optical response, for instance if the matter polarization depends nonlinearly on the applied electric field, this leads to effective interactions between photons.

To enter the many-body regime, these photon interactions need to become the dominant process where photons have enough time to collide with each other and become entangled before the many-body wavefunction collapses from the coupling to a dissipative environment. Generating such strong optical nonlinearities, at the single-photon level, has been a longstanding goal in quantum optics, and was first demonstrated in the field of cavity Quantum Electrodynamics (QED) [25], where photons confined in a single cavity are strongly coupled to a single atom. The field of nonlinear quantum optics has advanced beyond the single-mode single-atom picture, especially given the strong photon interactions achieved with Rydberg polaritons in atomic media [26]. One can quantify the degree of 'quantumness' for nonlinear photonic systems in terms of the magnitude of photon interactions divided by the rate of particle loss [16]. While various optical systems have reached several collisions per photon lifetime, microwave photons in a circuit QED architecture are deep in the quantum regime, with $\sim 10^4$ collisions per photon lifetime. Circuit QED [17] is the cavity QED version with superconducting circuits, and is the focus of this thesis for exploring platforms for quantum simulation. Strong photon nonlinearities are provided by the Josephson junctions, viewed as nonlinear inductors with a strong dependence on the applied current, by embedding them in microwave circuits whose multi-photon resonance spectrum displays large anharmonicity which dictates the interaction energy between microwave photons.

Motivated by the strong optical nonlinearities in single-cavity QED, pioneering theoretical works have explored the realization of strongly correlated photonic matter in arrays of coupled cavities. In these nonlinear cavity lattices, the competition between kinetic and on-site interactions energies gives rise to the Mott to superfluid phase transition of light [27, 28, 29]. Subsequent studies extended this platform to other many-body phenomena, including the fractional quantum Hall effect [30, 31, 32], effective spin models [33, 34, 35, 36] and the Luttinger liquid model [37]. While these early proposals have neglected photon loss, follow up studies addressed the dissipative nature of these optical systems [38], and develop schemes for combining the effects of drive and dissipation to generate strongly correlated state of photons in cavity lattices [39, 40, 41]. In fact, one could turn this unavoidable loss mechanism into a resource for stabilizing photonic materials with reservoir engineering. This promising approach relies on coupling the system to a non-Markovian bath with energy-dependent damping which compensates for particle loss while removing entropy from the system [42, 43, 44, 45].

Circuit QED presents a versatile platform for exploring many-body quantum optical systems [16] owing to the large light-matter coupling and flexibility in designing the system using conventional lithography. Early experiments performed on small systems demonstrated a delocalization-localization transition in a two-site Hubbard model [46], as well as cooling protocols [47] and chiral ground state currents [48] in a three-site Hubbard model. As circuit QED has matured in its experimental capabilities, larger nonlinear lattices have become accessible. The largest circuit QED lattice with 72 sites has been used to study a dissipative phase transition [49]. A popular approach is to implement low-disorder Hubbard lattices with arrays of transmon qubits, with recent results demonstrating the preparation of a photonic Mott insulator using reservoir engineering [50] and observing signatures of localization of interacting photons in a quasi-periodic potential [51]. These exciting developments establish circuit QED as a promising testbed for simulating quantum many-body phenomena with interacting photons. Going to larger lattices, with many more degrees of freedom, it starts to becomes experimentally challenging to maintain reasonable control of the system parameters and measure the microscopic properties of the many-body circuit. In fact, the complexity in controlling a lattice of transmons is not so different from implementing a quantum computing platform of the same size (ignoring the error correction overhead). So the question becomes, is it possible to perform useful analog quantum simulations that require less hardware overhead than a universal quantum computer? This is the theme of this thesis, where we will focus on simulating interacting photons with circuits, by exploring parametric interactions in synthetic dimensions and ultra-strong light-matter coupling.

1.3 Thesis overview

The focus of this thesis is to use superconducting circuits for studying interacting photons confined in a structured environment. As part of the growing effort of studying condensed matter physics with photons, the contribution of this work is to establish new ways of engineering nonlinear media used for mediating effective photon-photon interactions. Hopefully, these experimental studies will prove useful for future investigations of studying many-body physics with photons in well-controlled quantum simulators with larger system size.

Chapter 2 covers as a concise introduction to circuit QED. It starts with the formalism of quantizing macroscopic superconducting circuits and how these elements can be combined to create microwave cavities and artificial atoms, the building blocks of cQED. This is followed by discussions into coupling these circuits and making a connection to fundamental quantum optical models for light-matter coupling, such as the Jaynes Cummings model.

The first part of this thesis will cover a unique approach for stimulating photon nonlinearity in harmonic oscillators. This idea involves tailoring the oscillator Hilbert space using a dynamical three-wave mixing process induced by a Josephson circuit. In Chapter 3, we experimentally demonstrate this parametric scheme with the goal of implementing a Fock qubit with a microwave resonator. This new protocol for qubit design can prove beneficial for quantum computing since carefully engineered microwave resonators can achieve longer photon coherence times than state of the art Josephson qubits. Following this experimental development, we realized that the dynamical nonlinearity provides effective interactions between photons injected in the resonator. In Chapter 4, we develop a theoretical proposal for a field-programmable quantum simulator based on this type of nonlinearity. The system consists of a lattice of harmonic modes in synthetic dimensions, where each site corresponds to momentum eigenstates of a resonator chain. With only a single Josephson circuit we can induce photon hopping between sites and also stimulate on-site interactions, while having independent control over these parameters via frequency-selective flux modulation.

Instead of building many-body quantum optical systems from many nonlinear cavities, in Chapter 5 we focus on many harmonic modes coupled to a single nonlinear Josephson qubit. We reach the ultrastrong coupling regime, where the impurity is simultaneously hybridized to many modes of the harmonic environment and the dynamics of the system can no longer be described by single particle states. The bosonic bath is designed as a photonic crystal waveguide and we study the effect of multi-photon bound states on the elastic scattering of a single photon. Given the nonclassical many-body states that emerge from the strong hybridization of the qubit with the bath degrees of freedom, we characterize multi-mode entanglement in the system by probing correlations in the photon fields emitted from different discrete modes of the photonic crystal.

Chapter 2

Cavity QED with superconducting circuits

Cavity Quantum Electrodynamics (QED) is an empirical platform for studying the interaction of light and matter [25]. The physics of cavity QED can be explored with superconducting microwave circuits, as these can be engineered to act as artificial atoms with large dipole moments and cavities used for confining microwave photons. This platform, dubbed circuit QED, can easily reach the strong coupling regime of cavity QED, allowing us to integrate quantum optics techniques in solid state systems. Circuit QED combines good coherence with scalable fabrication and thus becomes a leading architecture for quantum information processing. This versatile technology has advanced beyond single qubit experiments and it has also become an attractive architecture for exploring quantum simulation of many-body models. Excellent state-of-the-art reviews can be found in these references [14, 52, 15, 53, 54, 17, 16]. This chapter will cover the necessary concepts for building quantum mechanical objects, atoms and cavities, from superconducting circuits. Emphasis will be placed on their fundamental interaction processes that underpin the techniques for controlling and measuring superconducting qubits as well as building materials from interacting microwave photons.

2.1 Quantization of electrical circuits

Before we dive into designing cavities and artificial atoms from macroscopic electrical circuits, we need to first tackle this remarkable problem of describing electromagnetic circuits in terms of quantum mechanical degrees of freedom. This has been introduced and thoroughly formalized by Yurke and Denker in Ref. [55] and Michel Devoret in Ref. [56, 57], before the field of circuit QED came into existence. In this framework, electromagnetic circuits composed of superconductors are associated with mesoscopic systems, in the sense that they are macroscopic objects composed of a large number of atoms but posses collective degrees of freedom that behave quantum mechanically.

First order of business is to engineer electromagnetic circuits with a simplified low energy spectrum by taking advantage of long-range Coulomb interactions. In Ref. [58], Steve Girvin describes a bulk piece of metal as an oscillating plasma consisting of a gas of electrons and ions. In this simple 'jellium' model, small displacements in the mean electron density are balanced by a restoring Coulomb force from the ions, causing the charge density to oscillate at the plasma frequency $\omega_p = ne^2/m\epsilon_0$, where n is the electron density, e is the electron charge, m is the mass of an electron and ϵ_0 is the vacuum permittivity. In the case of aluminum, this frequency corresponds to $\omega_p/2\pi \sim 3.6\times10^6$GHz. Since electromagnetic waves below the plasma frequency cannot propagate in a plasma, aluminum becomes highly reflective as electrons oscillate very fast and screen out any incoming visible light.

Since we will be operating circuits in the 4-10 GHz frequency range, the microwaves will not penetrate the metal bulk and the electromagnetic fields will be defined outside the metal border which will also set the the boundary conditions for

Maxwell's equations. Additionally, most of the circuits we will consider have a physical size much smaller than the wavelength of their resonant frequency. In this lumped element approximation, each piece of metal can be associated with a point-like node with a given charge or flux, as we will discuss in more detail in the next section. A network of these nodes can then be simply characterized by an inductance and capacitance matrix. For certain configurations, the capacitance and inductance matrices allow collective charge oscillation modes to exist in the microwave regimes. These low energy modes are completely decoupled from the continuum of bulk plasma modes, and are in fact the modes we want to quantize and control.

The second vital ingredient is superconductivity! Ordinary superconductivity is described by the condensation of pairs of electrons of opposite spin (Cooper pairs) into a ground state significantly gapped from the single-excitation band of states where a single Cooper pair is broken. This excitation gap is effectively responsible for reducing the number of degrees of freedom and allowing current to flow in the superconductor network without dissipation, thereby allowing these collective charge modes to be simply described by the charge built up at a node or by the supercurrent flowing in a wire connecting two nodes.

Reducing the Hilbert space of superconducting circuits to just a single degree of freedom (charge or flux) is not enough to justify a quantum mechanical treatment. Not only do we need to cool down the circuit to introduce superconductivity, but we need to operate at a temperature where the corresponding thermal fluctuations are much smaller than the quantum ones associated with the microwave resonance of the circuit $k_B T \ll \hbar\omega_0$. This is the reason why all circuit QED experiments involve anchoring the circuit to cold stage of a dilution refrigerator typically operating in the 10-15 mK. This temperature is much smaller than energy of a 5 GHz microwave photon which corresponds to 240 mK. These circuit are described by many levels associated with different quanta of microwave excitations. Therefore, it becomes equally critical to engineer modes with high quality factor $Q \gg 1$ [56] in order to distinguish these energy states and quantize the circuit.

2.2 Dissipationless circuit components

Any complicated multi-node superconducting circuit can be decomposed into a network of two-node components. Although the list of dissipationless two-node circuit elements is modest, combining them leads to a vast family of circuits with intriguing properties, and it is encouraging to see how this parameter space leaves plenty of room for further exploration.

In this section, we outline these core components, displayed in Fig. 2.1a, classified as linear and nonlinear circuit elements. Each two-node component is defined by the voltage $V(t)$ across the element and the current $I(t)$ flowing through it. The total energy stored in such an element is derived from these variables

$$E(t) = \int_{-\infty}^{t} V(\tau) I(\tau) d\tau. \tag{2.1}$$

Describing electrical circuits follows a similar approach used in classical mechanics, using the Lagrange-Hamilton formalism. This formalism is described in great detail in Ref. [55, 56, 57], and I refer the reader to these references for analyzing circuits in a full quantum picture. A Hamiltonian description requires introducing generalized coordinates for each circuit element. These coordinates can either be the branch fluxes or branch charges defined as

$$\begin{aligned} \Phi(t) &= \int_{-\infty}^{t} V(t') dt' \\ Q(t) &= \int_{-\infty}^{t} I(t') dt'. \end{aligned} \tag{2.2}$$

The choice of using flux or charge as a coordinate is arbitrary. However, it will become clear in the section describing Josephson junctions that choosing a flux coordinate representation is more natural. Depending on the circuit element, the stored energy defined by Eq. 2.1 can be electrical or magnetic, and the choice of coordinate determines if it is regarded as kinetic or potential energy. Since a circuit can contain more branches than there are degrees of freedom, it becomes more intuitive to define the network in terms of the flux and charge variables at each node. The reader is encouraged to visit a more detailed description of this *method of nodes* in [56, 57].

2.2.1 Linear elements: inductor and capacitors

The only linear circuit elements that do not introduce any dissipation are capacitors and inductors. The linearity comes from the fact that the voltage or current has a linear dependence on the generalized circuit coordinates and momenta. This linearity leads to quadratic energy terms in the Hamiltonian.

For instance, the voltage across a capacitor is linearly proportional to charge $V(t) = \frac{1}{C}\left(Q(t) - Q_{\text{ext}}\right)/C$, with a charge and time-independent factor defined as the linear capacitance C. The electrical energy stored in the capacitor is given by $E(t) = \frac{1}{2}CV(t)^2 = \frac{1}{2C}\left(Q(t) - Q_{\text{ext}}\right)^2$.

Similarly, the current flowing through an inductor is proportional to flux $I(t) = \frac{1}{L}\left(\Phi(t) - \Phi_{\text{ext}}\right)$, with a flux and time-independent factor defined as the linear inductance L. The magnetic energy stored in the inductor is given by $E(t) = \frac{1}{2}LI(t)^2 = \frac{1}{2L}\left(\Phi(t) - \Phi_{\text{ext}}\right)^2$. The variables Q_{ext} and Φ_{ext} account for any external charge and flux bias, which can be static or time-varying, and can arise from a classical drive source or from ground state fluctuations of an additional quantum circuit coupled to the these elements.

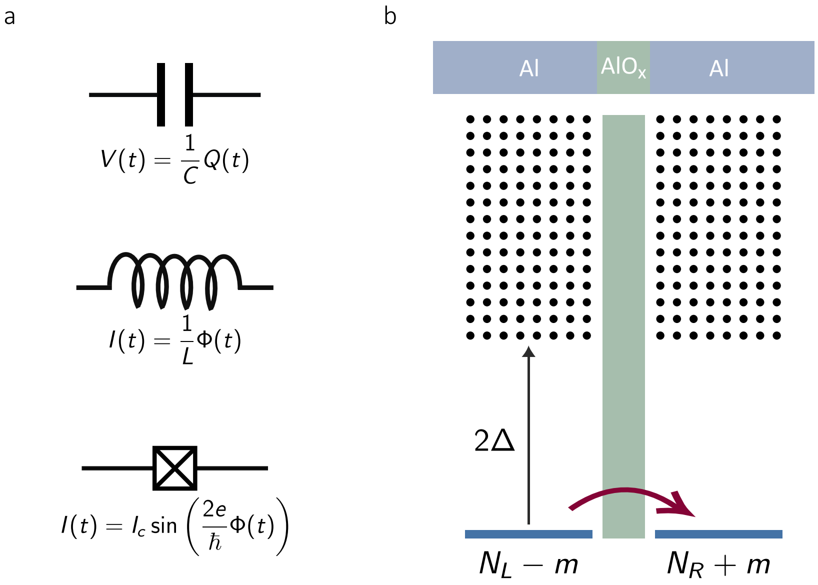

Figure 2.1: **Superconducting circuit components. a.** List of dissipationless circuit components: capacitor, inductor and Josephson tunnel junction. **b.** Energy spectrum of two isolated superconducting islands with gapped degenerate ground states connected by a tunnel barrier set by the Josephson junction.

2.2.2 Nonlinear elements: the Josephson junction

The list of superconducting circuit elements would be incomplete without the Josephson tunnel junction. This special element is the crucial ingredient for designing circuits with an anharmonic energy spectrum, which can function as artificial atoms (qubits), and for mediating interactions between microwave photons. To date, the Josephson junction (JJ) is considered the best electrical component that provides sufficient nonlinearity and introduces very little dissipation at the temperatures we quantize these circuits.

To understand the physical behavior of JJs, we start by considering a single piece of metallic superconductor. In this isolated electrode the total number of electrons is conserved and for now we will assume this number to be even. The physics behind type I superconductors, composed of pure metals, is described by BCS theory [59]. The basic picture is that electrons experience an attractive interaction, virtually mediated by interactions with the lattice phonons, and this leads to pairing of electrons with opposite spin into so-called Cooper pairs. Because we have an even number of electrons, the system is in a highly degenerate ground-state separated from the continuum of single-particle excitations by the superconducting energy gap 2Δ, as shown in Fig. 2.1b. This gap corresponds to the energy needed to break a Cooper pair into two separate quasiparticles. BCS theory predicts a dependence of this gap on the superconducting transition temperature T_c, which at zero temperature corresponds to of $\Delta(T \to 0) = 1.764 k_B T_c$. Aluminum has a transition temperature of $T_c \approx 1.1\mathrm{K}$ and this corresponds to an energy gap $2\Delta/\hbar \approx 140\mathrm{GHz}$. Since the microwaves in our circuits have energies well below the superconducting gap, we can safely reduce the large Hilbert space of this piece of superconductor to a single quantum state defined by the number of Cooper pairs and the phase of the condensate.

The Josephson tunnel junction is composed of two superconducting electrodes connected by a thin insulating barrier. We denote the number of Cooper pairs on each electrode with N_L and N_R, and again acknowledge that the total number $N_L + N_R$ is fixed. The ground-state superconducting wavefunctions on at the electrodes will have a small overlap near the junction, and this leads to coherent tunneling of Cooper pairs across the junction. This phenomena can be described by the following Hamiltonian

$$\mathbf{H}_{\mathrm{JJ}} = -\frac{1}{2} E_{\mathrm{J}} \sum_m \left(|m\rangle\langle m+1| + |m+1\rangle\langle m| \right) \tag{2.3}$$

where the set of degenerate states are labeled by the number of transferred Cooper pairs $|m\rangle = |N_L - m,\ N_R + m\rangle$. This process is shown schematically in Fig. 2.1b. The parameter E_J is termed the Josephson energy which determines the rate at which Cooper pairs can coherently tunnel between the two superconducting electrodes.

The tunneling process in Eq. 2.3 is identical to the model for a one-dimensional tight-binding lattice, with eigenstates described as plane-waves

$$|\varphi\rangle = \sum_{m=-\infty}^{+\infty} e^{im\varphi}|m\rangle, \tag{2.4}$$

where the momentum variables correspond to wavevectors $\varphi = ka$ for a lattice constant $a = 1$. Applying the plane-wave ansatz to the tunneling Hamiltonian, we recover the eigenvalues with the well known cosine dispersion

$$\mathbf{H}_{\mathrm{JJ}}|\varphi\rangle = -E_{\mathrm{J}}\cos\varphi|\varphi\rangle. \tag{2.5}$$

In this φ representation, any arbitrary wavefunction is given by $\psi(\varphi) = \langle\varphi|\phi\rangle$. If we define the total number of tunneled Cooper pairs

$$\mathbf{n} = \sum_{m} |m\rangle m\langle m|, \tag{2.6}$$

the action of this operator on the wavefunction follows the relation $\langle\varphi|\mathbf{n}|\psi\rangle = (\mathbf{n}|\varphi\rangle)^{\dagger}|\psi\rangle = i\frac{d}{d\varphi}\psi(\varphi)$. So it is quite fascinating to find that in this representation, where the dimensionless wavevector φ corresponds to the position of a particle in a potential defined by the Josephson energy $E_{\mathrm{J}}\cos\varphi$, the total number of Cooper pair $\mathbf{n}$ corresponds to the quantum mechanical momentum operator.

To further expand the physical picture of a Josephson junction, we need to include the effect of an external electric field which generates a voltage drop V across the electrodes. The Hamiltonian for this biased junction becomes

$$\mathbf{H}_{\mathrm{JJ}} = -E_{\mathrm{JJ}}\cos\varphi - 2eV\mathbf{n}. \tag{2.7}$$

Writing down Hamilton's equations of motion for the wavevector φ and number $\mathbf{n}$ operator, we can recover the celebrated Josephson relations as follows

$$\begin{aligned}\frac{\partial \mathbf{n}}{\partial t} &= \frac{\partial \mathbf{H}}{\hbar \partial \varphi} = \frac{1}{\hbar} E_J \sin\varphi \\ \frac{\hbar \partial \varphi}{\partial t} &= \frac{\partial \mathbf{H}}{\partial \mathbf{n}} = 2eV.\end{aligned} \tag{2.8}$$

Defining the current operator $\mathbf{I} = 2e\partial\mathbf{n}/\partial t$, the first Hamilton equation yields the DC Josephson relation. This reflects the current flowing through the junction, in the absence of any field, due to Cooper pair tunneling

$$I = I_c \sin\varphi \tag{2.9}$$

where we defined the critical current $I_c = \frac{2e}{\hbar} E_J$ as the maximum possible dissipationless ($V = 0$) current. If more current is forced to pass through the junction, this will induce a nonzero voltage above the excitation gap which will break the ground-state approximation assumed for circuit quantization.

From the second Hamilton equation $\partial_t \varphi = \frac{2e}{\hbar} V$, we recover the AC Josephson relation, inferring the linear time-dependence of the wavevector

$$\varphi(t) = \varphi(0) + \frac{2e}{\hbar} V t. \tag{2.10}$$

This DC voltage leads to an AC current $I(t) = I_c \sin(\varphi(0) + \omega t)$ with a frequency that depends on the applied voltage $\omega = 2eV/\hbar$. This presents a useful tool for measuring voltage with great accuracy.

In this analysis we have ignored Coulomb interactions. Since the Josephson junction also acts as a capacitor, there is a charging energy associated with moving a single electron across the junction. Additionally, an external capacitor can be added in parallel to the junction. This contribution will be included in the later sections outlining how to design qubits with Josephson circuits.

Given the time-derivative of the wavevector is proportional to the voltage leads to a very important insight. If we redefine the flux variable in Eq. 2.2 in reduce-flux units $2\pi\Phi(t)/\Phi_0$, normalized by the magnetic flux quantum $\Phi_0 = \frac{2e}{h}$, we reach the conclusion that the wavevector $\varphi(t) = \frac{2e}{\hbar}\int_{-\infty}^{t} V(t')dt' = 2\pi\Phi(t)/\Phi_0$ in fact corresponds to the reduced-flux across the Josephson junction! This reduced-flux is typically referred to as a dimensionless phase variable since it enters the cosine of the junction energy.

Hopefully the reader is now convinced why it is more intuitive to describe circuits, which will inevitably contain Josephson junction, in terms of generalized flux coordinates. In this representation, the generalized node fluxes φ will play the role of position coordinates, while the number of Cooper pairs at each node $\mathbf{n}$ will correspond to momentum coordinates. In a Lagrange-Hamilton formulation, this associates the electrical energy (from capacitors) with the kinetic term and the magnetic energy (from inductors and Josephson junctions) with the potential term.

2.3 cQED building blocks

So far we have discussed in detail each circuit component (capacitors, inductors, and importantly Josephson junctions) as an individual element. Moving forward, this section will focus on combining these elements into the basic building blocks found in the superconducting circuits toolbox.

2.3.1 Harmonic oscillators: microwave resonators

Thus far, we have parametrized both the linear and nonlinear circuit elements in terms of the generalized flux and total number of Cooper pairs at theirs nodes, without explicitly quantizing these degrees of freedom. To move to the quantum description

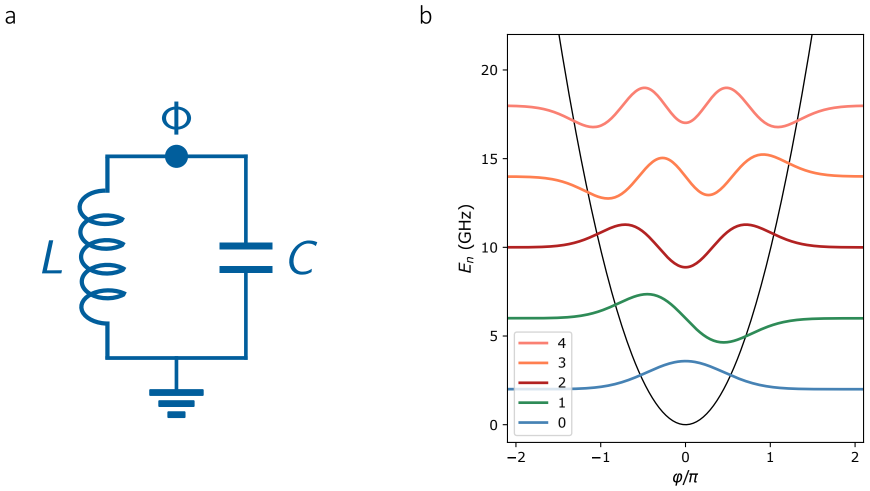

Figure 2.2: **Harmonic oscillator. a.** Circuit diagram of a microwave resonator. **b.** Oscillator wave functions in a parabolic potential, offset displays the energy spectrum of the harmonic ladder.

of these electrical circuits, we can start with the simplest example of a harmonic oscillator implemented with an LC resonator circuit illustrated by the circuit diagram in Fig. 2.2. Although this is a two-node circuit, without loss of generality we can study the dynamics of only one node by connecting the other to ground.

The complexity of this circuit is dramatically reduced to a single degree of freedom corresponding to the magnetic flux across the inductor Φ, or the charge capacitor Q, depending on which variable is associated to a position coordinate and which one is a momentum variable. As mentioned at the beginning of this chapter, this simplification arises from Coulomb interactions which decouple high-energy plasma degrees of freedom, the lumped element approximation (size of the oscillator $\ll \lambda$), and importantly superconductivity which eliminates dissipation and approximates the ground state wavefunction to a single degree of freedom. As elegantly pointed out by Steve Girvin [58], this LC circuit is simply described just by the collective motion of Cooper pairs along the inductor.

Moving to the flux representation, let us define the flux $\Phi(t)$ at the oscillator node. From the definition 2.2, the voltage is given by $V(t) = \dot{\Phi}$ and thus the electrical energy stored in the capacitor becomes $\mathcal{T} = \frac{1}{2}CV^2 = \frac{1}{2}C\dot{\Phi}^2$. From Faraday's law the node flux can be associated with the magnetic flux threading the inductor $\dot{\Phi} = V = L\dot{I}$ and thus the magnetic energy stored in the inductor becomes $\mathcal{U} = \frac{1}{2}LI^2 = \frac{1}{2L}\Phi^2$. Combining the kinetic and inductive contributions, we arrive at the circuit Lagrangian

$$\mathcal{L} = \mathcal{T} - \mathcal{U} = \frac{1}{2}C\dot{\Phi}^2 - \frac{1}{2L}\Phi^2. \tag{2.11}$$

The momentum conjugate to the flux is the charge across the capacitor

$$Q = \frac{\partial \mathcal{L}}{\partial \dot{\Phi}} = C\dot{\Phi}. \tag{2.12}$$

The Hamiltonian can be derived from the Lagrangian using the Legendre transformation

$$\mathbf{H} = Q\dot{\Phi} - \mathcal{L} = \frac{Q^2}{2C} + \frac{\Phi^2}{2L}. \tag{2.13}$$

Obviously, this Hamiltonian describes a harmonic oscillator since it contains quadratic terms in position and momentum. One can draw the analogy with the mechanical harmonic oscillator $\mathbf{H} = p^2/2m + m\omega^2x^2/2$, describing a particle, of mass $m = C$, defined by its position $x = \Phi$, moving in a quadratic potential $x^2/2L$ leading to an oscillating motion with a resonant frequency set by $\omega_r = 1/\sqrt{LC}$.

The coordinate Φ and its conjugate momentum Q can be promoted to quantum operators obeying the canonical commutation relation $[\boldsymbol{\Phi}, \boldsymbol{Q}] = i\hbar$. The Hamiltonian for a harmonic oscillator can be expressed in terms of ladder operators

$$\mathbf{H} = \frac{\boldsymbol{Q}^2}{2C} + \frac{\boldsymbol{\Phi}^2}{2L} = \hbar\omega_r\left(\boldsymbol{a}^\dagger\boldsymbol{a} + \frac{1}{2}\right), \tag{2.14}$$

where $\boldsymbol{a}^\dagger(\boldsymbol{a})$ is the creation (annihilation) operator of a single oscillator excitation (photon) set by the resonant frequency $\omega = 1/\sqrt{LC}$. The flux and charge operators can also be expressed in terms of these operators

$$\begin{aligned} \boldsymbol{Q} &= Q_{\mathrm{zpf}} \left(\boldsymbol{a}^\dagger + \boldsymbol{a}\right) \\ \boldsymbol{\Phi} &= i\Phi_{\mathrm{zpf}} \left(\boldsymbol{a}^\dagger - \boldsymbol{a}\right), \end{aligned} \tag{2.15}$$

where the zero-point fluctuation amplitudes $Q_{\mathrm{zpf}} = \sqrt{\hbar/2Z}$ and $\Phi_{\mathrm{zpf}} = \sqrt{\hbar Z/2}$ depend on the oscillator impedance $Z = \sqrt{L/C}$. The dimensionless parameters correspond to the Cooper pair number $\boldsymbol{n} = \boldsymbol{Q}/2e$ and generalized flux $\boldsymbol{\varphi} = 2\pi\boldsymbol{\Phi}/\Phi_0$.

Since we will later consider coupling qubits to resonators, it is useful to also express the resonator voltage and current in quantized operator form

$$\begin{aligned} \boldsymbol{V} &= \frac{\boldsymbol{Q}}{C} = \sqrt{\frac{\hbar\omega_r}{2C}} \left(\boldsymbol{a}^\dagger + \boldsymbol{a}\right) \\ \boldsymbol{I} &= \frac{\boldsymbol{\Phi}}{L} = i\sqrt{\frac{\hbar\omega_r}{2L}} \left(\boldsymbol{a}^\dagger - \boldsymbol{a}\right), \end{aligned} \tag{2.16}$$

where we identify the root mean square (r.m.s) voltage and current in the resonator ground state

$$\begin{aligned} V_{\mathrm{rms}} &= \langle 0|\boldsymbol{V}^2|0\rangle^{1/2} = \sqrt{\frac{\hbar\omega_r}{2C}} = \omega_r\sqrt{\frac{\hbar Z}{2}} \\ I_{\mathrm{rms}} &= \langle 0|\boldsymbol{I}^2|0\rangle^{1/2} = \sqrt{\frac{\hbar\omega_r}{2L}} = \omega_r\sqrt{\frac{\hbar}{2Z}} \end{aligned} \tag{2.17}$$

2.3.2 Artificial atoms: Josephson circuits

The physics one could explore with superconducting circuits would be limited if we only had harmonic oscillators in our toolbox. Fortunately, this is where the Josephson junction has a crucial contribution. Building circuits composed of JJs allows us to engineer artificial atoms with an anharmonic energy spectrum. This anharmonicity allows us to individually address a subsector of the vast circuit Hilbert space, defining the lowest two levels as our qubit logical subspace, and manipulate the energy states of the circuit using microwave drives resonant with the transition frequency between the logical $|0\rangle$ (ground) and $|1\rangle$ (excited) state.

There is an entire *Mendeleev table* [58] of superconducting qubits and for in this brief introduction we will focus on two widely used circuits with distinct topology. In the first example a single JJ is connected to two isolated superconducting islands and in the second one we consider a JJ embedded in a superconducting loop with a very large kinetic inductance.

Transmon circuit

The most commonly used superconducting qubit is the transmon circuit, a variant of the Cooper pair box (CPB) shown in Fig. 2.3a. The Cooper pair box consists of an superconducting island connected to ground via a JJ, or two islands connected through a JJ. In both cases the circuit is described by the same Hamiltonian. For simplicity, we will consider a single island with a capacitance C_q to ground. The junction itself also has a self-capacitance given by C_J. The superconducting island is electrostatically connected to a charge reservoir through a gate capacitor C_g. This reservoir is modeled as a bias (gate) voltage V_g which induces a dimensionless offset charge $n_g = -C_g V_g/2$. This gate voltage could be an intentionally applied dc or ac voltage, which would make n_g a continuous variable, or the fluctuating ground state voltage of a microwave resonator, which would make n_g a quantum operator. Additionally, this could also be a random voltage associated with local charge noise ubiquitous in solid state devices and this will have dramatic consequences on the lifetime of storing quantum states in this artificial atom.

This circuit is described by the number of Cooper pairs $n = Q/2e$ tunneling on and off the island through the JJ and its conjugate variable, the phase difference

φ across the junction. When describing the circuit Hamiltonian, these degrees of freedom correspond to the position and momentum variables.

The dynamics of the CPB is dictated by the competition between kinetic energy and Coulomb interactions, captured by the two terms in the circuit Hamiltonian

$$\mathbf{H} = -E_J \cos \boldsymbol{\varphi} + 4E_C(\boldsymbol{n} - n_g)^2. \tag{2.18}$$

We already discussed the first term given by the Josephson effect, which is responsible for the tunneling of Cooper pairs through the junction. From the tight-binding analogy, this term delocalizes Cooper pairs from the island.

We haven't discussed yet the second term in Eq. 2.18 when treating the Josephson junction. This corresponds to the charging energy required for electrostatically transferring n Cooper pair to the island. The charging energy for a single Cooper pair is defined as $4E_C = (2e)^2/2C_\Sigma$. The capacitance $C_\Sigma = C_J + C_q + C_g$ is the total capacitance across the junction electrodes, including the contribution from the gate circuit. This term is caused by the Coulomb interaction and has the effect of stabilizing the number of Cooper pairs in the island.

The CPB eigenstates can be precisely determined by numerically diagonalizing Eq. 2.18. It is more convenient to perform this calculation in the charge basis, replacing the Josephson term with Eq. 2.3 and arriving at a Hamiltonian

$$\mathbf{H} = -\frac{E_J}{2} \sum_n \left(|n\rangle\langle n+1| + |n+1\rangle\langle n|\right) + 4E_C \sum_n (n - n_g)^2 |n\rangle\langle n| \tag{2.19}$$

where the Coulomb term is a diagonal matrix and the Josephson term is tri-diagonal. Given the two competing effects from the Josephson and Coulomb terms, we should gain some intuition by comparing two extreme regimes in the parameter space.

When the charging energy dominates $E_C \gg E_J$, we are in the so called *charge regime* where $\boldsymbol{n}$ is a good quantum number. The eigenstates of Eq. 2.18 can be

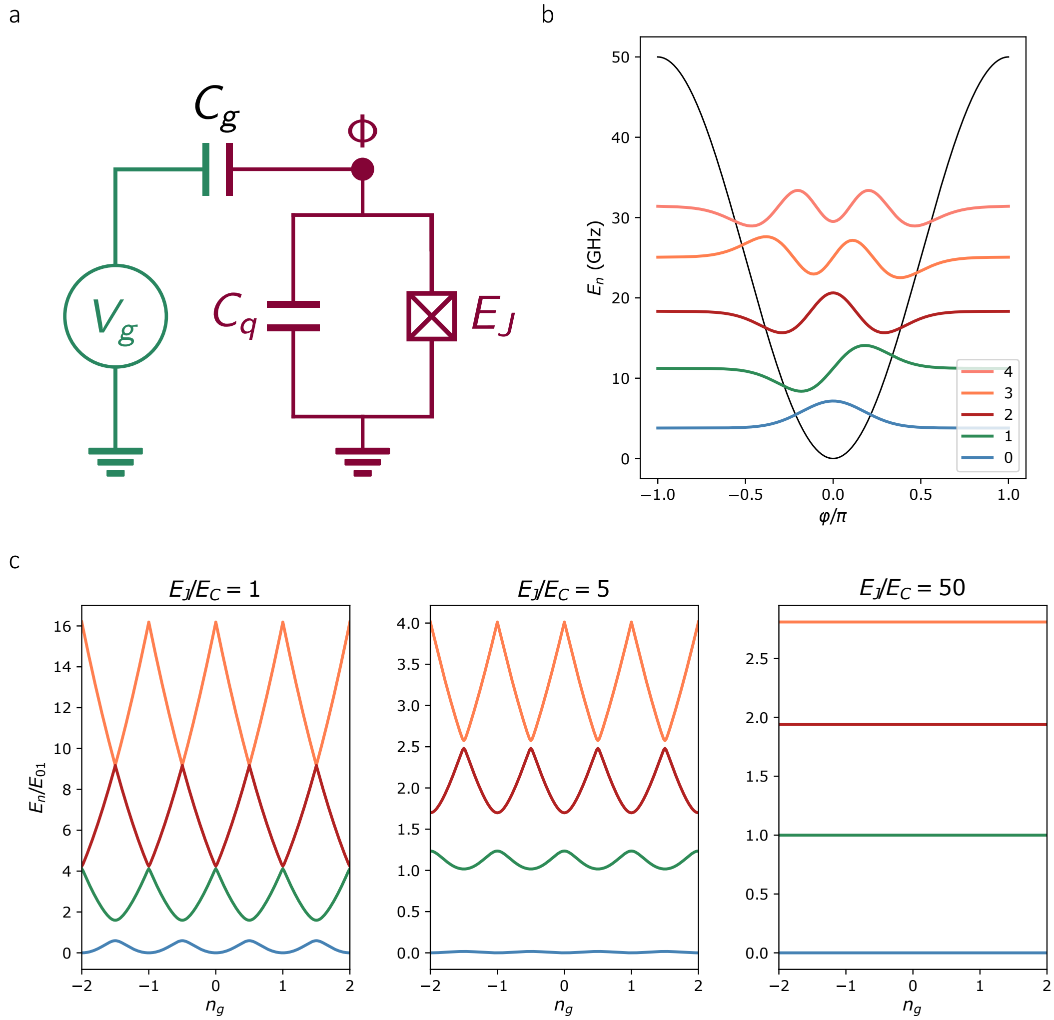

Figure 2.3: **Transmon qubit. a.** Circuit diagram of a Cooper pair box artificial atom. **b.** Energy spectrum in the transmon regime where the phase particle wave functions are localized in the cosine well and the circuit can be approximated as a weakly anharmonic oscillator. **c.** Energy spectrum as a function of gate charge n_g for different values of E_J/E_C, showing a clear exponential decrease in charge dispersion.

represented using only two nearest charge states. For example the ground and first excited states can be approximated using only the first two charge states $\alpha|n = 0\rangle + \beta|n = 1\rangle$. The drawback of encoding quantum states in this regime is that their energies are strongly sensitive to environmental charge noise in n_g, which severely reduces their coherence times.

Entering the *transmon regime* $E_J \gg E_C$ has been shown to provide significant immunity against charge noise [60]. Since the Josephson tunneling is the dominant process, the eigenstates become delocalized in charge space. This means that qubit energy depends on many charge states and is therefore less susceptible to local charge noise. The easiest method to build a CPB in the transmon regime is to increase the total capacitance C_Σ (simply by increasing C_q) which thereby decreases E_C.

Another way to interpret the charge noise susceptibility of the CPB is to discuss the boundary conditions of the wave function. The island charge $\boldsymbol{n}$ is well-defined and has discrete integer eigenvalues which implies that the conjugate phase φ is a compact variable which translates to the circuit eigenstates obeying periodic boundary conditions $|\psi(\varphi + 2\pi)\rangle = |\psi(\varphi)\rangle$. This allows the CPB circuit to be mapped to a charged quantum rotor [60], where $\boldsymbol{\varphi} \in [-\pi, \pi]$ is the angular coordinate and charge plays the role of the conjugate angular momentum $\boldsymbol{n} = \mathbf{L}_z/\hbar$, known to have integer eigenvalues. In this analogy, interestingly, the offset charge corresponds to an Aharanov-Bohm phase shift $n_g = \Phi_{\mathrm{AB}}/\Phi_0$.

In order to remove the offset charge from the CPB Hamiltonian we can perform the gauge transformation $\mathbf{U} = e^{-in_g\varphi}$ which gives $\mathbf{U}(\boldsymbol{n} - n_g)^2\mathbf{U}^\dagger = \boldsymbol{n}^2$. However, in this new frame the wavefunction $\mathbf{U}|\psi\rangle$ no longer obeys periodic boundary conditions $\mathbf{U}|\psi(\varphi + 2\pi)\rangle = e^{-i2\pi n_g}\,[\mathbf{U}|\psi(\varphi)\rangle]$. This change in the boundary condition leads to changes in the eigenstate energies and thus become susceptible to fluctuations in n_g. In this picture, going to the transmon regime $E_J/E_C \gg 1$ produces wave functions with exponentially small support at the boundary $\varphi = \pm\pi$ which dramatically suppresses their susceptibility to n_g noise since the eigenspectrum is less sensitive to changes in the boundary condition.

The dual treatment of the CPB circuit is to consider φ as a position coordinate instead of momentum. Thus the CPB dynamics is described in terms of a particle in phase space, with kinetic energy from the charging energy, moving in an extended cosine potential given by the Josephson energy. In this representation, the he Schrodinger equation takes the form of a Mathieu equation

$$\mathbf{H} = -4E_C\left(i\frac{\partial}{\partial\varphi} - n_g\right)^2 - E_J\cos\boldsymbol{\varphi}, \tag{2.20}$$

where the exact eigenvalue energies are given by Mathieu functions $E_m(n_g)$ [60]. Following the periodicity of the potential, the wave function have the following Bloch wave form $\psi_{mk}(\varphi) = e^{ik\varphi}u_m(\varphi)$, where m is the band index, $k \in \left[-\frac{1}{2}, \frac{1}{2}\right]$ is the wave vector, and u_m obeys periodic boundary conditions $u_m(\varphi + 2\pi) = u_m(\varphi)$. Applying the gauge transformation and boundary condition imposed in the previous analogy, we find the remarkable observation that the spectrum for the charged rotor is equivalent to the band structure of a one dimensional solid in a cosine potential [58], where the offset charge is equivalent to the Bloch wavevector.

In the limit of large E_J/E_C, we can approximate the lower energy levels using a tight binding model where the phase particle is hopping between adjacent wells in the cosine potential. The band structure for the m^{th} level has the expected cosine form $E_m(n_g) \approx E_m(n_g = 1/4) + \frac{1}{2}\epsilon_m\cos(2\pi n_g)$, where the bandwidth ϵ_m defines the charge dispersion. Within the WKB approximation [60], the charge dispersion becomes

$$\epsilon_m \approx (-1)^m E_C \frac{2^{4m+5}}{m!}\sqrt{\frac{2}{\pi}}\left(\frac{E_J}{2E_C}\right)^{\frac{m}{2}+\frac{3}{4}}\exp\left(-\sqrt{8E_J/E_C}\right), \tag{2.21}$$

which is valid for $E_J/E_C \gg 1$. Therefore it becomes clear how working in the transmon regime we can exponentially suppress charge noise sensitivity by increasing E_J/E_C. This is shown in Fig. 2.3c where we numerically calculate the CPB energy eigenvalues as a function of n_g for values of E_J/E_C covering both the charge and transmon regime. The upshot is that moving deeper in the transmon regime, the circuit becomes more harmonic. Nevertheless, we can operate in a comfortable parameter regime where charge noise susceptibility can be negligible while the anharmonicity

$(E_{12} - E_{01})/\hbar$ can be 150-250 MHz, which provides enough bandwidth to perform high-fidelity control pulses on the lowest two states of the transmon.

In the deep transmon regime $E_J/E_C \gg 1$, the phase particle wave function is strongly localized in the cosine well (Fig. 2.3b) with small phase excursions around the minimum. This justifies the Taylor series expansion of the cosine potential which leads to the following CPB Hamiltonian

$$\mathbf{H} \approx 4E_C\boldsymbol{n}^2 - E_J\left(-\frac{1}{2}\boldsymbol{\varphi}^2 + \frac{1}{24}\boldsymbol{\varphi}^4 + \mathcal{O}(\boldsymbol{\varphi}^6)\right). \tag{2.22}$$

We can write the quadratic part in terms of creation and annihilation operators $4E_C\boldsymbol{n}^2 + \frac{1}{2}E_J\boldsymbol{\varphi}^2 = \hbar\omega\boldsymbol{a}^\dagger\boldsymbol{a}$, where the phase operator becomes $\boldsymbol{\varphi} = \varphi_{\text{zpf}}(\boldsymbol{a}^\dagger + \boldsymbol{a})$,with $\varphi_{\text{zpf}} = \sqrt{2E_C/E_J}$. The quartic part of the Josephson potential is the leading nonlinearity in the circuit which can be expanded into $\frac{1}{24}E_J\varphi_{\text{zpf}}^4(\boldsymbol{a}^\dagger + \boldsymbol{a})^4 = -\frac{1}{2}E_C(\boldsymbol{a}^\dagger\boldsymbol{a}^\dagger\boldsymbol{a}\boldsymbol{a} + 2\boldsymbol{a}^\dagger\boldsymbol{a})$, where rapidly-rotating terms were removed (rotating wave approximation). Putting all these terms together we find that in the limit $E_J/E_C \gg 1$ the transmon can be described as a weakly Kerr-nonlinear oscillator

$$\mathbf{H}/\hbar \approx \omega_q\boldsymbol{a}^\dagger\boldsymbol{a} + \frac{\alpha}{2}\boldsymbol{a}^\dagger\boldsymbol{a}^\dagger\boldsymbol{a}\boldsymbol{a}, \tag{2.23}$$

where the transition frequency between the lowest two states is $\omega_q = \sqrt{8E_JE_C} - E_C$ and the anharmonicity corresponds to $\alpha = -E_C$. It needs to be emphasized that these expressions are valid in the asymptotic limit $E_J/E_C \to \infty$ and to get the precise values for the eigenspectrum and eigenstates one needs to numerically diagonalize the Hamiltonian in either the charge of phase representation. This perturbative form of the Hamiltonian makes the transmon an appealing building block for studying Bose-Hubbard physic in transmon lattices [50, 51], with on-site two-body interactions $U\boldsymbol{a}^\dagger\boldsymbol{a}^\dagger\boldsymbol{a}\boldsymbol{a}$ simply given by the anharmonicity.

Fluxonium circuit

A different class of superconducting qubits consists of a JJ shunted by an inductor. Early investigations on this type of qubit were performed with the flux qubit [61], a superconducting loop consisting of a small junction shunted by a few JJs with a comparable junction energy. In this circuit, the shunting inductor is nonlinear and the Hamiltonian description needs to include the cosine energy for all junctions. Given the large potential energy of the shunting inductor, flux qubits are very sensitive to flux noise. Nevertheless, recent work has shown that flux qubits shunted by a large capacitor can approach the coherence times of transmons [62]. In this thesis we will work with the fluxonium qubit [63], where the junction is shunted by a linear inductor with a large inductance value which decreases the qubit spectrum sensitivity to flux noise. This large inductance is provided by the kinetic inductance of a long chain of large Josephson junctions that behave as linear inductors, the fluxonium circuit is schematically shown in Fig. 2.4a.

In the CPB circuit, the two islands are only connected through the JJ which tunnels an integer number of Cooper pairs n. We also discussed how in this circuit topology the phase difference across the junction φ is a compact angular variable which implies that the eigenstates obey periodic boundary conditions $|\psi(\varphi)\rangle = |\psi(\varphi + 2\pi)\rangle$. This argument also comes from describing the CPB dynamics in terms of a phase particle in a periodic potential $E_J \cos\varphi$. This pictures changes profoundly when shunting a JJ with an external inductor. The energy stored in the inductor is given by $\frac{1}{2}E_L\varphi^2$, $E_L = \left(\frac{\Phi_0}{2\pi}\right)^2 \frac{1}{L}$, and it is not periodic in φ. As such, the potential energy is different at φ and $\varphi + 2\pi$ which also makes the eigenstates different. Since the system no longer obeys periodic boundary conditions, φ is no longer a compact variable and the charge variable n is no longer an integer since Cooper pairs can be continuously transfered through the external inductor.

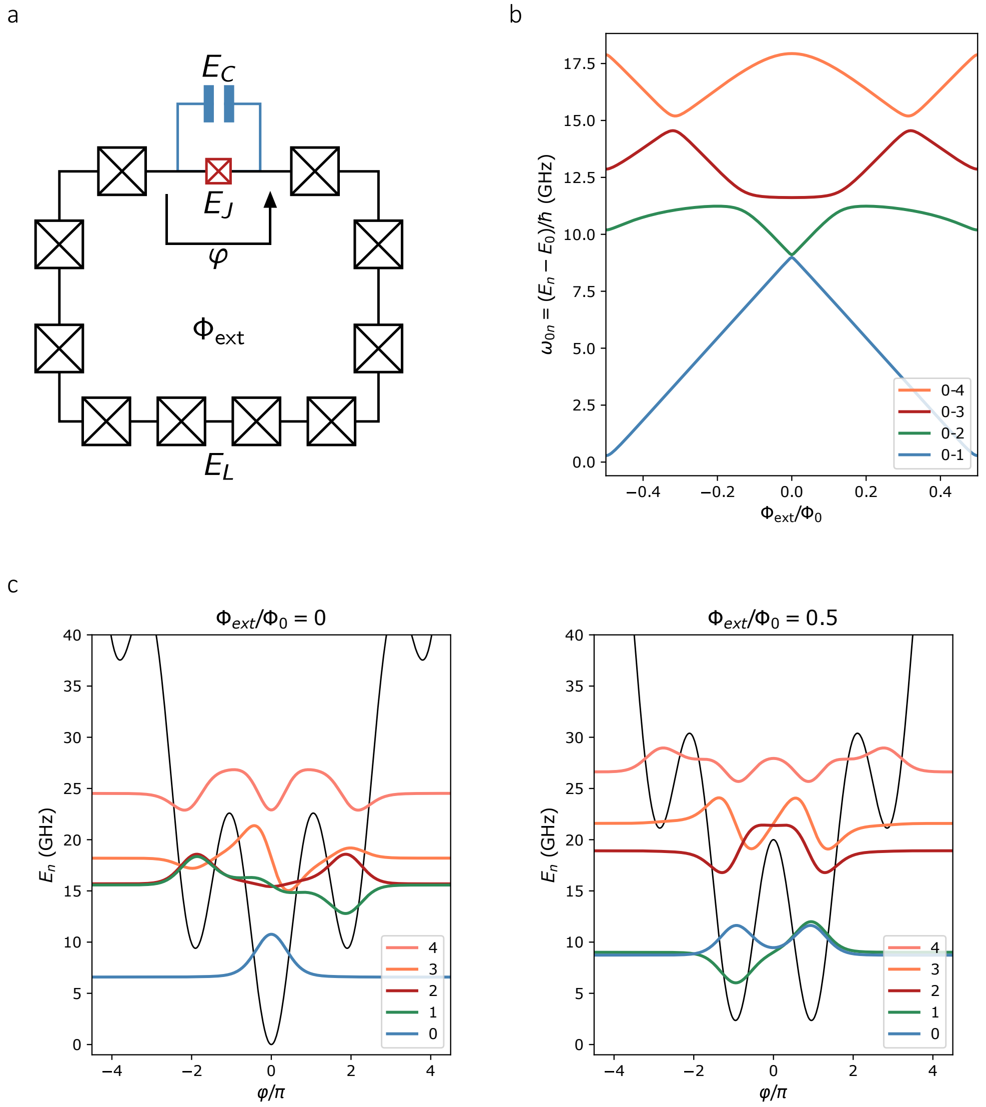

Figure 2.4: **Fluxonium qubit. a.** Circuit diagram of a fluxonium artificial atom. **b.**Transition energy spectrum for the fluxonium parameters $E_J/\hbar = 10\,\text{GHz}$, $E_C/\hbar = 2.5\,\text{GHz}$, $E_L/\hbar = 0.5\,\text{GHz}$. **c.** Eigenstate wave functions and energies in the fluxonium phase potential, biased at $\Phi_{\text{ext}}/\Phi_0 = 0$ (left) and $\Phi_{\text{ext}}/\Phi_0 = 0.5$ (right).

Given that n is now a continuous variable, the static offset charge n_g can be screened from the energy spectrum. A more solid argument comes from evaluating the wave functions boundary conditions and how they change with respect to the offset charge. For the CPB, we found that gauge transformation for removing the offset charge led to new wave functions which no longer satisfied periodic boundary conditions. For the fluxonium, due to the diverging inductive energy, the wave functions satisfy vanishing boundary conditions $\psi(\varphi \to \pm\infty) \to 0$, and the transformed wave functions $\mathbf{U}\psi$ obey the same condition. Thus the energy spectrum for inductively shunted qubits does not depend on the static offset charge.

Since the phase across the JJ is now a continuous, non-compact variable, we can now define it as an operator $\boldsymbol{\varphi}$. The fluxonium circuit Hamiltonian is given by

$$\mathbf{H} = 4E_C\boldsymbol{n}^2 - E_J\cos(\boldsymbol{\varphi} - \varphi_{\text{ext}}) + \frac{1}{2}E_L\boldsymbol{\varphi}^2. \tag{2.24}$$

The interplay between the quadratic inductive energy and the cosine Josephson energy gives rise to different potential energy profiles with unique level structure and wave function profiles. The potential energy landscape and therefore the qubit states are tuned with an applied magnetic flux enclosing the loop, $\varphi_{\text{ext}} = 2\pi\Phi_{\text{ext}}/\Phi_0$. This external control knob is equivalent to the gate offset charge in the CPB.

The potential energy profile and fluxonium wave functions are shown in Fig. 2.4c for circuit parameters of a light fluxonium $E_J = 10\text{GHz}, E_C = 2.5\text{GHz}, E_L = 0.5\text{GHz}$. When the external flux is zero $\phi_{\text{ext}} = 0$, the ground state eigenfunction is localized in the deep well around $\varphi = 0$ and higher excited states have support in the nearby higher potential wells. In this arrangement, the circuit resembles an artificial atom with a V level configuration. When the external flux is half a flux quantum $\phi_{\text{ext}} = \pi$, we have a double potential well profile where the first two eigenstates are symmetric and antisymmetric superpositions of states living in each well and are largely detuned in energy from the next excited state. In this arrangement, the circuit resembles an artificial atom with a Λ level configuration. Transitions between states lying in the same well are called *plasmon* transitions in connection to plasma oscillations in a JJ, while transitions between states in different wells are referred to as *fluxon* transitions described by a direction change of the persistent current in the fluxonium loop.

The transition energy spectrum of the fluxonium circuit is plotted in Fig. 2.4b. Fluxon transitions are strongly coupled to the applied flux, as shown by the zigzag dispersion of the lowest fluxon transition, while plasmon transitions are almost insensitive to the applied flux. An appealing feature of the fluxonium qubit, which makes it unique over the transmon, is its large anharmonicity when biased at half flux $\phi_{\text{ext}} = \pi$ where the fluxon transition is first order insensitive to flux noise and has been shown to achieve large coherence times $T_2 > 250\mu s$ [64, 65]. For the work outlined in Chapter 5, the fluxonium is an ideal quantum impurity given its large nonlinearity, making an ideal two-level system, and large magnetic dipole moment, ideal for reaching the ultra-strong coupling regime.

2.4 Coupling two resonators

After becoming familiar with the basic building blocks in circuit QED, it would be useful to understand how to formalize the coupling between these elements. Rather than focusing on each component individually, qubits and resonators give rise to more intriguing physics when you compile a multitude of these elements and have them interact with one another. The easiest example to start with is two LC resonators connected through a coupling capacitor as shown in Fig. 2.5. This will prepare us later on how to treat a lattice of microwave resonators as well as to understand the dipole coupling between a qubit and a resonator.

Describing both resonators in terms of their flux nodes Φ_a and Φ_b, the Lagrangian can be expressed as

$$\mathcal{L} = \frac{C_a}{2}\dot{\Phi}_a^2 + \frac{C_b}{2}\dot{\Phi}_b^2 + \frac{C_c}{2}\left(\dot{\Phi}_a - \dot{\Phi}_b\right)^2 - \frac{1}{2L_a}\Phi_a^2 - \frac{1}{2L_b}\Phi_b^2. \tag{2.25}$$

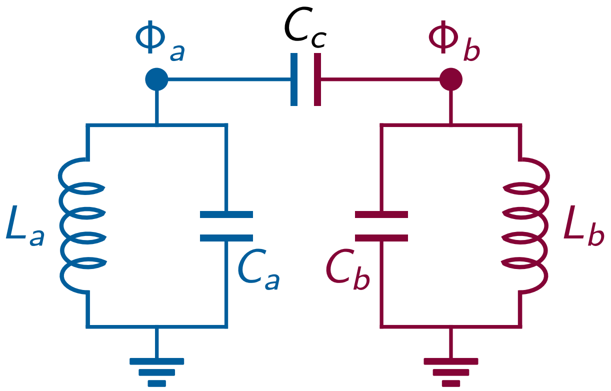

Figure 2.5: **Coupled harmonic oscillators.** Circuit diagram for coupling the nodes of two LC resonators coupled with a capacitor.

The Lagrangian is quadratic in the coordinate variables because the circuits consists only of linear elements. This allows us to conveniently rewrite it in matrix form

$$\mathcal{L} = \frac{1}{2}\dot{\vec{\boldsymbol{\Phi}}}^{\mathrm{t}}\hat{\boldsymbol{C}}\dot{\vec{\boldsymbol{\Phi}}} - \frac{1}{2}\vec{\boldsymbol{\Phi}}^{\mathrm{t}}\hat{\boldsymbol{L}}^{-1}\vec{\boldsymbol{\Phi}} \tag{2.26}$$

in terms of the flux and voltage coordinate vectors $\vec{\boldsymbol{\Phi}} = [\Phi_a, \Phi_b]^{\mathrm{t}}$ and $\dot{\vec{\boldsymbol{\Phi}}} = [\dot{\Phi}_a, \dot{\Phi}_b]^{\mathrm{t}}$, using the capacitance and inverse inductance matrices

$$\hat{\boldsymbol{C}} = \begin{pmatrix} C_a + C_c & -C_c \\ -C_c & C_b + C_c \end{pmatrix}, \ \hat{\boldsymbol{L}}^{-1} = \begin{pmatrix} \frac{1}{L_a} & 0 \\ 0 & \frac{1}{L_b} \end{pmatrix}. \tag{2.27}$$

The canonical momenta, which correspond to the charge variables, are simply found from $\vec{\boldsymbol{Q}} = \partial\mathcal{L}/\partial\dot{\vec{\boldsymbol{\Phi}}} = \hat{\mathbf{C}}\dot{\vec{\boldsymbol{\Phi}}}$. The Hamiltonian for the coupled resonators is given by the Legendre transformation $\mathbf{H} = \vec{\boldsymbol{Q}}^{\mathrm{t}}\dot{\vec{\boldsymbol{\Phi}}} - \mathcal{L}$ and takes a similar quadratic form

$$\mathbf{H} = \frac{1}{2}\vec{\boldsymbol{Q}}^{\mathrm{t}}\hat{\boldsymbol{C}}^{-1}\vec{\boldsymbol{Q}} + \frac{1}{2}\vec{\boldsymbol{\Phi}}^{\mathrm{t}}\hat{\boldsymbol{L}}^{-1}\vec{\boldsymbol{\Phi}}. \tag{2.28}$$

The inverse of the capacitance matrix is

$$\hat{\boldsymbol{C}}^{-1} = \frac{1}{C_aC_b + C_bC_c + C_cC_a} \begin{pmatrix} C_b + C_c & C_c \\ C_c & C_a + C_c \end{pmatrix}. \tag{2.29}$$

Without having to explicitly write down the values of the inductance and capacitance matrices, the Hamiltonian can be expanded in a more intuitive form

$$\mathbf{H} = \frac{1}{2}\hat{\boldsymbol{C}}^{-1}_{[1,1]}Q_a^2 + \frac{1}{2}\hat{\boldsymbol{L}}^{-1}_{[1,1]}\Phi_a^2 + \frac{1}{2}\hat{\boldsymbol{C}}^{-1}_{[2,2]}Q_b^2 + \frac{1}{2}\hat{\boldsymbol{L}}^{-1}_{[2,2]}\Phi_b^2 + \hat{\boldsymbol{C}}^{-1}_{[1,2]}Q_aQ_b \tag{2.30}$$

as a summation of two harmonic oscillator terms and a capacitive contribution which linearly couples their charge degrees of freedom. This representation will be useful later in this thesis when describing array of microwave resonators in a tight-binding lattice formalism. The resonators can also be inductively coupled through a mutually shared inductance which translates to a coupling term $\Phi_a\Phi_b$ in the Hamiltonian. We will revisit this discussion when considering the two types of dipole couplings between a Josephson qubit and a resonator, which will have a dramatic consequence on the magnitude of coupling strength.

Moving to the quantum mechanical picture, the flux Φ_j and charge Q_j variables are promoted to quantum variables, $\hat{\Phi}_j$ and $\hat{Q}_j$, which obey the canonical commutation relation for bosonic operators $\left[\hat{\Phi}_{\mathrm{n}}, \hat{Q}_{\mathrm{m}}\right] = \mathrm{i}\hbar\delta_{n,m}$. Given the harmonic oscillator terms in the Hamiltonian, we can express the charge and flux operators in terms of creation and annihilation operators $\hat{Q}_k = \sqrt{\frac{\hbar}{2}}\, Z_k^{-\frac{1}{2}} \left(\boldsymbol{k}^\dagger + \boldsymbol{k}\right)$ and $\hat{\Phi}_k = \mathrm{i}\sqrt{\frac{\hbar}{2}}\, Z_k^{\frac{1}{2}} \left(\boldsymbol{k}^\dagger - \boldsymbol{k}\right)$ for $k = a, b$. The resonators characteristic impedance entering the zero point fluctuation amplitudes has the expression $Z_k^2 = \hat{\boldsymbol{C}}^{-1}_{[k,k]}/\hat{\boldsymbol{L}}^{-1}_{[k,k]}$.

It is important to notice that in this uncoupled basis, each individual resonator has capacitive contributions from the neighboring resonator as well as the coupling capacitance. This is evident from the expression of the renormalized self-capacitance

$\hat{\boldsymbol{C}}^{-1}_{[1,1]} = \left(C_a + \frac{C_b C_c}{C_b + C_c}\right)^{-1}$, which is equal to the resonator self-capacitor in parallel with the series combination of the coupling capacitor and neighboring resonator capacitor. The same applies for the capacitance of the other resonator.

Rewriting the Hamiltonian in equation 2.30 in this second-quantized basis gives

$$\mathbf{H}/\hbar = \omega_a \left(\boldsymbol{a}^\dagger \boldsymbol{a} + \frac{1}{2}\right) + \omega_b \left(\boldsymbol{b}^\dagger \boldsymbol{b} + \frac{1}{2}\right) + J(\boldsymbol{a}^\dagger + \boldsymbol{a})(\boldsymbol{b}^\dagger + \boldsymbol{b}) \tag{2.31}$$

This describes two harmonic oscillators with resonant frequencies $\omega_k^2 = \hat{\boldsymbol{L}}^{-1}_{[k,k]} \hat{\boldsymbol{C}}^{-1}_{[k,k]}$, linearly coupled in a beam splitter fashion where microwave excitations can tunnel between these two resonators with a hopping rate $J = \frac{1}{2}\left(Z_a Z_b\right)^{\frac{1}{2}} \hat{\boldsymbol{C}}^{-1}_{[1,2]}$.

2.5 Coupling a Josephson qubit to a resonator: strong to ultrastrong

The interaction between light and matter is embodied in the alteration of each components physical properties from the mutual influence on each other. If we consider a single hydrogen-like atom coupled to the time-varying electromagnetic field in a cavity, the dielectric perturbation of the atom is manifested in the addition of the electromagnetic vector potential $\boldsymbol{A}$ in the atoms kinetic energy [25]

$$\mathbf{H} = \frac{1}{2m_e}\left(\vec{\boldsymbol{p}} + e\vec{\boldsymbol{A}}\right)^2 - \frac{e^2}{4\pi\epsilon_0 |\vec{\boldsymbol{r}}|}. \tag{2.32}$$

Expanding the kinetic term we arrive at the coupling between the light field and atom

$$\mathbf{H}_c = \frac{e\vec{\boldsymbol{p}} \cdot \vec{\boldsymbol{A}}}{m_e}, \tag{2.33}$$

which can be rewritten in a more familiar form $\mathbf{H}_c = \vec{\boldsymbol{d}} \cdot \vec{\boldsymbol{E}}$ which describes the atom electric dipole moment $\vec{\boldsymbol{d}} = e\vec{\boldsymbol{r}}$ coupled to the electric field of light.

In this section we explore light-matter coupling between an artificial Josephson atom to the electromagnetic field in a microwave resonator, where the presence of the qubit generates a strong perturbation in the resonator impedance. For simplicity, we chose the CPB as our Josephson atom. Nevertheless, the result will be formalized in a generic form, similar to the dipole coupling model for real atoms, that applies to any multi-level qubit with well understood selection rules.

In circuit language, separate components can interact in two ways, by capacitively coupling their voltages or inductively coupling their currents. In atomic physics language, these approaches are equivalent to coupling the field to the electric or magnetic dipole moment of the atom. The capacitive coupling between a qubit and resonator is the preferred approach adopted by the field, enough for exploiting strong-coupling physics. However, we will discover that the inductive coupling method can be adopted to explore light-matter coupling in the ultra-strong regime. This picture will later be generalized for a highly nonlinear Josephson atom coupled to a multi-mode lattice of microwave resonators in Chapter 5.

2.5.1 Capacitive coupling

We start with the circuit in Fig. 2.6 for a CPB coupled to a lumped element LC resonator. For simplicity, the resonator and CPB are each described by a single superconducting island with the corresponding node fluxes defined as Φ_r and Φ_q. The coupled circuit Lagrangian becomes

$$\mathcal{L} = \frac{C_r}{2}\dot{\Phi}_r^2 - \frac{1}{2L_r}{\Phi_r}^2 + \frac{C_q}{2}\dot{\Phi}_q^2 + E_J \cos\left(2\pi\frac{\Phi_q}{\Phi_0}\right) + \frac{C_g}{2}\left(\dot{\Phi}_q - \dot{\Phi}_r\right)^2. \tag{2.34}$$

The first two terms are associated with the resonator and the next two terms are associated with the CPB. The value of C_q contains the contributions from the junction self-capacitance and the external shunting capacitor. The last term accounts for the

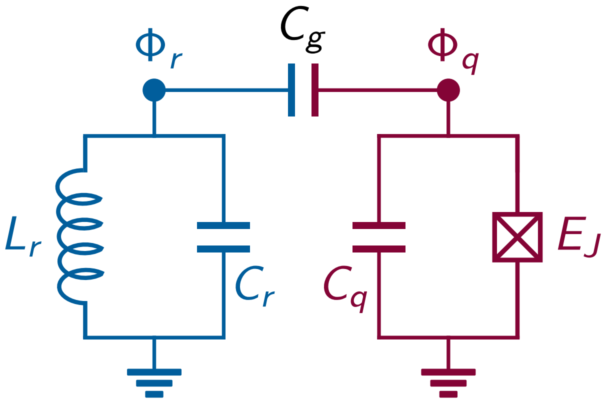

Figure 2.6: **Capacitive dipole coupling.** Circuit diagram of a transmon qubit capacitively coupled to a microwave resonator.

kinetic energy of the coupling capacitance C_g, which effectively leads to the charge coupling between the resonator and qubit as well as a renormalization of their effective capacitance. For simplicity we ignore the CPB offset charge from a dc bias voltage.

Given that the effective JJ inductance is nonlinear, we can't write the Lagrangian in a quadratic form similar to Eq. 2.26. Nevertheless, if we ignore the potential energy terms, we can notice that the capacitive network is similar to the coupled oscillator circuit and we therefore expect to get the same form for the inverse capacitance matrix derived in Eq. 2.27. The conjugate charge variables Q_r and Q_q for the resonator and qubit islands can determined using this inverse capacitance matrix $[\dot{\Phi}_r, \dot{\Phi}_q]^t = \hat{\mathbf{C}}^{-1}[Q_r, Q_q]^t$. Following the Legendre transformation, we arrive at the coupled resonator-qubit Hamiltonian

$$\begin{aligned}\mathbf{H} &= Q_r\dot{\Phi}_r + Q_q\dot{\Phi}_q - \mathcal{L}\\ &= \mathbf{H}_r + \mathbf{H}_q + \mathbf{H}_{\text{int}}\\ &= \frac{\boldsymbol{Q}_r^2}{2C_{r\Sigma}} + \frac{\boldsymbol{\Phi}_r^2}{2L_r} + \frac{\boldsymbol{Q}_q^2}{2C_{q\Sigma}} - E_J\cos\left(2\pi\frac{\boldsymbol{\Phi}_q}{\Phi_0}\right) + \frac{\beta_C}{C_{r\Sigma}}\boldsymbol{Q}_r\boldsymbol{Q}_q,\end{aligned} \tag{2.35}$$

divided into the individual Hamiltonians for the resonator $\mathbf{H}_r$ and CPB $\mathbf{H}_q$ and the interaction between their charge degrees of freedom $\mathbf{H}_{\text{int}}$ described by the last term. Note that the gate capacitor leads to the renormalization of the resonator $C_{r\Sigma} = C_r + \frac{C_q C_g}{C_q + C_g}$ and CPB capacitance $C_{q\Sigma} = C_q + \frac{C_r C_g}{C_r + C_g}$.

In the last line of Eq. 2.35 we already moved to the quantum picture by promoting the resonator and qubit variables to quantum operators. The resonator Hamiltonian can be rewritten as a harmonic oscillator in terms of raising and lowering operators (Eq. 2.14). This allows expressing the charge and flux operators in a second quantized form as $\boldsymbol{Q}_r = \sqrt{\frac{\hbar Z_r}{2}} \left(\boldsymbol{a}^\dagger + \boldsymbol{a}\right)$ and $\boldsymbol{\Phi}_r = i\sqrt{\frac{\hbar}{2 Z_r}} \left(\boldsymbol{a}^\dagger - \boldsymbol{a}\right)$, with the resonator impedance given by $Z_r = \sqrt{L/C_{r\Sigma}}$.

The CPB can also be written in terms of harmonic ladder operators in the deep transmon regime where it behaves as a Kerr-nonlinear resonator. Since we want to arrive at a general result, we will describe the qubit as a multilevel circuit $\mathbf{H}_q = \sum \varepsilon_k |k\rangle\langle k|$, with corresponding eigenenergies ε_k and eigenvectors $|k\rangle$. The charge operator can be simply decomposed into raising and lowering operators $|j\rangle\langle k|$ with their corresponding matrix elements $Q_{jk} = \langle j|\boldsymbol{Q}|k\rangle$, leading to the general form $\boldsymbol{Q}_q = \sum_{j,k} Q_{jk} |j\rangle\langle k|$. These matrix elements effectively dictate the selection rules for the artificial atom. We can further truncate the operator to focus only on the lowest two states, the ground $|g\rangle$ and first excited $|e\rangle$ states. This simplifies the expression into $\boldsymbol{Q}_q = 2e\langle g|\boldsymbol{N}|e\rangle \sigma_x$, written in terms of the Cooper pair number operator $\boldsymbol{N} = \boldsymbol{Q}/2e$ to decouple the fundamental constants from the final expression.

Finally we arrive at the dipole coupling for the effective two-level artificial atom to the quantized resonator field

$$\begin{aligned} \mathbf{H}_{\text{int}} &= 2e\boldsymbol{N} \cdot \beta_C \boldsymbol{V}_r \\ &= 2e\beta_C \omega_r \sqrt{\frac{\hbar Z_r}{2}} \langle g|\boldsymbol{N}|e\rangle \left(\boldsymbol{a}^\dagger + \boldsymbol{a}\right) \sigma_x \triangleq g_C \left(\boldsymbol{a}^\dagger + \boldsymbol{a}\right) \sigma_x. \end{aligned} \tag{2.36}$$

The first line is intentionally written to resemble the expression for the dipole interaction for a hydrogenic atom $\vec{\boldsymbol{d}} \cdot \vec{\boldsymbol{E}}$. From this it becomes clear that $2e\boldsymbol{N}$ plays the role of the dipole moment. The CPB atom can be envisioned as a $2e$ charged particle oscillating between the largely separated two capacitor pads, giving rise to a significant dipole moment. Additionally, the resonator electric field corresponds to the effective voltage bias induced by the resonator $\beta_C \boldsymbol{V}_r = \beta_C \boldsymbol{Q}_r / C_{r\Sigma}$. The prefactor $\beta_C = Cg/(Cg+Cq)$ represents the fraction of the resonator voltage effectively applied on the qubit node if you regard the capacitive network as a voltage divider.

At a higher level, this type of light-matter interaction $\sigma_x(\boldsymbol{a}^\dagger + \boldsymbol{a})$ is found in the quantum Rabi model [66] used for describing various physical phenomena in quantum optics and solid state systems. This model contains terms $(\boldsymbol{a}^\dagger \sigma_- + \boldsymbol{a}\sigma_+)$ that preserve particle number as well as counter-rotating terms $(\boldsymbol{a}^\dagger \sigma_+ + \boldsymbol{a}\sigma_-)$ that do not. For coupling strengths, defined as g_C in Eq. 2.36, orders of magnitude smaller than the natural frequencies of cavity and atom, one can perform the rotating wave approximation (RWA) to get rid of the counter-rotating terms and arrive at the well know Jaynes Cummings model [67]. Provided that the coupling strength is larger than the sources of loss in the system, this model yields the strong-coupling regime of light-matter interaction, used in the superconducting quantum computing field for performing gate operations and reading out the quantum state of the qubits [53].

When the coupling strength becomes comparable with the natural frequencies of the noninteracting system $g/\omega \geq 0.1$, the RWA is no longer valid. This is defined as the ultrastrong coupling regime (USC) where the presence of counter rotating terms produce novel physical phenomena [68, 69].

To understand the fundamental limitations for the capacitive coupling scheme, we can write the coupling strength in Eq. 2.36 in a dimensionless form normalized by the resonator frequency

$$\frac{g_C}{\omega_r} = \beta_C \sqrt{\frac{Z_r}{Z_{\text{vac}}}} \langle g|\boldsymbol{N}|e\rangle \alpha^{1/2}, \tag{2.37}$$

where $Z_{\text{vac}} = \sqrt{\mu_0/\varepsilon_0} \simeq 377\,\Omega$ is the vacuum impedance and $\alpha = 1/137$ is the fine structure constant. When the CPB circuit is in the charge regime, biased at the degeneracy point where the charge states are equal superpositions $|g\rangle, |e\rangle = \frac{1}{\sqrt{2}}(|0\rangle \pm |1\rangle)$, the dipole moment becomes $\langle g|\boldsymbol{N}|e\rangle = \frac{1}{\sqrt{2}}$. When biased in the transmon regime, the dipole moment is given by $\langle g|\boldsymbol{N}|e\rangle = \frac{1}{\sqrt{2}}\left(\frac{E_J}{8E_C}\right)^{1/4}$.

As pointed out by Devoret *et al.* [70], Eq. 2.40 bares resemblance with the dimensionless coupling of a Rydberg atom coupled to an optical cavity field given by

$$\frac{g}{\omega_r} = \frac{\alpha^{3/2}}{n}\frac{1}{\sqrt{V}}, \tag{2.38}$$

where V corresponds to the field mode volume and n corresponds to the principal quantum number of the atom. For the CPB in the transmon regime, we can see that the ratio $E_J/E_C \gg 1$ plays to role of the principal quantum number.

From this analogy we can see that the dimensionless capacitive coupling for superconducting circuit has the same limiting factor as its atomic analogues, namely constrained by the fact that the fine structure constant is a small number $\alpha = 1/137 \ll 1$. The fine structure constant in Eq. 2.40 enters as a square root instead of $\alpha^{3/2}$ in Eq. 2.38 due to the one-dimensional field in the resonator. In practice, for normal resonator impedances $Z = 50\,\Omega$, the coupling strength is too small to enter the ultrastrong coupling regime $g/\omega \simeq 10^{-2}$. Nevertheless, given that we can engineer superconducting circuit with huge quality factors allows us to easily enter the strong coupling limit of the Jaynes Cummings model.

One of course could persevere and engineer resonators with large impedances using kinetic inductance [71, 72], and engineer large capacitive participation ratios $\beta_C \approx 1$

for $C_g \gg C_q$, and reach the soft regime of USC. For instance, a recent experiment [73] coupling a transmon to a high impedance resonator with a vacuum gap capacitor achieved the largest charge coupling $g/\omega_r \simeq 0.19$ with superconducting circuits.

The situation presents itself very differently when coupling the Josephson qubit inductively to the resonator field. In the next section we will arrive at the expression for the dimensionless galvanic coupling strength and surprisingly find that the small fine structure constant can be exploited to easily reach USC conditions [70, 74].

2.5.2 Inductive coupling

The previous capacitive coupling scheme involved, at a higher level, coupling the voltages $\boldsymbol{V}_q \cdot \boldsymbol{V}_r$ of two circuits through a capacitor, where $\boldsymbol{V}_q$ is the effective voltage produced by the qubit. In this section we discuss the inductive coupling scheme, where the resonator current is coupled to the current flowing through the qubit junction $\boldsymbol{I}_q \cdot \boldsymbol{I}_r$. This can be achieved by sharing a linear inductance between the resonator and qubit circuit or by simply embedding the JJ directly into the resonator circuit [69].

The circuit for a CPB inductively coupled to a lumped element resonator is shown in Fig. 2.7. We will not go through the full circuit analysis since this will be done rigorously in Chapter 5 for a fluxonium atom inductively coupled to a cavity chain. Regardless on the type of inductive coupling or the choice of qubit, the interaction part of the Hamiltonian is described by the generic expression

$$\begin{aligned} \mathbf{H}_{\text{int}} &= \boldsymbol{\Phi}_q \cdot \beta_L \boldsymbol{I}_r \\ &= i\beta_L \omega_r \sqrt{\frac{\hbar}{2Z_r}} \frac{\Phi_0}{2\pi} \langle g|\boldsymbol{\varphi}_q|e\rangle \left(\boldsymbol{a}^\dagger + \boldsymbol{a}\right) \sigma_x \triangleq g_L \ \left(\boldsymbol{a}^\dagger - \boldsymbol{a}\right) \sigma_x, \end{aligned} \tag{2.39}$$

where $\boldsymbol{\varphi}_q = 2\pi \boldsymbol{\Phi}_q / \Phi_0$ is the reduced superconducting phase across the JJ, and the inductive participation ratio β_L corresponds to the fraction of resonator current coupled to the junction. This type of coupling is analogous to a magnetic dipole interaction

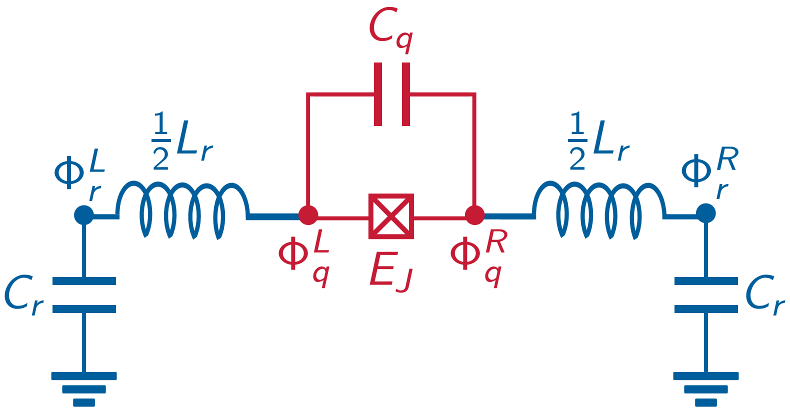

Figure 2.7: **Inductive dipole coupling.** Circuit diagram of a transmon qubit inductively coupled to a microwave resonator.

between the resonator $\vec{\boldsymbol{B}}$ field and the magnetic dipole moment $\langle g|\boldsymbol{\varphi}_q|e\rangle$ of the artificial atom.

For comparison to the charge scheme, the inductive coupling strength can be written in dimensionless units

$$\frac{g_L}{\omega_r} = i\beta_L\sqrt{\frac{Z_{\mathrm{vac}}}{Z_r}}\langle g|\boldsymbol{\varphi}_q|e\rangle\alpha^{-1/2}. \tag{2.40}$$

Inspecting this expression we can identify certain approaches for enhancing the inductive coupling strength g_L. One could maximize the inductive participation ratio $\beta_L \leq 1$ which can be set exactly to unity if the junction is fully embedded in the resonator. It now becomes desirable to couple to a low impedance resonator, which is much easier engineering constraint as opposed to using large impedance resonators with kinetic inductance. Finally it becomes desirable to use an artificial Josephson atom with a large magnetic dipole moment $\langle g|\boldsymbol{\varphi}_q|e\rangle$, and therefore we choose to use a fluxonium qubit in the USC experiment in Chapter 5.

The remarkable feature with inductive coupling is that the fine structure constant enters the expression with a negative power [70]. This gives you a dramatic advantage over the capacitive coupling scheme, where with reasonable circuit parameters one can easily reach coupling strengths comparable and even greater than the bare energies of the uncoupled system $g_L/\omega_r \sim 0.1-1$. This light-matter USC coupling regime has been demonstrated experimentally with flux qubits inductively coupled to single mode resonators [75, 76], reporting clear spectroscopic deviations from the conventional Jaynes Cummings model. In a recent experiment [77], the coupling strength was pushed even further in the deep strong coupling (DSC) regime $g_L/\omega_r > 1$ where the interaction can no longer be treated perturbatively and the joint qubit-cavity spectrum fitted the quantum Rabi model where the ground state is expected to be in an entangled cat state. This nonperturbative regime was also demonstrated for a flux qubit coupled to a continuum of modes in a 1D waveguide [78], reaching a regime where the spontaneous emission of the atom in the waveguide was comparable to its transition frequency.

2.6 Jaynes Cummings model

If we truncate the Josephson circuit to its lowest two levels and couple it (capacitively or inductively) to a single mode resonator, we recover the famous Jaynes Cummings (JC) model [67]

$$\mathbf{H}_{\mathrm{JC}}/\hbar = \omega_r \left(\boldsymbol{a}^\dagger \boldsymbol{a} + \frac{1}{2}\right) + \frac{\omega_q}{2}\sigma_z + g\left(\boldsymbol{a}^\dagger \sigma^- + \boldsymbol{a}\sigma^-\right), \tag{2.41}$$

which describes the interactions between a two-level atom and a single mode of the electromagnetic field. Since this interaction model assumes the RWA, where the total number of excitations $\boldsymbol{N} = \left(\boldsymbol{a}^\dagger \boldsymbol{a} + \sigma^+\sigma^-\right)$ is conserved, the eigenspectrum of the JC model is easily obtained. In matrix form, $\mathbf{H}_{\mathrm{JC}}$ is block diagonal with the N-excitation manifold has the form [79]

$$\mathbf{H}_{\mathrm{JC}}^{(N)}/\hbar = \begin{pmatrix} N\omega_r & g\sqrt{N} \\ g\sqrt{N} & N\omega_r + \Delta \end{pmatrix}, \tag{2.42}$$

where $\Delta = \omega_q - \omega_r$ represents the qubit-resonator frequency. Diagonalizing each N-excitation block we recover the eigenstate energies

$$E_{N\pm}/\hbar = N\omega_r + \frac{1}{2}\Delta \pm \sqrt{Ng^2 + \frac{1}{4}\Delta^2}. \tag{2.43}$$

The eigenstates are superpositions of states having N cavity photons with qubit in the ground state and $N-1$ cavity photons with qubit in the excited state [Schuster]

$$\begin{aligned} |\phi_-^{(N)}\rangle &= \cos\theta_N |N, g\rangle + \sin\theta_N |N-1, e\rangle \\ |\phi_+^{(N)}\rangle &= \sin\theta_N |N, g\rangle + \cos\theta_N |N-1, e\rangle, \end{aligned} \tag{2.44}$$

where the mixing angle is defined as $\theta_N = \frac{1}{2}\tan^{-1}\left(\frac{2g\sqrt{N}}{\Delta}\right)$. As we can see, the eigenstates of the coupled system have both qubit and photon-like character.

2.6.1 Resonant regime

If the qubit is on resonance with the cavity $\Delta = 0$, the two hybridized states have equal superposition of the qubit state $|\phi_\pm^{(N)}\rangle = \frac{1}{\sqrt{2}}\left(|N, g\rangle \pm |N-1, e\rangle\right)$. These states are referred to as polariton states with mode frequencies given by $\omega_{N\pm} = N\omega_r \pm \sqrt{N}g$. In the single excitation manifold these states become the maximally entangled atom-photon states $|\phi_\pm\rangle = \frac{1}{\sqrt{2}}\left(|1, g\rangle \pm |0, e\rangle\right)$ which can be resolved spectroscopically in a cavity transmission measurement if the polariton splitting is larger than the linewidth $2g \gg (\kappa + \gamma)/2$ which is tied with the strong coupling regime $g \gg \kappa, \gamma$ of cavity QED. Preparing the qubit in its excited state, even if there are no photons in the cavity, the qubit population oscillates at a rate g due to the quantized vacuum fluctuations of the cavity field. These oscillations are called vacuum Rabi oscillations and they reveal the quantum nature of the electromagnetic field in the cavity.

2.6.2 Dispersive regime

When the qubit and resonator are far detuned in frequency $g/\Delta \gg 1$, we can expand the dressed states in Eq. 2.44 in the single excitation sector

$$\begin{aligned} |\phi_-\rangle &\approx |1,g\rangle - \frac{g}{\Delta}|0,e\rangle \\ |\phi_+\rangle &\approx \frac{g}{\Delta}|1,g\rangle + |0,e\rangle, \end{aligned} \tag{2.45}$$

which correspond to states that are mostly qubit (photon) and have a little bit of photon (qubit) character. To understand the importance of this dispersive regime, we perform the unitary transformation $\mathbf{U} = \exp\left[\frac{g}{\Delta}\left(\boldsymbol{a}\sigma^+ - \boldsymbol{a}^\dagger\sigma^-\right)\right]$ and expand up to second order in g to obtain [80]

$$\mathbf{U}\mathbf{H}_{\mathrm{JC}}\mathbf{U}^\dagger/\hbar \approx \omega_r\left(\boldsymbol{a}^\dagger\boldsymbol{a} + \frac{1}{2}\right) + \frac{\omega_q}{2}\sigma_z + \frac{g^2}{\Delta}\boldsymbol{a}^\dagger\boldsymbol{a}\sigma_z + \frac{g^2}{2\Delta}\sigma_z. \tag{2.46}$$

The dispersive shift is defined as $\chi = g^2/\Delta$. In this new Hamiltonian, excitations are no longer swapped between the qubit and cavity, but instead their frequencies are renormalized. The qubit experiences a Lamb shift $\chi/2$ due to vacuum fluctuations in the cavity. The term $\chi\boldsymbol{a}^\dagger\boldsymbol{a}\sigma_z$ corresponds to a collective frequency shift which depends on both the qubit and cavity populations. Regrouping this term with the bare cavity and qubit terms, we can interpret this virtual process as a qubit state dependent frequency shift on the cavity $(\omega_r + \chi\sigma_z)\boldsymbol{a}^\dagger\boldsymbol{a}$ or as a cavity state dependent frequency shift on the qubit $(\omega_q/2 + \chi\boldsymbol{a}^\dagger\boldsymbol{a} + \chi/2)\sigma_z$. In the strong dispersive limit $\chi \gg \kappa, \gamma$, the state dependent shifts become spectroscopically resolvable. This allows the qubit state $\langle \sigma_z \rangle$ to be determined from the cavity transmission resonance, and the cavity photon number distribution $P(n) = \langle \boldsymbol{a}^\dagger \boldsymbol{a} \rangle_n$ from the dressed qubit frequency. In order to optimize SNR, for the qubit state measurement it is ideal to design a dispersive shift comparable to the cavity decay rate $\chi \sim \kappa$ [79].

Chapter 3

Photon interactions using a stimulated Josephson nonlinearity

3.1 Introduction

Quantized electromagnetic excitations in superconducting circuits have become a promising platform for processing quantum information [14, 52, 15]. A central piece to this hardware is the Josephson effect, which grants nonlinearity with negligible dissipation. Electrical circuits composed of Josephson junctions behave as quantum systems with discrete energy levels resembling artificial atoms [81]. Although the coherence properties of anharmonic Josephson circuits have been improving these past two decades, storing microwave photons in harmonic oscillators leads to significantly longer coherence times [82, 18]. This promising development has launched efforts in building hardware-efficient architectures based on quantum memories [83, 84]. Since it is impossible to selectively address individual energy levels in a harmonic system, Josephson qubits are used for manipulating oscillator states at rates limited by the dispersive interaction. In this work [85] we present a new paradigm in exploiting the

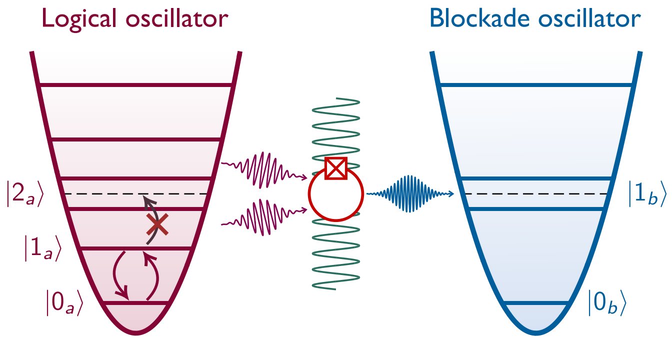

Figure 3.1: **Schematic energy spectrum for two coupled oscillators.** Periodically modulating the coupling element stimulates a three-wave frequency conversion process which leads to a nonequidistant energy ladder.

Josephson effect to perform faster logical operations directly on the oscillator Hilbert space using a dynamically activated nonlinearity.

The key concept behind this experiment is to engineer a three-wave interaction between the electromagnetic modes of two linear oscillators, which we refer to as *logical* and *blockade* oscillator (Fig. 3.1a). Parametrically modulating the interaction amplitude stimulates the conversion of two logical photons into one blockade photon and vice versa. Provided the conversion rate is larger than the oscillator dissipation, this stimulated process strongly hybridizes the logical two-photon state with the blockade single-photon state, resulting in an anharmonic energy spectrum which allows selective control over the single-photon manifold of the logical mode. This conversion process has been previously demonstrated with the quartic nonlinearity of a transmon qubit, implementing a degenerate parametric oscillator used for stabilizing the oscillator state into a quantum manifold [86, 87]. Our experiment focuses on engineering a Josephson circuit with cubic nonlinearity, benefiting from a larger conversion rate which would maximize the oscillator anharmonicity and further complement dissipative stabilization schemes with an efficient two-photon loss channel.

In contrast to conventional qubit designs where the tunnel junction is used primarily to induce a non-parabolic inductive potential, this work exclusively employs the Josephson nonlinearity for perturbing higher-lying eigenstates while maintaining a parabolic potential to still benefit from the intrinsic oscillator coherence. Dynamically confining a harmonic oscillator to a subset of energy levels has been demonstrated in superconducting circuits using the back action of a driven ancilla qubit[88]. However, the selectivity of the blocking tone is limited by the dispersive shift and parasitic leakage in the ancilla, making this approach unfeasible for implementing a qubit.

Our central tool for stimulating anharmonicity is parametric driving. This process is generally described by engineering a time-varying Hamiltonian for a coupled mode system with tunable degrees of freedom such as the coupling elements or mode resonance frequency, and periodically driving the system at the frequency detuning between energy states to be coupled. Parametrically activated interactions have been extensively employed in superconducting circuits, with applications in quantum computing, specifically in quantum gates [89, 90, 91] and parametric multi-mode architectures [84, 92], frequency conversion [93], dissipative stabilization [94], quantum limited amplification [95, 96, 97] and non-reciprocal signal processing [98]. This experiment extends the current toolbox with the functionality of dynamically inducing nonlinearity with a purpose of engineering highly coherent qubits.

3.2 Two cavity architecture

3.2.1 Circuit Lagrangian

This experiment is implemented using a circuit quantum electrodynamics architecture as shown in Fig. 3.2. The circuit consists of two superconducting microwave oscillators coupled inductively through a Josephson junction connected at the two voltage nodes. The resonators are composed of lumped element inductors $L_{a,b}$ and capacitors $C_{a,b}$, and can be described quantum mechanically by their reduced node fluxes $\boldsymbol{\varphi}_{a,b}$. The Josephson junction has a critical current I_c which sets an inductive contribution $L_J = 2\pi I_c/\Phi_0$. The closed loop composed of the resonator inductors and Josephson junction constitutes the circuit for a superconducting quantum interference device (rf-SQuID) which allows for the galvanic coupling between the resonator mode currents to be tuned with an external magnetic flux Φ_{ext}. Following standard circuit quantization techniques [56], we can write down the Lagrangian of our device

$$\begin{aligned}\boldsymbol{\mathcal{L}} = &\left(\frac{\Phi_0}{2\pi}\right)^2\left[\frac{C_a}{2}\dot{\boldsymbol{\varphi}}_a^2 + \frac{C_b}{2}\dot{\boldsymbol{\varphi}}_b^2 + \frac{C_J}{2}\left(\dot{\boldsymbol{\varphi}}_a - \dot{\boldsymbol{\varphi}}_b + \dot{\varphi}_{\text{ext}}\right)^2\right] \\ &- \left(\frac{\Phi_0}{2\pi}\right)^2\left[\frac{\boldsymbol{\varphi}_a^2}{2L_a} + \frac{\boldsymbol{\varphi}_b^2}{2L_b} - \frac{1}{L_J}\cos(\boldsymbol{\varphi}_a - \boldsymbol{\varphi}_b + \varphi_{\text{ext}})\right],\end{aligned} \tag{3.1}$$

with $\varphi_{\text{ext}} = 2\pi\Phi_{\text{ext}}/\Phi_0$. Due to fluxoid quantization inside the loop, the coupler degree of freedom given by the phase difference across the junction can be written in terms of the cavity degrees of freedom $\boldsymbol{\varphi}_{ab} = \boldsymbol{\varphi}_b - \boldsymbol{\varphi}_a$, thereby reducing the complexity of the full circuit analysis. A key ingredient in this experiment is the wave mixing capability of the Josephson junction captured in its inductive energy

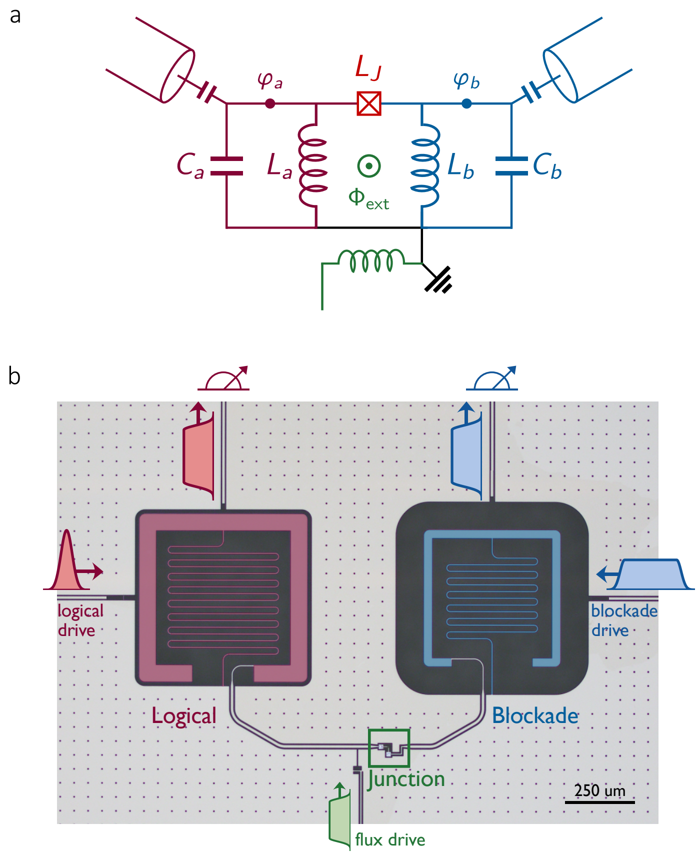

Figure 3.2: **Device circuit. a.** Schematic circuit diagram and **b.** false-color optical micrograph of the lumped element resonators, logical (red) and blockade (blue), coupled inductively through an rf-SQuID (green). Each cavity has a drive port and an output port for transmission measurements. The rf-SQuID has a broadband driving port used for sending the dc flux bias and the parametric pump tone.

$$\begin{aligned}\mathbf{U}_{\boldsymbol{J}}/E_J &= -\cos(\boldsymbol{\varphi}_{ab} + \varphi_{\text{ext}}) \\ &\approx -\left(1 - \frac{\widetilde{\boldsymbol{\varphi}}_{ab}^2}{2!} + \frac{\widetilde{\boldsymbol{\varphi}}_{ab}^4}{4!}\right)\cos\varphi_{\text{ext}} + \left(\widetilde{\boldsymbol{\varphi}}_{ab} - \frac{\widetilde{\boldsymbol{\varphi}}_{ab}^3}{3!}\right)\sin\varphi_{\text{ext}} + \mathcal{O}(\widetilde{\boldsymbol{\varphi}}_{ab}^5),\end{aligned} \tag{3.2}$$

where E_J is the Josephson energy. The junction nonlinearity becomes apparent in the second line of equation (3.2) obtained from Taylor expanding the potential about the minimum centered at $\overline{\boldsymbol{\varphi}}_{\mathrm{ab}}$ and arriving at an effective potential for the phase deviation $\widetilde{\boldsymbol{\varphi}}_{\mathrm{ab}} = \boldsymbol{\varphi}_{\mathrm{ab}} - \overline{\boldsymbol{\varphi}}_{\mathrm{ab}}$. The flux dependence is absorbed in the expansion coefficients.

By itself, a Josephson junction has an even potential and below its plasma frequency can be modeled to second-order $\tilde{\boldsymbol{\varphi}}^2$ as a linear inductor. The fourth-order correction from the cosine potential $\tilde{\boldsymbol{\varphi}}^4$ gives a Kerr nonlinearity used extensively for engineering photon interactions. Enforcing fluxoid quantization, in the rf-SQuID topology, generates an odd potential which ultimately yields the $\tilde{\boldsymbol{\varphi}}^3$ nonlinearity necessary for engineering the three-wave interaction. Other Josephson circuits with cubic nonlinearity have been implemented for applications in non-degenerate parametric amplification [99], driving forbidden transitions in an artificial Λ-system [100], and quantum simulation of the ultrastrong coupling regime [101].

We arrive at the Hamiltonian of this two mode circuit $\mathbf{H} = \sum_k \boldsymbol{n}_k \dot{\phi}_k - \boldsymbol{\mathcal{L}}$ by finding the conjugate charge variables $\boldsymbol{n}_k = \partial \boldsymbol{\mathcal{L}} / \partial \dot{\boldsymbol{\varphi}}_k$ for each node. This Hamiltonian reads

$$\mathbf{H} = \sum_{k=a,b} \left(4E_{Ck}\boldsymbol{n}_k^2 + E_{Lk}\boldsymbol{\varphi}_k^2\right) + 8E_{Cc}\boldsymbol{n}_a\boldsymbol{n}_b - E_J \cos\left(\boldsymbol{\varphi}_a - \boldsymbol{\varphi}_b + \varphi_{\mathrm{ext}}\right), \tag{3.3}$$

where we have defined the charging energy $E_{Ck} = e^2/2C'_k$, inductive energy $E_{Lk} = \left(\Phi_0/2\pi\right)^2/2L_k$ and Josephson energy $E_J = \left(\Phi_0/2\pi\right)^2/L_J$, with $L_J = 2\pi I_c/\Phi_0$. The effective capacitances are determined as $C'_a = C_d^2/(C_b + C_J)$, $C'_b = C_d^2/(C_a + C_J)$, and $C_c = C_d^2/C_J$ with $C_d^2 = C_J(C_a + C_b) + C_aC_b$. Promoting the node flux and charge variable to quantum operators, $\boldsymbol{\varphi}_k = \frac{1}{\sqrt{2}}\left(\frac{4E_{Ck}}{E_{Lk}}\right)^{1/4}\left(\boldsymbol{k}^\dagger + \boldsymbol{k}\right)$ and $\boldsymbol{n}_k = i\frac{1}{\sqrt{2}}\left(\frac{E_{Lk}}{4E_{Ck}}\right)^{1/4}\left(\boldsymbol{k}^\dagger - \boldsymbol{k}\right)$, allows us to describe the circuit with this second quantized Hamiltonian

$$\begin{aligned}\mathbf{H}/\hbar = {}& \omega_a \boldsymbol{a}^\dagger\boldsymbol{a} + \omega_b \boldsymbol{b}^\dagger\boldsymbol{b} + g(\boldsymbol{a}^\dagger\boldsymbol{b} + \boldsymbol{a}\boldsymbol{b}^\dagger) + g_2(\boldsymbol{a}^{\dagger 2}\boldsymbol{b} + \boldsymbol{a}^2\boldsymbol{b}^\dagger) \\ & + \chi_{ab}\boldsymbol{a}^\dagger\boldsymbol{a}\boldsymbol{b}^\dagger\boldsymbol{b} + \frac{\chi_{aa}}{2}\boldsymbol{a}^{\dagger 2}\boldsymbol{a}^2 + \frac{\chi_{bb}}{2}\boldsymbol{b}^{\dagger 2}\boldsymbol{b}^2.\end{aligned} \tag{3.4}$$

The operators $\boldsymbol{a}^\dagger(\boldsymbol{a})$ and $\boldsymbol{b}^\dagger(\boldsymbol{b})$ create (annihilate) photons in the logical (blockade) eigenmodes, where ω_a and ω_b are the mode frequencies. The linear Josephson inductance contributes to the total inductance of each resonator and provides a linear coupling between the modes at a rate g smaller than their detuning, effectively adding dispersive corrections to the mode frequencies. The amplitude g_2 corresponds to the rate of exchanging pairs of logical photons with single blockade photons. The second line in the Hamiltonian takes into account the Kerr nonlinearity that both modes inherit from the junction. All fast rotating terms, apart from the three-wave term, have been disregarded from equation (3.4) as they are not important. Details of the full quantum treatment of the circuit can be found in Appendix A.

Since all coefficients in the Hamiltonian depend on the applied magnetic flux, our circuit parameters are chosen ($L_J > L_{a,b}$) to ensure the mode frequencies have a weak flux dependence (Fig. 3.3a). The circuit parameters of this device have been characterized by fitting the measured flux-dependent resonances to the full Rabi Hamiltonian (see Supplemental Information). In order to minimize oscillator dephasing, we bias the rf-SQuID at zero magnetic flux. At this operating point the resonator frequencies are $\omega_a/2\pi = 4.284$ GHz and $\omega_b/2\pi = 7.073$ GHz, and their self-Kerr nonlinearities are $\chi_{aa}/2\pi = 3.0$ MHz and $\chi_{bb}/2\pi = 12.5$ MHz, respectively. The cross-Kerr nonlinearity $\chi_{ab}/2\pi = 10.0$ MHz will be used as a measurement tool for characterizing the logical mode state by probing transmission through the blockade resonator. Unlike the transmon circuit [60], the logical oscillator has a self-Kerr nonlinearity χ_{aa} two orders of magnitude smaller and will rely on the lower-order cubic nonlinearity for generating anharmonicity. The challenge with this approach is that the three-wave coupling rate g_2 is exactly zero at the flux sweet spot $\varphi_{\text{ext}} = 0$ (Fig. 3.3b).

3.2.2 Parametric flux driving

This compromise between coherence and nonlinearity can be overcome by parametric flux modulation. This is accomplished by applying a drive $\Phi_{\text{ext}}(t) = \delta \cos\omega_p t$ to the rf-SQuID flux bias which effectively turns all terms in equation (3.4) into time-dependent periodic functions. Using the Jacobi-Anger expansion, the flux dependent coefficients can be expanded into Bessel functions

$$\begin{aligned} \sin\varphi_{\text{ext}} &= -2\sum_{n=1}^{\infty}(-1)^n J_{2n-1}(\epsilon)\cos[(2n-1)\omega_p t], \\ \cos\varphi_{\text{ext}} &= J_0(\epsilon) + 2\sum_{n=1}^{\infty}(-1)^n J_{2n}(\epsilon)\cos(2n\omega_p t), \end{aligned} \tag{3.5}$$

with $\epsilon = 2\pi\delta/\Phi_0$. For the static bias $\varphi_{\text{ext}} = 0$, the inductive potential minimum is centered at $\overline{\boldsymbol{\varphi}}_a = \overline{\boldsymbol{\varphi}}_b = 0$. Due to the relatively small modulation strength ϵ, we truncate the Jacobi-Anger expansion to the lowest few orders, which translates to the following time-dependent junction potential

$$\begin{aligned} \mathbf{U}_{\boldsymbol{J}}(t)/E_J \approx &-\left(1 - \frac{\boldsymbol{\varphi}_{ab}^2}{2!} + \frac{\boldsymbol{\varphi}_{ab}^4}{4!}\right)[J_0(\epsilon) - 2J_2(\epsilon)\cos(2\omega_p t)] \\ &+ \left(\boldsymbol{\varphi}_{ab} - \frac{\boldsymbol{\varphi}_{ab}^3}{3!}\right)[2J_1(\epsilon)\cos\omega_p t]\,. \end{aligned} \tag{3.6}$$

To first order in flux, the three-wave coupling amplitude, coming from the term $\boldsymbol{\varphi}_{ab}^3$, can be approximated as $g_2 \approx \tilde{g}_2(\delta)\cos\omega_p t + \mathcal{O}(\delta^2)$. Although the static nonlinearity is zero at the sweet spot, we can take advantage of the linear flux dispersion around $\varphi_{\text{ext}} = 0$ and induce a non-zero dynamical amplitude $\tilde{g}_2(\delta) = \delta\partial g_2/\partial\Phi_{\text{ext}}$ that depends on the slope, in the case of small modulation amplitudes $\delta/\Phi_0 \ll 1$. For larger amplitudes $\delta/\Phi_0 \sim 0.1$, the coupling becomes $\tilde{g}_2(\delta) \approx E_J J_1(2\pi\delta/\Phi_0)\left(\varphi_a^{\text{zpf}}\right)^2\varphi_b^{\text{zpf}}$,

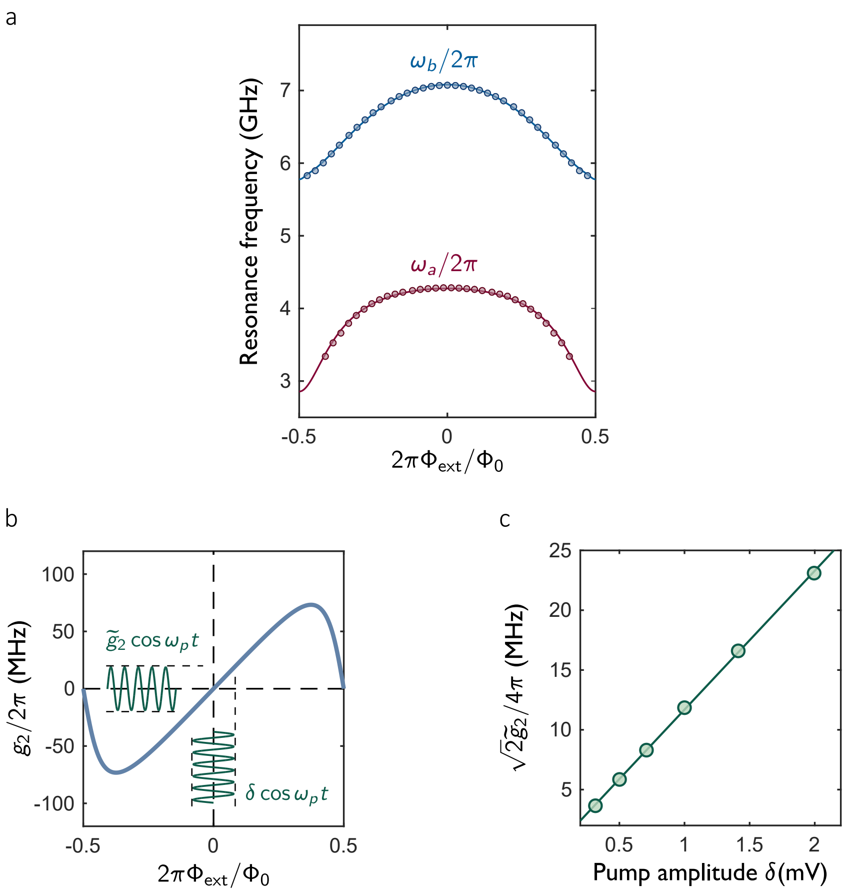

Figure 3.3: **Circuit response to magnetic flux control. a.** Measured resonance frequencies as a function of applied coupler dc flux bias. The agreement with the circuit model is captured by the solid theory line. **b.** Flux dependence for the three-wave coupling term g_2 calculated using the fitted circuit parameters. Flux modulation at the sweet spot yields a modulated coupling amplitude. **e.** Measured stimulated three-wave coupling as a function of flux modulation amplitude, following a linear dependence indicated by the solid line.

where $\varphi_{a,b}^{\mathrm{zpf}}$ are the zero-point fluctuation amplitudes. The full derivation of the time-dependent Hamiltonian can be found in Appendix A. By choosing the pump frequency to approximately match $\omega_p = 2\omega_a - \omega_b$, the three-wave interaction in the oscillator rotating frame $\frac{1}{2}\tilde{g}_2(\delta)\left(\boldsymbol{a}^{\dagger 2}\boldsymbol{b} + \mathrm{h.c.}\right)$ becomes effectively resonant.

The flux drive therefore stimulates a frequency conversion process which exchanges a pair of logical photons with a single blockade photon. This coherent interaction leads to new eigenstates defined as the symmetric and antisymmetric superposition of the two mode excitations $|2^{\pm}\rangle = (|2_a 0_b\rangle \pm |0_a 1_b\rangle)/\sqrt{2}$ (Fig. 3.4a). For relatively strong drive amplitudes, flux modulation will shift the oscillator frequencies by $-\delta^2/4(\partial^2\omega/\partial\Phi_{\text{ext}}^2)$ due to the non-linear flux dependence . These second-order corrections have been observed in other experiments[84, 91, 92, 93] and need to be taken into consideration when calibrating the parameters of the flux drive.

The final form for the three-wave coupling amplitude $\tilde{g}_2 = E_J J_1(\epsilon)(\varphi_a^{\text{zpf}})^2\varphi_b^{\text{zpf}}$ sets a limit on how fast we can perform gates on the logical oscillator. It is worth comparing it with the transmon-resonator dispersive coupling $\chi_{qr} = -E_J(\varphi_q^{\text{zpf}})^2(\varphi_r^{\text{zpf}})^2$, which sets the same limit for dispersive protocols[82]. Expanding the Bessel function to first order, an appropriate flux pump amplitude can be chosen such that $J_1(\varepsilon) \simeq \pi\delta/\Phi_0 > \varphi_r^{\text{zpf}} \sim 0.1$ to gain an advantage over dispersive gates. In practice, one can easily increase the dispersive coupling by decreasing the transmon-resonator frequency detuning, and reach similar gate times demonstrated with the three-wave coupling. However, this has drastic consequences on the resonator T_1 and T_2, due to Purcell loss from hybridization with the transmon and shot-noise dephasing from a thermally populated transmon[82]. The three-wave nonlinearity avoids this compromise between gate speed and coherence since $(a^2b^\dagger + a^{\dagger 2}b)$ does not shift the logical mode frequency due to stochastic photon number jumps in the blockade mode. The coupler Hamiltonian in our circuit design has a cross-Kerr term which introduces shot noise dephasing. However, such a term is not important for inducing nonlinearity and can be removed by adopting a Kerr-free three-wave Josephson coupler[102]. One potential drawback of the three-wave mixing process is leakage into higher logical photon states from converted thermal photons in the blockade mode. Nevertheless, one advantage of this parametric process is the freedom to design blockade cavities at higher frequencies which would exponentially suppress thermal occupation at no expense to the magnitude of the nonlinearity.

3.3 Spectroscopy of stimulated wave mixing

This dynamically induced nonlinearity is very sensitive to the selected pump frequency. The simplest calibration experiment is done in a continuous wave form by probing the transmission spectrum of the blockade resonator with a weak coherent tone and applying a flux pump tone at a fixed modulation amplitude. Sweeping both probe and flux pump frequencies, we get a well-resolved normal-mode splitting centered at $\omega_p = 2\omega_a - \omega_b \approx 2\pi \times 1.510$ GHz (Fig. 3.4b). This is clear evidence that we are operating in the strong conversion limit $\sqrt{2}\tilde{g}_2/2 > 2\kappa_a, \kappa_b$, where the three-wave coupling is stronger than the logical (blockade) dissipation rate $\kappa_a(\kappa_b)$. This experiment involved probing the overlap of a single blockade photon with the dynamically hybridized states $|2^{\pm}\rangle$.

Additionally, we can also probe the logical two-photon component by climbing the energy ladder using a pulsed pump-probe scheme while continuously applying the same flux pump tone. The first pulse populates the $|1_a\rangle$ state by resonantly driving the logical mode and, subsequently, the transmission spectrum of the logical resonator is probed using a second pulse. A similar avoided crossing is observed (Fig. 3.4c) when population is transferred to the logical two-photon manifold, specifically when the probe frequency matches the $|1_a\rangle \rightarrow |2^{\pm}\rangle$ transitions.

Both measurement approaches yield the same value for the dynamically activated three-wave coupling $\tilde{g}_2$; however, the latter provides spectroscopic evidence that for an optimal window in flux pump frequencies we can drive the logical mode as a qubit. This is possible since the energies required to leak into higher-lying eigenstates are significantly detuned from the single-photon transition. This calibration scheme is repeated for pump amplitudes up to $\delta/\Phi_0 \sim 0.2$, yielding nonlinearities as large as $\sqrt{2}\tilde{g}_2/4\pi \sim 25$ MHz (Fig. 3.3c), where the dynamical coupling strength increases linearly with the pump amplitude, as expected. The pump amplitude was not further

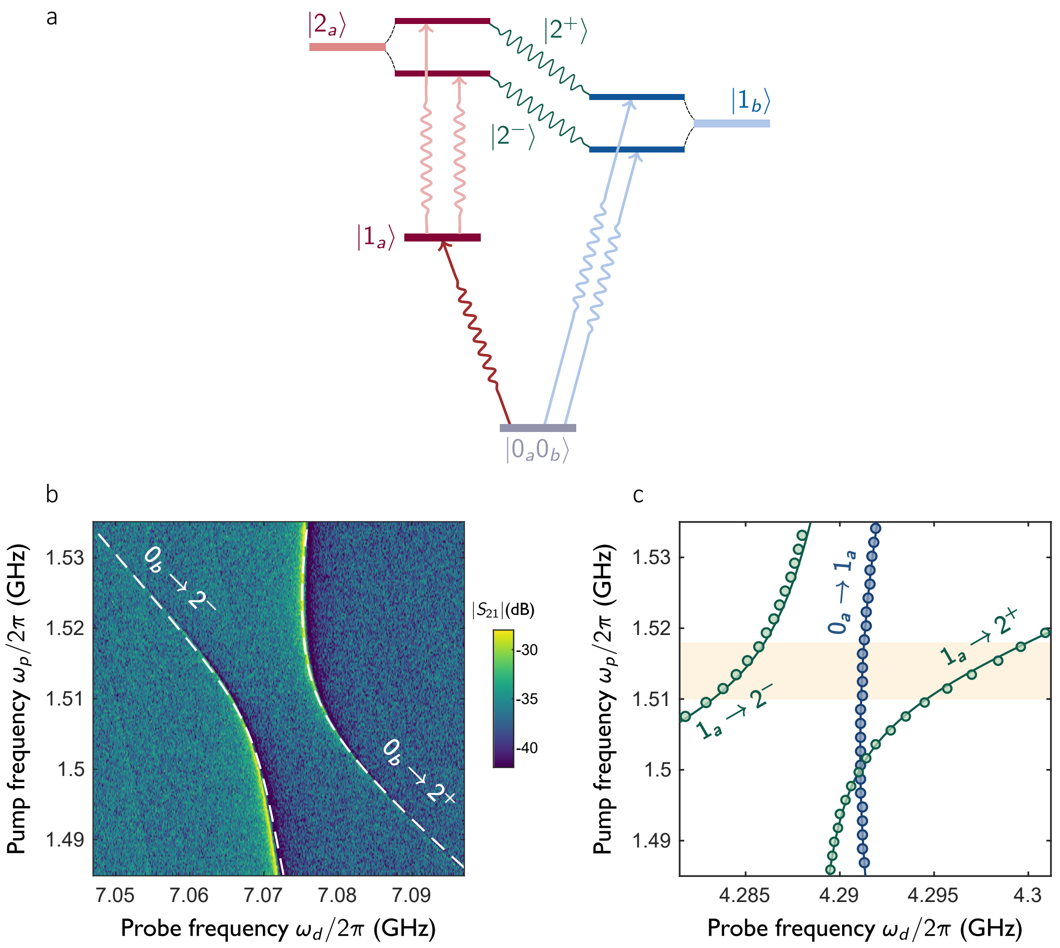

Figure 3.4: **Spectroscopy of dynamical three-wave interaction. a.** Energy level diagram for the coupled mode system outlining the stimulated nonlinearity arising from the dynamical Rabi splitting of the logical $|2_a\rangle$ state. The dynamical eigenstates $|2^\pm\rangle$ are probed by measuring their blockade component with a single photon probe (blue) or the logical component using a pump and probe (red). **b.** Measured transmission $|S_{21}|$ through the blockade resonator as a function of probe and flux pump frequency. The normal mode splitting was fitted (dashed line) in order to extract the dynamical three-wave coupling strength. **c.** Extracted resonance peaks in the pump-probe spectroscopy performed on the logical resonator. The avoided crossing was fitted (solid line) for confirming the magnitude of the oscillator anharmonicity $\sqrt{2}\tilde{g}_2/4\pi$. Shaded region: optimum flux pump frequency range. The flux modulation amplitude used in **c.** and **d.** was $\delta \simeq 0.5$ mV.

increased to avoid generating higher harmonics of the pump frequency as we deviate from the linear flux dispersion of $g_2(\Phi_{\text{ext}})$.

3.4 Time domain dynamics

In this section we aim to validate that the multi-level logical oscillator can be reduced to a simple qubit by studying the time dynamics of the driven two-mode system. The following experimental sequence is employed (Fig. 3.5a). First, the flux is modulated at the optimal pump frequency ω_p and amplitude δ which activates the anharmonicity. Subsequently, the logical resonator is excited with a drive pulse of varying amplitude and frequency. Finally, we measured the homodyne amplitude of a probe tone transmitted through the blockade cavity. Due to the cross-Kerr nonlinearity $\chi_{ab}\boldsymbol{a}^\dagger\boldsymbol{a}\boldsymbol{b}^\dagger\boldsymbol{b}$ resolved at the single photon level ($\chi_{ab} > \kappa_a, \kappa_b$), the blockade resonance acquires a frequency shift dependent on the number of photons in the logical mode [103], similar to the state dependent shift between a qubit and a cavity in the strong dispersive regime [104]. This allows indirect measurement of the logical mode population by weakly probing the blockade resonator transmission. Since the three-wave hybridization would further complicate the measurement, flux modulation is turned off before readout.

3.4.1 Rabi and multiphoton oscillations

The outcome of measuring the homodyne amplitude of the blockade tone as a function of drive amplitude and frequency is shown in Fig. 3.6b. At low drive amplitudes we observe a resonance peak near the single-photon transition frequency $\omega_{01}/2\pi$ and by further increasing the drive amplitude we observe clear oscillations in the peak height and a strong amplitude dependence of the line width (Fig. 3.5b). This is consistent with observing Rabi oscillations and power broadening for a resonantly driven spin 1/2 described by the Bloch equations. The effective spin in this case corresponds to the energetically isolated single-photon manifold of the logical mode.

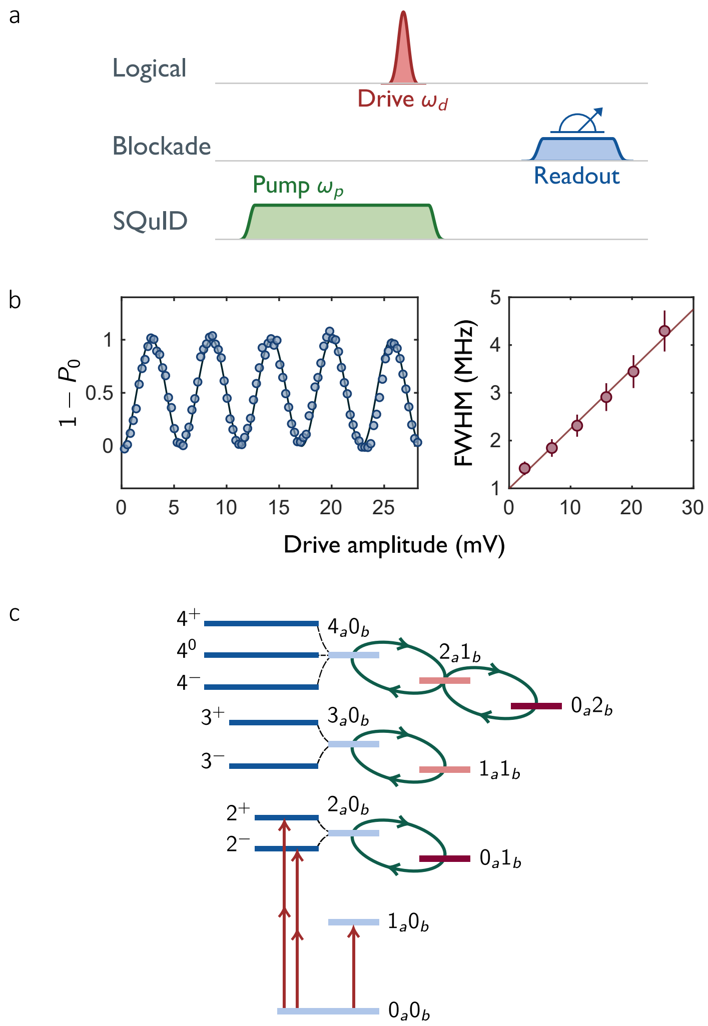

Figure 3.5: **Time domain spectroscopy.** **a.** Experimental pulse sequence for probing the anharmonic logical mode. The SQuID coupler is driven with a 10μs pulse with a microwave carrier frequency $\omega_p/2\pi = 1.557$ GHz and amplitude $\delta \simeq 2$ mV to reach a three-wave coupling strength $\sqrt{2}\tilde{g}_2/4\pi \simeq 25$ MHz. The logical cavity is driven with a narrow bandwidth Gaussian pulse ($4\sigma = 1\mu$s) in order to resolve all spectroscopic transitions. The blockade cavity is weakly probed at its resonance frequency when the logical mode is in vacuum, $\omega_b/2\pi = 7.037$ GHz. **b.** Left: Rabi oscillations in the homodyne voltage normalized as the probability of exciting the logical cavity. Right: fitted peak full width at half maximum (FWHM) showing linear dependence with drive amplitude (solid line) as predicted by Bloch equations. Error bars represent two standard deviations. **d.** Energy level diagram for the two cavity eigenstates with parametric three-wave coupling (green arrows) where higher-lying eigenstates are probed as multi-photon transitions (red arrows).

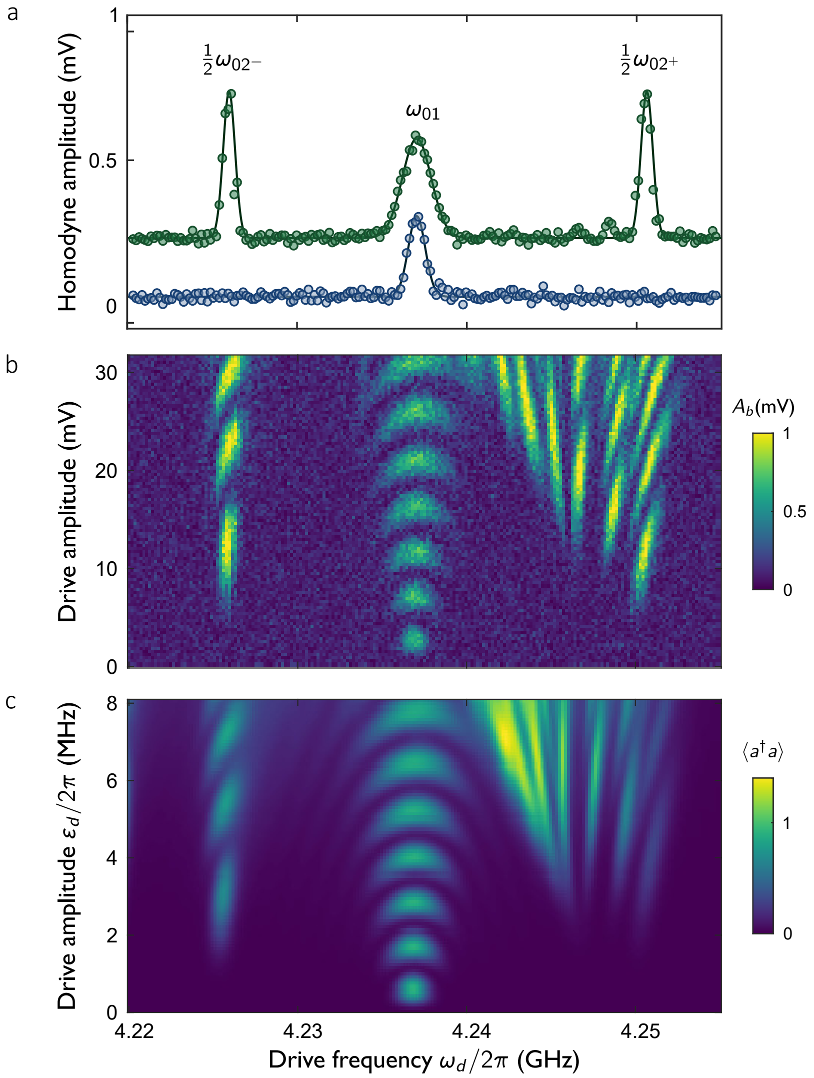

Figure 3.6: **Rabi driving the anharmonic oscillator.** Probing of the logical cavity spectrum using the transmitted blockade homodyne voltage A_b. **a.** spectroscopic features for two different drive amplitudes, 2.53 mV (blue) and 11.07 mV (green), showing a power broadened single-photon resonance and the appearance of a two-photon resonance. **b.** measured readout signal versus logical drive frequency and amplitude. **c.** Theoretical prediction based on master equation simulation.

Higher eigenstates of the coupled system become accessible with increasing drive amplitude via multi-photon transitions [105], since direct transitions from vacuum are suppressed by parity selection rules. These eigenstates are significantly perturbed under flux modulation as the dynamical three-wave interaction mixes states in different photon number manifolds (Fig. 3.5c). Transitions to the $|2^{\pm}\rangle$ states occur as two photon oscillations with resonance frequencies $\frac{1}{2}\omega_{02\pm}$ symmetrically detuned from the single-photon transition frequency ω_{01}. Spectroscopic features red-detuned from the two-photon resonance $\frac{1}{2}\omega_{02+}$ are multi-photon oscillations.

3.4.2 Master equation simulation

We model the dynamics of the Hamiltonian in equation (3.4) when it is subjected to a coherent drive on the logical cavity $\mathbf{H}_d = \varepsilon_d(t)\boldsymbol{a}^\dagger + \text{h.c.}$ and a time dependent flux drive. Moving to a rotating frame that combines both the coherent drive frequency $\omega_d/2\pi$ and flux pump frequency $\omega_p/2\pi$, the Hamiltonian becomes $\mathbf{H} = \Delta_a \boldsymbol{a}^\dagger\boldsymbol{a} + \Delta_b \boldsymbol{b}^\dagger\boldsymbol{b} + \frac{1}{2}\tilde{g}_2(\delta)(\boldsymbol{a}^{\dagger 2}\boldsymbol{b} + \text{h.c.}) + \mathbf{H}_{\text{Kerr}} + \widetilde{\mathbf{H}}_{\text{d}}$ where $\Delta_a = \omega'_a - \omega_d$, $\Delta_b = \omega'_b - 2\omega_d + \omega_p$ and $\widetilde{\mathbf{H}}_{\text{d}}$ is the drive term in the rotating frame. The non-resonant linear coupling terms are eliminated using a Schrieffer-Wolff transformation and $\omega'_{a,b}$ represent the dressed oscillator frequencies. Additionally, this model accounts for mode frequency corrections from the second harmonic of the flux tone. In order to study the dynamics of the reduced density matrix ρ, losses are incorporated by employing the quantum master equation written in the standard Lindblad form

$$\dot{\rho} = -\frac{i}{\hbar}[\mathbf{H}, \rho] + \kappa_a \mathcal{D}[\boldsymbol{a}]\rho + \kappa_b \mathcal{D}[\boldsymbol{b}]\rho \tag{3.7}$$

where we have the usual definition for the Lindblad damping superoperator $\mathcal{D}[\mathbf{L}]\rho = \mathbf{L}\rho\mathbf{L}^\dagger - \frac{1}{2}\mathbf{L}^\dagger\mathbf{L}\rho - \frac{1}{2}\rho\mathbf{L}^\dagger\mathbf{L}$ used for modeling the photon loss in the two resonators. The time-dependent envelopes for the coherent drive and three-wave interaction amplitudes have been modeled to replicate the experimentally implemented pulse sequence. At the end of every pulse instance the expectation value of the logical cavity population $\mathbf{Tr}(\rho\boldsymbol{a}^\dagger\boldsymbol{a})$ is calculated as a function of the drive amplitude and frequency. As shown in Fig. 3.6c, this theoretical framework clearly captures the experimentally measured Rabi oscillations and power broadening at the single-photon resonance. The numerical simulations also confirm that the leftmost and rightmost resonances belong to two-photon transitions to the states $|2^-\rangle$ and $|2^+\rangle$ respectively, and reveal that the spurious resonances redshifted from the two-photon resonance $\frac{1}{2}\omega_{02^+}$ correspond to complex multi-photon transitions involving the excitation of the states $|2^+\rangle, |3^+\rangle, |4^+\rangle$ and $|5^+\rangle$. We expect that the discrepancies in the multi-photon oscillation periods arise from distorted pulse waveforms in the experimental setup, which are not fully taken into consideration in our theory.

3.5 Cavity State Tomography

Following the Rabi experiment, we can prepare arbitrary states $|\psi\rangle = \alpha|0\rangle + \beta|1\rangle$ in the logical single-photon manifold by calibrating the amplitude of the drive pulse to perform $(\pi)_y$ and $(\pi/2)_y$ rotations. Using the protocol described in Fig. 3.8a, similar to the approach in references [106, 107], we perform cavity state tomography by measuring the Wigner function

$$W(\alpha) = \frac{2}{\pi}\langle\psi|\mathbf{D}_\alpha \mathbf{P} \mathbf{D}_\alpha^\dagger|\psi\rangle \tag{3.8}$$

defined in this form as the expectation value of the parity operator $\mathbf{P} = e^{i\pi \boldsymbol{a}^\dagger \boldsymbol{a}}$ evaluated over the complex plane spanned by the displacement operator $\mathbf{D}_\alpha = e^{\alpha \boldsymbol{a}^\dagger - \alpha^* \boldsymbol{a}}$.

3.5.1 Displacement calibration

The logical cavity is displaced using a $4\sigma = 10$ ns Gaussian pulse at the single-photon resonance frequency $\omega_{01}/2\pi$. When the cavity is in the vacuum state, this displacement prepares a coherent state. The displacement amplitude α is controlled by calibrating the voltage amplitude V_d of the displacement pulse $\alpha = \eta V_d$ by fitting

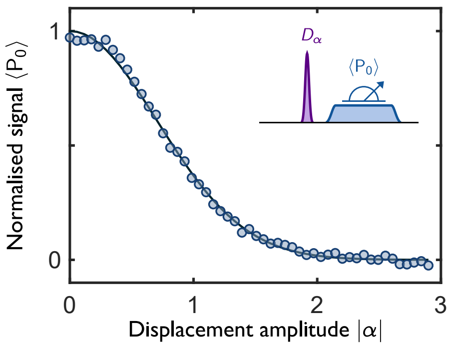

Figure 3.7: **Coherent displacement calibration.** Calibrating the displacement pulse amplitude by fitting the transmitted blockade signal to the Poisson probability of measuring the logical vacuum state $P_0(\alpha) = \mathrm{e}^{-\alpha^2}$.

the Poisson distribution to the logical mode photon number probabilities $P_n(V_d) = (\eta V_d)^{2n} \exp\left(-\eta^2 V_d^2\right)/n!$. The probability P_n of having n photons in the logical cavity is measured from the transmitted blockade voltage $V_b = V_n \cdot P_n + V_{\mathrm{bg}}$ probed at the $\omega_b - n\chi_{ab}$ resonance. The voltage prefactor V_n is used for normalization, and V_{bg} accounts for the digitizer noise background. Fig. 3.7 illustrates how the displacement amplitude is calibrated by measuring the probability of finding the logical mode in the ground state as a function of drive amplitude. In order to take advantage of the full AWG resolution in the Wigner tomography sequence, we calibrate the maximum voltage $V_d = 1\mathrm{V}$ to correspond to a coherent displacement magnitude $|\alpha| = 2\sqrt{2}$.

3.5.2 Wigner function tomography

Using the photon-number dependent frequency shift of the blockade resonance induced by the cross-Kerr nonlinearity, we can measure the overlap of the displaced logical state $\mathbf{D}_\alpha^\dagger|\psi\rangle$ with any Fock state, quantity known as the generalized Husimi Q function[107]

$$Q_n(\alpha) = \frac{1}{\pi} \left| \langle n | \mathbf{D}_\alpha^\dagger | \psi \rangle \right|^2 . \tag{3.9}$$

In this experiment we applied coherent displacements in a 21×21 grid and measured projections in a truncated Fock basis up to 3 photons. Fig. 3.8b illustrates the outcome of measuring the Q functions for the vacuum state $|\psi\rangle = |0\rangle$, which is used for normalizing the measured blockade voltage V_b to photon probabilities.

The Wigner distribution was measured as the expectation value of the parity operator $\mathbf{P} = e^{i\pi \boldsymbol{a}^\dagger \boldsymbol{a}} = \sum_n (-1)^n |n\rangle\langle n|$ as a function of the complex displacement [106, 107]. It can be decomposed into generalized Q function measurements

$$W(\alpha) = \frac{2}{\pi} \sum_n (-1)^n \langle \psi | \mathbf{D}_\alpha | n \rangle \langle n | \mathbf{D}_\alpha^\dagger | \psi \rangle = 2 \sum_n (-1)^n Q_n(\alpha). \tag{3.10}$$

The logical cavity density matrix ρ was reconstructed by solving the set of linear equations from the measured Q functions. For every complex displacement α_m and every measured photon projection n, we can rewrite Eq. (3.9) as

$$Q_n(\alpha_m) = \frac{1}{\pi} \langle n | \mathbf{D}_{\alpha_m}^\dagger \rho \mathbf{D}_{\alpha_m} | n \rangle = \sum_{i,j} M_{nmij} \rho_{ij} \tag{3.11}$$

where $M_{nmij} = \langle n | \mathbf{D}_{\alpha_m}^\dagger | i \rangle \langle j | \mathbf{D}_{\alpha_m} | n \rangle$ and $\rho_{ij} = \langle i | \rho | j \rangle$. This overdetermined linear system of equation was solved using least-squares regression. The fitted density matrix was truncated to five photons and was constrained to be Hermitian, positive semi-definite, of trace one by writing it in the form $\rho = \mathbf{T}^\dagger \mathbf{T} / \mathrm{Tr}(\mathbf{T}^\dagger \mathbf{T})$, where $\mathbf{T}$ is a triangular matrix. The reconstructed density matrix, shown in Fig. 3.9b, was used to calculate the state preparation fidelity $\mathcal{F} = \langle \psi | \rho | \psi \rangle$.

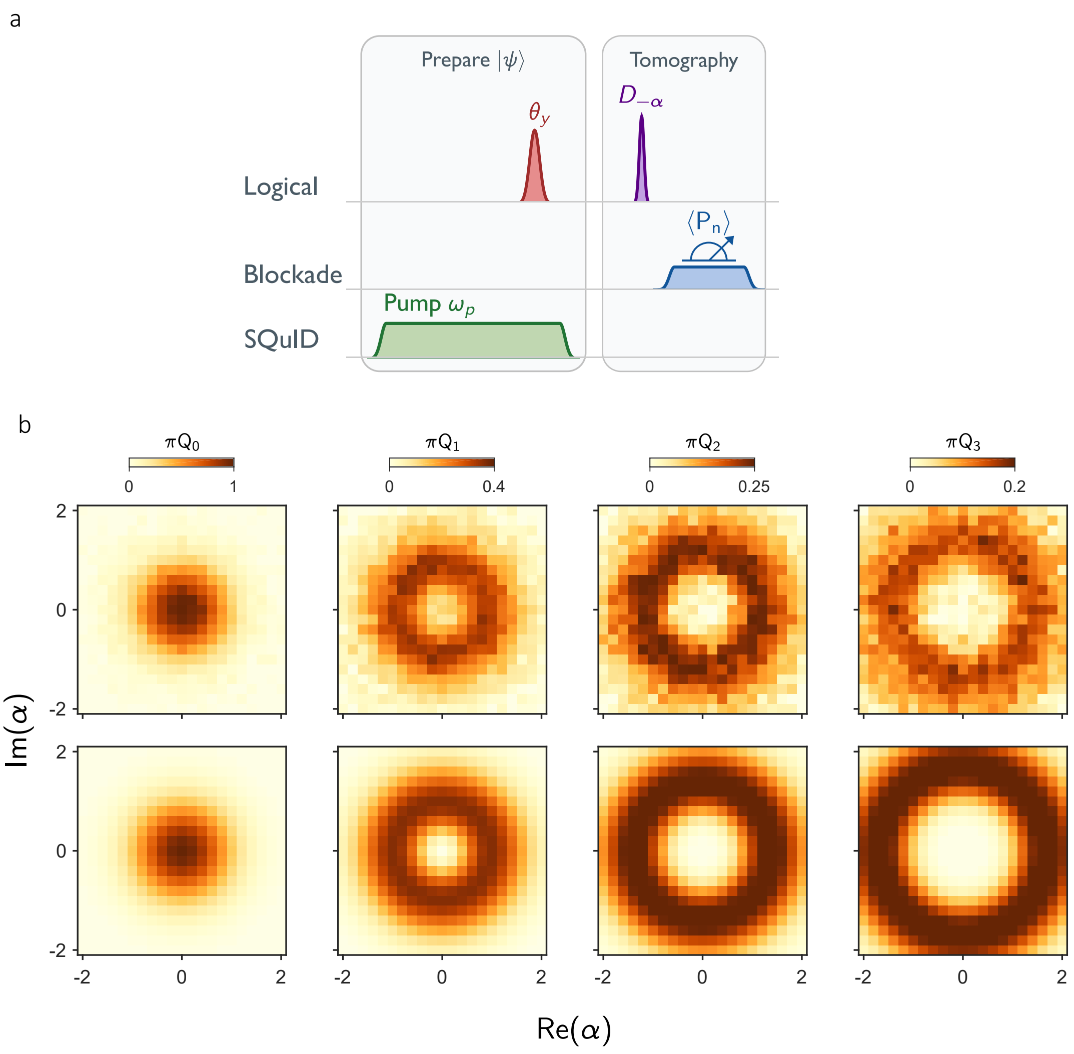

Figure 3.8: **Q function measurement. a.** Experimental pulse sequence for characterizing the logical resonator state. The preparation scheme is the same as in Fig. 3.5a. The logical cavity is driven with a $4\sigma = 100\,\text{ns}$ Gaussian pulse. The tomography sequence consists of a 10 ns resonant pulse, which displaces the prepared state by $-\alpha$, and a measurement pulse through the blockade cavity conditioned on having n photons in the logical cavity, probing the displaced state in Fock basis $p_n = \langle n|\mathbf{D}_{-\alpha}|\psi\rangle$. **b.** Generalized Q_n functions for the logical vacuum state. Top: Experimental results. Bottom: Theory calculation.

The tomography sequence starts with resonantly driving the logical mode with a short Gaussian pulse which can be approximated as a coherent displacement for a weakly anharmonic ($\chi_{aa} = 3$ MHz) logical mode, provided that the spectral bandwidth is large enough to resonantly drive many nearest level transitions [108]. The

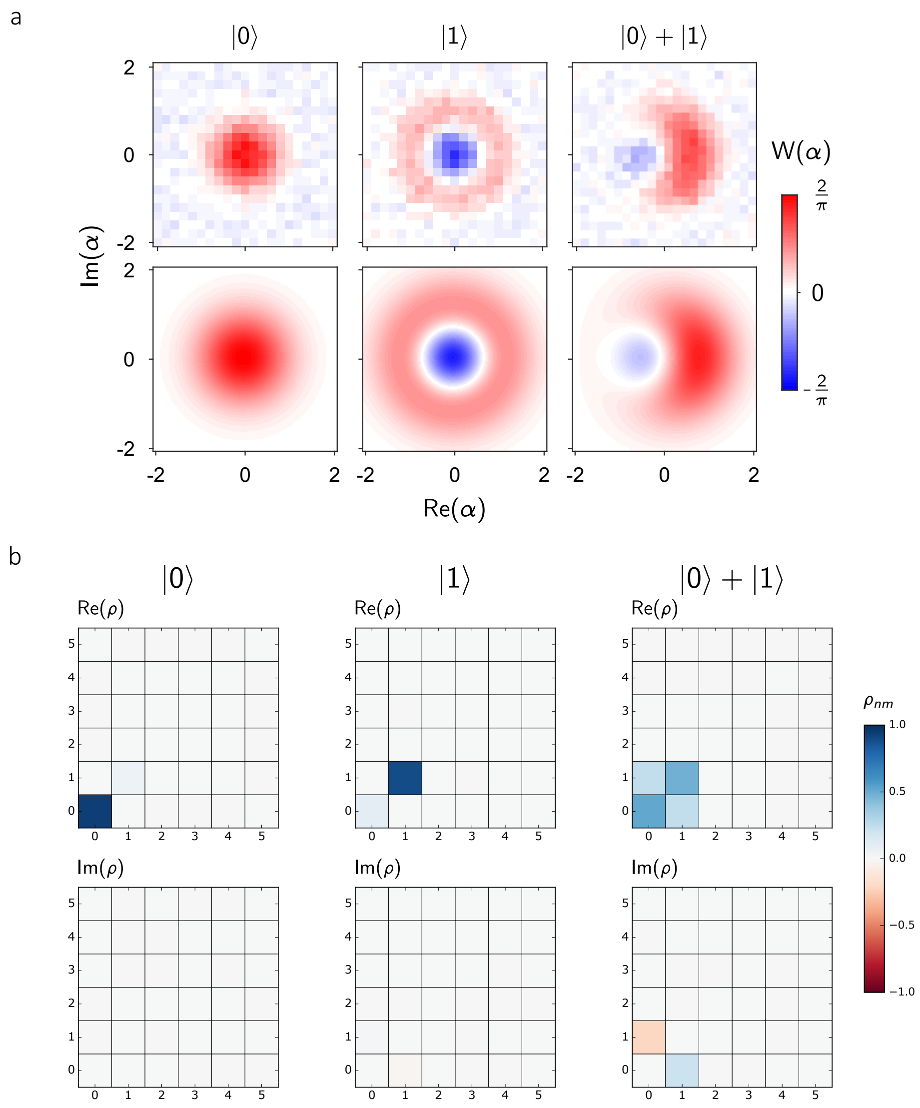

Figure 3.9: **Wigner function tomography.** **a.** Wigner functions for the prepared logical states $|0\rangle, |1\rangle, |+\rangle$. Top: Experimental results. Bottom: Theoretical prediction based on master equation simulation. **b.** Real (top) and imaginary (bottom) components of the reconstructed density matrices.

size and phase of the complex displacement α is controlled by the amplitude and phase of the displacement pulse. After displacing the prepared state by $-\alpha$ we measure the expectation value of the parity operator $\langle \mathbf{P} \rangle = \pi \sum_n (-1)^n P_n$ expressed in terms of the photon number occupation probabilities P_n. Using the photon number dependent frequency shift of the blockade resonance, the probability of having n photons in the logical mode is proportional to the transmitted homodyne signal through the blockade cavity probed at $\omega_b - n\chi_{ab}$. The displacement pulse amplitude is calibrated in units of $|\alpha|$ by fitting the number-selective readout voltage to a Poisson distribution which also normalizes the measured homodyne signal to occupation probabilities for photon numbers up to $n = 3$. The experimentally measured Wigner functions are shown in Fig. 3.9a for the prepared cavity states $|0\rangle$, $|1\rangle$ and $|+\rangle = (|0\rangle + |1\rangle)/\sqrt{2}$ respectively. Performing least-squares regression on the measured Wigner functions we can reconstruct the density matrix ρ for the logical mode. This density matrix is then used to calculate the state fidelity $\mathcal{F} = \langle\psi|\rho|\psi\rangle$ for all experimentally prepared states: $\mathcal{F}_{|0\rangle} = 0.94 \pm 0.009$, $\mathcal{F}_{|1\rangle} = 0.90 \pm 0.002$ and $\mathcal{F}_{|+\rangle} = 0.831 \pm 0.048$. The fidelity for preparing the ground state is limited by thermal occupation. In this experiment, the logical cavity is excited with a 100 ns drive pulse, which highlights how this circuit design can perform cavity operations faster than dispersive protocols[82] by an order of magnitude, with negligible leakage into higher photon states inferred from the reconstructed density matrix.

3.6 Coherence properties

3.6.1 Energy relaxation

The oscillator coherence is bounded by the classical energy decay rate κ_a at the single photon level. This was measured in the absence of flux modulation. We prepare the logical mode in a coherent state with $\alpha_0 \simeq 3$ using a calibrated displacement pulse and after a delay time τ, we measure the population of the vacuum state $P_0(\tau)$ [82] by probing the number-selective transmission of the blockade resonator. The initial state decays as $\alpha(t) = \alpha_0 \exp(-\kappa t)$ and following Poisson statistics, the probability of measuring vacuum is $P_0(\tau) = \exp(-|\alpha(\tau)|^2)$. Fitting the double exponential decay

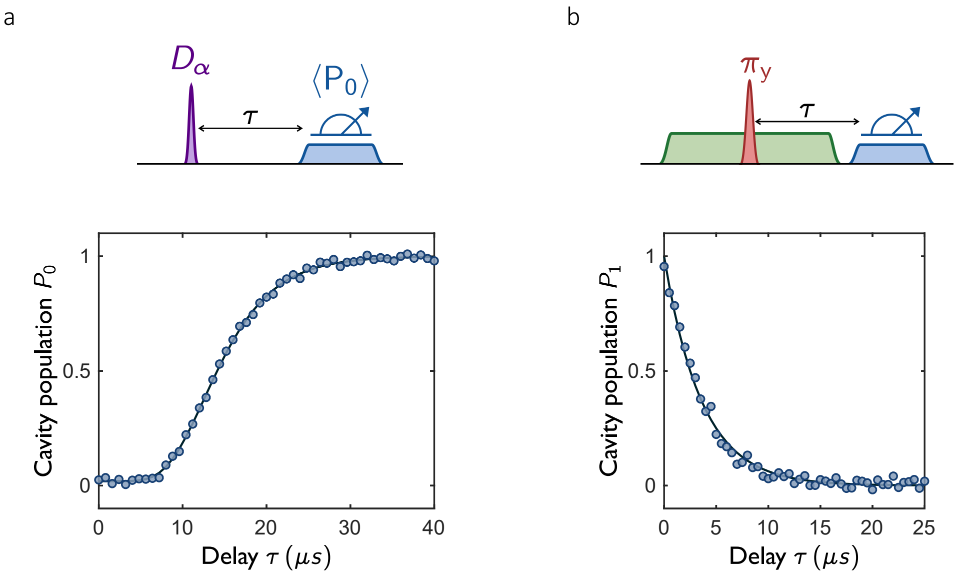

Figure 3.10: **Oscillator energy relaxation. a.** Measuring the cavity decay rate κ_a by probing the vacuum population after displacing the cavity. **b.** Single-photon energy decay. $|1_a\rangle$ state is prepared using a calibrated π_y pulse with $4\sigma = 100\,\mathrm{ns}$. Top diagrams represent the pulse sequences used for each measurement.

to the readout signal (Fig. 3.10a) we extract $\kappa_a/2\pi = 35.2 \pm 0.3\,\mathrm{kHz}$ corresponding to a lifetime $T_\kappa = 1/\kappa = 4.52 \pm 0.04\,\mu\mathrm{s}$.

The relaxation time T_1 of a resonator can be characterized by preparing the $|1\rangle$ state and measuring the probability of finding the oscillator in vacuum as a function of delay. We find a $T_1 = 4.0 \pm 0.22\,\mu\mathrm{s}$ (Fig. 3.10b), which is in close agreement with the measured classical decay rate of a coherent state. Based on this result we speculate that the measured fidelity $\mathcal{F}_{|1\rangle}$ of preparing a single photon is limited by relaxation.

3.6.2 Decoherence

Using a Ramsey-type measurement, we can prepare the $(|0\rangle + |1\rangle)/\sqrt{2}$ state and measure the decay of phase coherence as well as calibrate the $\omega_{01}/2\pi$ transition frequency. The measured decay rate $T_{2*} = 2.1 \pm 0.17\,\mu\mathrm{s}$ (Fig. 3.11a) effectively translates to a dephasing time $T_\phi = 2.91 \pm 0.32\,\mu\mathrm{s}$. We believe this dephasing rate to be limited by low-frequency flux noise which was filtered out in a single-echo measurement to get a

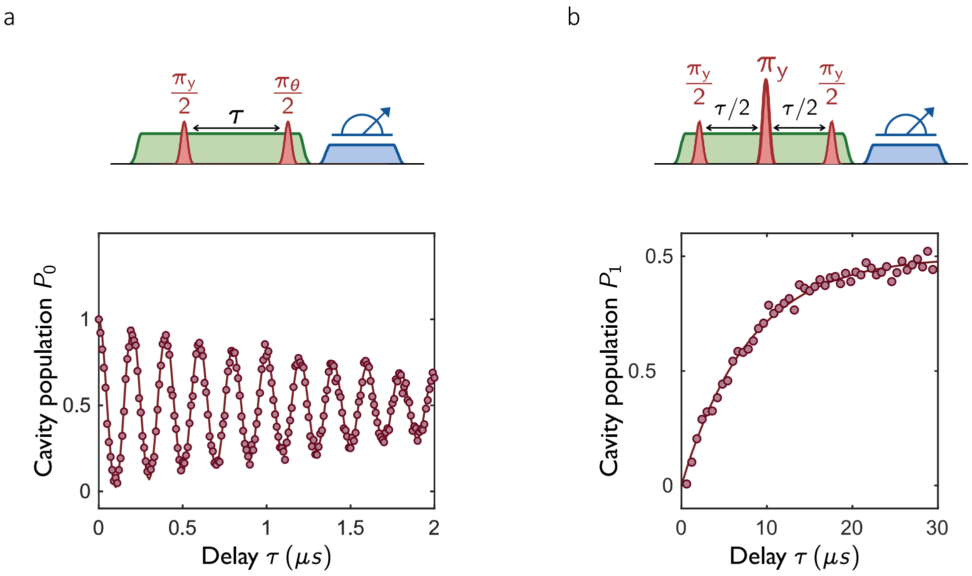

Figure 3.11: **Oscillator decoherence.** **a.** Ramsey experiment to measure phase coherence by applying two resonant $(\pi/2)_y$ pulses with a delay τ in between. The fringe frequency $\omega_{\rm fr}$ is set artificially by varying the azimuth of the second pulse by $\Delta\theta = \omega_{\rm fr}\tau$. **b.** Spin-echo decay measurement. Top diagrams represent the pulse sequences used for each measurement.

relaxation-limited decoherence time $T_{2\rm e} = 7.95 \pm 0.82\,\mu$s $\approx 2T_1$ (Fig. 3.11b). We calculate relaxation and dephasing rates from various noise sources affecting our circuit. Based on estimates for the loss tangent at the material interface for planar resonators and transmon qubits [109, 110], we find T_1 to be limited by dielectric loss present in the resonator capacitance to ground. This loss can be reduced by three orders of magnitude using three-dimensional cavities which are less sensitive to dielectric and conductor loss [111]. The dephasing rate was found to be limited by critical current noise induced by the inductive contribution of the rf-SQuID, which can be further reduced by setting $L_J \gg L_a$ or moving to a capacitively coupled rf-SQuID circuit.

3.6.3 Noise estimations

We use standard methods[60, 112, 113, 114] to estimate T_1 and T_φ due to the effects of various noise channels affecting the circuit. In all the noise calculations outlined in sections below, we use the full circuit Hamiltonian shown in Eq. (A.2). We use the estimated circuit parameters from fitting the measured cavity resonances to the full circuit model as shown in Fig. 3.3a.

Depolarization T_1

For a given noise channel λ, we consider an effective depolarization T_1^λ time to be defined as

$$T_1^\lambda = \left(\frac{1}{T_{1\to 0}^\lambda} + \frac{1}{T_{0\to 1}^\lambda} \right)^{-1}, \tag{3.12}$$

Here, states with labels 0 or 1 correspond to appropriate eigenstates of Eq. (A.2) that correspond to (dressed) logical mode population of 0 and 1 respectively. We assume the blockade mode is in a (dressed) ground state.

Charge noise— The first type of noise we consider is due to coupling of our circuit to external waveguide lines. It leads to the effective $T_{j\to k}^{\mathrm{Q,Ohm}}$ time defined as [115]

$$\frac{1}{T_{j\to k}^{\mathrm{Q,Ohm}}} = \frac{1}{\phi_0^2} \beta_c^2 |\langle k|\boldsymbol{n}_a|j\rangle|^2 R\hbar\omega_{jk} \left[1 + \coth\left(\frac{\hbar\omega_{jk}}{2k_B T} \right) \right], \tag{3.13}$$

with, $R = 50\Omega$, $\beta_c = C_{\mathrm{ext}} / \left(C_a + C_{\mathrm{ext}}\right)$ and C_{ext} representing the coupling capacitance between the logical resonator node and an external driving and readout waveguide. Based on electrostatic simulations, we use $\beta_c = 10^{-3}$.

Flux noise from bias line— This calculation takes into account the Ohmic current noise in the flux-bias line[60, 114] given by the spectral density

$$S_I(\omega) = \frac{2\hbar\omega}{R} \left[1 + \coth\left(\frac{\hbar\omega}{2k_B T} \right) \right]$$

with $R = 50\Omega$. The flux noise spectral density is given by $S_\Phi(\omega) = M^2 S_I(\omega)$, where we assumed the mutual inductance between the coupler loop and the biasing line to be $M = 1500\Phi_0/A$. The effective relaxation rate is given by $1/T_1^{\Phi,\mathrm{Ohm}} = |\langle 0|\partial H/\partial \Phi_{\mathrm{ext}}|1\rangle|^2 S_\Phi(\omega_{01})$.

Dielectric noise— In the case of dielectric noise, we use the definition from Ref. [116] where

$$\frac{1}{T^{\mathrm{d}}_{j\to k}} = \tan\delta R_Q C_a \omega_{jk}^2 |\langle j|\boldsymbol{\varphi}_a|k\rangle|^2 \left[1 + \coth\left(\frac{\hbar\omega_{jk}}{2k_B T}\right)\right], \tag{3.14}$$

with $\tan\delta$ defined as the dielectric loss tangent and $R_Q = \hbar/2e$.

We combine all relaxation rates to yield the effective depolarization time $T_1 = \left(\sum_\lambda 1/T_1^\lambda\right)^{-1}$ and plot the results in Fig. 3.12a. We find that our theory matches the experimentally observed single photon relaxation time for a dielectric loss tangent of $\tan\delta \simeq 4\times 10^{-6}$.

Dephasing

In this section we look at standard calculations which consider effects of noise on a pure dephasing rate T_φ. Exposing the circuit to a noise channel λ with a $1/f$ spectrum and noise amplitude A_λ yields a pure-dephasing time[112, 60, 114]

$$T_\varphi^\lambda = \left\{2A_\lambda^2(\partial_\lambda\omega_a)^2|\ln\omega_{\mathrm{ir}}t|\right\}^{-1/2}. \tag{3.15}$$

We assume that the noise has a low frequency cutoff, $\omega_{\mathrm{ir}} = 1$ Hz, and use a measurement time scale of $t = 10\ \mu$s.

1/f Flux Noise. — We first consider 1/f flux noise. The noise strength is taken as $A_{\Phi_{\mathrm{ext}}} = 1.4\,\mu\Phi_0$[117], and the corresponding pure dephasing time is labeled $T_\varphi^{\Phi_x,1/\mathrm{f}}$.

1/f Critical Current Noise. — Next, we calculate the effects of 1/f critical current noise. The noise strength is taken as $A_{I_c} = 10^{-6}\,I_c$ [118, 60], and the corresponding pure dephasing time is labeled $T_\varphi^{I_c,1/\mathrm{f}}$.

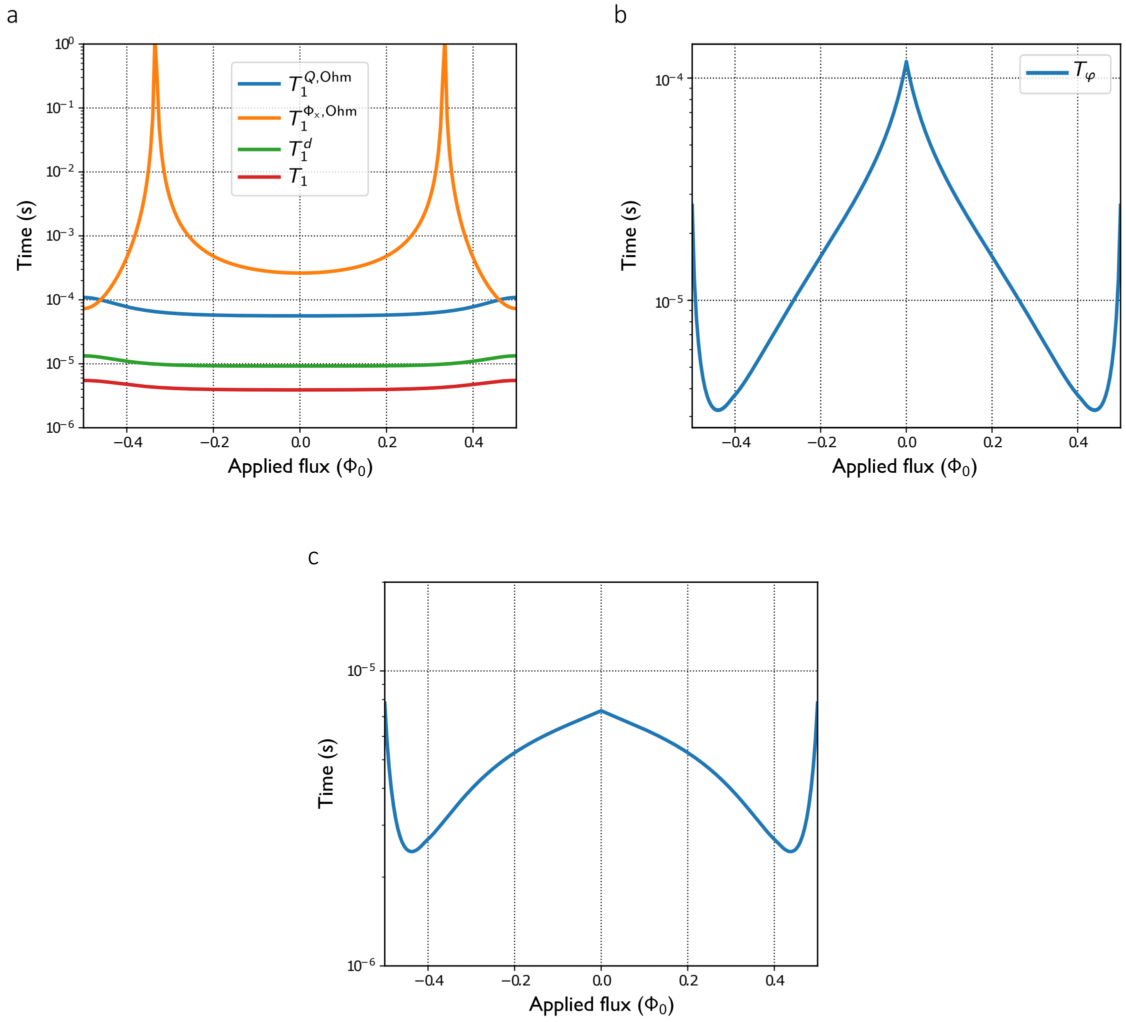

Figure 3.12: **Calculated coherence times for the full circuit model. a.** Relaxation times due to charge noise $T_1^{Q,\mathrm{Ohm}}$ (Ohmic environment due to coupled transmission lines), flux noise $T_1^{\Phi_x,\mathrm{Ohm}}$ (Ohmic flux-generating bias current), and dielectric loss T_1^d. **b.** Effective pure dephasing time due to $1/f$ flux and critical current noise. **c.** Dechoherence time T_2.

1/f Charge Noise. — We expect our circuit to be protected from 1/f charge noise by arguments presented in Ref. [119].

Similarly, we combine all dephasing rates to yield the effective dephasing time $T_\varphi = \left(\sum_\lambda 1/T_\varphi^\lambda\right)^{-1}$ and plot the results in Fig. 3.12b. Finally, we plot the effective decoherence time $T_2 = (1/2T_1 + 1/T_\varphi)^{-1}$ in Fig. 3.12c.

Based on these calculations, we estimate the dephasing rate of the oscillator, at the operating point of zero static flux, to be limited by critical current noise induced by the Josephson junction. This junction noise has maximal effect for the transmon, as the inductive energy is entirely given by the junction energy E_J and the qubit transition sensitivity scales with $\partial\omega_{01}/\partial E_J \approx \sqrt{2E_C/E_J}$. However, in the case of our circuit design described by the Hamiltonian (A.2), the participation of the junction in the total inductive energy is smaller, which leads to a smaller sensitivity of the single photon resonance $\partial\omega_{01}/\partial E_J \approx \sqrt{2E_C/(2E_L + E_J \cos\varphi_{\text{ext}})} \cos\varphi_{\text{ext}}$. With this reduced sensitivity the cavity becomes less susceptible to dephasing induced by the junction as well as reduced disorder in fabricating these resonators with a target single-photon resonance. At the static flux $\varphi_{ext} = 0$, this E_J-sensitivity is reduced, relative to the transmon, by $\sqrt{L_a/(L_a + L_J)}$. For the device described in the main text, this reduction is only 0.5; however, it can be further decreased by either choosing $L_J \gg L_a$ or moving to a capacitive coupling scheme as described in the next section.

3.7 Implementation with 3D cavities

The motivation behind this theoretical study is to present an alternative design which can be implemented in a three-dimensional architecture to benefit from the orders of magnitude improvement in quality factor for microwave resonators[82, 111, 120]. In this section we investigate a different circuit which demonstrates the same underlying principle of introducing nonlinearity in a harmonic oscillator by hybridizing the two-photon state with an external mode via a three-wave mixing process. The circuit, as shown in Fig. 3.13a, consists of a lumped-element resonator capacitively coupled to a fluxonium-like circuit, a Josephson junction with junction energy E_J shunted by a linear inductor L_b and a capacitor C_b. There are two main differences between this circuit and the one presented in Fig.3.2a in the main text: the galvanic coupling to the logical cavity, which is problematic to implement in a 3D architecture, is replaced with a capacitive coupling; and the fluxonium circuit introduces a degree of freedom which fulfills the role of both a blockade mode and a three-wave mixing element. We emphasize that the fluxonium inductance used in this study is different from experimental values commonly used in fluxonium qubits. Fluxonium qubits capacitively coupled to 3D resonators have been studied in previous experiments[121].

Following the same circuit quantization convention, the fluxonium Hamiltonian can be separated into its static and dynamic parts

$$\begin{aligned}\mathbf{H}_{\mathrm{b}} &= \mathbf{H}_{\mathrm{b},0} + \mathbf{H}_{\mathrm{b},d} \\ &= \left(E_{C_b} \boldsymbol{n}_b^2 - E_J J_0(\epsilon) \cos \boldsymbol{\varphi}_b + \frac{1}{2} E_L \boldsymbol{\varphi}_b^2 \right) \\ &\quad - E_J \left(2 \sum_{n=1}^{\infty} (-1)^n J_{2n}(\epsilon) \cos(2n\omega_p t) \cos \boldsymbol{\varphi}_b + (-1)^n J_{2n-1}(\epsilon) \cos[(2n-1)\omega_p t] \sin \boldsymbol{\varphi}_b \right).\end{aligned} \tag{3.16}$$

and the full-circuit Hamiltonian is given by

$$\mathbf{H} = \omega_a \boldsymbol{a}^\dagger \boldsymbol{a} + \sum_k E_k |k\rangle\langle k| + \sum_{j,k} i g_{jk} (\boldsymbol{a}^\dagger - \boldsymbol{a}) |j\rangle\langle k| + \mathbf{H}_{\mathrm{b},d}, \tag{3.17}$$

where $|k\rangle$ and E_k stand for the kth eigenstate and eigenenergy of the static fluxonium Hamiltonian $\mathbf{H}_{\mathrm{b},0}$. The charge operators were expressed as $\boldsymbol{n}_a = i n_a^{\mathrm{zpf}} (\boldsymbol{a}^\dagger - \boldsymbol{a})$ and $\boldsymbol{n}_b = \sum_{j,k} n_{jk} |j\rangle\langle k|$, $n_{jk} = \langle j | \boldsymbol{n}_b | k \rangle$, with the coupling amplitudes defined as $g_{jk} = E_{Cc} n_a^{\mathrm{zpf}} n_{jk}$ and $n_a^{\mathrm{zpf}} = (E_{La}/4E_{Ca})^{1/4}/\sqrt{2}$. To avoid compromising the logical cavity coherence, the linear capacitive coupling needs to be sufficiently small to keep the resonator and fluxonium qubit in the dispersive regime, while still ensuring a large enough three-wave mixing coupling.

In a similar fashion we apply a flux drive to the fluxonium circuit to generate a time-dependent three-wave interaction term in the Hamiltonian of the form $g_2(t)(\boldsymbol{a}^{\dagger 2}|0\rangle\langle 1| + \boldsymbol{a}^2 |1\rangle\langle 0|)$, with $g_2(t) = g_{2,d} \cos(\omega_p t)$. Choosing the pump frequency

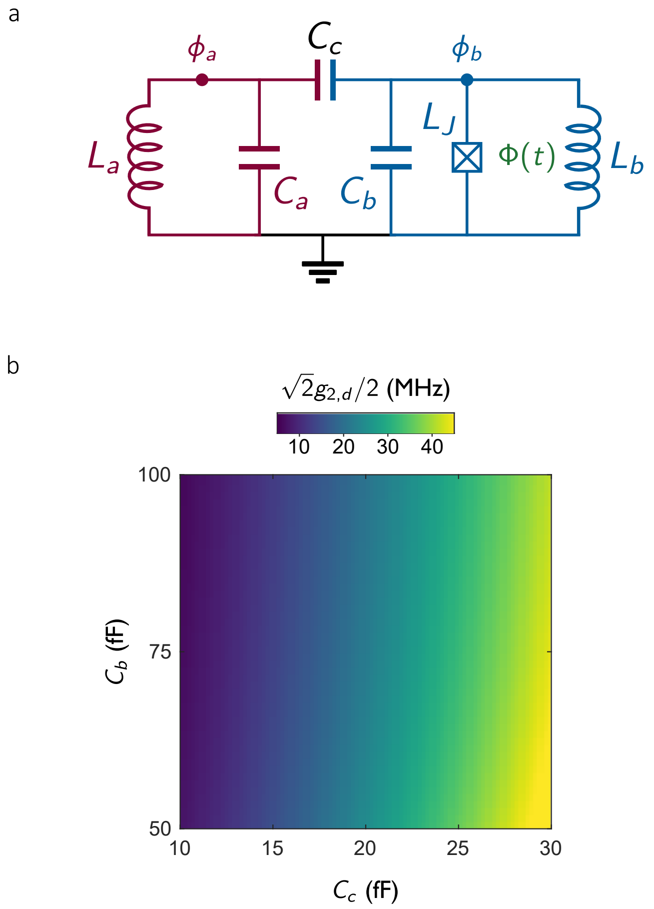

Figure 3.13: **Circuit model for 3D implementation. a.** Schematic circuit diagram for a resonator (red) capacitively coupled to a fluxonium-like circuit (blue) used for hybridizing the resonator two-photon state. **b.** Estimated induced anharmonicity based on equation (A.35).

such that $\omega_p = |2\omega_a - \epsilon_{01}|$ yields an effective anharmonicity of magnitude $\sqrt{2}g_{2,d}/2$. The full quantization treatment of this circuit, as well as the final expression for the anharmonicity, is provided in Appendix A.

Calculation for dynamical anharmonicities was carried out for physically achievable circuit parameters aimed at reaching large three-wave coupling rates. Going with the geometry of a quarter-wave coaxial resonator [82], the cavity parameters were chosen to be $\omega_a = 4\,\text{GHz}$ and $Z_a = 180\,\Omega$, which corresponds to $C_a = 221\,\text{fF}$ and $L_a = 7.16\,\text{nH}$. The chosen parameters for the fluxonium circuit were $E_J = 16\,\text{GHz}$

and $E_{Lb} = 10\,\mathrm{GHz}$, while the values of the shunting capacitor C_b and coupling capacitor C_c were varied within a reasonable parameter range. The three-wave mixing amplitude $g_{2,d}$ was evaluated using a flux modulation amplitude of $\delta/\Phi_0 \simeq 0.18$. The estimated anharmonicity is plotted in Fig. 3.13b as a function of capacitive parameters. For $C_b = 90\,\mathrm{fF}$ and $C_c = 30\,\mathrm{fF}$, the anharmonicity becomes $\sqrt{2}g_{2,d}/2 \simeq 30\,\mathrm{MHz}$.

To summarize the analysis in this section, we find that in a suitable rage of physically achievable parameters this minimal circuit design can achieve similar anharmonicities as the ones experimentally demonstrated with the galvanic coupling. This encouraging observation offers a pathway to implement these nonlinear cavities in a 3D architecture in order to benefit from orders of magnitude improvement in quality factor.

3.8 Summary and Outlook

In summary, we have demonstrated the capability of tailoring the Hilbert space of a superconducting oscillator by dynamically activating a three-wave interaction with an ancillary mode. Owing to the large three-wave coupling, this platform can be advantageous to dissipative stabilization schemes[86, 87], which rely on two-photon loss for confining a state in a manifold protected against dephasing errors[83]. The novelty of this work is centered around using this stimulated nonlinearity for selectively driving the single-photon manifold as an effective two-level system at rates faster than dispersive protocols[82]. Despite the modest coherence of lithographically defined resonators, this proof of principle can be easily extended to three-dimensional microwave cavities, under a modified circuit model discussed in the previous section, thus providing a pathway for engineering qubits with millisecond[82, 111], and even up to second[120], coherence times.

Chapter 4

Photon crystallization in synthetic dimensions

4.1 Introduction

The dynamical photon nonlinearity introduced in the previous chapter was used for inducing anharmonicity in the Hilbert space of a microwave resonator. This led to engineering a new type of superconducting qubit for applications in quantum computing. The outline of this chapter is to introduce a theoretical proposal for exploiting this dynamical nonlinearity for quantum simulation of interacting photons in a lattice.

As pointed out in the introductory chapter, a promising testbed for investigating condensed matter physics with strongly correlated photons is to confine photons in a lattice of coupled cavities and engineer photon-photon interactions through strong optical nonlinearities induced by atomic media [28, 27, 29].

Circuit QED becomes a promising platform for exploring many-body physics in coupled lattices of superconducting circuits, recent reviews can be found in [16, 23, 22, 20]. One can easily engineer low-disorder lattices of microwave resonators using standard lithographic and machining techniques. More importantly, superconducting circuits composed of Josephson junctions can be harnessed as a resource for mediating interactions between microwave photons [105]. Bose-Hubbard lattices have been investigated in various platforms. Following the theory work in [22], early experiments embedded transmon qubits on every cavity lattice to induce (resonant) Jaynes-Cummings photon repulsion [46] and observed a dynamical localization transition from the competition between coherent tunneling and on-site photon interactions. Recent experiments have shifted the focus to transmon lattices, where each qubit site can be treated as nonlinear resonators with an on-site Kerr nonlinearity set by the transmon anharmonicity. This platform was used for the dissipative stabilization of a photonic Mott insulator [50] and for reproducing the energy spectrum for 2D electrons in a magnetic field [51]. Additionally, there is the approach of creating non-local photon interactions using tunable dc-SQuID coupling elements between resonators [122, 123], where the photons are predicted to have density wave ordering.

The common challenge with all these platforms is that by scaling these many-body circuits it becomes experimentally difficult to realize full control of your system and to read out its microscopic properties. Our approach is to utilize the dynamical nonlinearity demonstrated for a single cavity in Chapter 3 and extend it to engineering photon interactions in a synthetic lattice composed of the eigenmodes in a cavity array. This proposal presents a field-programmable simulator with individual parametric control over photon tunneling and interactions. Inspired by the initial experiments demonstrating arbitrary control of a multi-mode quantum RAM [84], this platform is hardware-efficient as we need only a single nonlinear Josephson circuit coupled to all the modes of the lattice.

The first theoretical studies concerning the many-body aspects of interacting photons in a lattice focused on closed optical systems at thermal equilibrium. However, photonic structures are inherently dissipative and the driven-dissipative nature of these nonlinear optical systems was later recognized in [38]. The theoretical study in [39] was the first to investigate the many body features of a nonlinear cavity array in a non-equilibrium setting, where the interplay of coherent driving and dissipation can generate strongly-correlated photonic states. The nonlinearity considered in [39] was a Kerr nonlinearity, this open-system model being investigated later in [40] to reveal the onset of polariton crystallization for strong nonlinearities. In this chapter we investigate if such a strongly-correlated regime can be achieved with the dynamical nonlinearity implemented in Chapter 3.

4.2 Field programmable cavity array

In this section we outline the details of the proposed platform for a nonlinear lattice of microwave photons. The model consists of a one dimensional tight-binding chain of microwave resonators, coupled on one edge to an ancillary blockade resonator via a nonlinear Josephson element, as shown in Fig. 4.1. This system is a natural extension to the two resonator experiment analyzed in the previous chapter. The relevant harmonic degrees of freedom are the distributed momentum states of the chain, which correspond to the diagonal states in the normal mode basis

$$\mathbf{H}_{\rm cca} = \sum_j \omega_a \boldsymbol{a}_j^\dagger \boldsymbol{a}_j + g \sum_{\langle i,j \rangle} (\boldsymbol{a}_i^\dagger \boldsymbol{a}_j + \boldsymbol{a}_i \boldsymbol{a}_j^\dagger) = \sum_k \omega_k \boldsymbol{a}_k^\dagger \boldsymbol{a}_k. \tag{4.1}$$

The Hamiltonian arrives at a decoupled form simply by using the Fourier transform $\boldsymbol{a}_j^\dagger = \frac{1}{\sqrt{N+1}} \sum_k \mathrm{e}^{-i\pi k j/(N+1)} \boldsymbol{a}_k^\dagger$, which yields the eigenmode dispersion $\omega_k = \omega_a - 2g\cos(\pi k/(N+1))$ for open boundary conditions. The blockade cavity is coupled to one end of the chain (without loss of generality take it to be $n = 1$), which has the following decomposition in the eigenmode basis

$$\boldsymbol{a}_1^\dagger = \sum_k \frac{\cos(\frac{\pi k}{N+1})}{\sqrt{(N+1)/2}} \boldsymbol{a}_k^\dagger \triangleq \sum_k u_{1,k} \boldsymbol{a}_k^\dagger. \tag{4.2}$$

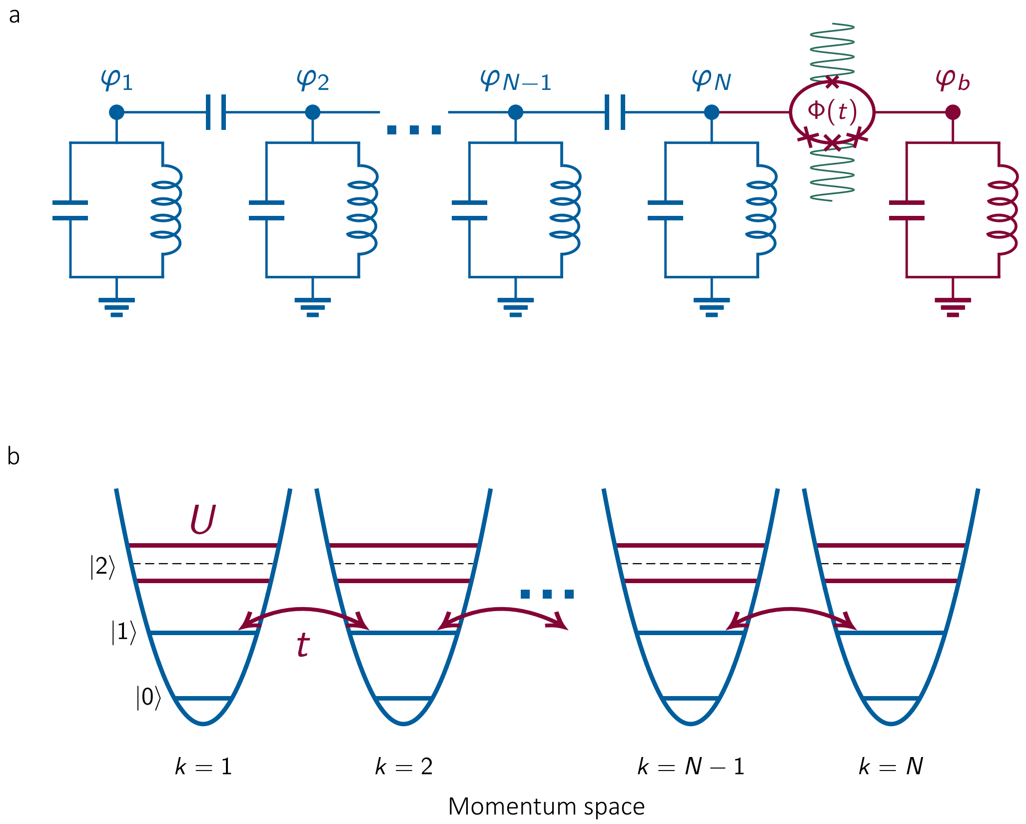

Figure 4.1: **Model for a field programmable cavity array. a.** Schematic circuit diagram for a resonator chain coupled to an ancillary blockade mode via a nonlinear Josephson circuit subject to a multi-tone flux drive. **b.** Schematic diagram of the distributed momentum states with stimulated nearest neighbor photon hopping and nonlinearity induced by the hybridized two-photon states.

We can write the decomposition in a generic form where the weight of each eigenmode $u_{1,k}$ is equal to the complex value of its wavefunction at the edge. It is important for the blockade resonator and Josephson circuit to be coupled to every eigenmode, $|u_{1,k}| \neq 0 \ \ \forall k$, in order to introduce nonlinearity to each momentum site and mediate photon propagation in the lattice.

The Josephson coupling circuit is implemented as a Kerr-free pure three-wave mixing element, superconducting loop composed of one small junction and several larger junctions, which has been implemented in several experiments [99, 102, 124].

The coupler potential has the functional form $\mathbf{U}_c(\boldsymbol{\varphi}) = \eta_2(\varphi_{\text{ext}})\boldsymbol{\varphi}^2 + \eta_3(\varphi_{\text{ext}})\boldsymbol{\varphi}^3$ in terms of the phase difference operator $\boldsymbol{\varphi}$ across the coupler nodes. The coupler loop is threaded with both DC and RF magnetic flux $\varphi_{\text{ext}} = \bar{\varphi}_{\text{ext}} + \varphi(t)$, where the time dependent component can have multiple drive tones. The coefficients η_n arise from expanding the coupler potential biased at $\bar{\varphi}_{\text{ext}}$, where the junction energies and asymmetry is absorbed in the coefficients. The effect of the coupler on the multimode structure becomes evident when expanding the phase across the circuit in terms of the eigenmode and blockade field operators

$$\begin{aligned}\boldsymbol{\varphi} &= \varphi_b^{\text{zpf}}\left(\boldsymbol{b}^\dagger + \boldsymbol{b}\right) - \varphi_1^{\text{zpf}}\left(\boldsymbol{a}_1^\dagger + \boldsymbol{a}_1\right)\\ &= \varphi_b^{\text{zpf}}\left(\boldsymbol{b}^\dagger + \boldsymbol{b}\right) - \sum_k u_{1,k}\varphi_k^{\text{zpf}}\left(\boldsymbol{a}_k^\dagger + \boldsymbol{a}_k\right).\end{aligned} \tag{4.3}$$

Applying a single-tone drive $\varphi(t) = \varepsilon\cos(\omega_p t)$, with a small drive amplitude ε, the combined system Hamiltonian becomes

$$\begin{aligned}\mathbf{H} =& \sum_k \omega_k \boldsymbol{a}_k^\dagger \boldsymbol{a}_k + \omega_b \boldsymbol{b}^\dagger \boldsymbol{b}\\ &+ \left(\beta_0(\epsilon) + \beta_2(\epsilon)\cos(2\omega_p t)\right)\left[\varphi_b^{\text{zpf}}\left(\boldsymbol{b}^\dagger + \boldsymbol{b}\right) - \sum_k u_{1,k}\varphi_k^{\text{zpf}}\left(\boldsymbol{a}_k^\dagger + \boldsymbol{a}_k\right)\right]^2\\ &+ \beta_3(\epsilon)\cos(\omega_p t)\left[\varphi_b^{\text{zpf}}\left(\boldsymbol{b}^\dagger + \boldsymbol{b}\right) - \sum_k u_{1,k}\varphi_k^{\text{zpf}}\left(\boldsymbol{a}_k^\dagger + \boldsymbol{a}_k\right)\right]^3\end{aligned} \tag{4.4}$$

where the β_n terms arise from the Jacobi-Anger expansion on the coupler coefficients η biased at the static flux point. The resonance frequency of the blockade cavity is given by $\omega_b/2\pi$. From this Hamiltonian it becomes clear how the initially orthogonal momentum states become coupled through the quadratic term $\boldsymbol{\varphi}^2$ from the coupler inductive energy, and additionally can acquire nonlinearity from the cubic term $\boldsymbol{\varphi}^3$.

Expanding the coupler inductive energy we get all possible linear coupling terms between the eigenmodes and blockade mode. Photon hopping can be parametrically induced by simply modulating the inductive terms at the frequency detuning between the momentum sites you want to couple. This has been achieved in several experiments [48, 123, 93]. Assuming the relevant pump frequencies are $2\omega_p \approx (\omega_{k'} - \omega_k) \triangleq \Delta_{k,k'}$, it is safe to ignore off-resonant terms which couple the eigenmodes to the blockade mode $a_k^\dagger b$, given that the blockade resonator is far detuned from the eigenmode band. Within RWA the quadratic part of the Hamiltonian becomes

$$\mathbf{H}_c^{(2)} = \sum_k \delta\omega_k \boldsymbol{a}_k^\dagger \boldsymbol{a}_k + \delta\omega_b \boldsymbol{b}^\dagger \boldsymbol{b} + \sum_{k,k'} t_{k,k'}(\varepsilon)\cos(2\omega_p t)(\boldsymbol{a}_k^\dagger \boldsymbol{a}_{k'} + \boldsymbol{a}_k \boldsymbol{a}_{k'}^\dagger) \tag{4.5}$$

where $\delta\omega_k = \beta_0(\varepsilon) u_{1,k}^2 (\varphi_k^{\mathrm{zpf}})^2$ and $\delta\omega_b = \beta_0(\varepsilon)(\varphi_b^{\mathrm{zpf}})^2$ are static frequency shifts due to the parametric flux drive, as highlighted in the previous chapter. This leads to renormalized mode frequencies $\widetilde{\omega}_k = \omega_k + \delta\omega_k$, $\widetilde{\omega}_b = \omega_b + \delta\omega_b$. Choosing discrete pump frequencies that match the criteria $2\omega_p = \tilde{\Delta}_{k,k'}$ leads to a resonant swap of photons between modes k, k' with an effective hopping rate $t_{k,k'}(\varepsilon) = u_{1,k} u_{1,k'} \beta_2(\varepsilon) \varphi_k^{\mathrm{zpf}} \varphi_{k'}^{\mathrm{zpf}}$. If the cavity chain has a linear dispersion $\tilde{\Delta}_{k-1,k} = \tilde{\Delta}_{k,k+1}$, then inducing propagation of photons between nearest neighbor momentum sites is achieved trivially by driving the coupler with a single tone at the free spectral range [125]. However, this can lead to complications when introducing nonlinearity, as discussed in the next paragraph. As such, we will assume a nonlinear dispersion $\tilde{\Delta}_{k-1,k} \neq \tilde{\Delta}_{k,k+1}$ which has the drawback in needing more drive tones to engineer the desired linear couplings.

Expanding the cubic part of the coupler Hamiltonian generates all possible combinations of three-wave processes. The terms of interest are those which exchange two photons in every eigenmode with one photon in the blockade mode. We can parametrically activate these nonlinear terms, and thereby cancel all remaining fast rotating ones, by driving the coupler at the frequencies $\omega_p = 2\widetilde{\omega}_k - \widetilde{\omega}_b$. Going to the rotating frame of these combined drives give the following Hamiltonian.

$$\mathbf{H}_c^{(3)} = \sum_k U_k(\varepsilon)\cos(\omega_p t)\left(\boldsymbol{a}_k^{\dagger 2}\boldsymbol{b} + \boldsymbol{a}_k^2\boldsymbol{b}^\dagger\right) \tag{4.6}$$

where the stimulated nonlinearity is given by $U_k(\varepsilon) = u_{1,k}\beta_2(\varepsilon)(\varphi_k^{\text{zpf}})^2\varphi_b^{\text{zpf}}$. If the eigenmodes are linear spaced $\omega_k = \nu k$, then a flux drive $\omega_p = 2\widetilde{\omega}_k - \widetilde{\omega}_b$ which activates the resonant process $\boldsymbol{a}_k^2\boldsymbol{b}^\dagger$ will also activate the process $\boldsymbol{a}_p\boldsymbol{a}_q\boldsymbol{b}^\dagger$, for any integers $p, q \neq k$ that satisfy $p + q = 2k$. At the time of this study we are not certain what consequences this complication will bring to the physics observed in this synthetic lattice. For now we will continue the analysis by assuming the eigenmode dispersion is nonlinear, equivalent to $2\widetilde{\omega}_k \neq \widetilde{\omega}_p + \widetilde{\omega}_q$, and the chosen drive frequency will only induce the necessary two-photon blockade interaction.

Moving to the full model, the coupler circuit is flux-driven with a set of drives at the eigenmode detunings $\widetilde{\Delta}_{k,k+1}$ and drives which satisfy the two-photon blockade conditions $\omega_{p,k} = 2\widetilde{\omega}_a - \widetilde{\omega}_b$. Additionally, photons are injected into every eigenmode using a set of coherent drives $\mathbf{H}_d = \sum_k \left(\Omega_k e^{-i\omega_{d,k}t}\boldsymbol{a}_k^\dagger + \text{h.c.}\right)$, with their corresponding drive strengths Ω_k and frequencies $\omega_{d,k}$. Moving to the rotating frame for the combined coherent drives and flux-drives using the following transformation

$$\mathbf{R} = \exp\left[\sum_k i\omega_{d,k}t\boldsymbol{a}_k^\dagger\boldsymbol{a}_k + \frac{1}{N}\sum_k i(2\omega_{d,k} - \omega_{p,k})t\boldsymbol{b}^\dagger\boldsymbol{b}\right], \tag{4.7}$$

gives the Hamiltonian $\widetilde{\mathbf{H}} = \mathbf{R}\mathbf{H}\mathbf{R}^\dagger + i\dot{\mathbf{R}}\mathbf{R}^\dagger$ with a more intuitive form

$$\begin{aligned}\mathbf{H} = &\sum_k \Delta\widetilde{\omega}_k\boldsymbol{a}_k^\dagger\boldsymbol{a}_k + \Delta\widetilde{\omega}_b\boldsymbol{b}_b^\dagger\boldsymbol{b} + \sum_{\langle k,k'\rangle} t_{k,k'}(\varepsilon)(\boldsymbol{a}_k^\dagger\boldsymbol{a}_{k'} + \boldsymbol{a}_k\boldsymbol{a}_{k'}^\dagger)\\ &+ \sum_k \frac{1}{2}U_k(\varepsilon)(\boldsymbol{a}_k^{\dagger 2}\boldsymbol{b} + \boldsymbol{a}_k^2\boldsymbol{b}^\dagger) + \sum_k(\Omega_k^*\boldsymbol{a}_k^\dagger + \Omega_k\boldsymbol{a}_k).\end{aligned} \tag{4.8}$$

The frequency detunings are defined as $\Delta\widetilde{\omega}_k = \widetilde{\omega}_k - \omega_{d,k}$ and $\Delta\widetilde{\omega}_b = \widetilde{\omega}_b - \frac{1}{N}\sum_k(2\omega_{d,k} - \omega_{p,k})$, both equal to zero when resonantly driving each eigenmode $\omega_{d,k} = \widetilde{\omega}_k$.

In this convenient frame the system is described by an interacting photonic lattice in momentum space. More precisely, we have a chain of coupled photonic modes where microwave photons can propagate between nearest sites in this synthetic dimension and experience on-site photon-photon interactions from the energy penalty induced by the strongly hybridized two-photon states. From this theoretical description it becomes clear how this field-programmable bosonic simulator allows both the tunneling and nonlinearity parameters to be tuned in-situ through their corresponding flux drive amplitudes ε. This is an attractive platform compared to other implementations, and the hardware efficiency is limited by the experimental cost of applying all the necessary microwave flux drives. Nevertheless, this is not completely out of reach, since it is possible to directly synthesis all microwave waveforms using a very fast (30 GS/s) arbitrary wave generator, instead of requiring an analog microwave generator for every drive term. This approach has been readily implemented in quantum computing experiments [84, 126], demonstrating gate fidelities comparable to conventional up-conversion techniques.

4.3 Quantum trajectory simulation

For the remainder of this chapter, we will perform numerical simulations of the multimode circuit described by the Hamiltonian 4.8 using an open quantum system approach. In this framework, we describe the dissipation of every mode m into the environment in terms of the non-Hermitian operator $\boldsymbol{a}_m$ with a characteristic loss rate κ_m, which can be combined into a defined collapse operator $\widetilde{\boldsymbol{a}}_m = \sqrt{\kappa_m}\boldsymbol{a}_m$. We can think of these collapse operators as quantum jumps in the system wavefunction resulting from continuous measurement operators acting on the environment. Tracing out the environment degrees of freedom, the equation of motion for the system density matrix is given by the Markovian master equation [127, 128]

$$\begin{aligned}\dot{\rho} =& - i\left[\mathbf{H}, \rho\right] - \frac{1}{2}\left[\widetilde{\boldsymbol{a}}_m^\dagger \widetilde{\boldsymbol{a}}_m \rho + \rho \widetilde{\boldsymbol{a}}_m^\dagger \widetilde{\boldsymbol{a}}_m - 2\widetilde{\boldsymbol{a}}_m \rho \widetilde{\boldsymbol{a}}_m^\dagger\right] \\ =& - i\left(\mathbf{H}_{\text{eff}}\rho - \rho\mathbf{H}_{\text{eff}}^\dagger\right) + \sum_m \widetilde{\boldsymbol{a}}_m \rho \widetilde{\boldsymbol{a}}_m^\dagger \end{aligned} \tag{4.9}$$

where in the second line we expressed it as a Schrödinger equation with an effective non-Hermitian Hamiltonian $\mathbf{H}_{\text{eff}} = \mathbf{H} - \frac{i}{2}\sum_m \widetilde{\boldsymbol{a}}_m^\dagger \widetilde{\boldsymbol{a}}_m$. For our study, we are interested in the steady-state response of the system subjected to dissipation and coherent drives. In particular, we are evaluating the expectation values of certain observables $\langle \boldsymbol{A} \rangle = \mathrm{Tr}\left(\boldsymbol{A}\rho_{\text{ss}}\right)$ from the steady-state density matrix satisfying $\dot{\rho}_{\text{ss}} = 0$. For a system with only a handful of modes ($N \geq 5$), each with a cutoff of three photons, computing this matrix can be rather time consuming for fixed hardware resources.

The quantum trajectory approach can be more computationally efficient given that it handles the dynamics of wavefunctions instead of the whole density matrix. Ref. [129] offers an insightful review on the quantum trajectory approach, with focus on open many-body systems. This method involves discretizing the master equation in infinitesimal time steps δt and evaluate individual trajectories for the system wavefunction $|\psi(t)\rangle$. Starting with an initial state at time $t = 0$ (for example all the modes are in their vacuum state), the state propagates forward in time, where during a single time step the new wavefunction can become

$$|\psi^{(1)}(t + \delta t)\rangle = (1 - i\mathbf{H}_{\text{eff}}\delta t)\,|\psi(t)\rangle. \tag{4.10}$$

However, since $\mathbf{H}_{\text{eff}}$ is non-Hermitian, the outcome of each time step evolution is stochastic. With a probability $\langle\psi^{(1)}(t+\delta t)|\psi^{(1)}(t+\delta t)\rangle = 1-\delta p$, the state is projected to $|\psi(t + \delta t)\rangle = |\psi^{(1)}(t + \delta t)\rangle/\sqrt{1 - \delta p}$. With a probability δp, the wavefunction undergoes a jump $\widetilde{\boldsymbol{a}}_m$ (for a randomly chosen m) and the states is projected to

$|\psi(t+\delta t)\rangle = \widetilde{\boldsymbol{a}}_m|\psi(t)\rangle/\sqrt{\langle\psi(t)|\widetilde{\boldsymbol{a}}_m^\dagger\widetilde{\boldsymbol{a}}_m|\psi(t)\rangle}$. This procedure is then repeated for all the other evolution intervals until the final time is reached. The expectation value of a particular operator $\boldsymbol{A}$ at a given time t is evaluated by averaging each stochastic expectation value over all the trajectories

$$\langle\boldsymbol{A}\rangle_t = \overline{\langle\psi(t)|\boldsymbol{A}|\psi(t)\rangle} \tag{4.11}$$

In a nutshell this is how the Monte Carlo solver in QuTip [130] calculates the trajectories for the wavefunction evolution. We use this package for all the numerical results presented in this chapter. The total number of trajectories for each simulation is around five hundred to one thousand and it was conditioned on the convergence of $\langle\boldsymbol{A}\rangle_t$. Additionally, since we are interested in the steady state response, the trajectories were evaluated up to a final time t_f chosen such that expectation values reached their steady state values expected from the master equation $\langle\boldsymbol{A}\rangle_{t_f} = \langle\boldsymbol{A}\rangle_{ss}$.

4.4 Single site nonlinearity

Engineering nonlinear optical media with substantial nonlinearities at the single-photon level can lead to emitted light fields with non-classical statistics. This has been studied extensively in the framework of light-matter interaction in quantum optics [25, 26]. Such strong nonlinearities have been observed in the early cavity QED experiments with atomic systems [131, 132] due to the photon blockade effect.

In this section we revisit the case of a single resonator with a stimulated nonlinearity which was experimentally studied in Chapter 3. Specifically, this nonlinearity arises from the strong hybridization of the two-photon state which can be interpreted as a two-photon blockade effect. Photon correlation measurements are effective probes for investigating the phases of driven-dissipative many-body optical systems [133, 38]. In these engineered quantum simulators, interacting photons are explored in a non-equilibrium regime, where photon losses are compensated through coherent drives that continuously pump photons back into the system. For a single nonlinear resonator, we reveal the effects of this nonlinearity by probing the photon statistics of the emitted light through the second order correlation function

$$g^{(2)}(\tau) = \frac{\langle \boldsymbol{a}^\dagger(0)\boldsymbol{a}^\dagger(\tau)\boldsymbol{a}(\tau)\boldsymbol{a}(0)\rangle}{\langle \boldsymbol{a}^\dagger\boldsymbol{a}\rangle^2}. \tag{4.12}$$

In Fig 4.2 we plot the zero-time-delay correlation function $g^{(2)}(\tau = 0)$, as a function of the coherent drive strength Ω and photon nonlinearity U scaled in units of the dissipation rate κ. The function $g^{(2)}(0) = \mathrm{Tr}\left[\boldsymbol{a}^\dagger\boldsymbol{a}^\dagger\boldsymbol{a}\boldsymbol{a}\rho_{ss}\right]/\mathrm{Tr}\left[\boldsymbol{a}^\dagger\boldsymbol{a}\rho_{ss}\right]^2$ is numerically evaluated for the steady state found with the quantum trajectory method. This values basically represents the probability of simultaneously emitting two photons, normalized by the two-photon emission probability for a coherent (random) source. A coherent light source, for example a laser, emits photons at random interval spacings and yields a Poissonian photon number distribution where the variance is equal to the mean. In this phase diagram, $g^{(2)}(0)$ displays a sharp transition from Poissonian statistics ($g^{(2)}(0) = 1$) to sub-Poissonian statistics ($g^{(2)}(0) < 1$). Light sources that exhibit sub-Poissonian statistics, for example individual atoms, emit a train of single-photons well separated in time. This phenomena is termed photon antibunching and this is a unique quantum feature of strongly nonlinear optical systems. The presence of a strong nonlinearity prevents more than a single drive photon from entering the resonator. This is not surprising given the Rabi oscillations observed in Fig. 3.5b.

The threshold for antibunched emission U_{th} depends on the drive strength Ω/κ. In the weak drive limit $\Omega/\kappa \ll 1$, the threshold satisfies $2\sqrt{2}U_{\mathrm{th}}/\kappa = 1$. This is simply the condition for strong nonlinearity discussed in Chapter 3, the frequency shift $2\sqrt{2}U$ of the hybridized two-photon state needs to be larger than the resonator broadening. In this situation the single-photon and two-photon states are no longer separated in

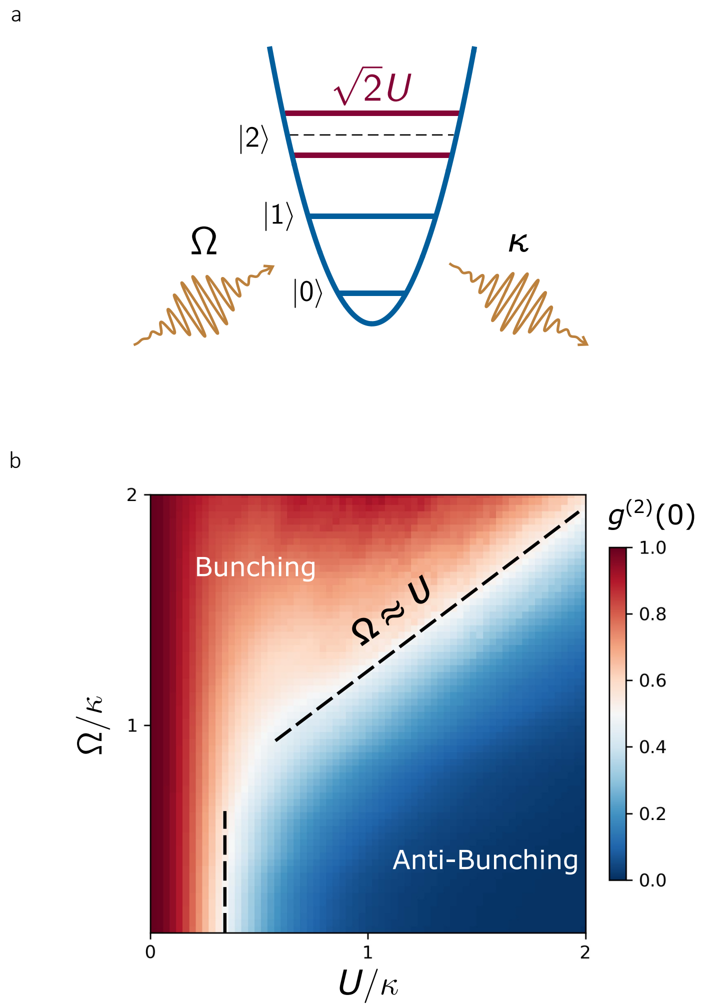

Figure 4.2: **Photon statistics in a single nonlinear resonator. a.** Schematic diagram for a single harmonic mode with a two-photon blockade nonlinearity. **b.** Second-order correlation function $g^{(2)}(0)$ as a function of drive amplitude Ω and interaction strength U, showing a sharp transition from Poissonian (red) to sub-Poissonian (blue) photon statistics.

energy by a single drive photon, and this energy penalty basically constrains photon occupation in the resonator beyond the Fock states $|0\rangle, |1\rangle$.

In the strong drive limit $\Omega/\kappa > 1$, we find the threshold to scale with the pump strength $U_{\text{th}} \approx \Omega$. This phenomena has been observed in the theoretical study in Ref. [38], for a driven cavity with on-site Kerr nonlinearity, and it ties to the picture of the cavity being dressed by the coherent drive. We can regard the classical driving field as an additional cavity linearly coupled to the nonlinear cavity, with the hopping rate J proportional to the drive strength Ω. As the driving strength and thus J is increased, the eigenstates of the coupled system are superpositions of the drive and nonlinear cavity, and these dressed states will have an energy separation proportional to their coupling J. In this non-perturbative regime for the coupling, the nonlinearity needs to be stronger than this frequency separation $U_{\mathrm{th}} > J$ in order to again decouple the single-photon and two-photon manifolds and observe antibunching. Another interpretation relies on the optical Bloch equations for a driven two level system, taken in this case to be single-photon manifold. Solving the Bloch equations in the steady state [134], the linewidth of the two-level resonance has a drive strength dependence $2\pi\delta\nu = \sqrt{\Gamma_2^2 + \Omega^2\Gamma_2/\Gamma_1}$, where $\Gamma_1,\ \Gamma_2$ are the intrinsic relaxation and decoherence rates. For strong drives $\Omega \gg \Gamma_2$ the linewidth increases linearly with Ω, and since we want the nonlinearity to be larger than the power broadening, this leads to the same condition for antibunching.

The results of this single cavity calculation indicate that this type of nonlinearity can lead to significant photon interactions. As is the case for the Kerr interactions, strong nonlinearity (larger than the dressed broadening) can lead to photon blockade giving rise to antibunching, a clear sign of interactions in correlated optical systems.

4.5 Fermionization in a nonlinear dimer

In the previous section it was established how the stimulated three-wave nonlinearity leads to photon interactions in a single cavity, giving rise to antibunching. In this section, we explore this interaction in a driven-dissipative system of two coupled cavities, as illustrated in Fig. 4.3a. The Hamiltonian for this nonlinear dimer corresponds to the simple case $N = 2$ in equation 4.8. The two modes have an on-site nonlinearity

U, are linearly coupled with a hopping rate t, and are both resonantly driven at a rate Ω to compensate for their photon loss rate κ.

Even such a small system can give rise to interesting physics [46, 123]. We explore the competition between coherent tunneling and interactions by tunning the on-site interaction strength U over four orders of magnitude with respect to the hopping rate kept at a fixed value $t = \kappa$. Since we are in the nonequilibrium regime, we also study the the competition between drive and dissipation by choosing these rates to be comparable $\Omega = 0.5\kappa$.

The steady state of this uniformly driven nonlinear two-mode system is characterized by probing the second order on-site $g^{(2)}_{aa,bb}$ and cross correlation $g^{(2)}_{ab}$ of the emitted field, at zero time delay, as a function of U/t (see Fig. 4.3b). As the magnitude of photon interactions is varied with respect to the tunneling rate, the correlations show a crossover from a localized to a delocalized regime. In the weak nonlinearity limit $U \ll t, \kappa$, the photons are completely delocalized as they tunnel between the two driven sites. The emitted field form each sites is coherent showing Poissonian statistics $g^{(2)}_{aa}(0) = g^{(2)}_{bb}(0) = 1$ and the cross correlator $g^{(2)}_{ab}(0) = 1$ indicates that the photon populations in each mode are independent of each other.

In the strongly interacting limit $U \gg t, \kappa$, the photons enter a localized regime as the on-site blockade prohibits introducing more than a single particle in every mode, thereby preventing tunneling between sites already populated with a photon. This is indicated by the on-site anibunching $g^{(2)}_{aa}(0) = g^{(2)}_{bb}(0) < 1$. Additionally, we observe strong bunching in the cross correlation $g^{(2)}_{ab}(0) > 1$ which indicates that the photon populations in these modes are strongly correlated. This bunching can occur if we are driving pairs of photons into the system. Since we are driving each mode at their uncoupled ($t = 1$) frequency, this coincides with resonantly driving the two-particle peak $|11\rangle$. For strong nonlinearities, the $|2^{\pm}0\rangle, |02^{\pm}\rangle$ states are energetically separated from the $|11\rangle$ peak. This explains how the continuous drives on both sites introduces

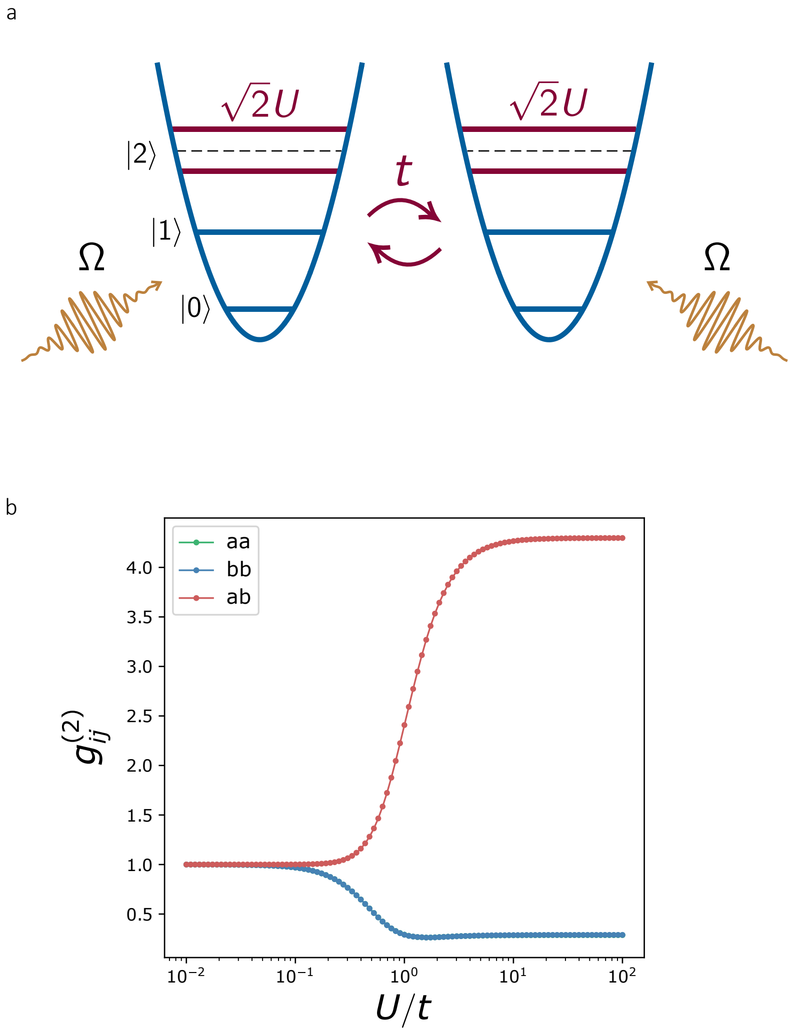

Figure 4.3: **Photon interactions in two coupled cavities. a.** Schematic energy diagram for two linearly coupled modes (dimer) with on-site two-photon blockade nonlinearity. **b.** On-site (cross) zero-time-delay correlation function $g^{(2)}_{aa}(0)$ ($g^{(2)}_{ab}(0)$) as a function of the on-site nonlinearity U normalized to the photon hopping term t.

pairs of excitations which are distributed to avoid double occupancy in the same mode, from the strong on-site interactions, resulting in substantial cross correlations.

Complimentary insight into these correlations can be gained from the first theoretical studies on a driven-dissipative Bose-Hubbard model in Ref.[39], investigating an array of optical cavities with on-site Kerr nonlinearity $U\boldsymbol{a}_j^\dagger\boldsymbol{a}_j^\dagger\boldsymbol{a}_j\boldsymbol{a}_j$. In the ultra-strong nonlinearity regime, or so called impenetrable boson limit $U/J \to \infty$, any bosonic wavefunction can be exactly mapped onto an equivalent fermionic wavefunction through a Jordan-Wigner transformation [135]. This argument holds for one-dimensional systems. The bosonic system has a one-to-one correspondence with a spinless noninteracting fermionic system where the eigenstates can be classified as occupation numbers of single particle orbitals [39]. In this interpretation, the fermionized form of the two-particle state leads to strong bunching while the on-site antibunching simply comes from fermionic statistics which forbids double occupancy.

This phenomena of photon fermionization in drive-dissipative resonator arrays has also been shown to hold for optical nonlinearities that arise from the Jaynes-Cummings interaction of each cavity to a two-level system [136]. While there are noticeable differences between the Bose-Hubbard and Jaynes-Cummings nonlinearities evident in the spectroscopy of the system, both models display the same steady state correlations in the strong photon blockade limit. It is encouraging to see from our numerical study that also the two-photon blockade nonlinearity displays similar signatures to the impenetrable boson regime.

4.6 Hardcore bosons in a nonlinear chain

Crystallization is another interesting phenomena of interacting photons in multi-mode systems, as was predicted in Ref [40] exploring a one-dimensional chain of resonators with Bose-Hubbard interactions from the on-site Kerr nonlinearity. This has also been predicted for the Jaynes-Cummings nonlinearity [136]. We perform a similar analysis on a one-dimensional chain of coupled eigenmodes in momentum space instead of couple real-space resonators, and the on-site nonlinearity is given by the three-wave interaction which hybridizes the two-excitation sector and induces photon blockade.

The nonlinear momentum chain is described by the Hamiltonian in equation 4.8 with nearest neighbor hopping. For the given computational resources at hand, we performed numerics on a chain of 9 eigenmodes (see Fig. 4.4), with a Hilbert space cutoff of three photons for each mode. We investigate the steady state behavior for a homogeneously driven system $\Omega_k = \Omega \ \forall k$, with the interaction strength kept fixed in the hard-core boson limit $U/\kappa = 10$. The only variable parameter is the nearest neighbor hopping rate t.

In order to probe the microscopic properties of this many-body system, we inspect the density correlations, at zero-time delay, between different modes defined as

$$g^{(2)}(j,k) = \frac{\langle \boldsymbol{a}_j^\dagger \boldsymbol{a}_k^\dagger \boldsymbol{a}_k \boldsymbol{a}_j \rangle}{\langle \boldsymbol{a}_j^\dagger \boldsymbol{a}_j \rangle \langle \boldsymbol{a}_k^\dagger \boldsymbol{a}_k \rangle}. \tag{4.13}$$

The correlations with respect to the middle site $g^{(2)}(5,k)$ are plotted in Fig. 4.4 as a function of hopping rate t/κ while the system is pumped in the weak-drive (quantum) limit $\Omega = 0.5\kappa$. There is pronounced anti-bunching from the auto-correlation $g^{(2)}(5,5) < 1$ and this is due to the large on-site photon blockade interaction which prevents double occupancy in the middle site. As a sanity check, when the eigenmodes are uncoupled $t/\kappa = 0$ the photon density in the middle site is totally uncorrelated with the other sites $g^{(2)}(5, k \neq 5) = 1$. This is expected, although all eigenmodes have pronounced nonlinearities, since they are uncoupled these modes can be treated independently and their photon emission statistics should also be independent.

The intriguing phenomena that occurs is when the hopping is increase to values comparable to the photon loss, as shown in Fig. 4.4. We observe that the photon density in the middle site becomes strongly correlated with the neighboring and next-nearest neighboring sites $g^{(2)}(5, |k-5| < 3) > 1$, and anti-correlated with the further separated sites $g^{(2)}(5, |k-5| > 2) > 1$. This behavior indicates that if there is a photon populating the middle site, the probability to find a second photon in sites $k \in \{3,4,6,7\}$ is larger than for independent particles, and the probability is lower for the other distant sites $k \in \{1,2,8,9\}$.

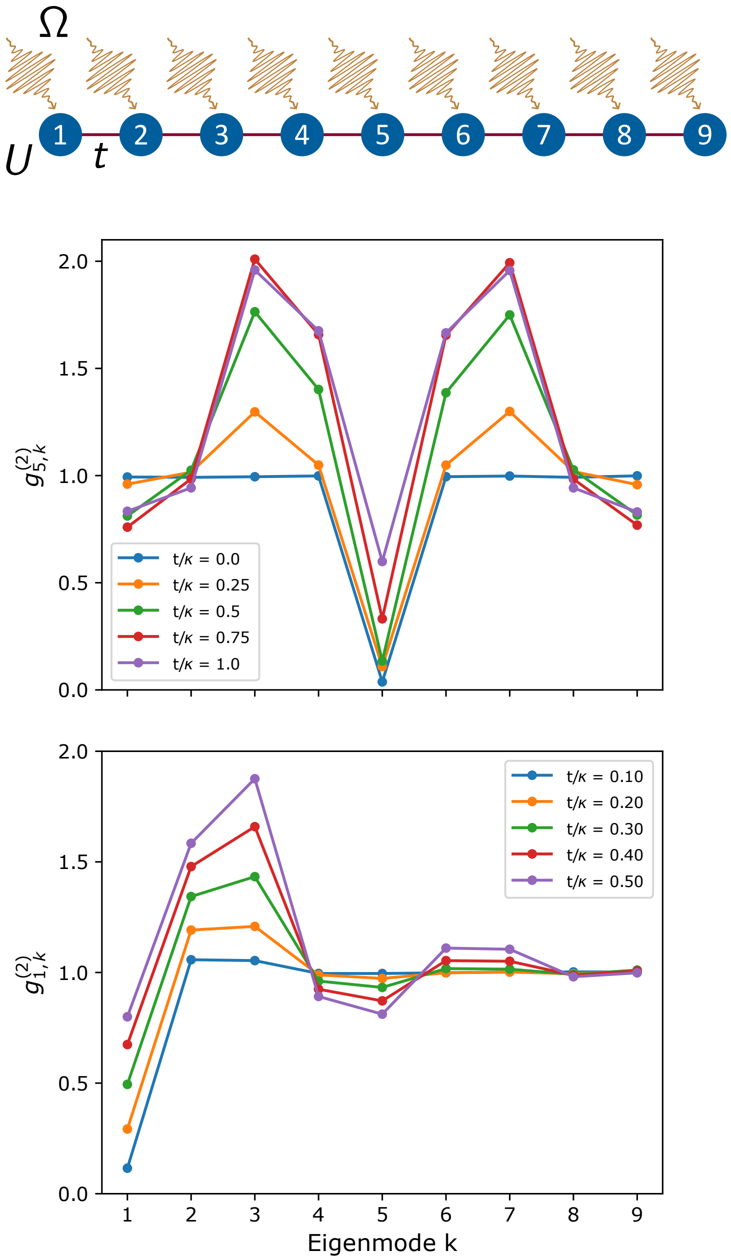

Figure 4.4: **Steady state density-density correlations in a nonlinear chain.** Homogeneously driven one-dimensional chain of nine coupled resonator modes in momentum space, with strong on-site interactions $U/\kappa = 10$. Density correlations are calculated with respect (**a**) to the middle $j = 5$ and (**b**) edge site $j = 1$ as a function of the nearest neighbor hopping t/κ.

In order to increase the resolution in the measured inter-site correlations, since we are computationally limited to nine sites, we calculate the same correlations with respect to the edge site $g^{(2)}(1,k)$. The mirror symmetry is avoided by choosing open boundary conditions for the chain $t(1,9) = 0$. As shown in Fig. 4.4, increasing the hopping rate we can clearly resolve oscillating correlations, where the first two neighboring sites are correlated with edge site, the next two sites are anti-correlated, the following sites are again correlated and so on. The amplitude of these oscillations are decaying from the edge, implying these correlations have a finite range, but nevertheless longer than the Bose-Hubbard and Jaynes-Cummings models [40, 136].

The take-home message from these oscillating correlations is that photons tend to be predominantly organized at specific ”distances” from each other in this momentum chain despite uniformly pumping photons into the system. This is a clear signature of photon crystallization as predicted in Refs [39, 40, 136], with the important distinction that photons are crystallized in a synthetic dimension instead of real space.

4.7 Summary and Outlook

As we reach the conclusion of this theoretical study, it is worth examining this proposed platform at a higher level, as shown in Fig. 4.5. We initially started with a discrete set of linear eigenmodes, provided by a resonator array, as a site basis for our synthetic lattice. We coupled a nonlinear Josephson circuit to the chain and with the right choice of parametric flux drives we allow microwave excitations to propagate between these momentum sites, where the lattice dimension and connectivity can be programmed arbitrarily.

In this chapter, we primarily focused on a one-dimensional chain, but one could equally engineer a two-dimensional square lattice in momentum space. Additionally, not only do we have control over the magnitude of photon hoping, but also on the relative phase. This idea of controlling the phase of the flux drive can be used to engineer synthetic magnetic fields for photons, as demonstrated in [48].

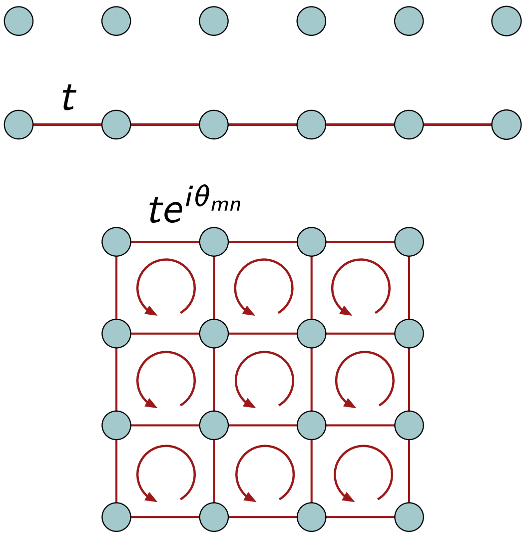

Figure 4.5: **Lattice configurations in momentum space.** Bosonic sites (blue circles) in a synthetic dimension defined by the momentum states in a cavity array. The sites can be coupled in a 1D chain or in a 2D square lattice, where photons can tunnel from one site to its neighbor at a rate t. Additionally, the tunneling rate can be complex, with a Peierls phase $\theta_{m,n}$, to simulate photons propagating in an artificial magnetic field $\pi\Phi/\Phi_0 = \sum \theta_{m,n}$ applied in each plaquette.

This idea of engineering lattices in synthetic dimensions has been experimentally demonstrated in various physical platforms. The focus has been on minimizing the overhead in developing large-scale lattice experiments, with the addition of artificial gauge fields for studying unique topological properties. Experiments have been performed with ultracold atoms [137, 138, 139, 140, 141, 142], optical waveguide arrays [143, 144], fiber optical systems [145, 146], and recently also with superconducting circuits [125, 93].

The figure of merit in this proposed quantum simulator is the ability to introduce and control interactions in these synthetic lattices to go beyond the single particle picture, which has been lacking in these previous experiments. This numerical study indeed shows that this proposed synthetic nonlinear lattice is an attractive platform for studying strongly correlated states of photons where we have full control over the lattice dimensions and connectivity as well as the magnitude of photon interactions.

Chapter 5

Multi-mode ultrastrong coupling in a photonic crystal waveguide

5.1 Introduction

As part of the growing research area of many-body quantum optics, the work presented in chapters 3 and 4 follows the path of building large scale systems composed of many coupled nonlinear cavities. In this chapter we present an alternative path which relies on coupling a single nonlinear element, an artificial Josephson atom, to the many linear degrees of freedom in a harmonic environment. This architecture is more forgiving in terms of the complexity for controlling the microscopic parameters, since we only have to tune one nonlinear element and the harmonic environment can be built from arrays of linear cavities with negligible disorder. In this platform we can study complex multimode dynamics, as the qubit exchanges a photon with multiple modes of its environment. To go beyond the single particle picture and enter the many-body regime, the coupling between the qubit and the environment needs to reach the ultrastrong coupling regime [69], where the total number of excitations is no longer conserved. Pushing the light-matter interaction in this regime,

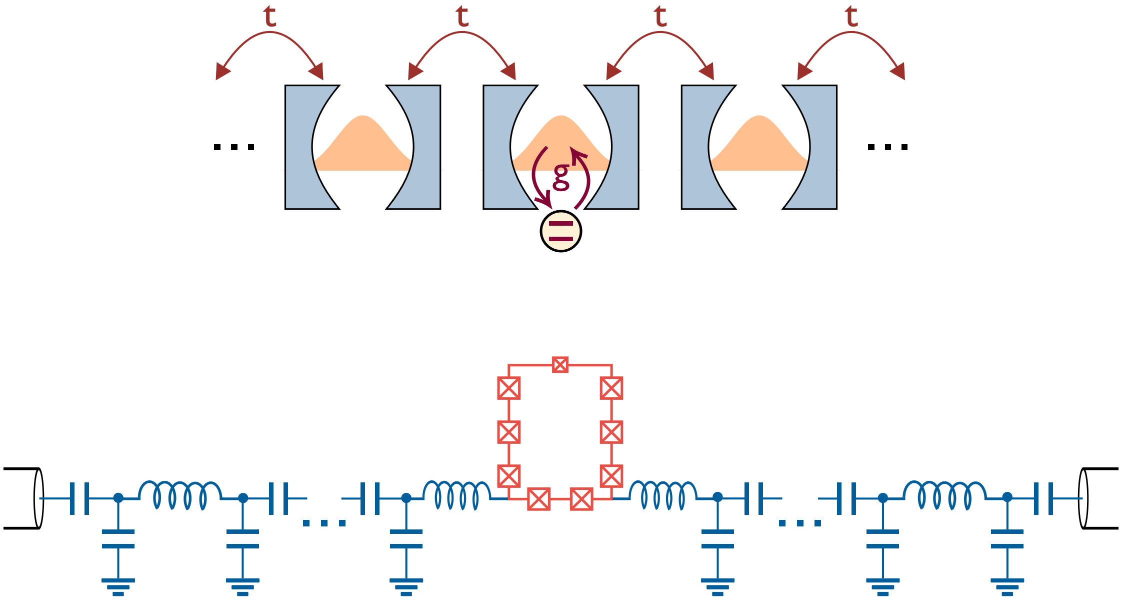

Figure 5.1: **Quantum impurity model with superconducting circuits.** Qubit dipole coupled to a photonic crystal waveguide, designed as a chain of coupled cavities. Bottom diagram depicts an implementation with superconducting circuits.

multimode entangled states are expected to emerge [147], and this system becomes a promising platform for studying quantum impurity models of condensed matter physics [148, 149, 150, 151].

There have been a number of experimental efforts realizing spin-boson models with superconducting circuits, coupling qubits to linear waveguides with both discrete [152, 153] and continuous mode spectra [78]. The work presented in this chapter focuses on implementing the bosonic environment as a photonic crystal waveguide (Fig. 5.1) with a nonlinear dispersion. Strong light-matter coupling in a waveguide with band edges gives rise to photonic bound states exponentially localized around the qubit position [154], as these qubit-photon dressed states lie inside the band gap. Single excitation qubit-photon bound states have been experimentally observed in the strong coupling regime [155, 156]. In the ultrastrong coupling regime it is predicted that multi-photon bound states modify the scattering dynamics of a single propagating photon due to the energy nonconserving terms [157]. The experimental platform presented in this chapter will explore this regime by investigating the single-photon transport through the waveguide as a many-body problem. Furthermore, given the discrete spectrum of the waveguide, we characterize multi-mode entanglement, induced by the qubit nonlinearity, by probing field correlations between different modes.

5.2 Photonic crystal implementation

Let us first start with the harmonic environment. The aim of this section is to cover all complementary methods of describing the lumped element model for the photonic crystal. This will be useful for experimentally implementing the resonator chain.

5.2.1 Circuit model of a coupled cavity array

In this section we describe the formalism for characterizing the eigenmodes of the cavity array in terms of its Lagrangian. The circuit diagram of the bare (qubit-less) resonator chain is shown in Fig. 5.2. The chain consists of N lumped-element resonators, composed of inductors of inductance L and capacitors of capacitance C_g, and their voltages are coupled through a series capacitor of capacitance C_c. This circuit has $2N$ degrees of freedom, equal to the number of nodes, and as it will be made clear later in this section, half of these degrees of freedom are relevant for this experimental study. In the realistic experimental scenario, the resonator array is capacitively coupled to waveguides at the input and output ports, which we model as impedance terminations Z_{in} and Z_{out}, respectfully.

The useful variables to describe the Lagrangian of this circuit are the flux Φ_n and electric voltages $\dot{\Phi}_n$ at each node $n \in [1, 2N]$. The drawback of this Lagrangian formalism is not being able to take into account the impedances at the input and output ports, except for the limits when they tend to zero or infinity. The Lagrangian of the cavity chain for the boundary conditions Z_{in}, $Z_{\text{out}} \to 0$ is given by

$$\mathcal{L}_{\text{cca}} = \sum_{n=1}^{N} \left[\frac{C_\Sigma}{2} \left(\dot{\Phi}_{2n-1}^2 + \dot{\Phi}_{2n}^2 \right) - C_c \dot{\Phi}_{2n} \dot{\Phi}_{2n+1} - \frac{1}{2L} \left(\Phi_{2n} - \Phi_{2n-1} \right)^2 \right], \tag{5.1}$$

where the summation is performed over every resonator unit cell, and we define $C_\Sigma \triangleq C_g + C_c$. Given that the chain contains only linear elements, it should not be surprising that the Lagrangian is quadratic in the coordinate variables. This allows the Lagrangian to be written in a compact matrix form

$$\mathcal{L}_{\text{cca}} = \frac{1}{2} \dot{\vec{\boldsymbol{\Phi}}}^{\text{t}} \hat{\boldsymbol{C}} \dot{\vec{\boldsymbol{\Phi}}} - \frac{1}{2} \vec{\boldsymbol{\Phi}}^{\text{t}} \hat{\boldsymbol{L}}^{-1} \vec{\boldsymbol{\Phi}} \tag{5.2}$$

where we define the flux and voltage coordinate vectors as

$$\vec{\boldsymbol{\Phi}} = \begin{pmatrix} \Phi_1 \\ \Phi_2 \\ \vdots \\ \Phi_{2N} \end{pmatrix} \quad , \quad \dot{\vec{\boldsymbol{\Phi}}} = \begin{pmatrix} \dot{\Phi}_1 \\ \dot{\Phi}_2 \\ \vdots \\ \dot{\Phi}_{2N} \end{pmatrix} \tag{5.3}$$

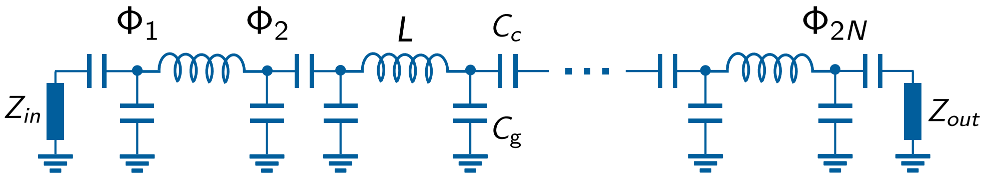

Figure 5.2: **Circuit diagram for a discretized photonic crystal.** Schematic diagram of a one-dimensional chain of capacitively coupled microwave resonators. The boundary conditions are set by the impedance terminations of the input and output waveguide ports.

and we used the following capacitance $\hat{\boldsymbol{C}}$ and inductance $\hat{\boldsymbol{L}}$ matrices

$$\hat{\boldsymbol{C}} = \begin{pmatrix} C_\Sigma & & & & & & \\ & C_\Sigma & -C_c & & & & \\ & -C_c & C_\Sigma & & & & \\ & & \ddots & \ddots & \ddots & & \\ & & & & C_\Sigma & -C_c & \\ & & & & -C_c & C_\Sigma & \\ & & & & & & C_\Sigma \end{pmatrix}, \hat{\boldsymbol{L}}^{-1} = \frac{1}{L} \begin{pmatrix} 1 & -1 & & & & & \\ -1 & 1 & & & & & \\ & & 1 & -1 & & & \\ & & -1 & 1 & & & \\ & & & \ddots & \ddots & \ddots & \\ & & & & & 1 & -1 \\ & & & & & -1 & 1 \end{pmatrix}. \tag{5.4}$$

If we focus on a single unit cell, we can characterize the resonator in terms of the voltage $\dot{\Phi}_{2n} - \dot{\Phi}_{2n-1}$ across the series ground capacitor and current $\Phi_{2n} - \Phi_{2n-1}$ flowing through the inductor. This argument will also become clear when visiting the formalism for galvanically coupling the artificial atom to a unit cell, as treated in the next section. With that in mind, it becomes more intuitive to describe the resonator chain in a different coordinate basis $\Phi_n^\pm \triangleq \Phi_{2n} \pm \Phi_{2n-1}$, in terms of *differential* Φ_n^- and *center of mass* (COM) Φ_n^+ degrees of freedom for $n \in [0, N]$. The corresponding Lagrangian in this differential/COM basis reads as

$$\mathcal{L}_{\text{cca}}^\pm = \sum_{n=1}^{N} \left[\frac{C_\Sigma}{4} \left(\dot{\Phi}_n^{-2} + \dot{\Phi}_n^{+2} \right) - \frac{C_c}{4} \left(\dot{\Phi}_n^+ + \dot{\Phi}_n^- \right) \left(\dot{\Phi}_{n+1}^+ + \dot{\Phi}_{n+1}^- \right) - \frac{1}{2L} \Phi_n^{-2} \right]. \tag{5.5}$$

We can also write it in a similar compact matrix form

$$\mathcal{L}_{\text{cca}}^\pm = \frac{1}{2} \dot{\vec{\boldsymbol{\Phi}}}_\pm^{\mathrm{t}} \hat{\boldsymbol{C}}_\pm \dot{\vec{\boldsymbol{\Phi}}}_\pm - \frac{1}{2} \vec{\boldsymbol{\Phi}}_\pm^{\mathrm{t}} \hat{\boldsymbol{L}}_\pm^{-1} \vec{\boldsymbol{\Phi}}_\pm \tag{5.6}$$

with basis vectors in the differential/COM coordinates

$$\vec{\boldsymbol{\Phi}}_\pm = \begin{pmatrix} \Phi_1^\pm \\ \Phi_2^\pm \\ \vdots \\ \Phi_{2N}^\pm \end{pmatrix} \quad , \quad \dot{\vec{\boldsymbol{\Phi}}}_\pm = \begin{pmatrix} \dot{\Phi}_1^\pm \\ \dot{\Phi}_2^\pm \\ \vdots \\ \dot{\Phi}_N^\pm \end{pmatrix}. \tag{5.7}$$

and with different capacitance and inductance matrices

$$\hat{\boldsymbol{C}}_\pm = \begin{pmatrix} C_\alpha & & C_\beta & -C_\beta & & & & & & \\ & C_\alpha & C_\beta & -C_\beta & & & & & & \\ C_\beta & C_\beta & C_\alpha & & C_\beta & C_\beta & & & & \\ -C_\beta & -C_\beta & & C_\alpha & -C_\beta & -C_\beta & & & & \\ & & C_\beta & -C_\beta & C_\alpha & & & & & \\ & & C_\beta & -C_\beta & & C_\alpha & & & & \\ & & & & & & \ddots & & C_\beta & -C_\beta \\ & & & & & & & & C_\beta & -C_\beta \\ & & & & & & C_\beta & C_\beta & C_\alpha & \\ & & & & & & -C_\beta & -C_\beta & & C_\alpha \end{pmatrix}, \; \hat{\boldsymbol{L}}_\pm^{-1} = \frac{1}{L} \begin{pmatrix} 1 & & & & & & \\ & 0 & & & & & \\ & & 1 & & & & \\ & & & 0 & & & \\ & & & & \ddots & & \\ & & & & & 1 & \\ & & & & & & 0 \end{pmatrix}, \tag{5.8}$$

where for abbreviation purposes we defined $C_\alpha = C_\Sigma/2$ and $C_\beta = C_c/4$.

The Euler-Lagrange equation of motion takes the form of a wave equation

$$\ddot{\vec{\boldsymbol{\Phi}}}_\pm + \hat{\boldsymbol{C}}_\pm^{-1} \hat{\boldsymbol{L}}_\pm^{-1} \dot{\vec{\boldsymbol{\Phi}}}_\pm = 0, \tag{5.9}$$

where the normal mode resonance frequencies of the chain ω_k are the positive square roots of the eigenvalues of the $2N \times 2N$ matrix $\hat{\boldsymbol{C}}_\pm^{-1} \hat{\boldsymbol{L}}_\pm^{-1}$. The matrices $\hat{\boldsymbol{C}}^{-1} \hat{\boldsymbol{L}}^{-1}$ and $\hat{\boldsymbol{C}}_\pm^{-1} \hat{\boldsymbol{L}}_\pm^{-1}$ are connected thought a basis transformation $\vec{\boldsymbol{\Phi}}_\pm = \mathbf{U}_\pm \vec{\boldsymbol{\Phi}}$ and therefore have the same eigenfrequencies. The total number of eigenvalues is given of course by size of these matrices, equal to the number of circuit nodes $2N$. Inspecting the eigenvalue spectrum we realize that N of these modes have zero-frequency while the other N modes have the desired cosine dispersion one would expect for a tight-binding chain of coupled cavities. These zero-frequency eigenvalues correspond to the static COM variables Φ_n^+, while the dispersive band centered around the bare resonator frequency corresponds to the dynamics of the coupled differential variables Φ_n^-. So, in fact, this transformation $\mathbf{U}_\pm$ becomes useful for rewriting the eigenvectors in a different basis that allows us to differentiate static degrees of freedom from the oscillator degrees of freedom. In the end the bath is composed of N resonators, so we would expect only N harmonic modes. Although, from Eq. 5.6, the differential and COM variables are coupled to each other through their voltages, the effect on the tight-binding model for the differential degrees of freedom is a minimal, small renormalization of the hopping parameters. For the remainder of this chapter, we will not consider these zero frequency modes and focus only on half of the eigenmode spectrum: the differential normal modes of the chain.

5.2.2 ABCD matrix simulation

Here we present a numerical technique for calculating the scattering parameters of a circuit with arbitrary topology, probed at any given frequency. Scattering parameters are used for characterizing microwave circuits with multiple ports, however, in practice such circuits are composed of several two-port circuits connected in series. It therefore becomes convenient to describe such networks in terms of 2×2 matrices, called ABCD matrices, which relate the voltage V_{j} and current I_{j} at one port to the second port as

$$\begin{pmatrix} V_1 \\ I_1 \end{pmatrix} = \begin{pmatrix} A & B \\ C & D \end{pmatrix} \begin{pmatrix} V_2 \\ I_2 \end{pmatrix}. \tag{5.10}$$

The convenience lies in the fact that the ABCD matrix of several two-port networks connected in series is given by the product of the ABCD matrices of each network.

For the case of our photonic crystal circuit, the ABCD matrix of a single lumped-element resonator can be extracted from the individual matrices for the series inductor and parallel capacitor to ground

$$\begin{aligned}\mathbf{M}_{\mathrm{uc}}(\omega) &= \mathbf{M}_{\mathrm{C_g}}\mathbf{M}_{\mathrm{L}}\mathbf{M}_{\mathrm{C_g}} \\ &= \begin{pmatrix} 1 & 0 \\ \mathrm{j}\omega C_g & 1 \end{pmatrix} \cdot \begin{pmatrix} 1 & \mathrm{j}\omega L \\ 0 & 1 \end{pmatrix} \cdot \begin{pmatrix} 1 & 0 \\ \mathrm{j}\omega C_g & 1 \end{pmatrix}.\end{aligned} \tag{5.11}$$

The unit cells are connected in series through a coupling capacitor, and the edge unit cells are capacitvely coupled to a section L of a coplanar waveguide with a characteristic impedance $Z_0 = 50\,\Omega$ and phase velocity υ_p. The matrix terms for these additional components are given by

$$\mathbf{M}_{\mathrm{C_c}} = \begin{pmatrix} 1 & \mathrm{j}/\omega C_c \\ 0 & 1 \end{pmatrix} \;,\; \mathbf{M}_{\mathrm{cpw}} = \begin{pmatrix} \cos\left(\omega L/\upsilon_p\right) & \mathrm{j}Z_0 \sin\left(\omega L/\upsilon_p\right) \\ \mathrm{j}\sin\left(\omega L/\upsilon_p\right)/Z_0 & \cos\left(\omega L/\upsilon_p\right) \end{pmatrix}. \tag{5.12}$$

From the periodicity of the circuit, we can arrive at the ABCD matrix of the entire resonator chain by multiplying the matrix for the unit cell and coupling capacitance N times and concatenating the waveguide input and output ports as follows

$$\mathbf{M}_{\mathrm{cca}}(\omega) = \mathbf{M}_{\mathrm{cpw}}\,\mathbf{M}_{\mathrm{C_c}}\,\left[\mathbf{M}_{\mathrm{uc}}\mathbf{M}_{\mathrm{C_c}}\right]^N\,\mathbf{M}_{\mathrm{cpw}}. \tag{5.13}$$

Since we are interested in the transmission coefficient through the device, we can easily calculate the scattering parameter S_{21} using the ABCD matrix of the chain

$$S_{21}(\omega) = \frac{2}{A + B/Z_0 + CZ_0 + D}. \tag{5.14}$$

where A, B, C, and D are functions of ω.

The advantage of this method over the Lagrangian approach is the capability of finding the eigenmodes of the circuit for arbitrary boundary conditions set by input

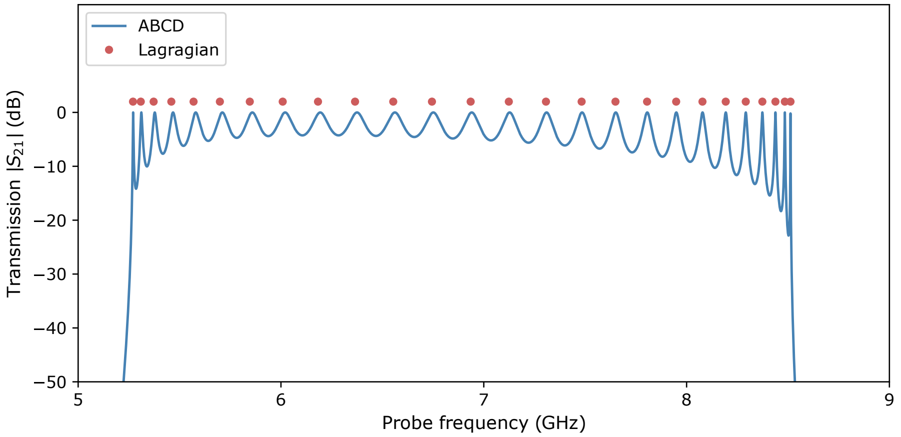

Figure 5.3: **Calculated transmission in a cavity chain using ABCD matrices.** Solid line (blue) corresponds to the magnitude of the transmission coefficient determined using the ABCD matrix approach. Data points (red) correspond to the eigenfrequencies of the circuit Lagrangian inferred from the same circuit parameters.

and output port impedances Z_{in} and Z_{out}, which are set to $50\,\Omega$ for this experiment. The eigenmode frequencies are the resonance frequencies observed in transmission. In the Lagrangian case, as mentioned in the previous section, these impedances can only be set to zero or infinity. The small disadvantage of this method is that the precision of eigenmode values is set by the resolution of frequency grid in which you are evaluating the ABCD matrices, whereas diagonalizing a $2N \times 2N$ matrix can be more efficient. In the end we use combine methods for determining the circuit parameters of the device.

For completeness, we compare these two methods as shown in Fig. 5.3. The eigenfrequencies of the differential modes, inferred from the positive square root of the $\hat{\boldsymbol{C}}_{\pm}^{-1}\hat{\boldsymbol{L}}_{\pm}^{-1}$ matrix, are overlayed on top of the magnitude of the transmission coefficient $|S_{21}|$ evaluated over a frequency range that captures the eigenmode band. The eigenfrequencies align with the resonance frequencies found as Lorentzian peaks in transmission, with small discrepancies ranging between $1-10\,\mathrm{MHz}$. Both calculations are performed using the same circuit parameters used in the experiment, these parameters are displayed in Table 5.1. It seems that for the choice of circuit parameters and boundary conditions, both approaches yield similar eigenmode frequencies.

5.2.3 Tight-binding model

The aim of this section is to translate the circuit Lagrangian into a tight-binding model, which is a more familiar formalism for describing lattices in condensed matter. The first step is to move to the Hamiltonian picture, described using the flux Φ_n and charge Q_n at each node. The charge variables are conjugate momenta of the node fluxes, and are found from $\vec{\boldsymbol{Q}} = \partial\mathcal{L}_{\text{cca}}/\partial\dot{\vec{\boldsymbol{\Phi}}} = \hat{\mathbf{C}}\dot{\vec{\boldsymbol{\Phi}}}$, where $\vec{\boldsymbol{Q}}$ represents the basis vector for all the node charges $(Q_1, Q_2, \dots Q_{2N})^{\text{t}}$. A similar relationship holds in the differential/COM basis $\vec{\boldsymbol{Q}}_\pm = \hat{\mathbf{C}}_\pm\dot{\vec{\boldsymbol{\Phi}}}_\pm$. Using the Lagrangian in Eq. 5.6, we can obtain the Hamiltonian for the resonator chain from a Legendre transformation

$$\mathbf{H}^{\pm}_{\text{cca}} = \frac{1}{2}\vec{\boldsymbol{Q}}^{\text{t}}_{\pm}\hat{\boldsymbol{C}}^{-1}_{\pm}\vec{\boldsymbol{Q}}_{\pm} + \frac{1}{2}\vec{\boldsymbol{\Phi}}^{\text{t}}_{\pm}\hat{\boldsymbol{L}}^{-1}_{\pm}\vec{\boldsymbol{\Phi}}_{\pm} \tag{5.15}$$

Following the discussion from section 5.2.1, we can expand the Hamiltonian in terms of differential variables, and purposefully write it in this form

$$\mathbf{H}^{\pm}_{\text{cca}} = \sum_{j}\left(\frac{1}{2}\left[\hat{\boldsymbol{C}}^{-1}_{\pm}\right]_{j,j} {Q^{-}_{j}}^{2} + \frac{1}{2}\left[\hat{\boldsymbol{L}}^{-1}_{\pm}\right]_{j,j} {\Phi^{-}_{j}}^{2}\right) + \sum_{\langle i,j\rangle}\left[\hat{\boldsymbol{C}}^{-1}_{\pm}\right]_{i,j} Q^{-}_{i} Q^{-}_{j}, \tag{5.16}$$

where we decouple harmonic oscillator terms containing quadratic charge and flux variables with the same resonator coordinate, from terms which couple the charge degrees of freedom of different resonators.

Moving to the quantum picture, the flux Φ and charge Q variables are promoted to quantum variables, $\boldsymbol{\Phi}$ and $\mathbf{Q}$, which obey the canonical commutation relation for bosonic operators $[\boldsymbol{\Phi}_n, \mathbf{Q}_m] = \mathrm{i}\hbar\delta_{n,m}$. As we do for the case of a single harmonic oscillator, we can express the charge and flux operators in terms of ladder operators

$$\begin{aligned}\mathbf{Q}_j^- &= \mathrm{i}\sqrt{\frac{\hbar}{2}}\, Z_j^{-\frac{1}{2}} \left(\boldsymbol{a}_j^\dagger - \boldsymbol{a}_j\right) \\ \boldsymbol{\Phi}_j^- &= \sqrt{\frac{\hbar}{2}}\, Z_j^{\frac{1}{2}} \left(\boldsymbol{a}_j^\dagger + \boldsymbol{a}_j\right),\end{aligned} \tag{5.17}$$

where $\boldsymbol{a}_j^\dagger$ ($\boldsymbol{a}_j$) create (annihilate) photons in the j^{th} resonator, and the resonator's characteristic impedance which enters in the zero point fluctuation amplitudes is given by $Z_j \triangleq \left[\hat{\boldsymbol{C}}_\pm^{-1}\right]_{j,j}^{\frac{1}{2}} / \left[\hat{\boldsymbol{L}}_\pm^{-1}\right]_{j,j}^{\frac{1}{2}}$. Inserting the quantum operators into the Hamiltonian in Eq. 5.15 gives the following tight-binding model for describing the photonic lattice

$$\mathbf{H}_{\mathrm{tb}}/\hbar = \sum_j \omega_j \left(\boldsymbol{a}_j^\dagger \boldsymbol{a}_j + \frac{1}{2}\right) + \sum_{\langle i,j\rangle} t_{i,j} \left(\boldsymbol{a}_i^\dagger - \boldsymbol{a}_i\right)\left(\boldsymbol{a}_j^\dagger - \boldsymbol{a}_j\right), \tag{5.18}$$

where the first summation takes into account the on-site energy at every oscillator given by their resonant frequency ω_j, and the second summation accounts for the tunneling of microwave excitations between nearest neighbor oscillators with a tunneling rate $t_{i,j}$. These terms can be easily extracted from the capacitance and inductance matrices in the circuit model

$$\begin{aligned}\omega_j &\triangleq \left[\hat{\boldsymbol{L}}_\pm^{-1}\right]_{j,j}^{\frac{1}{2}} \left[\hat{\boldsymbol{C}}_\pm^{-1}\right]_{j,j}^{\frac{1}{2}} \\ t_{i,j} &\triangleq -\frac{1}{2}\left(Z_i Z_j\right)^{-\frac{1}{2}} \left[\hat{\boldsymbol{C}}_\pm^{-1}\right]_{i,j}.\end{aligned} \tag{5.19}$$

Characterizing the photonic crystal in this tight-binding model is a more intuitive condensed matter tool for describing the band structure and it will prove useful later for modeling transport through the cavity lattice doped with an impurity.

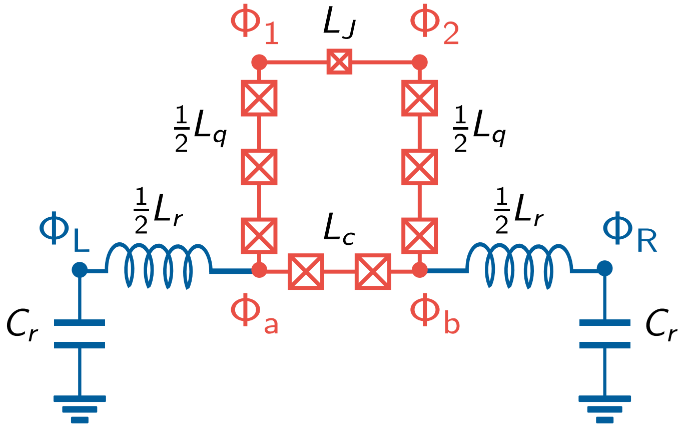

Figure 5.4: **Circuit diagram for a galvanically coupled fluxonium.** Schematic diagram for a fluxonium artificial atom current-coupled to a single microwave resonator, through a mutually shared inductor L_c.

5.3 Galvanically coupled impurity

In this section we analyze and derive the microscopic model for a fluxonium circuit, which acts as our highly nonlinear impurity, embedded in the photonic crystal. At first we will consider the case of coupling to a single unit cell, a resonator, and extend that to the full oscillator chain.

5.3.1 Coupling to a single unit cell

The circuit diagram for a fluxonium qubit galvanically coupled to a single lumped-element resonator is shown in Fig. 5.4. The independent resonator circuit has a total inductance of L_r and a capacitance to ground C_r at both resonator nodes. The fluxonium circuit consists of a Josephson junction, with a characteristic critical current I_c and energy E_J, shunted by its self-capacitance C_q and by an inductance implemented using a linear array of larger Josephson junctions. The total inductance consists of two sections: one section of total inductance L_q independent from the resonator circuit, and a smaller section of inductance L_c shared between the resonator and fluxonium which leads to their currents being coupled. This mutual inductive coupling will lead to a magnetic dipole interaction between the resonator field and the qubit phase difference across the Josephson junction. A static magnetic flux Φ_{ext} is externally applied to the fluxonium loop.

The first step is to write down the equations of motion by applying Kirchoff's law of current conservation at each node of the circuit

$$\begin{aligned}
\frac{2}{L_r}\left(\Phi_R - \Phi_b\right) + C_r \ddot{\Phi}_R &= 0 \quad \text{(node R)} \\
\frac{2}{L_r}\left(\Phi_L - \Phi_a\right) + C_r \ddot{\Phi}_L &= 0 \quad \text{(node L)} \\
\frac{2}{L_q}\left(\Phi_2 - \Phi_b\right) + I_c \sin\frac{2\pi}{\Phi_0}\left(\Phi_2 - \Phi_1 - \Phi_{\text{ext}}\right) + C_q\left(\ddot{\Phi}_2 - \ddot{\Phi}_1\right) &= 0 \quad \text{(node 1)} \\
\frac{2}{L_q}\left(\Phi_1 - \Phi_a\right) - I_c \sin\frac{2\pi}{\Phi_0}\left(\Phi_2 - \Phi_1 - \Phi_{\text{ext}}\right) - C_q\left(\ddot{\Phi}_2 - \ddot{\Phi}_1\right) &= 0 \quad \text{(node 2)} \\
\frac{2}{L_r}\left(\Phi_R - \Phi_b\right) - \frac{1}{L_c}\left(\Phi_b - \Phi_a\right) - \frac{2}{L_q}\left(\Phi_b - \Phi_2\right) &= 0 \quad \text{(node a)} \\
\frac{2}{L_r}\left(\Phi_L - \Phi_a\right) + \frac{1}{L_c}\left(\Phi_b - \Phi_a\right) - \frac{2}{L_q}\left(\Phi_a - \Phi_1\right) &= 0 \quad \text{(node b).}
\end{aligned} \tag{5.20}$$

Similar to the analysis for the resonator chain, we define the new variables $\Phi_r^{\pm} \triangleq \Phi_R \pm \Phi_L$, $\Phi_q^{\pm} \triangleq \Phi_2 \pm \Phi_1$, $\Phi_s^{\pm} \triangleq \Phi_b \pm \Phi_a$. Combining the above equations, we arrive at the following equations of motion for the differential variables

$$\begin{aligned}
\frac{2}{L_r}\left(\Phi_r^- - \Phi_s^-\right) + C_r \ddot{\Phi}_r^- &= 0 \\
\frac{2}{L_q}\left(\Phi_q^- - \Phi_s^-\right) + 2I_c \sin\frac{2\pi}{\Phi_0}\left(\Phi_q^- - \Phi_{\text{ext}}\right) + 2C_q \ddot{\Phi}_q^- &= 0 \\
\frac{2}{L_r}\left(\Phi_r^- - \Phi_s^-\right) - \frac{2}{L_c}\Phi_s^- - \frac{2}{L_q}\left(\Phi_s^- - \Phi_q^-\right) &= 0.
\end{aligned} \tag{5.21}$$

where from the last relation we can express the shunt differential variable Φ_s^- in terms of the resonator Φ_r^- and fluxonium Φ_q^- differential variables

$$\Phi_s^- = \frac{L_q L_c}{L_\Sigma^2}\Phi_r^- + \frac{L_r L_c}{L_\Sigma^2}\Phi_q^-. \tag{5.22}$$

where for brevity we define $L_\Sigma^2 \triangleq L_r L_q + L_q L_c + L_c L_r$.

In combining Eqs. 5.20 we find that the fluxonium and resonator have the same center of mass $\Phi_q^+ = \Phi_r^+ = \Phi_s^+$, which is not surprising given the C_2 symmetry of the circuit. Additionally, the COM variables are not coupled to the differential ones, in particular the phase difference across the qubit junction Φ_q^- which dictates the internal fluxonium states. For the remainder of the analysis we consider the differential variables. Replacing the shunt variable (Eq. 5.22) in Eq. 5.21 gives a set of equations just for the resonator and fluxonium

$$\begin{aligned} \frac{L_q + L_c}{L_\Sigma^2}\Phi_r^- + \frac{C_r}{2}\ddot{\Phi}_r^- - \frac{L_c}{L_\Sigma^2}\Phi_q^- &= 0 \\ \frac{L_r + L_c}{L_\Sigma^2}\Phi_q^- + I_c \sin\frac{2\pi}{\Phi_0}\left(\Phi_q^- - \Phi_{\text{ext}}\right) + C_q\ddot{\Phi}_q^- - \frac{L_c}{L_\Sigma^2}\Phi_r^- &= 0. \end{aligned} \tag{5.23}$$

Following the usual Euler-Lagrange equations, these equations of motion can be directly linked to the following Lagrangian

$$\begin{aligned} \mathcal{L} = {} & \frac{1}{2}\left(\frac{C_r}{2}\right)^2 \dot{\Phi}_r^{-2} - \frac{1}{2}\frac{L_q + L_c}{L_\Sigma^2}\Phi_r^{-2} + \frac{L_c}{L_\Sigma^2}\Phi_r^-\Phi_q^- \\ & + \frac{1}{2}C_q\dot{\Phi}_q^{-2} - \frac{1}{2}\frac{L_r + L_c}{L_\Sigma^2}\Phi_q^{-2} + E_J\cos\frac{2\pi}{\Phi_0}\left(\Phi_q^- - \Phi_{\text{ext}}\right). \end{aligned} \tag{5.24}$$

We find the canonical conjugate momenta, corresponding to the charge variable, to be $Q_r^- = \partial\mathcal{L}/\partial\dot{\Phi}_r^- = (C_r/2)\dot{\Phi}_r^-$ for the resonator and $Q_q^- = \partial\mathcal{L}/\partial\dot{\Phi}_q^- = C_q\dot{\Phi}_q^-$ for the fluxonium. Following the Legendre transformation we obtain the circuit Hamiltonian

$$\begin{aligned}
\mathrm{H} &= Q_r^- \dot{\Phi}_r^- + Q_q^- \dot{\Phi}_q^- - \mathcal{L} \\
&= \frac{1}{C_r} Q_r^{-2} + \frac{1}{2L'_r} \Phi_r^{-2} + \frac{L_c}{L_\Sigma^2} \Phi_r^- \Phi_q^- \\
&+ \frac{1}{2C_q} Q_q^{-2} + \frac{1}{2L'_r} \Phi_q^{-2} - E_J \cos \frac{2\pi}{\Phi_0} \left(\Phi_q^- - \Phi_{\text{ext}} \right)
\end{aligned} \tag{5.25}$$

Moving to the quantum picture, the flux and charge variables are promoted to quantum variables, $\boldsymbol{\Phi}_n$ and $\boldsymbol{Q}_n$, which again obey the canonical commutation relation for bosonic operators $[\boldsymbol{\Phi}_n, \boldsymbol{Q}_m] = \mathrm{i}\hbar\delta_{n,m}$. For brevity, the minus superscript is removed since all variables are differential. The total Hamiltonian can be decomposed as $\mathbf{H} = \mathbf{H}_{\text{r}} + \mathbf{H}_{\text{q}} + \mathbf{H}_{\text{int}}$ with separate terms corresponding to the resonator, fluxonium and fluxonium-resonator dipole interaction, respectively.

The resonator Hamiltonian can be written in a second quantized form as

$$\mathbf{H}_{\text{r}} = \frac{1}{C_r} \boldsymbol{Q}_r{}^2 + \frac{1}{2L'_r} \boldsymbol{\Phi}_r^2 = \hbar\omega_r \left(\boldsymbol{a}^\dagger \boldsymbol{a} + \frac{1}{2} \right), \tag{5.26}$$

writing the charge and flux operators in terms of raising (lowering) operators $\boldsymbol{a}^\dagger$ ($\boldsymbol{a}$), $\boldsymbol{\Phi}_r = \sqrt{\hbar Z_r/2}\left(\boldsymbol{a}^\dagger + \boldsymbol{a}\right)$ and $\boldsymbol{Q}_r = \mathrm{i}\sqrt{\hbar/2Z_r}\left(\boldsymbol{a}^\dagger - \boldsymbol{a}\right)$. The cavity resonance frequency and impedance is given by $\omega_r = \sqrt{2/L'_r C_r}$ and $Z_r = \sqrt{2L'_r/C_r}$. One important note is that due to the galvanic coupling with the fluxonium circuit the renormalised resonator inductance becomes $L'_r = L_\Sigma^2/(L_q + L_c) = L_r + (L_q \parallel L_c)$, which effectively translates to an additional inductive contribution from the parallel combination of the bare fluxonium inductance and coupling inductance.

Moving to the fluxonium Hamiltonian, we can write it in the familiar form

$$\mathbf{H}_{\text{q}} = 4E_C \boldsymbol{n}_q^2 + \frac{1}{2} E_L \boldsymbol{\varphi}_q^2 - E_J \cos\left(\boldsymbol{\varphi}_q - \varphi_{\text{ext}}\right) = \sum_l \varepsilon_l |l\rangle\langle l|, \tag{5.27}$$

using the charge number $\boldsymbol{n}_q = \boldsymbol{Q}_q/2e$ and phase $\boldsymbol{\varphi}_q = 2\pi\boldsymbol{\Phi}_q/\Phi_0$ operators. The charging and inductive energies are defined as $E_C = e^2/2C_q$ and $E_L = (\Phi_0/2\pi)^2/L'_q$, and the flux bias phase is defined as $\varphi_{\text{ext}} = 2\pi\Phi_{\text{ext}}/\Phi_0$. A similar important note is that due to the galvanic coupling the renormalized fluxonium inductance becomes $L'_q = L_\Sigma^2/(L_r + L_c) = L_q + (L_r \parallel L_c)$, which effectively translates to an additional inductive contribution from the parallel combination of the bare resonator inductance and coupling inductance.

To calculate the fluxonium eigenspectrum, the phase difference across the junction is discretized in a 1D grid and the operators are expressed in matrix form in this grid basis. The eigenvalues ε_l and eigenstates $|l\rangle$ are essentially calculated by diagonalization of the fluxonium Hamiltonian. Due to the quadratic terms for the charging and inductive energies, another approach would be to express the charge and flux operators in a harmonic oscillator basis, same as the resonator Hamiltonian. However, in order to take into account the full cosine nonlinearity of the junction, without truncating the Taylor expansion, the Josephson energy needs to be expressed in terms of Laguerre polynomials [158]. This approach can be cumbersome and we find the phase grid expansion method to be more straightforward.

Finally, we move on to the most important part of the Hamiltonian, the magnetic dipole coupling given by the inductive term

$$\begin{aligned}\mathbf{H}_{\text{int}} &= \frac{L_c}{L_\Sigma^2}\boldsymbol{\Phi}_r \cdot \boldsymbol{\Phi}_q \\ &= \frac{\omega_r}{Z_r}\frac{L_c}{L_c + L_q}\sqrt{\frac{\hbar Z_r}{2}}\left(\boldsymbol{a}^\dagger + \boldsymbol{a}\right) \cdot \frac{\Phi_0}{2\pi}\sum_{l,l'}\langle l|\boldsymbol{\varphi}_q|l'\rangle |l\rangle\langle l'| \\ &= \sum_{l,l'}\hbar g_{l,l'}\boldsymbol{\sigma}_{l,l'}\left(\boldsymbol{a}^\dagger + \boldsymbol{a}\right), \end{aligned} \tag{5.28}$$

where we expanded the qubit flux operator in terms of all possible transitions between fluxonium eigenstates $l \to l'$, coupled to the cavity field through the dipole matrix elements $\langle l|\boldsymbol{\varphi}_q|l'\rangle$. These matrix elements dictate the selection rules for the fluxonium atom which, unlike the transmon, allow non-trivial dipole transitions between eigenstates differing by more than one quanta.

We can rewrite the coupling amplitude between the oscillator current and the fluxonium dipole, normalized by the oscillator resonance frequency

$$\frac{g_{l,l'}}{\omega_r} = \frac{\Phi_0}{2\pi}\frac{L_c}{L_c + L_q}\left(2\hbar Z_r\right)^{-\frac{1}{2}}\ \langle l|\boldsymbol{\varphi}_q|l'\rangle. \tag{5.29}$$

This form emphasizes how the normalized coupling strength depends on properties of the resonator (from the resonator impedance), of the fluxonium (from the dipole matrix element) and most importantly of the coupling circuit, given by the inductive participation $L_c/L_c + L_q$, which can be intuitively identified as the fraction of the phase bias across the coupler inductor which corresponds to the effective phase bias over the qubit junction. The parameters for the full circuit will be chosen such that one can easily reach the ultrastrong coupling (USC) regime, $g_{0,1}/\omega_r \geq 1$, for the resonator and the lowest two states of the fluxonium.

5.3.2 Tunable coupling

For this experiment we would like to have control over the normalized coupling strength between the fluxonium and the resonator, which also applies to the resonator chain. From Eq. 5.29, two approaches become apparent. First, the dipole matrix element $\langle l|\boldsymbol{\varphi}_q|l'\rangle$ can be tuned through the applied magnetic flux Φ_{ext} or through varying the fluxonium junction energy E_J by replacing the small junction with a flux-tunable SQuID. However, we would also like to design the experiment such that the light-matter coupling is tuned quasi-independently from the fluxonium energy spectrum, and this approach would not achieve this additional objective.

Second, the inductive participation ratio can also be varied by tuning the coupling inductor L_c. If we operate in the parameter regime $L_q > L_c \gg L_r$, then the effective fluxonium inductance is $L'_q = L_q + (L_r \parallel L_c) \approx L_q$, and hence E_L does not significantly depend on L_c. Given that the other parameters, E_J and E_C, remain fixed, this approach is suitable for maintaining the same fluxonium energy spectrum while varying the light-matter coupling.

The coupling inductor is implemented as a chain of flux-tunable asymmetric SQuIDs as shown in Fig. 5.6. Each SQuID is defined as a ring interrupted by two junctions with different energies, E_{J1} and E_{J2}, with a relative asymmetry defined as $d = (E_{J2} - E_{J1})/(E_{J2} + E_{J1})$. The Hamiltonian for a single SQuID is given by the sum of Josephson energies $\mathbf{H}_J = -E_{J1} \cos \boldsymbol{\varphi}_1 - E_{J2} \cos \boldsymbol{\varphi}_2$, where $\boldsymbol{\varphi}_1, \boldsymbol{\varphi}_2$ denote the phase difference across each junction. For an externally applied magnetic flux Φ_{ext}, these phase differences satisfy the fluxoid quantization condition in the loop $\boldsymbol{\varphi}_2 - \boldsymbol{\varphi}_1 + 2\pi\Phi_{\text{ext}}/\Phi_0 = 2\pi m$, where $m \in \mathbb{Z}$. By defining the SQuID phase difference as $\boldsymbol{\varphi} = (\boldsymbol{\varphi}_2 + \boldsymbol{\varphi}_1)/2$, the Hamiltonian can be rewritten as a single cosine potential [60]

$$\begin{aligned}\mathbf{H}_J &= -(E_{J1} + E_{J2}) \cos\left(\pi \frac{\Phi_{\text{ext}}}{\Phi_0}\right) \sqrt{1 + d^2 \tan^2\left(\pi \frac{\Phi_{\text{ext}}}{\Phi_0}\right)} \cos(\hat{\boldsymbol{\varphi}} - \varphi_0) \\ &\triangleq -E'_J(\Phi_{\text{ext}}) \cos(\hat{\boldsymbol{\varphi}} - \varphi_0),\end{aligned} \tag{5.30}$$

where the static phase shift in the potential $\varphi_0 = \tan^{-1}[d \tan(\pi\Phi_{\text{ext}}/\Phi_0)]$ can be safely disregarded by a change of variables. The key insight of Eq. 5.30 is the fact that the split junction ring can be regarded as a single Josephson junction with a flux-tunable junction energy E'_J which translates to an effective flux-tunable inductance $L'_J = (\Phi_0/2\pi)^2 / E'_J$. Therefore, implementing the coupling element as M SQuIDs connected in series, the coupling inductance becomes $L_c = ML'_J$. Since we are using junctions of similar size as the fluxonium inductance, we can treat the SQuID array as a linear inductor and ignore any nonlinearities coming from the cosine potential.

5.3.3 Coupling to a cavity array

After describing the linear resonator chain in Eq. 5.18 and the inductive coupling between a resonator and a qubit in Eq. 5.28, it becomes straightforward to combine these two to describe an effective qubit-bath Hamiltonian $\mathbf{H}_{\mathrm{qb}} = \mathbf{H}_{\mathrm{tb}} + \mathbf{H}_{\mathrm{int}}$,

$$\begin{aligned} \mathbf{H}_{\mathrm{qb}}/\hbar = & \sum_j \omega_j \left(\boldsymbol{a}_j^\dagger \boldsymbol{a}_j + \frac{1}{2} \right) + \sum_{\langle i,j \rangle} t_{i,j} \left(\boldsymbol{a}_i^\dagger - \boldsymbol{a}_i \right) \left(\boldsymbol{a}_j^\dagger - \boldsymbol{a}_j \right) \\ & + \sum_l \varepsilon_l |l\rangle\langle l| + \sum_{l,l'} g_{l,l'} \boldsymbol{\sigma}_{l,l'} \left(\boldsymbol{a}_1^\dagger + \boldsymbol{a}_1 \right), \end{aligned} \tag{5.31}$$

where the fluxonium dipole is coupled to the edge resonator (site 1) in the tight-binding chain. The expression for the on-site cavity resonances ω_j and photon hopping rates t_{ij} still follow the relations in Eq. 5.19, with modifications from the inductive coupling element at the edge and finite size of the chain. Similar to the single-unit-cell analysis in section 5.3.1, we will assume the fluxonium circuit and the SQuID coupler do not perturb the resonator chain capacitance matrix $\hat{\boldsymbol{C}}$.

The resonator sites excluding the edge have the same resonance frequency and impedance, given by $\omega_r = L_r^{-\frac{1}{2}} \left[\hat{\boldsymbol{C}}_\pm^{-1} \right]_{j,j}^{\frac{1}{2}}$ and $Z_r = L_r^{\frac{1}{2}} \left[\hat{\boldsymbol{C}}_\pm^{-1} \right]_{j,j}^{\frac{1}{2}}$ $(j \neq 1, N)$. This makes the hopping rate between the bulk sites the same $t = t_{ij} = -\frac{1}{2} Z_r \left[\hat{\boldsymbol{C}}_\pm^{-1} \right]_{i,j}$ $(i, j \neq 1, N)$. For the edge site not coupled to the qubit $(j = N)$, the diagonal and off-diagonal capacitance matrix elements are different from the bulk since the the edge is coupled on side to another resonator and on the other to the $50\,\Omega$ waveguide. This difference in the capacitive loading leads to a small change in the on-site resonance $\omega_N \simeq \omega_r$ and hopping rate $t_{N,N-1} \simeq t$, which is nevertheless taken into consideration in the numerical analysis. In addition to a capacitive perturbation, the edge site coupled to the qubit has a considerable inductive perturbation as outlined in section 5.19. The edge resonator inductance has contributions from both the coupler and qubit $L'_r = L_r + (L_q \parallel L_c)$, which leads to different values for the resonance frequency $\omega'_r = L'^{\frac{1}{2}}_r \left[\hat{\boldsymbol{C}}^{-1}_\pm\right]^{\frac{1}{2}}_{1,1}$, impedance $Z'_r = L'^{\frac{1}{2}}_r \left[\hat{\boldsymbol{C}}^{-1}_\pm\right]^{\frac{1}{2}}_{1,1}$ and hopping $t' = -\frac{1}{2}\sqrt{Z_r Z'_r}\left[\hat{\boldsymbol{C}}^{-1}_\pm\right]_{1,2}$. As we will observe in experimental measurements, this ω'_r L'_r perturbation leads to a waveguide mode being pushed outside the single-particle band of bandwidth $4t$, becoming more localized at the edge resonator. Nevertheless, this frequency shift is smaller than the hopping rate t and the qubit coupling strength g, which means that the edge resonator is not completely decoupled from the photonic crystal spectrum and that although the qubit is coupled to the edge, it is also coupled to the bulk eigenmodes of the cavity chain, as we will see in the elastic transmission measurements.

We can rewrite Eq. 5.31 in the eigenmode basis of the chain, using the matrix U to diagonalize the tight-binding part into $\sum \omega_k \boldsymbol{a}^\dagger_k \boldsymbol{a}$, where $\boldsymbol{a}^\dagger_j = U_{jk}\boldsymbol{a}^\dagger_k$. In the case of a qubit-free resonator chain, the matrix operation corresponds to a Fourier transform $\boldsymbol{a}^\dagger_j = \frac{1}{N+1}\sum_k e^{-i\pi jk/(N+1)}\boldsymbol{a}^\dagger_k$ and the dispersion is simply $\omega_k = \omega_r - 2t\cos\left(\frac{\pi k}{N+1}\right)$. The qubit-bath Hamiltonian in the momentum basis becomes

$$\mathbf{H}_{\mathrm{k,qb}}/\hbar = \sum_k \omega_k \boldsymbol{a}^\dagger_k \boldsymbol{a}_k + \sum_l \varepsilon_l |l\rangle\langle l| + \sum_{l,l'}\sum_k \boldsymbol{\sigma}_{l,l'}\left(g_{k,ll'}\boldsymbol{a}^\dagger_k + g^*_{k,ll'}\boldsymbol{a}_k\right), \tag{5.32}$$

where each $l \to l'$ fluxonium dipole transition is coupled to every eigenmode with a coupling strength $g_{k,ll'} = g_{ll'}U_{1,k}$. If we truncate the fluxonium to a two-level system, then Eq. 5.32 becomes the celebrated spin-boson Hamiltonian [159]. In a superconducting circuit platform, this model has typically been studied for a continuous Ohmic bath $\omega_k = \nu k$ [160, 150, 161], and has been demonstrated experimentally [162, 163, 78]. Only recently has the attention shifted to photonic reservoirs with a band edge giving rise to localized single-photon atom-photon bound states [155, 156]. The following experiments aim at probing multi-photon dressed bound states in the ultrastrong coupling regime and multi-mode entanglement in the bath degrees of freedom induced by the strong qubit nonlinearity.

5.4 Experimental implementation

The photonic crystal is experimentally implemented using 26 lumped-element microwave resonators, capacitively connected in a chain as shown in Fig. 5.5. These planar circuits are fabricated using a 200 nm-thick sputtered Nb film on a 525μm-thick high-purity C-plane sapphire substrate. The components are defined using optical lithography and reactive ion etching, with an attainable minimum feature size of 1μm. The capacitive elements are implemented as interdigitated structures where the values for both the ground and coupling capacitances are calibrated using ANSYS Maxwell, a commercially available electrostatic solver. The resonator inductors are implemented as meandered microstrip wires with a 4μm width. Note that for the resonator coupled to the fluxonium, the inductor is considerably shorter to accommodate for the inductive contribution from the coupling inductor. The resonance frequency of one resonator and thus its inductor is calibrated using other commercial solvers, such as ANSYS HFSS (eigenmode solver) and AWR Microwave Office (AXIEM solver). The circuit parameters for the cavity chain are summarized in Table. 5.1. These values stem from fitting the experimental data to the theoretical model.

The two edges of the chain are capacitively connected to 50 Ω coplanar waveguides with launch pads that are wire-bonded to coplanar waveguide traces on a dedicate PCB board with microwave connectors. These waveguide ports are connected to input and output coaxial lines in the dilution refrigerator used specifically for sending microwaves and amplifying outgoing signals from the device.

The fluxonium artificial atom is composed of a small Josephson junction inductively shunted by an array of 38 larger Josephson junctions and a chain of four asym-

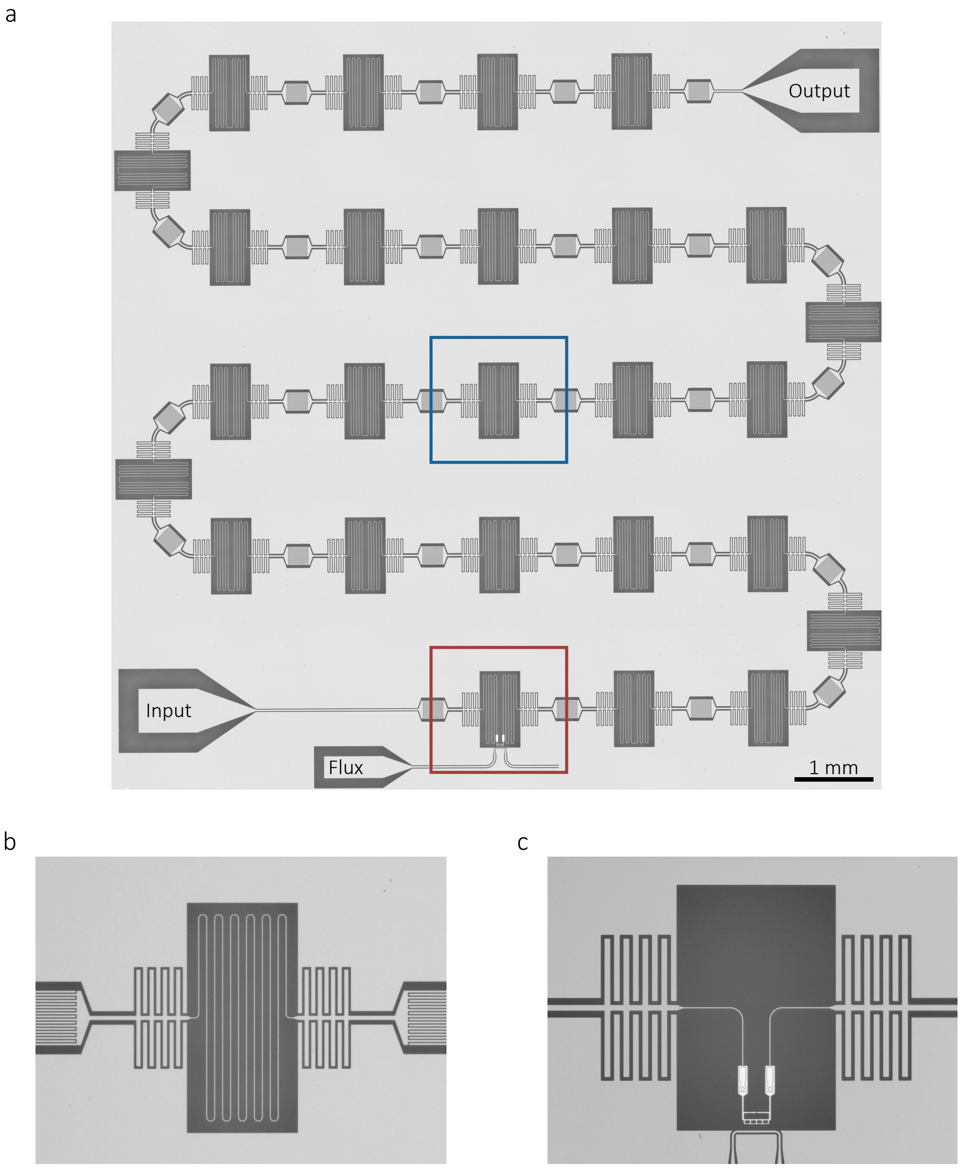

Figure 5.5: **Photonic crystal device description. a.** Optical image of a photonic crystal consisting of a chain of 26 coupled superconducting resonators. The blue box highlights the unit cell resonator and the red box highlights the edge resonator coupled to the fluxonium. **b.** Optical image a of a single lumped-element resonator composed of interdigitated capacitors and a meandered inductor. **c.** Optical image of the edge resonator inductively coupled to the fluxonium qubit

metric SQuIDs. The optical image and schematic diagram of the fluxonium circuit is shown in Fig. 5.6. The Josephson junctions and superconducting loop were defined via electron-beam lithography using a bi-layer resist (MMA-PMMA). The junctions

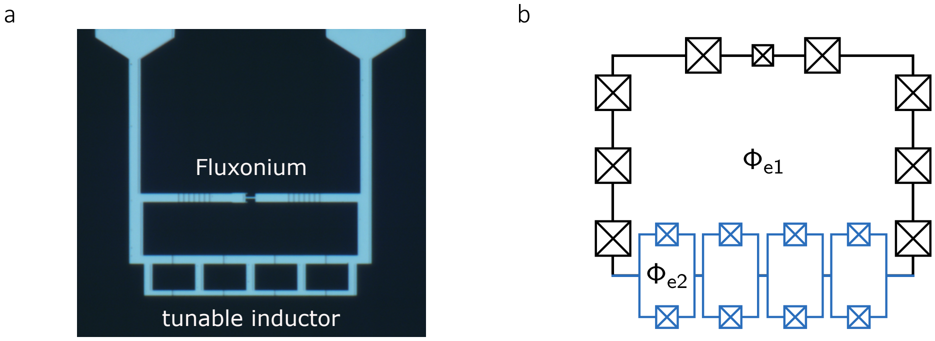

Figure 5.6: **Fluxonium artificial atom. a.** Optical image of the fluxonium circuit after e-beam evaporation and lift-off. **b.** Circuit diagram of the fluxonium circuit with the flux-tunable coupling inductance implemented as a chain of SQuIDs.

were fabricated via double-angle electron-beam evaporation using a Dolan bridge technique [115]. Aluminum films, with a thickness of 30 nm and 60 nm respectively, were deposited at different angles. The junction electrodes were separated by an AlO$_\mathrm{x}$ oxide grown at ambient temperature for 10 minutes in 200 mbar static pressure of a Ar:O$_2$ (85%:15%) gas mixture. The fluxonium is inductively coupled to the edge resonator on the input side. The contact pads for the galvanic connection between the edge-resonator inductor and the fluxonium loop is intentionally made larger $(20 \times 50\mu m^2)$ than the inductor width to ensure a small contact resistance.

The fluxonium loop and tunable inductor are magnetically biased using an on-chip flux line where we apply a DC current I in order to induce a magnetic field at position $\vec{\boldsymbol{r}}$ from the Biot-Savart law

$$\vec{\boldsymbol{B}}(\vec{\boldsymbol{r}}) = \int \frac{\mu_0 I}{4\pi} \frac{\mathrm{d}\vec{\boldsymbol{l}} \times \vec{\boldsymbol{r}}}{|\vec{\boldsymbol{r}}|^3}. \tag{5.33}$$

Fluxonium	
$E_J/\hbar$	8.17 GHz
$E_L/\hbar$	5.56 GHz
$E_C/\hbar$	3.50 GHz
Resonator chain	
L_r	2.80 nH
L_r' (edge)	$\sim$ 0.1nH
L_c	4 - 14 nH
C_g	249.15 fF
C_c	202.70 fF

Table 5.1: **Parameters for the joint qubit and photonic crystal circuit.**

Following the treatment in [164], we can model the flux line as a wire of length L and calculate the field inside a rectangular loop positioned a specific distance from the line. The field in planar coordinates has the following analytical expression

$$B(x,y) = \frac{\mu_0 I}{4\pi y}\left[\frac{L/2-x}{\sqrt{(L/2-x)^2+y^2}} + \frac{L/2+x}{\sqrt{(L/2+x)^2+y^2}}\right]. \tag{5.34}$$

The magnetic flux threading the loop can be calculated by integrating the field $B(x,y)$ over the rectangular area. Using this methodology, we design the area of the fluxonium and SQuID loops as well as their relative distances to the flux bias line to achieve the desired ratios of magnetic flux. Specifically, for a given applied current bias, we want the magnetic flux in each SQuID loop to be the same Φ_{e2}, and we want the magnetic flux enclosing the fluxonium loop to be at least an order of magnitude larger $\Phi_{\mathrm{e1}}/\Phi_{\mathrm{e2}} \geq 10$. This large asymmetry allows the flexibility of biasing the qubit to have the same energy spectrum, while sampling various coupling regimes set by different values of $g_{l,l'}/\omega_r$. As pointed out in [164], this treatment does not take into account screening currents due to the Meissner effect, which would reduce the the amount of flux threading any given loop. However, since we are interested in the ratio of applied flux $\Phi_{\mathrm{e1}}/\Phi_{\mathrm{e2}}$ instead of the absolute magnitude, such a complication is not critical to this particular analysis.

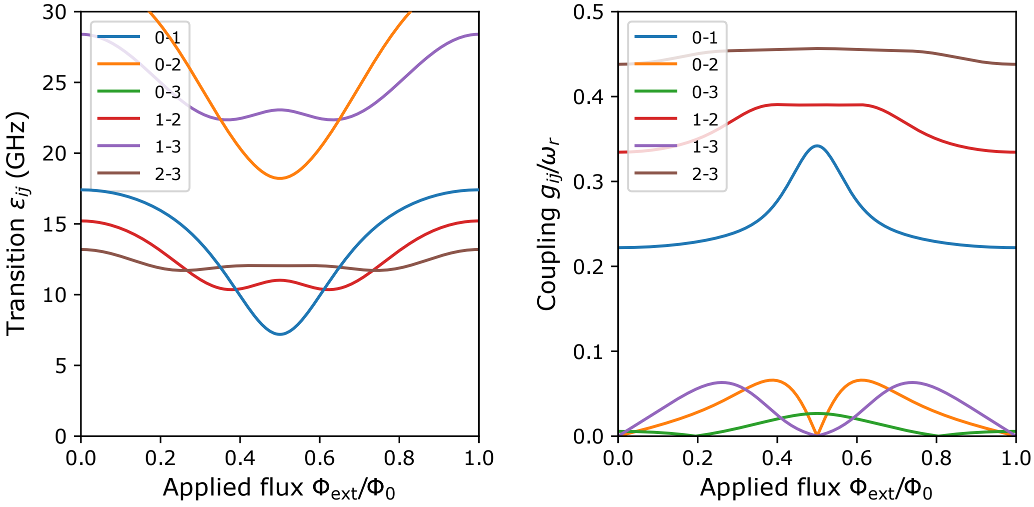

Figure 5.7: **Fluxonium-resonator coupling strength.** (left) Calculated transition frequencies $\varepsilon_{l,l'}$ between the ground state ($l = 0$) and first three excited states of the fluxonium circuit and (right) their normalized coupling strength with the edge-resonator as a function of applied flux. The numerics are based on the parameters summarized in Table 5.1 for the coupling inductor value $L_c = 4$ nH .

We summarize the parameters of the full circuit in Table 5.1. The values for the fluxonium parameters (E_J, E_L and E_C) and the tunable range for the coupling inductor L_c are extracted from the experimental data presented in the sections to follow. In Fig. 5.7 we plot the transition frequencies between the first four eigenstates of the fluxonium, and their corresponding coupling strength to the edge resonator for the choice of lowest value for the coupling inductor, $L_c = 4$ nH. This plot shows that biasing the qubit loop at $\Phi_{\mathrm{e1}} = \Phi_0/2$, also referred to as the degeneracy point, is optimal for achieving large dipole coupling. At this bias point, the wavefunctions in the two wells of the fluxonium potential become degenerate and hybridize due to the finite potential barrier. This hybridization leads to a large dipole matrix element $\langle 0|\hat{\varphi}_q|1\rangle$ and a large coupling strength (≥ 0.3 in this case) as emphasized in Eq. 5.29. The fluxonium parameters are tailored to ensure this fluxon transition resonance enters the single-photon band of the cavity chain. Since the qubit starts in its ground state, ignoring thermal occupation, we are mainly concerned with transitions between the ground state and higher excited states.

5.5 Elastic scattering

In this section we focus on the first type of measurement aimed at probing transport through the doped photonic crystal. In particular we are interested in the elastic scattering of a single incoming photon entering the cavity chain and interacting with the artificial atom. This is easily performed in a transmission measurement.

5.5.1 Transmission measurement

In this scenario we are probing the response of the system at a particular frequency ω_{p} using a weak probe field applied at the input port of the chain, and measuring the outgoing field at the output port of the chain, at the same frequency $\omega_{\mathrm{out}} = \omega_{\mathrm{p}}$. This experiment is easily implemented in a network analyzer setup. The transmission coefficient S_{21} is defined as the ratio between the voltage amplitudes of the outgoing microwave field to the incident field $t(\omega) = V_{\mathrm{out}}/V_{\mathrm{p}}$. The magnitude of the transmission coefficient $|t|$ as a function of the incident frequency and applied magnetic flux is shown in Fig. 5.8. The probe frequency is swept over a broad range ($5 - 9$ GHz) that covers the passband of the photonic crystal. The amplitude of the probe field is chosen such that on average there is less then one photon pumped into the system.

From this initial measurement we can identify frequency regions with high transmission. This defines the passband of the photonic crystal which spans the eigenmode spectrum ω_k of the resonator chain. Each horizontal line in the color plot in Fig. 5.8 corresponds to the dressed normal modes of the chain. These resonances do not exactly coincide with the bare (uncoupled) eigenmode frequencies due to hybridization with the artificial atom, and these modes experience a frequency shift when the atom transition resonance is tuned into the passband spectrum.

For frequency regions outside the passband we observe diminishing transmission with a sharp roll-off near the band edges at frequencies of approximately 5.27GHz and 8.51GHz, respectively. These frequency regions correspond to bandgaps of the photonic metamaterial, similar to band gaps for electrons in solid state materials. Due to the confined nonlinear dispersion of the chain, transport is forbidden and incoming microwave fields are completely reflected from the lack of photonic states outside the band. Since the metamaterial is composed of a discrete number of resonators, transmission in the passband is decreased when detuned from the dressed eigenmode resonances, similar to the transmission for a single-mode cavity. However, the transmission between the modes does not drop as dramatically as in the band gap. This is given by the fact that the capacitive coupling to the 50Ω waveguides at the edge is large, and this ultimately broadens the resonances and delocalizes these states in frequency. If the number of cavities tends to infinity, we approach the waveguide limit characterized by a continuum of harmonic modes and uniform transmission over the photonic band.

Nevertheless, the fact that we can individually resolve these resonances allows us to spectroscopically characterize this many-body circuit. The aim of this experimental study is to reach large couplings between a single nonlinear artificial atom and the many harmonic modes of a photonic reservoir which could lead to potentially complex many-body states that can be studied by directly probing these dressed modes.

There are noticeable reflections in the passband for periodic values of applied magnetic flux (Fig. 5.8). At these flux bias regions, the fluxonium resonance, defined as the transition between its internal states, is tuned through the photonic band and scatters incoming photons resonant with its transition. The period in the applied voltage bias effectively translates to the incremental current needed to apply a flux

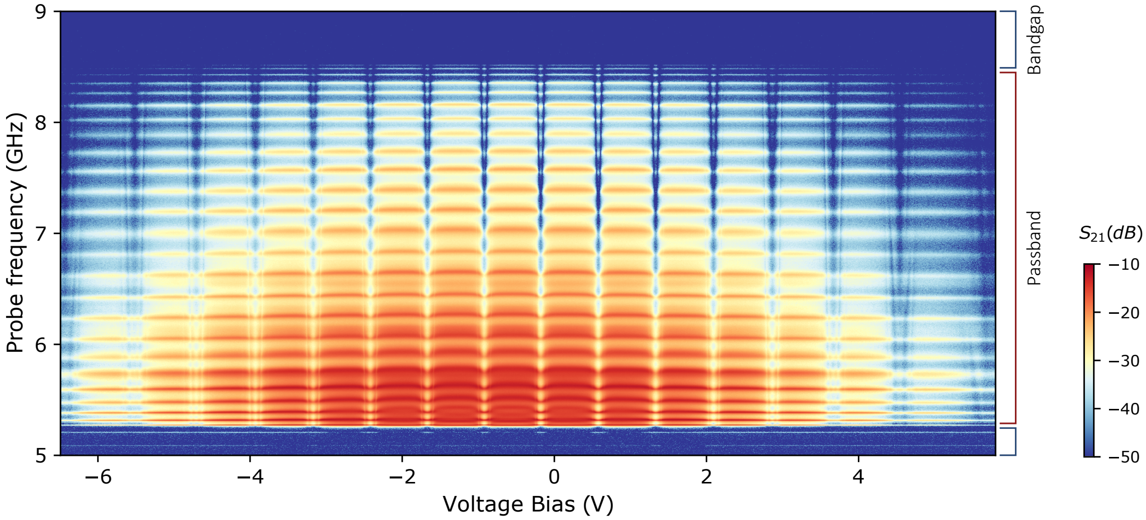

Figure 5.8: **Spectroscopy of cavity chain with tunable coupling.** Measured transmission coefficient $|S_{21}|$ with incident microwave fields in the frequency range around the photonic crystal passband. The transmission response is studied as a function of the magnetic flux applied to the fluxonium and coupler circuit.

quantum through the fluxonium loop. The full span of applied voltage in Fig. 5.8 roughly corresponds to the effective current needed to apply a flux quantum through the loops of the inductive coupling SQUIDs. In the voltage range $|V_{\mathrm{b}}| < 1$ V, the shared inductor between the qubit and edge cavity is biased at its smallest value and it gradually increases with the applied bias $|V_{\mathrm{b}}|$. In this broad flux bias sweep we can comparatively observe significant deviations in transmission through the cavity chain as its coupling to the qubit is increased. The rest of this discussion will be aimed at transmission measurements centered around the flux bias points where the fluxonium transition resonance is tuned in the passband.

First we can focus on transmission near the weaker coupling bias point $V_b \simeq 0.6$V, where the flux-dependent transmission coefficient $|t|$ is plotted in Fig. 5.9a. As the fluxonium transition is tuned through the passband there is a clear extinction in the transmitted amplitude centered at the qubit frequency. Since this transmission dip follows the flux dispersion of the qubit energy, we fit this transmission data to the fluxonium spectrum. The solid line in Fig. 5.9a corresponds to the fluxon transition frequency from the ground state to the first excited state, following the expected fluxonium parameters in Table. 5.1. The bias voltage where the fluxon transition is tuned to its minimum corresponds to the half-flux quantum point where the fluxon wavefunctions in the double-well potential hybridize, which gives a large magnetic dipole moment $\langle 0|\boldsymbol{\varphi}_q|1\rangle$ and thus large inductive coupling g. All other transitions from the ground state are detuned from waveguide single-photon band, inferred from the calculated fluxonium spectrum in Fig. 5.7.

The appearance of a transmission dip at the qubit frequency can be understood from a semiclassical picture of a two-level dipole coupled to the electromagnetic waves in a 1D transmission line. This description was adapted from references [162, 165]. We can start by treating the incoming fields as classical waves $I(x,t) = I_0 e^{i(kx-i\omega t)}$ reaching the qubit position $x = 0$. From the dipole interaction, this external field polarizes the dipole which induces an oscillating voltage across the qubit $V_q(t) = \langle \dot{\Phi}_q \rangle$. The dipole starts to radiate in both directions in the waveguide and will interfere with the drive. Given the inductive coupling, the boundary conditions at the qubit are

$$V(0^-,t) = V(0^+,t) + \langle \dot{\Phi}_q \rangle \ , \ I(0^-,t) = I(0^+,t) \tag{5.35}$$

The combined drive and dipole fields on the left and right of the qubit can be written in terms of the reflection and transmission coefficients

$$\begin{aligned} I(x<0,t) &= I_0 e^{i(kx-i\omega t)} + I_q e^{-i(kx+i\omega t)} \triangleq I_0 e^{i(kx-i\omega t)} - r I_0 e^{-i(kx+i\omega t)} \\ I(x>0,t) &= I_0 e^{i(kx-i\omega t)} + I_q e^{i(kx-i\omega t)} \triangleq t I_0 e^{i(kx-i\omega t)} \end{aligned} \tag{5.36}$$

Using these expressions in the telegraph equation for the propagating voltages and currents in a transmission line of impedance Z we can reach the expression for the reflection and transmission coefficients in terms of the drive amplitude $V_0 = I_0 Z$ and the oscillating dipole voltage

$$r = \frac{1}{2V_0}\frac{\partial\langle\Phi_q\rangle}{\partial t}e^{i\omega t}\ ,\ t = 1 - \frac{1}{2V_0}\frac{\partial\langle\Phi_q\rangle}{\partial t}e^{i\omega t} \tag{5.37}$$

Up to this point we have regarded the qubit as a driven classical dipole. To find the expression for r and t coefficients as a function of the qubit parameters, we go to the quantum picture for a driven two level system described by the Hamiltonian $\mathbf{H}/\hbar = \frac{\Delta}{2}\sigma_z + \Omega\cos(\omega t)\sigma_x$. The drive term originates from the inductive dipole interaction with the incoming field $\mathbf{H}_{\text{int}} = I_0\mathbf{\Phi}_q = \Omega\sigma_x$. We substitute the qubit flux operator with $\mathbf{\Phi}_q = MI_q\sigma_x$, where M is the mutual inductive coupling to the transmission line, and the Rabi drive amplitude becomes $\Omega = MI_0I_q$. The qubit density matrix satisfies the master equation

$$\dot{\rho} = \frac{i}{\hbar}[\mathbf{H}, \rho] - \Gamma_1\sigma_z\rho_{11} - \Gamma_2(\sigma^+\rho_{01} + \sigma^-\rho_{10}) \tag{5.38}$$

where we have defined qubit energy relaxation rate Γ_1 and decoherence rate Γ_2 caused by treating the coupling to the 1D transmission line as a Markovian bath. The stationary response of the qubit $\langle\sigma_x\rangle = \mathrm{Tr}\,[\rho\sigma_x]$ matrix can be found from steady-state density matrix $\dot{\rho}_{\text{ss}} = 0$. Substituting $\langle\sigma_x\rangle$ into Eq. 5.37 and assuming we operate in the weak driving regime $\Omega^2 \ll \Gamma_1\Gamma_2$ yields the reflection and transmission coefficients for a two level system in a 1D transmission line

$$r = \eta\frac{\Gamma_1}{2\Gamma_2}\frac{1}{1 + i\Delta\omega/\Gamma_2}\ ,\ t = 1 - \eta\frac{\Gamma_1}{2\Gamma_2}\frac{1}{1 + i\Delta\omega/\Gamma_2}, \tag{5.39}$$

where we defined the detuning between the driving field and qubit resonance frequency $\Delta\omega = \omega_q - \omega$. Because the qubit can be susceptible to other sources of loss, the factor η is introduced to account for the qubit emission into other channels. The expression for

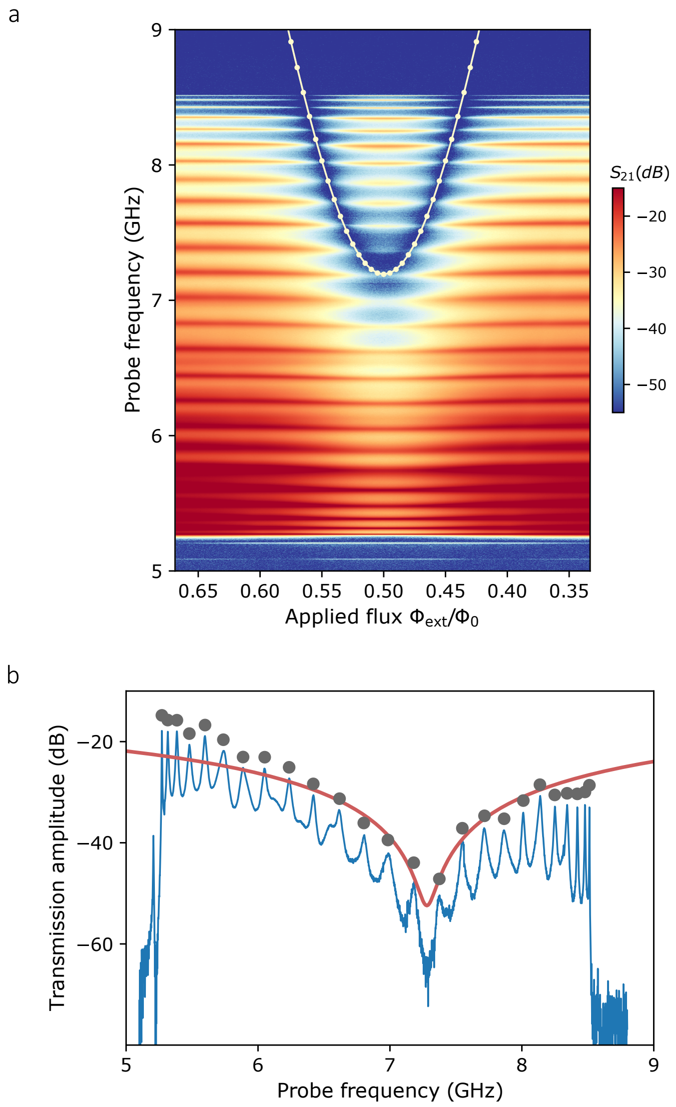

Figure 5.9: **Transmission near the fluxonium degeneracy point. a.** Amplitude of transmitted probe field as the fluxon transition frequency (solid line) is tuned in resonance with the pass band. **b.** Transmission trace at $\Phi_{\text{ext}} = \Phi_0/2$ showing an extinction in the transmission amplitude at the qubit frequency. Gray circles correspond to the transmission amplitude probed at each eigenmode frequency. This data is fitted (solid red line) to the elastic transmission coefficient $t(\omega)$ (Eq. 5.39) in a 1D waveguide coupled to a two-level system.

the complex transmission coefficient clearly captures the suppression in $|t|$ when the qubit is resonantly driven. This can be understood from the destructive interference between the incoming field and the forward propagating field radiated by the qubit, while the reflected field interferes constructively with the drive and leads to a sharp increase in the reflection amplitude $|r|$ on resonance.

To quantify how strongly coupled the fluxonium qubit and the waveguide are, we can try to fit the transmission data near the qubit resonance to Eq. 5.39, which is the same approach adopted in previous waveguide QED experiments [162, 163, 78]. In Fig. 5.9b we plot the transmission trace when the fluxonium is biased at the $\Phi_0/2$, together with a fit to Eq. 5.39 given by the solid line. Given that our waveguide has a discrete number of modes, the fit is constrained to the transmission amplitude at the eigenmode peaks. The spontaneous emission rate Γ_1 is estimated to be comparable to the qubit resonance frequency $\Gamma_1/\omega_q \approx 0.7$. This regime has been previously explored in experiments coupling flux qubits to the continuum of a coplanar waveguide [78, 166], and is clear evidence that the qubit is simultaneously hybridized with many modes in the waveguide. It is important to note that Eq. 5.39 comes from applying the RWA approximation to the master equation. However, even in this ultrastrong coupling regime $\Gamma_1/\omega_q \sim 1$ the qubit lineshape in the elastic transmission is still found to be approximately Lorentzian from the polaron transformation [167].

The circuit parameters for the resonator chain were extracted by fitting transmission to both the normal modes of the circuit Lagrangian and the simulated transmission using the ABCD matrix method. Since both models do not take into consideration the nonlinear fluxonium circuit, we fit the transmission profile when the qubit is maximally detuned in frequency from the pass band. However, the SQuID coupler is assumed to behave as a tunable linear inductor $L_c(\Phi_{\mathrm{ext}})$ and is therefore included in the Lagrangian inductance matrix and in the ABCD matrix of the edge resonator. The coupling SQuID increases the inductance of the edge resonator and pushes the lowest chain eigenmode outside the band as shown in Fig. 5.10. Constraining the fit to both the normal modes inside the band and the shifted mode gives estimates for the

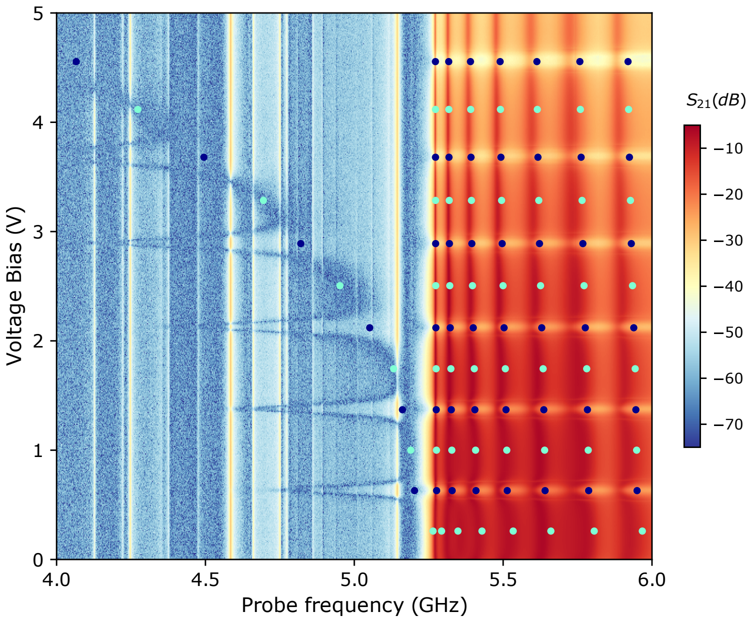

Figure 5.10: **Transmission near the band edge.** Due to the coupling inductor, there is an eigenmode resonance shifted below the band edge. When the fluxon transition is tuned in the band, the resonance corresponds to a single-photon bound state. Blue circles correspond to the normal modes of the (qubit-free) resonator chain calculated from the estimated values in Table. 5.1. The qubit flux bias is tuned to $\varphi_{\text{ext}} = \pi (\text{mod}\, 2\pi)$ and $\varphi_{\text{ext}} = 0 (\text{mod}\, 2\pi)$ at the dark and light blue circles, respectively.

circuit parameters for the bare resonator and the flux-dependent SQuID inductance. The parameters are listed in Table 5.1.

In order to estimate the coupling inductor at the bias points where the fluxon transition is tuned in the band, we constrain the range of values for L_c at the adjacent bias points where the qubit is maximally detuned, and we fit them to the expected flux dependence given by Eq. 5.30 for an asymmetric SQuID. As shown in the transmission data focused near the lower band edge (Fig. 5.10), when the fluxon transition enters the band the lowest eigenmode acquires an additional frequency shift which follows the fluxon dispersion. That resonance now corresponds to the qubit-photon bound state in the single-excitation manifold, which is no longer described by a single eigenstate $\boldsymbol{a}_k^\dagger|0\rangle$ $(k=0)$ but a dressed eigenstate $|0\rangle|e\rangle + \sum_k c_k \boldsymbol{a}_k^\dagger |0\rangle|g\rangle$ combining the qubit and multiple mode excitations [155].

Furthermore, we can estimate the inductive coupling strength $g_{ll'}$ from Eq. 5.29 using the circuit parameters for fluxonium, resonator and coupling inductor. This coupling strength enters the tight-binding model in the lab frame described by Eq. 5.31. For the bias range in the transmission data presented in Fig. 5.9, the fluxon resonance at $\Phi_0/2$ is coupled to the edge resonator with an estimated normalized coupling strength $g_{01}/\omega_r' \approx 0.31$. This is already strong enough to be in the USC regime.

5.5.2 Bound state mediated scattering

Since we have the capability of tuning the coupler inductance independently from the fluxonium spectrum, we can perform the same transmission measurement at larger flux bias values where the dipole coupling is larger. The experimental transmission scans are plotted in Fig. 5.11 and Fig. 5.12. When the bias voltage is tuned around $V_b \sim 3.7$ V, the coupling strength at half flux quantum is estimated to be $g/\omega_r' \simeq 0.42$. At this bias range we observe an additional transmission dip in the single-photon band (Fig. 5.11a) which follows a similar flux dispersion as the qubit transition. Moving to the transmission data biased around $V_b \sim 4.55$ V (Fig. 5.11c), this extra resonance shifts down in frequency when the coupling is increased to $g/\omega_r' \simeq 0.50$. Going to the largest inductive coupling $g/\omega_r' \simeq 0.67$ reached around the bias range $V_b \sim 5.75$ V we observe a second resonance dip appearing in the pass band with a similar flux dispersion.

These extra resonances appearing in the transmission spectrum indicate that there are new states entering the scattering dynamics of a single photon. Investigating the many-body spectrum and simulating the scattering dynamics in the next sections, we will find that these peculiar resonances correspond to multi-photon bound states entering the single-photon band and mixing in the scattering dynamics due to the counter-rotating terms in Hamiltonian 5.32.

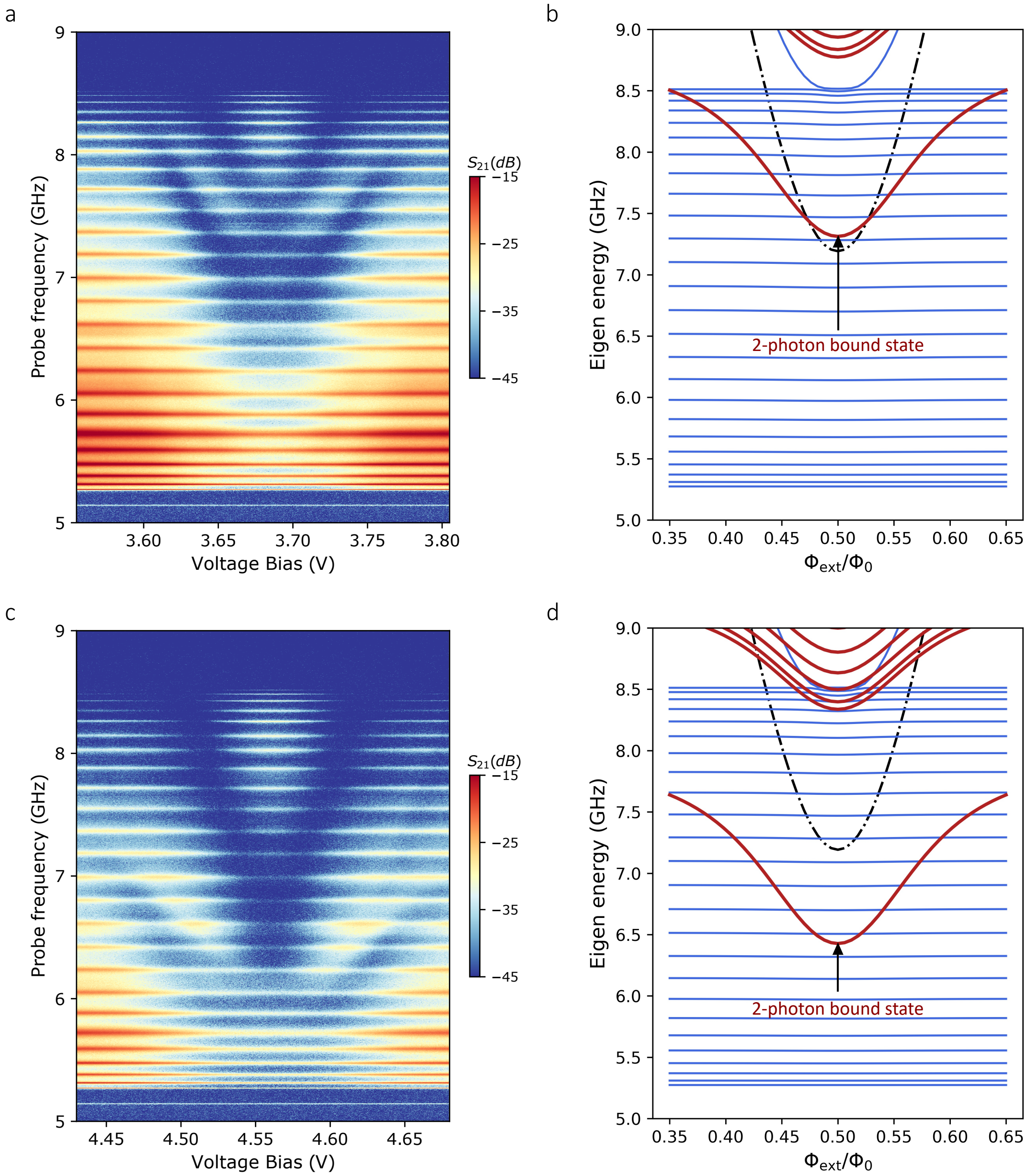

Figure 5.11: **Two-photon bound state scattering. a**,**c**. Transmission near the fluxonium degeneracy point biased at larger coupler inductance and (**b**,**d**) corresponding RWA spectrum. The appearance of an additional resonance dip in transmission qualitatively matches the dispersion of the two-photon bound state (red).

5.5.3 RWA many-body spectrum

To investigate these new states appearing in the elastic scattering, we determine the many-body spectrum of the combined system - qubit and cavity array - when we

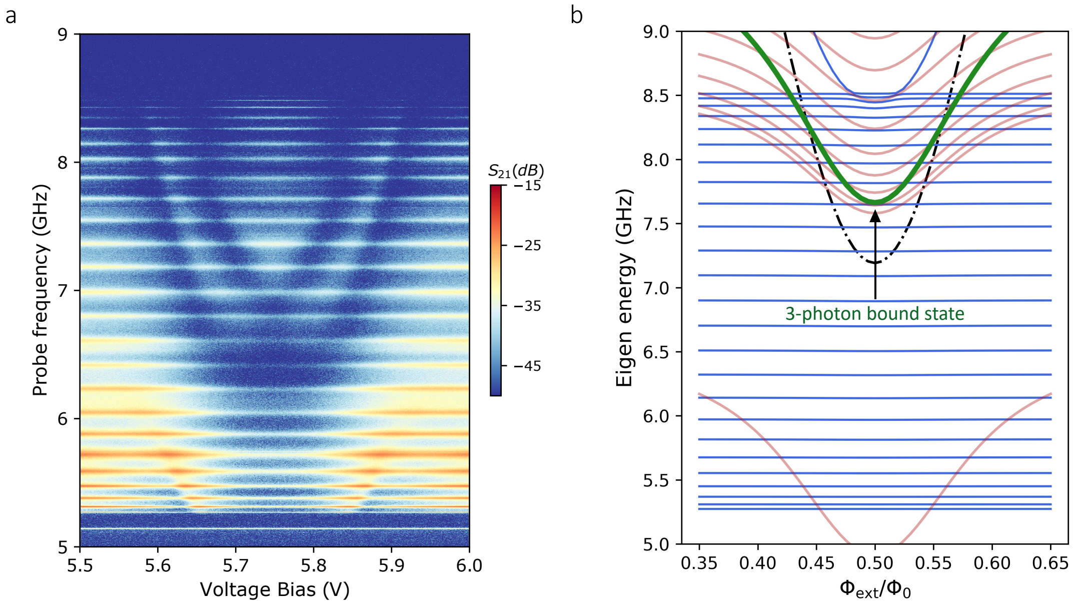

Figure 5.12: **Three-photon bound state scattering. a.** Transmission near the fluxonium degeneracy point biased at maximum coupler inductance and (**b.**) corresponding RWA spectrum. Additional resonance dip in transmission qualitatively matches the dispersion of the three-photon bound state (green)

have multiple excitations (photons) injected in the waveguide. Since it is computationally inefficient to diagonalize the full qubit-waveguide Hamiltonian in Eq. 5.31, we will perform this calculation in the RWA. In this approximation, the total number of excitations $N = \sum_x \boldsymbol{a}_x^\dagger \boldsymbol{a}_x + \sum_l |l\rangle\langle l|$ is conserved as the counter-rotating terms in the coupling Hamiltonian are ignored. This allows us to find the many-body spectrum by finding the eigenstates of each individual excitation sector, which is a more efficient computational task given the reduction in the matrix size. Of course, this approximate method is not valid in the USC regime where these excitation sectors are no longer decoupled. Nevertheless, the aim is to first identify what many-body states are participating in the scattering dynamics. The next section will deal with the simulating the scattering dynamics under the full (non-RWA) Hamiltonian.

To proceed with generating the Hamiltonian for different particle sectors, we first need to generate the correct basis vectors. We adopt the method in Ref. [168] for

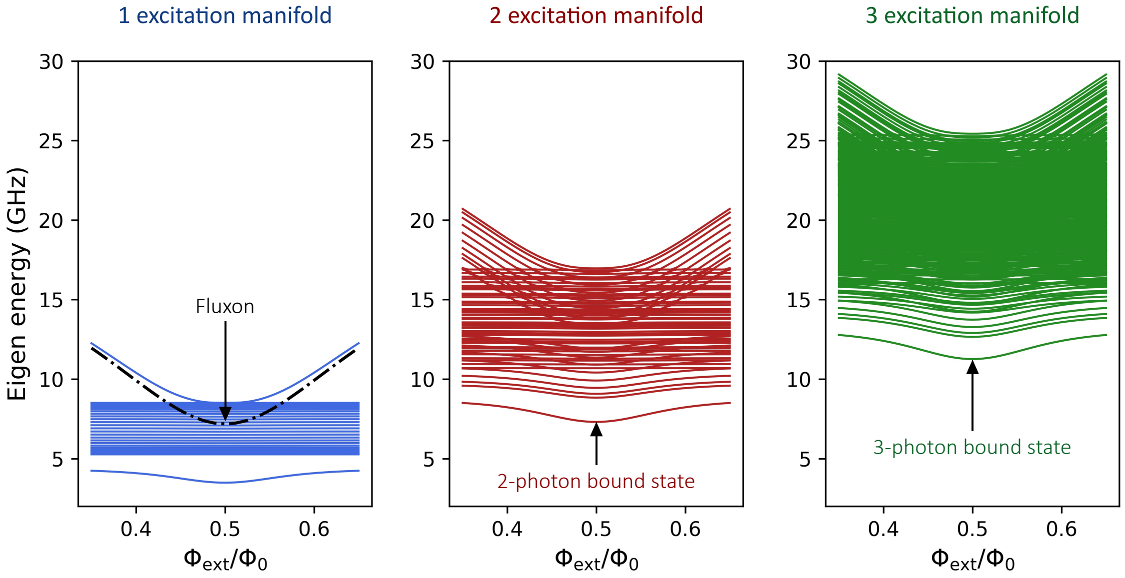

Figure 5.13: **RWA many-body spectrum.** Calculated eigenstates for the one, two and three-photon manifolds using the tight-binding parameters inferred from the transmission data in Fig. 5.11a.

generating the occupation number basis. For a system with M degrees of freedom and a total number of N excitations, we generate basis vectors $|v\rangle = |n_1, n_2, ...n_M\rangle$ which satisfy $\sum n_i = N$. The dimension of this subspace is $D = \frac{(N+M-1)!}{N!\,(M-1)!}$. The $(D \times D)$ Hamiltonian $\mathbf{H}^{(N)}$ for each manifold is simply found by applying the full Hamiltonian (Eq. 5.31) to each basis vector and if it produces another basis vector in the same orthonormal set, then we can introduce the matrix element $\mathbf{H}^{(N)}_{uv} = \langle u|\mathbf{H}_{\mathrm{qb}}|v\rangle$.

In our system, the number of degrees of freedom M includes 26 resonators and several fluxonium excited states up to some cutoff. We calculate the eigenspectrum up to the $N = 3$ photon manifold as shown in Fig. 5.13, using the circuit parameters extracted at the flux bias range associated with the transmission data in Fig. 5.11a. Note that the inductive participation from the SQuID coupler is included to account for the lower eigenmode shifted in frequency.

In the single-particle spectrum we recover the expected band of propagating single-photon states ω_k over the approximate range of $\omega_r \pm 2t$, when the fluxon transition (black dotted line) is detuned. When the fluxon enters the band, eigenstates emerge from the lower and upper band edge and become dressed qubit-photon bound states represented by the single-photon wavefunctions [154]

$$|\psi_{1\mathrm{ph}}\rangle = \left(\cos\theta\ \sigma^{+} \pm \sin\theta\ \boldsymbol{a}_{\lambda}^{\dagger}\right)|g,0\rangle. \tag{5.40}$$

These dressed states contain a qubit excitation and a photonic component from the resonator chain $\boldsymbol{a}_{\lambda}^{\dagger} = \sum_{x} c_{x} e^{\frac{-|x_q - x|}{\lambda}} \boldsymbol{a}_{x}^{\dagger}$ which is localized around the qubit position ($x_q = 1$). This is a multi-mode extension to the Jaynes Cummings dressed states.

Going to the two-excitation sector, the eigenspectrum becomes a bit more complicated. Similar to the single-photon case, we have a band of free-propagating two-photon states with approximate energies in the range $2\omega_r \pm 4t$. Additionally, we have bands consisting of a single-photon bound state combined with a propagating photon state. Most importantly, we observe two-photon bound states defined as [154]

$$|\psi_{2\mathrm{ph}}\rangle = \left(\cos\theta\ \sigma^{+}\boldsymbol{A}^{\dagger} \pm \sin\theta\ \boldsymbol{B}^{\dagger}\right)|g,0\rangle, \tag{5.41}$$

where $\boldsymbol{A}^{\dagger}$ and $\boldsymbol{B}^{\dagger}$ are one- and two-photon operators defined as $\boldsymbol{A}^{\dagger} \simeq c_{\lambda 2}\boldsymbol{a}_{\lambda 1}^{\dagger} + c_{\lambda 1}\boldsymbol{a}_{\lambda 2}^{\dagger}$ and $\boldsymbol{B}^{\dagger} \simeq \boldsymbol{a}_{\lambda 1}^{\dagger}\boldsymbol{a}_{\lambda 2}^{\dagger}$. These dressed states consist of a single-particle qubit-photon dressed state combined with a more weakly bound photon $\lambda_2 > \lambda_1$.

The same applies for the three-excitation sector. We have a $12t$ three-photon propagating band, two bands with one bound and two propagating photons, two bands with two bound and one propagating photon and two separate three-photon bound states. The bound state wavefunctions can be easily generalized to [154]

$$|\psi_{3\mathrm{ph}}\rangle = \left(\cos\theta\ \sigma^{+}\boldsymbol{C}^{\dagger} \pm \sin\theta\ \boldsymbol{D}^{\dagger}\right)|g,0\rangle, \tag{5.42}$$

where $\boldsymbol{C}^\dagger$ and $\boldsymbol{D}^\dagger$ are two- and three-photon operators defined as $\boldsymbol{C}^\dagger \simeq c_{\lambda 1}\boldsymbol{a}^\dagger_{\lambda 2}\boldsymbol{a}^\dagger_{\lambda 3} + c_{\lambda 2}\boldsymbol{a}^\dagger_{\lambda 1}\boldsymbol{a}^\dagger_{\lambda 3} + c_{\lambda 3}\boldsymbol{a}^\dagger_{\lambda 1}\boldsymbol{a}^\dagger_{\lambda 2}$ and $\boldsymbol{D}^\dagger \simeq \boldsymbol{a}^\dagger_{\lambda 1}\boldsymbol{a}^\dagger_{\lambda 2}\boldsymbol{a}^\dagger_{\lambda 3}$. The two- and three-photon bound states are highlighted in Fig. 5.13 as the lowest eigenstates in each respective manifold.

This RWA calculation reveals that for the system parameters near the flux bias $V_b \sim 3.7$ V, the two-photon bound state enters the single-photon band. This is further highlighted in Fig. 5.11b displaying the combined RWA spectrum in the frequency window used for probing transmission. Indeed, the two-photon bound state line qualitatively matches the extra resonance observed in transmission (Fig. 5.11a). Moving to the flux bias range $V_b \sim 4.55$ V, the calculated RWA spectrum, shown in Fig. 5.11d, shows a two-photon bound state shifted down in frequency as it is further repelled from the two-photon band edge due to the increased dipole coupling. This matches the experimental data in Fig. 5.11c where the resonance dispersion is shifted down in frequency.

When biasing the device at $V_b \sim 5.75$ V, we reach the largest normalized dipole coupling $g/\omega_r' \simeq 0.67$. In this parameter regime the RWA spectrum, displayed in Fig. 5.12b, reveals the three-photon bound state crossing the single-photon band, matching the additional resonance we observe in transmission shown in Fig. 5.12a.

Overall, from calculating the many-body spectrum it becomes clear that as the normalized coupling strength is increased the multi-photon manifolds begin to merge with the single-photon band. Since we are in the USC regime where processes permit the spontaneous creation and annihilation of pairs of excitations, we find that the scattering of even a single photon becomes a many-body problem as higher excitation manifolds need to be considered. For our device parameters, both the two and three-photon bound states cross the pass-band and become energetically accessible to a single propagating photon through the counter-rotating terms. This nonlinear phenomena has been theoretically predicted in [157].

5.5.4 Scattering simulations

The eigenspectrum calculation in the previous section is a straightforward numerical task when the RWA approximation is satisfied. However, we are operating in the USC regime, where this approximation is not valid. To consider the full Hamiltonian with counter-rotating terms we perform the following elastic scattering calculation adapted from reference [157]. We start with a single-photon propagating wave entering the waveguide with a frequency ω_k and corresponding momentum k. The wavefunction at time $t = 0$ is generated from the ground state $|\mathrm{GS}\rangle$ using the appropriate creation operator, $|\phi(t = 0)\rangle = \boldsymbol{a}_k^\dagger|\mathrm{GS}\rangle$. It is important to clarify that for the values of g/ω_r' we are considering, the ground state is not the vacuum state and consists of a photon cloud around the qubit position, with considerable real-space occupation in the cavity directly coupled to the qubit and its nearest neighbor. The wavefunction is evaluated over repeated applications of the full Hamiltonian 5.31 over a small time window $|\phi(t + \delta t)\rangle = \exp\left(-\frac{i}{\hbar}\mathbf{H}_{qb}\delta t\right)|\phi(t)\rangle$. As time evolves, the wave propagates through the waveguide. After it reaches the qubit position, the incoming photon interacts with the qubit and develops reflected and transmitted wave packets. To characterize this scattering process we evaluate the emitted field at each resonator site $\varphi_x(t) = \langle \mathrm{GS}|\boldsymbol{a}_x|\phi(t)\rangle$ and perform the Fourier transform to calculate the transmitted field at the incoming frequency. The transmission amplitude is evaluated as $t(\omega_k) = \varphi_k(t_f)/\varphi_k^{\mathrm{free}}(t_f)$, where t_f is taken to be longer than the scattering time. We use $\varphi_k^{\mathrm{free}}(t_f)$ as a normalization factor in the transmission coefficient, which accounts for the amplitude of the propagating wave in a qubit-less waveguide.

We use this method to validate the elastic scattering mediated by the two- and three-photon bound states in Fig. 5.11 and Fig. 5.12. For the two-photon case, the scattering cannot be explained by a two-level system coupled to the bath in the USC regime. Although counter-rotating terms do not conserve the total number of excitations N_{exc}, the parity $P = (-1)^{N_{\mathrm{exc}}}$ is still a conserved quantity, which

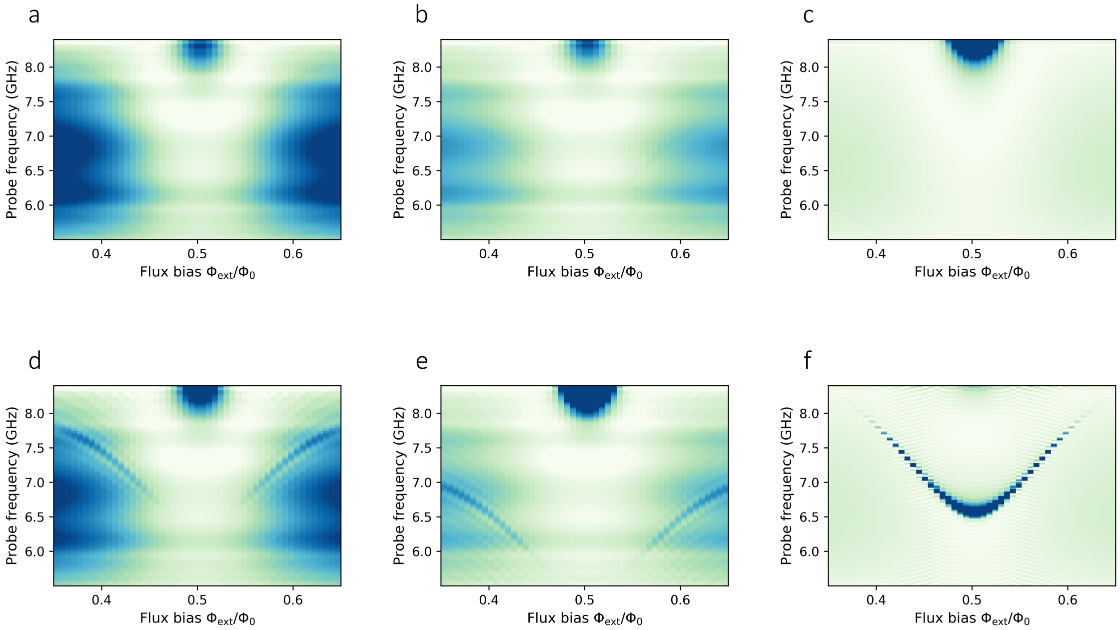

Figure 5.14: **Elastic scattering simulation.** Calculated elastic spectrum using RWA (**a**,**b**,**c**) and including counter-rotating terms (**d**,**e**,**f**) for the qubit-bath parameters describing the experimental data in Fig. 5.11 and Fig. 5.12. The resonances observed in the non-RWA simulation correspond to scattering processes involving the two and three-photon bound states entering the single-photon band.

means that with a single photon and a two-level impurity one cannot go from the single-particle sector to the two-particle sector. To break parity conservation, we include the second excited state of the fluxonium in our scattering model, which has the non-trivial selection rule $g_{02} \neq 0$. In the RWA calculation, the scattering of a flying photon from a two-photon bound state becomes a higher-order virtual process which makes the two-photon resonance very weak (Fig. 5.14a,b). As we add counter-rotating terms to the model this scattering process becomes more efficient as fewer virtual photons are needed and we can resolve more clearly the two-photon resonance as shown in Fig. 5.14d,e. Moving to the parameter regime in Fig. 5.12 we find that the transmission data can be entirely justified by the USC regime. As shown in Fig. 5.14c, the RWA scattering calculation, including a three-level fluxonium, does not show any scattering feature. Including the counter-rotating terms leads to the transmission resonance observed in Fig. 5.14f which further supports the claim that a single propagating photon is directly scattered by the localized three-photon bound state as a consequence of the counter-rotating terms in the Hamiltonian.

5.6 Inelastic scattering

In this section we measure the inelastic scattering response to further explore the nonlinear transport phenomena in the waveguide due to the strong nonlinearity of the artificial impurity. The measurements described in this section where performed at $\Phi_{\mathrm{e1}} = \Phi_0/2$ around the bias voltage $V_b \simeq 0.6\mathrm{V}$, where the qubit transition frequency lies inside the passband and the estimate normalized dipole coupling is $g/\omega_{r'} \approx 0.31$.

5.6.1 Nonlinear frequency conversion

In contrast to the elastic transmission measurement, in this experiment we are pumping the system with a single-tone drive ω_p and probing the flux of photons leaving the waveguide at different energies $\omega_{\mathrm{out}} \neq \omega_p$. This approach is similar to an analog spectrum analyzer where we measure the power of the detected microwave field $\sim \langle \boldsymbol{a}_k^\dagger \boldsymbol{a}_\omega \rangle$ at the frequency ω. Measuring optical fields is typically done by probing the field quadratures $X_\phi = \frac{1}{2}(\boldsymbol{a}e^{-i\phi} + \boldsymbol{a}^\dagger e^{i\phi})$ using homodyne schemes, instead of the photon number $\langle \boldsymbol{a}^\dagger \boldsymbol{a} \rangle$, especially if one is interested in reconstructing the full quantum state and the associated photon statistics. Homodyne detection of microwave fields is done by down-converting the signal to DC-100 MHz with a local oscillator using a microwave frequency mixer. The down-converted signals are then sampled with analog to digital converters (ADC). Since the signals coming from the device are too weak to be sampled with the homodyne setup, a linear amplifier stage becomes necessary and this adds noise which ultimately limits the detection efficiency.

We adopt the formalism in reference [169] to describe the detected microwave fields and how to extract the quantum observables and correlations. The microwave mixer splits the signal and measures the in-phase $I = X_0$ and quadrature $Q = X_{\frac{\pi}{2}}$ components. These components can be combined into a single complex field amplitude $S(t) = I(t) + iQ(t)$, where the time dependence is introduced to emphasize that we are measuring signal traces with multiple data points for averaging these stochastic signals. This complex operator can also be represented in terms of the signal and noise terms, $\hat{S}(t) = \hat{a} + \hat{h}^\dagger(t)$, where $\hat{a}(t)$ corresponds to the quantum field emitted from the waveguide. The total noise term $\hat{h}^\dagger(t) = \sqrt{\frac{G-1}{G}}\hat{h}_{\mathrm{amp}} + \sqrt{\frac{1}{G}}\hat{h}_{\mathrm{mix}}$ corresponds to the noise introduced by the phase-insensitive linear amplifier, with a gain G, and the noise from the mixing process. For large gain $G \gg 1$, the amplifier noise is dominant.

In order to extract expectation values of various moments of $\hat{a}$, we need to measure moments of both the signal $\hat{S}$ and noise $\hat{h}$ terms. For extracting the average photon power $\langle \hat{a}^\dagger \hat{a} \rangle$ we use the following relation

$$\begin{aligned}\langle \hat{S}^\dagger(t)\hat{S}(t')\rangle &= \langle(\hat{a}^\dagger(t) + \hat{h}(t)(\hat{a}(t') + \hat{h}^\dagger(t'))\rangle \\ &= \langle \hat{a}^\dagger(t)\hat{a}(t')\rangle + \langle \hat{a}^\dagger(t)\hat{h}^\dagger(t')\rangle + \langle \hat{h}(t)\hat{a}(t')\rangle + \langle \hat{h}(t)\hat{h}^\dagger(t')\rangle \\ &= \langle \hat{a}^\dagger(t)\hat{a}(t')\rangle + \langle \hat{h}(t)\hat{h}^\dagger(t')\rangle, \qquad (5.43)\end{aligned}$$

where we assumed that the signal $\hat{a}$ and noise $\hat{h}$ are uncorrelated at equal and different times and that the noise has zero mean $\langle \hat{h}(t)\rangle = 0$. From this relation it becomes clear than in order to detect $\langle \hat{a}^\dagger \hat{a}\rangle$, we simply measure the signal power $\langle \hat{S}^\dagger \hat{S}\rangle = \langle I^2(t) + Q^2(t)\rangle$ and subtract the noise power $\langle \hat{h}^\dagger \hat{h}\rangle$. The noise term is determined by measuring $\langle \hat{S}^\dagger \hat{S}\rangle$ when the waveguide is not driven with the pump tone.

The power spectrum $\langle \hat{a}^\dagger_\omega \hat{a}_\omega\rangle$ is measured in this homodyne scheme by sweeping the local oscillator frequency around the single-photon band. We pump the waveguide at

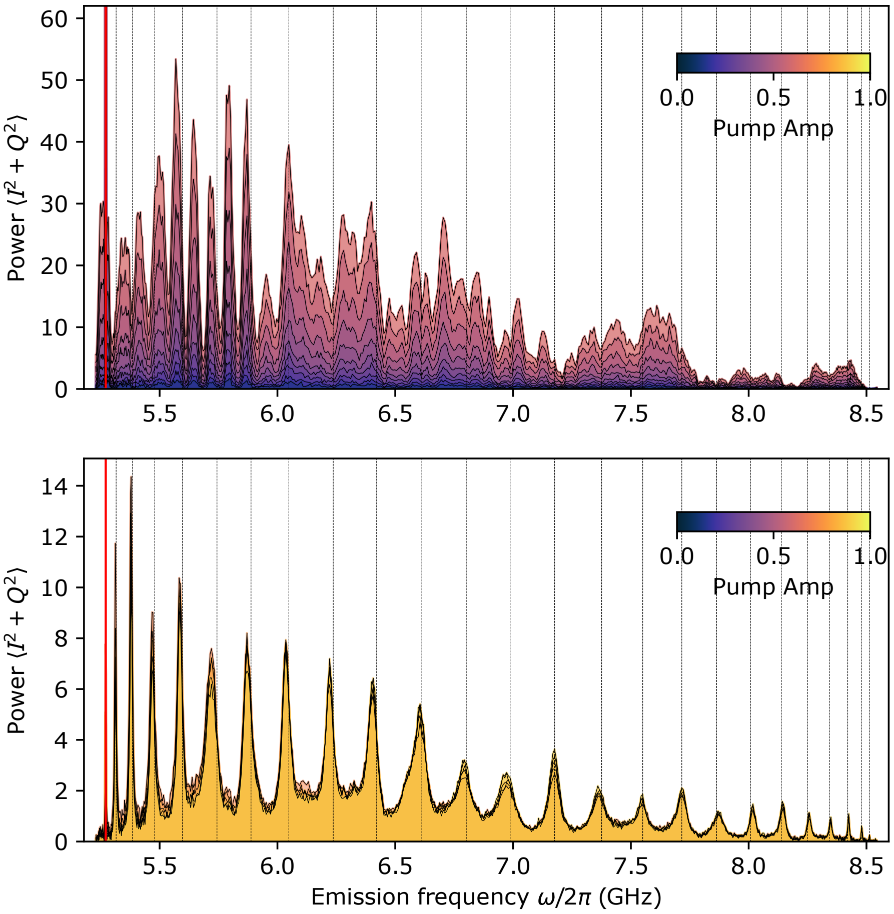

Figure 5.15: **Inelastic multi-mode emission.** Power spectrum in the waveguide pass band when driving the photonic crystal at the band-edge mode (vertical red line). Dotted vertical lines correspond to the eigenmode peak frequencies from the low power transmission spectrum.

each eigenmode frequency with a drive amplitude stronger than the one used in the elastic transmission measurements in order to witness inelastic emission above the noise floor. Although we do not have a direct measure of average photon number, we can qualitatively assume that we are injecting more than a single drive photon. The external pump is provided with a microwave source generating a fixed output power that is amplitude-modulated as a square pulse with an arbitrary waveform generator (AWG). This allows us to vary the pump amplitude by changing the envelope of the AWG pulse from 0 to 1, in normalized units. As we seep the pump amplitude and monitor the power spectrum, we observe that driving eigenmodes closer to the

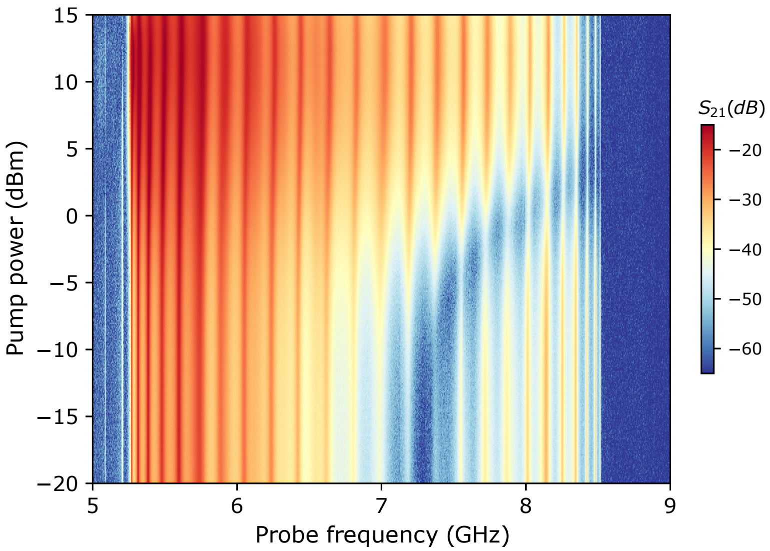

Figure 5.16: **Pump and probe response.** Transmission amplitude measured with a weak probe field, as a function of drive power for a pump tone fixed at the eigenmode frequency 5.271 GHz.

lower band-edge stimulates significant inelastic emission over the entire pass-band. In Fig. 5.15 we plot the power spectrum over the single-photon band, for a pump drive with a frequency fixed at the lowest band-edge mode $\omega_p/2\pi = 5.271\,\text{GHz}$, where two distinct emission regimes are identified. For drive amplitudes up to a critical value (0.6 in normalized AWG units) the inelastic spectrum displays a broad emission profile with resonances which are almost equally spaced in frequency and which do not match the eigenmode dispersion of the chain. The power spectrum increases with drive amplitude while maintaining the same frequency structure. Above the critical drive amplitude we witness a sharp decrease in the overall emission amplitude and the spectrum is now reduced to 25 resonances which approximately match the eigenmode frequencies in the band.

To gain some intuition over the critical drive amplitude that drastically changes the inelastic emission properties, we perform the following pump-probe measurement to inspect the properties of the qubit. We measure transmission through the cavity chain using a weak probe tone. This yields the elastic spectrum shown in Fig. 5.9b, with a reduction in the transmitted amplitude near the fluxon transition resonance. Using the same pump tone applied in the inelastic measurement, we investigate how the weak-probe transmission profile changes with respect to the pump amplitude. The drive amplitude is changed by varying the output power of the pump generator. The outcome of the measurement is shown in Fig. 5.16. Qualitatively, we observe that the depth of the qubit resonance decreases with increasing drive power which suggests the qubit nonlinearity gets saturated by drive photons. Additionally, the qubit resonance becomes blueshifted as the drive power is further increased. The key observation is that the drive power at which the the qubit resonance is completely detuned outside the passband corresponds to the critical drive amplitude in the inelastic measurement. This suggests that the contrast in the two distinct inelastic emission regimes can be explained by a diminishing qubit nonlinearity.

5.6.2 Correlated emission

This multi-mode circuit offers a novel regime of light-matter interaction, where the qubit is simultaneously coupled to multiple modes in the photonic crystal and the total number of excitations is not conserved. This regime has been theoretically predicted to lead to multi-mode entanglement [147] for an Ohmic bath with a continuous spectrum. It would be interesting to test this prediction using the nonlinear frequency conversion process under consideration. We observe how pumping photons in one eigenmode generates photons at other modes and we want to investigate if these emitted photons are strongly correlated.

To characterize the entanglement properties of the created multi-mode state we rely on established entanglement conditions for two-mode states [170, 171]. Let us consider two harmonic modes with creation (annihilation) operators set by $\boldsymbol{a}^\dagger$ and $\boldsymbol{b}^\dagger$ ($\boldsymbol{a}$ and $\boldsymbol{b}$). A pure product state satisfies the relation $|\langle \boldsymbol{ab}\rangle| = |\langle \boldsymbol{a}\rangle\langle \boldsymbol{b}\rangle|$, and

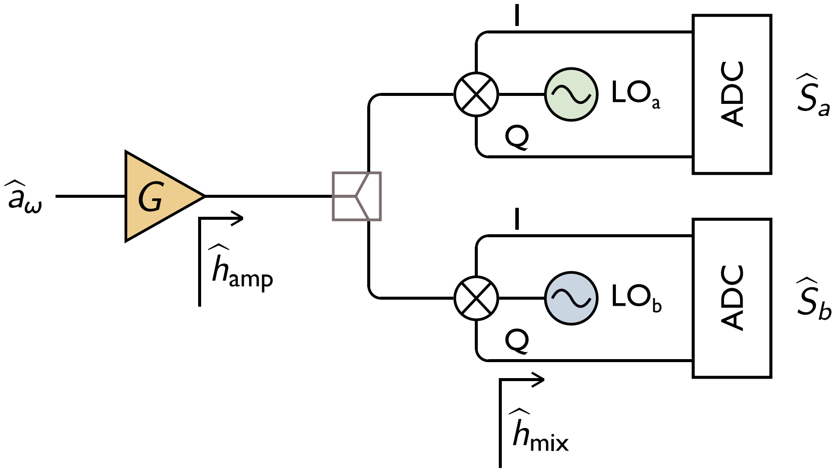

Figure 5.17: **Two-mode correlation measurement.** Homodyne chain for measuring equal-time correlations in the field emission for distinct modes.

applying the Cauchy-Schwarz inequality on the left hand side implies that $|\langle \boldsymbol{a}\boldsymbol{b}\rangle| \leq \left[\langle \boldsymbol{a}^\dagger \boldsymbol{a}\rangle\langle \boldsymbol{b}^\dagger \boldsymbol{b}\rangle\right]^{1/2}$. It was shown by Hillery and Zubairy [170] that this inequality holds for any separable state, expressed as a density matrix for a mixture of pure product states. Therefore, a violation of this inequality implies that the two-mode state is entangled. This is, of course, a necessary but not sufficient condition since there exist two-mode entangled states that satisfy this inequality, for example $|0_a 1_b\rangle + |1_a 0_b\rangle$. Using this metric, we proceed with measuring the following field correlations

$$\mathcal{C}_{ij}^{(2)} = \frac{|\langle \boldsymbol{a}_i \boldsymbol{a}_j\rangle|^2}{\langle \boldsymbol{a}_i^\dagger \boldsymbol{a}_i\rangle\langle \boldsymbol{a}_j^\dagger \boldsymbol{a}_j\rangle}, \tag{5.44}$$

for the simultaneous emission of photons at eigenmode frequencies ω_i and ω_j, normalized by the field intensity at each mode. A measurement outcome that satisfies $\mathcal{C}_{ij}^{(2)} > 1$ implies that the reduced two-mode state, after tracing out the other modes of the bath, is entangled. This is a relatively straightforward entanglement witness to measure. This measurement is performed by splitting the waveguide output signal into two branches with a separate homodyne setup. Each branch has a separate local oscillator set to the eigenmode frequencies ω_i and ω_j, and similarly we record

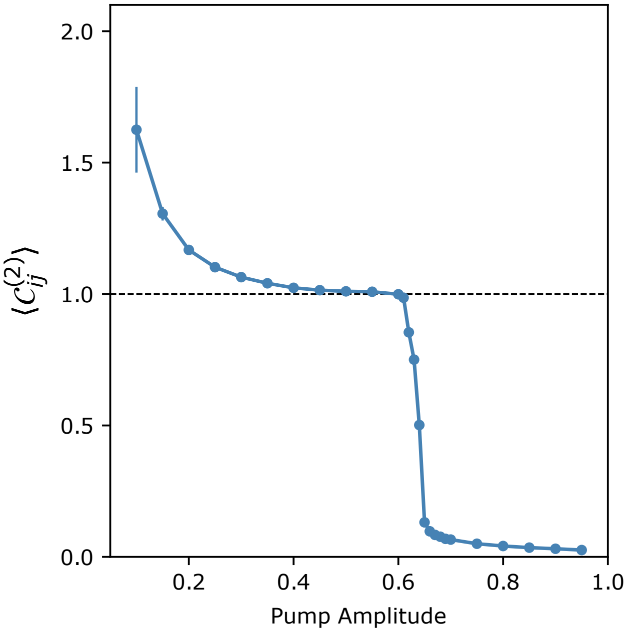

Figure 5.18: **Two-mode entanglement metric.** Averaged correlator $\mathcal{C}_{ij}^{(2)}$ over waveguide eigenmodes i, j. Error bars represent one standard deviation

time domain traces of the complex field at each mode $\hat{S}_{i,j}(t) = \hat{a}_{i,j}(t) + \hat{h}_{i,j}^{\dagger}(t)$. The measurement setup is displayed in Fig. 5.17. We already mentioned how to measure photon intensity and in a similar fashion we can calculate the field correlators from

$$\langle \hat{S}_i(t)\hat{S}_j(t')\rangle = \langle \hat{a}_i(t)\hat{a}_j(t')\rangle + \langle \hat{h}_i^{\dagger}(t)\hat{h}_j^{\dagger}(t')\rangle. \tag{5.45}$$

We find that noise correlators are much smaller than the noise power given that noise fields at different frequencies are typically uncorrelated. Nevertheless, $\langle \hat{h}_i^{\dagger}(t)\hat{h}_j^{\dagger}(t')\rangle$ cannot be completely ignored given that both homodyne branches use sampling channels on the same ADC board which can lead to nonzero coupling of the measured transient DC signals. Both $\langle \hat{S}_i(t)\hat{S}_j(t')\rangle$ and $\langle \hat{S}_i^{\dagger}(t)\hat{S}_i(t')\rangle$ are measured at equal time $t = t'$ for evaluating the ratio in Eq. 5.44.

The entanglement witness $\mathcal{C}_{ij}^{(2)}$ is measured for all the possible two-mode combinations (i, j) for eigenmodes that show considerable inelastic emission above the noise floor. We record the correlators as we sweep the drive amplitude for the same pump frequency at the band-edge mode $\omega_p/2\pi = 5.271\text{GHz}$. Because we find that the values and drive-dependence of $\mathcal{C}_{ij}^{(2)}$ are uniform across the two-mode map, we plot in Fig. 5.18 the average correlator across all the modes $\langle \mathcal{C}^{(2)} \rangle = \sum_{i,j} \mathcal{C}_{ij}^{(2)}$ as a function of the drive amplitude. For low drive amplitudes we find average values $\langle \mathcal{C}^{(2)} \rangle > 1$, which suggests that this nonlinear inelastic scattering process creates entangled pairs of photons at different frequencies, over the full bandwidth of the waveguide. The correlator $\langle \mathcal{C}^{(2)} \rangle$ asymptotically reaches 1 as the drive amplitude is increased. As the drive amplitude is increased above the critical value, discussed in the previous section, $\langle \mathcal{C}^{(2)} \rangle$ drops sharply to small values between 10^{-1} and 10^{-2}. The drive-dependence on the entanglement witness suggests that although the number of emitted photons increases with the drive amplitude, the strong drive can saturate the qubit to the point where the nonlinearity per photon is diminished and the generated multi-mode state becomes less likely to be entangled.

5.7 Summary

This work provides the first demonstration of ultrastrong light-matter coupling between a fluxonium qubit and a photonic crystal waveguide. Despite having only a single nonlinear element, this platform is suitable for exploring many-body physics with photons by focusing on the nontrivial dynamics of the multi-mode states of the environment. We found the propagation of a single photon in the waveguide to go beyond the single particle picture as multi-photon bound states participate in the scattering dynamics. Furthermore, the effective photon-photon interactions mediated by the qubit nonlinearity stimulates multimode wave mixing processes, as inferred from the observed inelastic emission of entangled pairs of photons.

Chapter 6

Conclusion

In this thesis, I have presented a series of experiments and theoretical developments aimed at studying quantum states of strongly interacting photons using the circuit QED toolbox. The physical systems under investigation are large scale lattices of superconducting circuits probed in the non-equilibrium regime, where particles are coherently injected into the lattice to compensate for dissipation. As part of the growing effort of studying many-body physics with photons, this dissertation is focused primarily on establishing new ways of mediating photon interactions and developing circuit platforms with many degrees of freedom, that are unique from previous large scale cQED systems owing to their reduced complexity in hardware and control.

In Chapter 3 we introduced this very simple idea of designing nonlinearity in a harmonic oscillator by hybridizing its two-photon state that would blockade photons from leaking out of the single-excitation sector. This idea was demonstrated experimentally with two microwave resonators and a Josephson coupling element that induced an effective three-wave mixing process through parametric flux driving. This work was initially dedicated to engineering qubits from microwave resonators, which have shown great potential in reaching long photon storage times. Nevertheless, we later realized this blockade nonlinearity imposes an energy penalty for adding an additional photon into the resonator, similar to the Jaynes Cummings nonlinearity, and therefore mediates interactions among photons entering this cavity.

In Chapter 4, we extend this dynamical nonlinearity beyond a single resonator and use it as a resource for stimulating photon interactions in a lattice of harmonic modes. The special feature in this platform is that this lattice is defined in synthetic dimensions, where each site corresponds to one of the orthogonal momentum states of a resonator chain, and that the interactions and photon hopping between each node can be individually controlled with parametric drives applied to a single Josephson circuit. Given the simplicity of this circuit, we were excited to discover that this type of nonlinear lattice can sustain strongly correlated photons entering a crystalline phase in the hard-core interaction regime.

The most common path to developing many-body quantum optical systems is centered around lattices of strongly nonlinear cavities. In Chapter 5 we approach this problem from a different perspective, by coupling a single well-controlled quantum impurity to a harmonic environment with many degrees of freedom, a photonic crystal waveguide. This quantum impurity is implemented using a highly nonlinear Josephson qubit where the coupling strength to the environment goes beyond the single photon regime, into the so called ultrastrong coupling regime. In this regime it is known that counter-rotating terms play an important role, and in our system we found that the propagation of a single photon becomes a many-body problem as multi-photon bound states participate in the scattering dynamics. Additionally, the effective photon interactions induced by just this single impurity leads to interesting inelastic emission of photons. Probing the correlations in the emitted fields, we found that pairs of emitted photons are entangled which is quite an impressive feature for yet another simple lattice simulator which can be easily scaled to many more degrees of freedom, and can be easily probed and controlled as it involves only a single nonlinear circuit element.

Hopefully the work demonstrated in the nonlinear synthetic lattices and quantum impurity projects paves the way to many more interesting experiments aimed at building quantum materials from large scale cQED systems.

6.1 Future work

6.1.1 3D resonator qubit architecture

The work presented in Chapter 3 can be extended to 3D microwave resonators, as outlined in the theoretical proposal in section 3.7. This would allow us to harness the improved photon lifetimes ($\sim 1 - 10$ ms) demonstrated with carefully engineered 3D resonators. Furthermore, the fluxonium circuit used for stimulating the nonlinearity can be shared with additional resonator modes, similar to the setup in [84] applied in 3D, and two qubit gates (iSWAP) can be achieved by simply modulating the coupler circuit at the mode frequency detuning [91]. This presents a hardware efficient platform for implementing qubits and allowing arbitrary all-to-all two qubit gates.

6.1.2 Nonlinear lattices with synthetic gauge fields

Given the exciting theoretical developments in Chapter 4, the first short term goal would to implement this experiment for a one dimensional chain of nearest coupled eigenmodes. When driving all momentum sites equally strong, The transition to a crystalline phase can be probed with standard quantum optical techniques for measuring second order intensity correlations with linear detectors. Furthermore, as mentioned in the conclusion section of Chapter 4, the dynamical hopping between sites can be organized in a two dimensional square lattice grid, where additional complex phases can be controlled to introduce an artificial magnetic field for photons. With the insertion of on-site blockade induced interactions it would interesting to investigate, even theoretically, if this system gives rise to quantum Hall states of light. In the case of Bose-Hubbard type of interactions this is know to be case, which begs the question if these type of contact interactions can also be dynamically stimulated in a synthetic lattice model.

6.1.3 Frustration of decoherence: coupling the impurity to two baths

One interesting extension to the experiment presented in Chapter 5 is to consider a generalized impurity model where the artificial two level system is coupled to two or more bosonic environments with the prospect of studying the competition between these dissipative channels which could lead to tailoring the qubit coherence through bath engineering. This idea has already been theoretically investigated in the so called two-bath spin-boson model, where the two baths are dipole coupled to two orthogonal spin components of the two-level system, σ_x and σ_y. When these two couplings are equal, the baths are competing against each other in screening the qubit. Since σ_x and σ_y do not commute, there is no common eigenbasis for the spin to localize in, which leads to a *frustration of decoherence* [172, 173, 174]. Furthermore, given the observation of two-mode entanglement, it would interesting to measure correlations of photons emitted from separate waveguides coupled to the qubit and perform similar entanglement tests. This could potentially promote this multi-channel impurity system as router for entangled photons,

Appendix A

Quantum treatment of parametrically coupled circuits

A.1 Galvanically coupled resonators

In this section we outline the full derivation of the effective Hamiltonian of the circuit shown in Fig. 3.2a in the main text. Our system consists of two lumped-element resonators composed of linear inductors $L_{a,b}$ and capacitors $C_{a,b}$, which are coupled through a Josephson junction with a critical current I_c. An externally applied magnetic flux Φ_{ext} through the circuit loop is used to tune the effective interaction energy between the two modes. Following standard circuit quantization techniques [56], we can write down the Lagrangian of our device

$$\begin{aligned}\boldsymbol{\mathcal{L}} = &\left(\frac{\Phi_0}{2\pi}\right)^2 \left[\frac{C_a}{2}\dot{\boldsymbol{\varphi}}_a^2 + \frac{C_b}{2}\dot{\boldsymbol{\varphi}}_b^2 + \frac{C_J}{2}\left(\dot{\boldsymbol{\varphi}}_a - \dot{\boldsymbol{\varphi}}_b + \dot{\varphi}_{\text{ext}}\right)^2\right] \\ &- \left(\frac{\Phi_0}{2\pi}\right)^2 \left[\frac{\boldsymbol{\varphi}_a^2}{2L_a} + \frac{\boldsymbol{\varphi}_b^2}{2L_b} - \frac{1}{L_J}\cos(\boldsymbol{\varphi}_a - \boldsymbol{\varphi}_b + \varphi_{\text{ext}})\right], \end{aligned} \tag{A.1}$$

with $\varphi_{\text{ext}} = 2\pi\Phi_{\text{ext}}/\Phi_0$. Taking $\boldsymbol{n}_k = \partial\boldsymbol{\mathcal{L}}/\partial\dot{\boldsymbol{\varphi}}_k$, the corresponding Hamiltonian reads

$$\begin{aligned}\mathbf{H} = &\sum_{k=a,b}\left(4E_{Ck}\boldsymbol{n}_k^2 + E_{Lk}\boldsymbol{\varphi}_k^2\right) + 8E_{Cc}\boldsymbol{n}_a\boldsymbol{n}_b - \hbar\frac{C_b}{C_c}\dot{\varphi}_{\text{ext}}\boldsymbol{n}_a + \hbar\frac{C_a}{C_c}\dot{\varphi}_{\text{ext}}\boldsymbol{n}_b \\ &- E_J\cos\left(\boldsymbol{\varphi}_a - \boldsymbol{\varphi}_b + \varphi_{\text{ext}}\right),\end{aligned} \tag{A.2}$$

where we have defined the charging energy $E_{Ck} = e^2/2C'_k$, inductive energy $E_{Lk} = \left(\Phi_0/2\pi\right)^2/2L_k$ and Josephson energy $E_J = \left(\Phi_0/2\pi\right)^2/L_J$, with $L_J = 2\pi I_c/\Phi_0$. The effective capacitances are determined as $C'_a = C_d^2/(C_b + C_J)$, $C'_b = C_d^2/(C_a + C_J)$, and $C_c = C_d^2/C_J$ with $C_d^2 = C_J(C_a + C_b) + C_aC_b$. The Hamiltonian presented in the above equation (A.2) was used during fitting in order to characterize the circuit parameters of the device, as well as in noise estimation calculations. In both of those cases, the external flux was assumed to be static (i.e. $\dot{\varphi}_{\text{ext}} \to 0$).

During the experiment, the flux through the circuit loop was modulated around the $\varphi_{\text{ext}} = 0$, such that $\varphi_{\text{ext}} = \epsilon\cos\omega_p t$, with $\epsilon = 2\pi\delta/\Phi_0$ and $\epsilon/2\pi \sim 0.1$. It is worth noting that for the static bias $\varphi_{\text{ext}} = 0$, the inductive potential minimum is centered at $\overline{\boldsymbol{\varphi}}_a = \overline{\boldsymbol{\varphi}}_b = 0$. Hence, in the parameter regime of $L_{a,b} < L_J$, we can expand the cosine term in the potential energy of equation (A.2) as

$$\cos(\boldsymbol{\varphi}_{ab} + \varphi_{\text{ext}}) \approx \left(1 - \frac{\boldsymbol{\varphi}_{ab}^2}{2!} + \frac{\boldsymbol{\varphi}_{ab}^4}{4!}\right)\cos\varphi_{\text{ext}} - \left(\boldsymbol{\varphi}_{ab} - \frac{\boldsymbol{\varphi}_{ab}^3}{3!}\right)\sin\varphi_{\text{ext}} + \mathcal{O}(\boldsymbol{\varphi}_{ab}^5), \tag{A.3}$$

where, for convenience, we define $\boldsymbol{\varphi}_{ab} = \boldsymbol{\varphi}_a - \boldsymbol{\varphi}_b$. Using Jacobi-Anger expansion, we further expand the above cosine and sine functions as

$$\begin{aligned}\sin\varphi_{\text{ext}} &= -2\sum_{n=1}^{\infty}(-1)^n J_{2n-1}(\epsilon)\cos[(2n-1)\omega_p t], \\ \cos\varphi_{\text{ext}} &= J_0(\epsilon) + 2\sum_{n=1}^{\infty}(-1)^n J_{2n}(\epsilon)\cos(2n\omega_p t).\end{aligned} \tag{A.4}$$

Due to the relatively small modulation strength ϵ, we truncate the Jacobi-Anger expansion to the lowest few orders, and finally arrive at the expression

$$\begin{aligned}\cos(\boldsymbol{\varphi}_{ab} + \varphi_{\text{ext}}) \approx& \left(1 - \frac{\boldsymbol{\varphi}_{ab}^2}{2!} + \frac{\boldsymbol{\varphi}_{ab}^4}{4!}\right)\left[J_0(\epsilon) - 2J_2(\epsilon)\cos(2\omega_p t)\right] \\ &- \left(\boldsymbol{\varphi}_{ab} - \frac{\boldsymbol{\varphi}_{ab}^3}{3!}\right)\left[2J_1(\epsilon)\cos\omega_p t\right]. \end{aligned} \tag{A.5}$$

Inserting this expression into Eq. (A.2), the dynamical Hamiltonian is now given by

$$\begin{aligned}\mathbf{H} \approx& \,\omega_a \boldsymbol{a}^\dagger \boldsymbol{a} + \omega_b \boldsymbol{b}^\dagger \boldsymbol{b} - 8E_{Cc} n_a^{\text{zpf}} n_b^{\text{zpf}} (\boldsymbol{a}^\dagger - \boldsymbol{a})(\boldsymbol{b}^\dagger - \boldsymbol{b}) \\ &+ i\hbar\epsilon\omega_p \sin\omega_p t \left[\frac{C_b}{C_c} n_a^{\text{zpf}}(\boldsymbol{a}^\dagger - \boldsymbol{a}) - \frac{C_a}{C_c} n_b^{\text{zpf}}(\boldsymbol{b}^\dagger - \boldsymbol{b})\right] \\ &+ E_J \left[2J_1(\epsilon)\cos\omega_p t\right]\left[\varphi_a^{\text{zpf}}(\boldsymbol{a}^\dagger + \boldsymbol{a}) - \varphi_b^{\text{zpf}}(\boldsymbol{b}^\dagger + \boldsymbol{b})\right] \\ &+ \frac{E_J}{2}\left[J_0(\epsilon) - 2J_2(\epsilon)\cos(2\omega_p t)\right]\left[\varphi_a^{\text{zpf}}(\boldsymbol{a}^\dagger + \boldsymbol{a}) - \varphi_b^{\text{zpf}}(\boldsymbol{b}^\dagger + \boldsymbol{b})\right]^2 \\ &- \frac{E_J}{6}\left[2J_1(\epsilon)\cos\omega_p t\right]\left[\varphi_a^{\text{zpf}}(\boldsymbol{a}^\dagger + \boldsymbol{a}) - \varphi_b^{\text{zpf}}(\boldsymbol{b}^\dagger + \boldsymbol{b})\right]^3 \\ &- \frac{E_J}{24}\left[J_0(\epsilon) - 2J_2(\epsilon)\cos(2\omega_p t)\right]\left[\varphi_a^{\text{zpf}}(\boldsymbol{a}^\dagger + \boldsymbol{a}) - \varphi_b^{\text{zpf}}(\boldsymbol{b}^\dagger + \boldsymbol{b})\right]^4, \end{aligned} \tag{A.6}$$

where we redefine $\varphi_k^{\text{zpf}} = \frac{1}{\sqrt{2}}\left(\frac{4E_{Ck}}{E_{Lk}}\right)^{1/4}$, $n_k^{\text{zpf}} = \frac{1}{\sqrt{2}}\left(\frac{E_{Lk}}{4E_{Ck}}\right)^{1/4}$, $\varphi_k = \varphi_k^{\text{zpf}}\left(\boldsymbol{k}^\dagger + \boldsymbol{k}\right)$ and $n_k = in_k^{\text{zpf}}\left(\boldsymbol{k}^\dagger - \boldsymbol{k}\right)$.

In order to simplify the above Hamiltonian, we first transform-away the the linear "drive"-like terms in the second and third lines. It can be easily verified that the charge "drive" terms in the second line are orders of magnitude smaller than not only those in the third line, but also other relevant terms in equation (A.6), and therefore can be neglected. The terms in the third line can be eliminated by a time-dependent displacement transformation, defined by the unitary operator

$$\boldsymbol{D}(t) = \exp[-\alpha\boldsymbol{a}^\dagger + \alpha^*\boldsymbol{a} - \beta\boldsymbol{b}^\dagger + \beta^*\boldsymbol{b}], \tag{A.7}$$

where $\alpha(t)$ and $\beta(t)$ are given by

$$\begin{aligned}\alpha(t) &= \frac{E_J J_1(\epsilon)\varphi_a^{\text{zpf}}}{\omega_p - \omega_a}\exp(-i\omega_p t) + \frac{E_J J_1(\epsilon)\varphi_a^{\text{zpf}}}{-\omega_p - \omega_a}\exp(i\omega_p t),\\ \beta(t) &= -\frac{E_J J_1(\epsilon)\varphi_b^{\text{zpf}}}{\omega_p - \omega_b}\exp(-i\omega_p t) - \frac{E_J J_1(\epsilon)\varphi_b^{\text{zpf}}}{-\omega_p - \omega_b}\exp(i\omega_p t).\end{aligned} \tag{A.8}$$

The annihilation operators are transformed to

$$\boldsymbol{D}(t)\boldsymbol{a}\boldsymbol{D}^\dagger(t) = \boldsymbol{a} + \alpha(t), \quad \boldsymbol{D}(t)\boldsymbol{b}\boldsymbol{D}^\dagger(t) = \boldsymbol{b} + \beta(t). \tag{A.9}$$

Under this transformation, the third line in equation (A.6) vanishes, while the bilinear coupling terms in the first line will give rise to some much smaller corrections, which can be eliminated by adding higher-order terms in equation (A.8). Other coefficients in equation (A.6), including ω_a and ω_b, will be weakly shifted after the displacement transformation, which we find unnecessary to keep track of considering their magnitude. The transformed Hamiltonian then becomes

$$\begin{aligned}\widetilde{\mathbf{H}}_{\mathbf{1}} \approx\, & \boldsymbol{D}(t)\mathbf{H}\boldsymbol{D}^\dagger(t) + i\dot{\boldsymbol{D}}\boldsymbol{D}^\dagger\\ &\approx \omega_a\boldsymbol{a}^\dagger\boldsymbol{a} + \omega_b\boldsymbol{b}^\dagger\boldsymbol{b} - 8E_{Cc}n_a^{\text{zpf}}n_b^{\text{zpf}}(\boldsymbol{a}^\dagger - \boldsymbol{a})(\boldsymbol{b}^\dagger - \boldsymbol{b})\\ &\quad + \frac{E_J}{2}\left[J_0(\epsilon) - 2J_2(\epsilon)\cos(2\omega_p t)\right]\left[\varphi_a^{\text{zpf}}(\boldsymbol{a}^\dagger + \boldsymbol{a}) - \varphi_b^{\text{zpf}}(\boldsymbol{b}^\dagger + \boldsymbol{b})\right]^2\\ &\quad - \frac{E_J}{6}\left[2J_1(\epsilon)\cos\omega_p t\right]\left[\varphi_a^{\text{zpf}}(\boldsymbol{a}^\dagger + \boldsymbol{a}) - \varphi_b^{\text{zpf}}(\boldsymbol{b}^\dagger + \boldsymbol{b})\right]^3\\ &\quad - \frac{E_J}{24}\left[J_0(\epsilon) - 2J_2(\epsilon)\cos(2\omega_p t)\right]\left[\varphi_a^{\text{zpf}}(\boldsymbol{a}^\dagger + \boldsymbol{a}) - \varphi_b^{\text{zpf}}(\boldsymbol{b}^\dagger + \boldsymbol{b})\right]^4.\end{aligned} \tag{A.10}$$

Neglecting small and off-resonant terms, we simplify it further to

$$\begin{aligned}\widetilde{\boldsymbol{\mathcal{H}}}_{\mathbf{1}} =\, & \omega_a'\boldsymbol{a}^\dagger\boldsymbol{a} + \omega_b'\boldsymbol{b}^\dagger\boldsymbol{b} + g_\varphi\left(\boldsymbol{a}^\dagger + \boldsymbol{a}\right)\left(\boldsymbol{b}^\dagger + \boldsymbol{b}\right) + g_n\left(\boldsymbol{a}^\dagger - \boldsymbol{a}\right)\left(\boldsymbol{b}^\dagger - \boldsymbol{b}\right) \qquad \text{(A.11)}\\ & + g_2\left(\boldsymbol{a}^{\dagger 2}\boldsymbol{b} + \boldsymbol{a}^2\boldsymbol{b}^\dagger\right) + \frac{\chi_{aa}}{2}\boldsymbol{a}^{\dagger 2}\boldsymbol{a}^2 + \frac{\chi_{bb}}{2}\boldsymbol{b}^{\dagger 2}\boldsymbol{b}^2 + \chi_{ab}\boldsymbol{a}^\dagger\boldsymbol{a}\boldsymbol{b}^\dagger\boldsymbol{b},\end{aligned}$$

where the coefficients are given by

$$\begin{aligned}
\omega_a' &= \omega_a + E_J J_0(\epsilon)(\varphi_a^{\text{zpf}})^2 + \chi_{aa} + \frac{\chi_{ab}}{2}, \\
\omega_b' &= \omega_b + E_J J_0(\epsilon)(\varphi_b^{\text{zpf}})^2 + \chi_{bb} + \frac{\chi_{ab}}{2}, \\
g_\varphi &= -E_J[J_0(\epsilon) - 2J_2(\epsilon)\cos(2\omega_p t)]\varphi_a^{\text{zpf}}\varphi_b^{\text{zpf}}, \\
g_n &= -8E_{Cc} n_a^{\text{zpf}} n_b^{\text{zpf}}, \\
g_2 &= E_J J_1(\epsilon)\cos\omega_p t(\varphi_a^{\text{zpf}})^2\varphi_b^{\text{zpf}}, \\
\chi_{aa} &= -\frac{E_J}{2}[J_0(\epsilon) - 2J_2(\epsilon)\cos(2\omega_p t)](\varphi_a^{\text{zpf}})^4, \\
\chi_{bb} &= -\frac{E_J}{2}[J_0(\epsilon) - 2J_2(\epsilon)\cos(2\omega_p t)](\varphi_b^{\text{zpf}})^4, \\
\chi_{ab} &= -E_J[J_0(\epsilon) - 2J_2(\epsilon)\cos(2\omega_p t)](\varphi_a^{\text{zpf}})^2(\varphi_b^{\text{zpf}})^2.
\end{aligned} \tag{A.12}$$

The Hamiltonian derived in equation (A.11) arrives at the same model presented in the main text. In order to simplify equation (A.11) further, we perform a Schrieffer-Wolff transformation to eliminate the bilinear coupling terms in the first line of equation (A.11). For simplicity, we denote $g_2 = g_{\varphi 0} + 2g_{\varphi 2}\cos(2\omega_p t)$, where $g_{\varphi 0} = -E_J J_0(\epsilon)\varphi_a^{\text{zpf}}\varphi_b^{\text{zpf}}$ and $g_{\varphi 2} = E_J(\epsilon)J_2(\epsilon)\varphi_a^{\text{zpf}}\varphi_b^{\text{zpf}}$, and define the unitary transformation

$$\boldsymbol{T} = \exp \boldsymbol{S}, \tag{A.13}$$

$$\begin{aligned}
\boldsymbol{S} = \frac{g_{\varphi 0} - g_n}{\omega_a' - \omega_b'}\boldsymbol{a}^\dagger\boldsymbol{b} - \frac{g_{\varphi 0} - g_n}{\omega_a' - \omega_b'}\boldsymbol{a}\boldsymbol{b}^\dagger + \frac{g_{\varphi 0} + g_n}{\omega_a' + \omega_b'}\boldsymbol{a}^\dagger\boldsymbol{b}^\dagger - \frac{g_{\varphi 0} + g_n}{\omega_a' + \omega_b'}\boldsymbol{a}\boldsymbol{b} \\
- \frac{g_{\varphi 2}\exp(2i\omega_p t)}{\omega_b' - \omega_a' - 2\omega_p}\boldsymbol{a}^\dagger\boldsymbol{b} + \frac{g_{\varphi 2}\exp(-2i\omega_p t)}{\omega_b' - \omega_a' - 2\omega_p}\boldsymbol{a}\boldsymbol{b}^\dagger \\
- \frac{g_{\varphi 2}\exp(-2i\omega_p t)}{\omega_b' - \omega_a' + 2\omega_p}\boldsymbol{a}^\dagger\boldsymbol{b} + \frac{g_{\varphi 2}\exp(2i\omega_p t)}{\omega_b' - \omega_a' + 2\omega_p}\boldsymbol{a}\boldsymbol{b}^\dagger \\
+ \frac{g_{\varphi 2}\exp(2i\omega_p t)}{\omega_b' + \omega_a' + 2\omega_p}\boldsymbol{a}^\dagger\boldsymbol{b}^\dagger - \frac{g_{\varphi 2}\exp(-2i\omega_p t)}{\omega_b' + \omega_a' + 2\omega_p}\boldsymbol{a}\boldsymbol{b} \\
+ \frac{g_{\varphi 2}\exp(-2i\omega_p t)}{\omega_b' + \omega_a' - 2\omega_p}\boldsymbol{a}^\dagger\boldsymbol{b}^\dagger - \frac{g_{\varphi 2}\exp(2i\omega_p t)}{\omega_b' + \omega_a' - 2\omega_p}\boldsymbol{a}\boldsymbol{b}.
\end{aligned} \tag{A.14}$$

Up to the second order in $g_{\varphi 0}$, g_n and $g_{\varphi 2}$, the transformed Hamiltonian becomes

$$\begin{aligned}\widetilde{\mathbf{H}}_{\mathbf{2}} =& \boldsymbol{T}\widetilde{\mathbf{H}}_{\mathbf{1}}\boldsymbol{T}^{\dagger} + i\dot{\boldsymbol{T}}\boldsymbol{T}^{\dagger} \\ \approx& \omega_a''\boldsymbol{a}^{\dagger}\boldsymbol{a} + \omega_b''\boldsymbol{b}^{\dagger}\boldsymbol{b} + g_2\left(\boldsymbol{a}^{\dagger 2}\boldsymbol{b} + \boldsymbol{a}^2\boldsymbol{b}^{\dagger}\right) + \frac{\chi_{aa}}{2}\boldsymbol{a}^{\dagger 2}\boldsymbol{a}^2 + \frac{\chi_{bb}}{2}\boldsymbol{b}^{\dagger 2}\boldsymbol{b}^2 + \chi_{ab}\boldsymbol{a}^{\dagger}\boldsymbol{a}\boldsymbol{b}^{\dagger}\boldsymbol{b},\end{aligned} \tag{A.15}$$

where the modified frequencies are

$$\begin{aligned}\omega_a'' \approx& \omega_a' - \frac{(g_{\varphi 0} - g_n)^2}{\omega_b' - \omega_a'} - \frac{(g_{\varphi 0} + g_n)^2}{\omega_b' + \omega_a'} - \frac{g_{\varphi 2}^2}{\omega_b' - \omega_a' + 2\omega_p} \\ &- \frac{g_{\varphi 2}^2}{\omega_b' - \omega_a' - 2\omega_p} - \frac{g_{\varphi 2}^2}{\omega_b' + \omega_a' + 2\omega_p} - \frac{g_{\varphi 2}^2}{\omega_b' + \omega_a' - 2\omega_p}, \\ \omega_b'' \approx& \omega_b' + \frac{(g_{\varphi 0} - g_n)^2}{\omega_b' - \omega_a'} - \frac{(g_{\varphi 0} + g_n)^2}{\omega_b' + \omega_a'} + \frac{g_{\varphi 2}^2}{\omega_b' - \omega_a' + 2\omega_p} \\ &+ \frac{g_{\varphi 2}^2}{\omega_b' - \omega_a' - 2\omega_p} - \frac{g_{\varphi 2}^2}{\omega_b' + \omega_a' + 2\omega_p} - \frac{g_{\varphi 2}^2}{\omega_b' + \omega_a' - 2\omega_p}.\end{aligned} \tag{A.16}$$

In equation (A.15) we have neglected small shifts that come from applying the transformation to the three wave and Kerr terms in the Hamiltonian.

Finally, we add a single-tone probing term $\mathbf{H}_{\boldsymbol{d}} = \epsilon_d[\boldsymbol{a}\exp(i\omega_d t) + \text{h.c.}]$ to equation (A.15) and move to the rotating frame defined by the transformation operator

$$\boldsymbol{R} = \exp[i\omega_d t\boldsymbol{a}^{\dagger}\boldsymbol{a} + i(2\omega_d - \omega_p)t\boldsymbol{b}^{\dagger}\boldsymbol{b}]. \tag{A.17}$$

The new, effective Hamiltonian is given by $\widetilde{\mathbf{H}}_{\mathbf{3}} = \boldsymbol{R}\widetilde{\mathbf{H}}_{\mathbf{2}}\boldsymbol{R}^{\dagger} + i\dot{\boldsymbol{R}}\boldsymbol{R}^{\dagger}$. Neglecting all fast-rotating terms, we finally arrive at the Hamiltonian suitable for simulating Fig. 3.6 in the main text

$$\widetilde{\mathbf{H}}_{\mathbf{3}} \approx \Delta_a\boldsymbol{a}^{\dagger}\boldsymbol{a} + \Delta_b\boldsymbol{b}^{\dagger}\boldsymbol{b} + \frac{\tilde{g}_2}{2}(\boldsymbol{a}^{\dagger 2}\boldsymbol{b} + \boldsymbol{a}^2\boldsymbol{b}^{\dagger}) + \frac{\tilde{\chi}_{aa}}{2}\boldsymbol{a}^{\dagger 2}\boldsymbol{a}^2 + \frac{\tilde{\chi}_{bb}}{2}\boldsymbol{b}^{\dagger 2}\boldsymbol{b}^2 + \tilde{\chi}_{ab}\boldsymbol{a}^{\dagger}\boldsymbol{a}\boldsymbol{b}^{\dagger}\boldsymbol{b}, \tag{A.18}$$

using a numerical master equation solver[130]. The dynamical coefficients are

$$\begin{aligned}
\Delta_a =& \omega_a'' - \omega_d, \\
\Delta_b =& \omega_b'' - 2\omega_d + \omega_p, \\
\tilde{g}_2 =& E_J J_1(\epsilon)(\varphi_a^{\text{zpf}})^2 \varphi_b^{\text{zpf}}, \\
\tilde{\chi}_{aa} =& -\frac{E_J J_0(\epsilon)}{2}(\varphi_a^{\text{zpf}})^4, \\
\tilde{\chi}_{bb} =& -\frac{E_J J_0(\epsilon)}{2}(\varphi_b^{\text{zpf}})^4, \\
\tilde{\chi}_{ab} =& -E_J J_0(\epsilon)(\varphi_a^{\text{zpf}})^2(\varphi_b^{\text{zpf}})^2.
\end{aligned} \tag{A.19}$$

After these transformations, the lab-frame annihilation operators $\boldsymbol{a}$ and $\boldsymbol{b}$ become

$$\begin{aligned}
\boldsymbol{a} \rightarrow & \boldsymbol{RTDaD}^\dagger \boldsymbol{T}^\dagger \boldsymbol{R}^\dagger \\
\approx & \boldsymbol{a} \exp(-i\omega_d t) + f_{ab^\dagger}(t)\boldsymbol{b}^\dagger + f_{ab}(t)\boldsymbol{b} + \alpha(t), \\
\boldsymbol{b} \rightarrow & \boldsymbol{RTDbD}^\dagger \boldsymbol{T}^\dagger \boldsymbol{R}^\dagger \\
\approx & \boldsymbol{b} \exp[-i(2\omega_d - \omega_p)t] + f_{ba^\dagger}(t)\boldsymbol{a}^\dagger + f_{ba}(t)\boldsymbol{a} + \beta(t),
\end{aligned} \tag{A.20}$$

where the coefficients $f_{p,q}(t)\,(p, q = a, b, a^\dagger, b^\dagger)$ can by obtained by carrying out the transformations. All these coefficients $\alpha(t)$, $\beta(t)$ and $f_{p,q}(t)$ are much smaller than 1, which, along with dropping fast-rotating terms, allows us to use the same effective form of the dissipators in the frame of equation (A.18), as in the lab frame.

A.2 Resonator capacitively coupled to a Josephson qubit

In this section we outline the full derivation of the effective Hamiltonian for a lumped-element resonator capacitively coupled to a flux driven flux qubit. The circuit is shown in Fig. 3.13a in the main text. Following the same circuit quantization convention, the full-circuit Lagrangian is given by

$$\begin{aligned}\boldsymbol{\mathcal{L}} = &\left(\frac{\Phi_0}{2\pi}\right)^2 \left[\frac{C_a + C_c}{2}\dot{\boldsymbol{\varphi}}_a^2 + \frac{C_b + C_c}{2}\dot{\boldsymbol{\varphi}}_b^2 - C_c\dot{\boldsymbol{\varphi}}_a\dot{\boldsymbol{\varphi}}_b\right] \\ &- \left(\frac{\Phi_0}{2\pi}\right)^2 \left[\frac{\boldsymbol{\varphi}_a^2}{2L_a} + \frac{\boldsymbol{\varphi}_b^2}{2L_b} - E_J\cos(\boldsymbol{\varphi}_b + \varphi_{\text{ext}})\right].\end{aligned} \tag{A.21}$$

Legendre transformation leads to the following Hamiltonian

$$\mathbf{H} = \sum_{k=a,b}\left(4E_{Ck}\boldsymbol{n}_k^2 + E_{Lk}\boldsymbol{\varphi}_k^2\right) + E_{Cc}\boldsymbol{n}_a\boldsymbol{n}_b - E_J\cos\left(\boldsymbol{\varphi}_b + \varphi_{\text{ext}}\right) \tag{A.22}$$

with the inductive energy terms given as $E_{Lk} = (\Phi_0/2\pi)^2/2L_k$ and the capacitive ones given as $E_{Ca} = e^2(C_b + C_c)/2C_\Sigma^2$, $E_{Cb} = e^2(C_a + C_c)/2C_\Sigma^2$ and $E_{Cc} = 4e^2C_c/C_\Sigma$, where we denote $C_\Sigma^2 = C_aC_b + C_bC_c + C_cC_a$. Note the relation $E_{Ca}, E_{Cb} > E_{Cc}/8$ always holds however we choose the capacitance configuration. Again, we choose to modulated the applied flux as $\phi_{\text{ext}} = \epsilon\cos\omega_p t$. Following the Jacobi-Anger expansion

$$\begin{aligned}\cos(\boldsymbol{\varphi}_b + \varphi_{\text{ext}}) &= \cos\boldsymbol{\varphi}_b\cos\varphi_{\text{ext}} - \sin\boldsymbol{\varphi}_b\sin\varphi_{\text{ext}} \\ &= \left(J_0(\epsilon) + 2\sum_{n=1}^{\infty}(-1)^n J_{2n}(\epsilon)\cos(2n\omega_p t)\right)\cos\boldsymbol{\varphi}_b \\ &\quad + \left(2\sum_{n=1}^{\infty}(-1)^n J_{2n-1}(\epsilon)\cos[(2n-1)\omega_p t]\right)\sin\boldsymbol{\varphi}_b,\end{aligned} \tag{A.23}$$

the fluxonium Hamiltonian can be separated into static and dynamic parts

$$\begin{aligned}\mathbf{H}_{\mathrm{b}} =& \mathbf{H}_{\mathrm{b},0} + \mathbf{H}_{\mathrm{b},d} \\ =& \left(E_{Cb}\boldsymbol{n}_b^2 - E_J J_0(\epsilon)\cos\boldsymbol{\varphi}_b + \frac{1}{2}E_L\boldsymbol{\varphi}_b^2\right) \\ & - E_J\left(2\sum_{n=1}^{\infty}(-1)^n J_{2n}(\epsilon)\cos(2n\omega_p t)\cos\boldsymbol{\varphi}_b + (-1)^n J_{2n-1}(\epsilon)\cos[(2n-1)\omega_p t]\sin\boldsymbol{\varphi}_b\right).\end{aligned} \tag{A.24}$$

We can rewrite the full Hamiltonian as

$$\mathbf{H} = \omega_a\boldsymbol{a}^\dagger\boldsymbol{a} + \sum_k E_k|k\rangle\langle k| + \sum_{j,k} ig_{jk}(\boldsymbol{a}^\dagger - \boldsymbol{a})|j\rangle\langle k| + \mathbf{H}_{\mathrm{b},d}, \tag{A.25}$$

where $|k\rangle$ and E_k stand for the kth eigenstate and eigenenergy of the static rf-SQuID Hamiltonian $H_{\mathrm{b},0}$. The charge operators were expressed as $\boldsymbol{n}_a = in_a^{\mathrm{zpf}}(\boldsymbol{a}^\dagger - \boldsymbol{a})$ and $\boldsymbol{n}_b = \sum_{j,k} n_{jk}|j\rangle\langle k|$, $n_{jk} = \langle j|\boldsymbol{n}_b|k\rangle$, with the coupling amplitudes defined as $g_{jk} = E_{Cc}n_a^{\mathrm{zpf}}n_{jk}$ and $n_a^{\mathrm{zpf}} = (E_{La}/4E_{Ca})^{1/4}/\sqrt{2}$.

To avoid compromising the logical cavity coherence, the linear capacitive coupling needs to be sufficiently small to keep the resonator and fluxonium qubit in the dispersive regime, while still ensuring a large enough three-wave mixing coupling.

We perform the dispersive transformation to second order by treating the linear coupling perturbatively, using the unitary transformation $\boldsymbol{\mathcal{U}} = \exp(-\boldsymbol{\mathcal{S}})$, where $\boldsymbol{\mathcal{S}} = \sum_n \lambda^n\boldsymbol{\mathcal{S}}_n$. Here we use λ to track the order, but will set $\lambda = 1$ at the end. We denote $\mathbf{H}_0 = \omega_a\boldsymbol{a}^\dagger\boldsymbol{a} + \sum_k E_k|k\rangle\langle k|$ and $\boldsymbol{\mathcal{V}} = E_{Cc}\boldsymbol{n}_a\boldsymbol{n}_b$. The unitary transformation[175] on the static Hamiltonian $\mathbf{H}_0 + \lambda\boldsymbol{\mathcal{V}}$ leads to

$$\begin{aligned}\mathrm{e}^{\boldsymbol{\mathcal{S}}}(\mathbf{H}_0 + \lambda\boldsymbol{\mathcal{V}})\mathrm{e}^{-\boldsymbol{\mathcal{S}}} =& \boldsymbol{\mathcal{H}}_0 + \lambda([\boldsymbol{\mathcal{S}}_1, \mathbf{H}_0] + \boldsymbol{\mathcal{V}}) \\ & + \lambda^2([\boldsymbol{\mathcal{S}}_2, \mathbf{H}_0] + \frac{1}{2}[\boldsymbol{\mathcal{S}}_1, [\boldsymbol{\mathcal{S}}_1, \mathbf{H}_0]] + [\boldsymbol{\mathcal{S}}_1, \boldsymbol{\mathcal{V}}]) + O(\lambda^3).\end{aligned} \tag{A.26}$$

To block-diagonalize the static Hamiltonian, we first choose

$$\boldsymbol{\mathcal{S}}_1 = \sum_{jk} \left[\frac{i g_{jk} \boldsymbol{a}}{\omega_a - \epsilon_{jk}} + \frac{i g_{jk} \boldsymbol{a}^\dagger}{\omega_a - \epsilon_{kj}} \right] |j\rangle\langle k|, \tag{A.27}$$

which satisfies $[\boldsymbol{\mathcal{S}}_1, \mathbf{H}_0] = -\boldsymbol{\mathcal{V}}$.

We used the simplified notation $\epsilon_{kj} = E_k - E_j$. Following

$$\begin{aligned}
[\boldsymbol{\mathcal{S}}_1, \boldsymbol{\mathcal{V}}] = & \sum_{jkk'} \left[\frac{-g_{jk} g_{kk'}}{\omega_a - \epsilon_{jk}} + \frac{-g_{jk} g_{kk'}}{\omega_a - \epsilon_{kj}} \right] |j\rangle\langle k'| \\
& + \sum_{jkk'} (\boldsymbol{a}^\dagger - \boldsymbol{a}) \left[\frac{i g_{jk} \boldsymbol{a}}{\omega_a - \epsilon_{jk}} + \frac{i g_{jk} \boldsymbol{a}^\dagger}{\omega_a - \epsilon_{kj}} \right] \left(i g_{kk'} |j\rangle\langle k'| - i g_{k'j} |k'\rangle\langle k| \right),
\end{aligned} \tag{A.28}$$

we can block-diagonalize the Hamiltonian to the second order by choosing

$$\begin{aligned}
\boldsymbol{\mathcal{S}}_2 = & -\frac{1}{2} \sum_{jkk'} \left[\frac{g_{jk} g_{kk'} \boldsymbol{a}^{\dagger 2}}{(\omega_a - \epsilon_{kj})(2\omega_a - \epsilon_{k'j})} + \frac{g_{jk} g_{kk'} \boldsymbol{a}^2}{(\omega_a - \epsilon_{kj})(2\omega_a - \epsilon_{jk'})} \right] |j\rangle\langle k'| \\
& + \frac{1}{2} \sum_{jkk'} \left[\frac{g_{jk} g_{k'j} \boldsymbol{a}^{\dagger 2}}{(\omega_a - \epsilon_{kj})(2\omega_a - \epsilon_{kk'})} + \frac{g_{jk} g_{k'j} \boldsymbol{a}^2}{(\omega_a - \epsilon_{jk})(2\omega_a - \epsilon_{k'k})} \right] |k'\rangle\langle k| \\
& - \sum_{k, j \neq k'} \frac{|j\rangle\langle k'|}{2\epsilon_{k'j}} \Big[\frac{-g_{jk} g_{kk'}}{\omega_a - \epsilon_{jk}} + \frac{-g_{jk} g_{kk'}}{\omega_a - \epsilon_{kj}} + \frac{-g_{jk} g_{kk'} \boldsymbol{a}^\dagger \boldsymbol{a}}{\omega_a - \epsilon_{jk}} \\
& + \frac{g_{jk} g_{kk'} \boldsymbol{a} \boldsymbol{a}^\dagger}{\omega_a - \epsilon_{kj}} + \frac{g_{kk'} g_{jk} \boldsymbol{a}^\dagger \boldsymbol{a}}{\omega_a - \epsilon_{kk'}} + \frac{-g_{kk'} g_{jk} \boldsymbol{a} \boldsymbol{a}^\dagger}{\omega_a - \epsilon_{k'k}} \Big].
\end{aligned} \tag{A.29}$$

Similarly, we apply the dispersive transformation to the dynamical part of the Hamiltonian $\mathbf{H}'_d = \boldsymbol{\mathcal{U}} \mathbf{H}_{\mathrm{b},d} \boldsymbol{\mathcal{U}}^\dagger$ and find the corresponding three-wave mixing amplitude. Given the choice of flux pump frequency $\omega_p = \pm(2\omega_a - \epsilon_{01})$, only the $\sin \boldsymbol{\varphi}_b$ term in Eq. (A.23) yields the on-resonance three-wave mixing coupling. We rewrite

$$\sin \boldsymbol{\varphi}_b = \sum_{jk} \Lambda_{jk} |j\rangle\langle k|, \tag{A.30}$$

where $\Lambda_{jk} = \langle j|\sin\boldsymbol{\varphi}_b|k\rangle$. Up to second-order this leads to

$$\begin{aligned}\boldsymbol{\mathcal{U}}^\dagger \sum_{jk} \Lambda_{jk}|j\rangle\langle k|\boldsymbol{\mathcal{U}} = \sum_{jk} \Lambda_{jk}|j\rangle\langle k| + \lambda[\boldsymbol{\mathcal{S}}_1, \sum_{jk} \Lambda_{jk}|j\rangle\langle k|] \\ + \lambda^2[\boldsymbol{\mathcal{S}}_2, \Lambda_{jk}|j\rangle\langle k|] + \frac{1}{2}\lambda^2[\boldsymbol{\mathcal{S}}_1, [\boldsymbol{\mathcal{S}}_1, \sum_{jk} \Lambda_{jk}|j\rangle\langle k|]] + O(\lambda^3).\end{aligned} \tag{A.31}$$

First we have

$$[\boldsymbol{\mathcal{S}}_1, \sum_{j'k'} \Lambda_{j'k'}|j'\rangle\langle k'|] = \sum_{jkk'} \left[\frac{ig_{jk}\boldsymbol{a}}{\omega_a - \epsilon_{jk}} + \frac{ig_{jk}\boldsymbol{a}^\dagger}{\omega_a - \epsilon_{kj}}\right] (\Lambda_{kk'}|j\rangle\langle k'| - \Lambda_{k'j}|k'\rangle\langle k|), \tag{A.32}$$

and then

$$\begin{aligned}&[\boldsymbol{\mathcal{S}}_1, [\boldsymbol{\mathcal{S}}_1, \sum_{j''k''} \Lambda_{j''k''}|j''\rangle\langle k''|]] = \\ &- \sum_{jkk'k''} \left[\frac{g_{jk}g_{j'k'}}{(\omega_a - \epsilon_{jk})(\omega_a - \epsilon_{k'j'})} - \frac{g_{jk}g_{j'k'}}{(\omega_a - \epsilon_{kj})(\omega_a - \epsilon_{j'k'})}\right] \Lambda_{k'j}|j'\rangle\langle k'| \\ &+ \sum_{jkk'k''} \left[\frac{g_{jk}g_{k'j}}{(\omega_a - \epsilon_{jk})(\omega_a - \epsilon_{jk'})} - \frac{g_{jk}g_{k'j}}{(\omega_a - \epsilon_{kj})(\omega_a - \epsilon_{k'j})}\right] \Lambda_{k''k'}|k''\rangle\langle k| \\ &+ \sum_{jkk'k''} \left[\frac{ig_{jk}\boldsymbol{a}}{\omega_a - \epsilon_{jk}} + \frac{ig_{jk}\boldsymbol{a}^\dagger}{\omega_a - \epsilon_{kj}}\right] \left[\frac{ig_{kk'}\boldsymbol{a}}{\omega_a - \epsilon_{kk'}} + \frac{ig_{kk'}\boldsymbol{a}^\dagger}{\omega_a - \epsilon_{k'k}}\right] \Lambda_{k'k''}|j\rangle\langle k''| \\ &- \sum_{jkk'k''} \left[\frac{ig_{jk}\boldsymbol{a}}{\omega_a - \epsilon_{jk}} + \frac{ig_{jk}\boldsymbol{a}^\dagger}{\omega_a - \epsilon_{kj}}\right] \left[\frac{ig_{k''k'}\boldsymbol{a}}{\omega_a - \epsilon_{k''k'}} + \frac{ig_{k''k'}\boldsymbol{a}^\dagger}{\omega_a - \epsilon_{k'k''}}\right] \Lambda_{k'j}|k''\rangle\langle k| \\ &- \sum_{jkk'k''} \left[\frac{ig_{jk}\boldsymbol{a}}{\omega_a - \epsilon_{jk}} + \frac{ig_{jk}\boldsymbol{a}^\dagger}{\omega_a - \epsilon_{kj}}\right] \left[\frac{ig_{k''k'}\boldsymbol{a}}{\omega_a - \epsilon_{k''k'}} + \frac{ig_{k''k'}\boldsymbol{a}^\dagger}{\omega_a - \epsilon_{k'k''}}\right] \Lambda_{kk''}|j\rangle\langle k'| \\ &+ \sum_{jkk'k''} \left[\frac{ig_{jk}\boldsymbol{a}}{\omega_a - \epsilon_{jk}} + \frac{ig_{jk}\boldsymbol{a}^\dagger}{\omega_a - \epsilon_{kj}}\right] \left[\frac{ig_{k'j}\boldsymbol{a}}{\omega_a - \epsilon_{k'j}} + \frac{ig_{k'j}\boldsymbol{a}^\dagger}{\omega_a - \epsilon_{jk'}}\right] \Lambda_{k''j}|k''\rangle\langle k|,\end{aligned} \tag{A.33}$$

together with

$$
\begin{aligned}
&[\boldsymbol{\mathcal{S}}_2, \sum_{j''k''} \Lambda_{j''k''}|j''\rangle\langle k''|] = \\
&-\frac{1}{2}\sum_{jkk'k''}\left[\frac{g_{jk}g_{kk'}\boldsymbol{a}^{\dagger 2}}{(\omega_a-\epsilon_{kj})(2\omega_a-\epsilon_{k'j})}+\frac{g_{jk}g_{kk'}\boldsymbol{a}^{2}}{(\omega_a-\epsilon_{kj})(2\omega_a-\epsilon_{jk'})}\right]\Lambda_{k'k''}|j\rangle\langle k''| \\
&+\frac{1}{2}\sum_{jkk'k''}\left[\frac{g_{jk}g_{kk'}\boldsymbol{a}^{\dagger 2}}{(\omega_a-\epsilon_{kj})(2\omega_a-\epsilon_{k'j})}+\frac{g_{jk}g_{kk'}\boldsymbol{a}^{2}}{(\omega_a-\epsilon_{kj})(2\omega_a-\epsilon_{jk'})}\right]\Lambda_{k''j}|k''\rangle\langle k'| \\
&+\frac{1}{2}\sum_{jkk'k''}\left[\frac{g_{jk}g_{k'j}\boldsymbol{a}^{\dagger 2}}{(\omega_a-\epsilon_{kj})(2\omega_a-\epsilon_{kk'})}+\frac{g_{jk}g_{k'j}\boldsymbol{a}^{2}}{(\omega_a-\epsilon_{jk})(2\omega_a-\epsilon_{k'k})}\right]\Lambda_{kk''}|k'\rangle\langle k''| \\
&-\frac{1}{2}\sum_{jkk'k''}\left[\frac{g_{jk}g_{k'j}\boldsymbol{a}^{\dagger 2}}{(\omega_a-\epsilon_{kj})(2\omega_a-\epsilon_{kk'})}+\frac{g_{jk}g_{k'j}\boldsymbol{a}^{2}}{(\omega_a-\epsilon_{jk})(2\omega_a-\epsilon_{k'k})}\right]\Lambda_{k''k'}|k''\rangle\langle k| \\
&-\frac{1}{2}\sum_{kk'',j\neq k'}\Bigg[\frac{1}{\epsilon_{k'j}}(\Lambda_{k'k''}|j\rangle\langle k''|-\Lambda_{k''j}|k''\rangle\langle k'|) \\
&\times\left(\frac{-g_{jk}g_{kk'}}{\omega_a-\epsilon_{jk}}+\frac{-g_{jk}g_{kk'}}{\omega_a-\epsilon_{kj}}+\frac{-g_{jk}g_{kk'}\boldsymbol{a}^{\dagger}\boldsymbol{a}}{\omega_a-\epsilon_{jk}}+\frac{g_{jk}g_{kk'}\boldsymbol{a}\boldsymbol{a}^{\dagger}}{\omega_a-\epsilon_{kj}}+\frac{g_{kk'}g_{jk}\boldsymbol{a}^{\dagger}\boldsymbol{a}}{\omega_a-\epsilon_{kk'}}+\frac{-g_{kk'}g_{jk}\boldsymbol{a}\boldsymbol{a}^{\dagger}}{\omega_a-\epsilon_{k'k}}\right)\Bigg].
\end{aligned}
\tag{A.34}
$$

Based on the calculations shown above, the final expression for the dynamical three-wave mixing amplitude is given by

$$
\begin{aligned}
g_{2,d} = \; & E_J J_1(\epsilon)\Bigg(\sum_{jk}\Lambda_{j1}\frac{ig_{0k}}{\omega_a-\epsilon_{k0}}\frac{ig_{kj}}{\omega_a-\epsilon_{jk}}-2\Lambda_{kj}\frac{ig_{0k}}{\omega_a-\epsilon_{k0}}\frac{ig_{j1}}{\omega_a-\epsilon_{1j}}+\Lambda_{0j}\frac{ig_{j1}}{\omega_a-\epsilon_{1j}}\frac{ig_{kj}}{\omega_a-\epsilon_{jk}} \\
&+\Lambda_{j1}\frac{ig_{0k}}{\omega_a-\epsilon_{k0}}\frac{ig_{kj}}{2\omega_a-\epsilon_{j0}}-\Lambda_{0j}\frac{ig_{jk}}{\omega_a-\epsilon_{kj}}\frac{ig_{k1}}{2\omega_a-\epsilon_{1j}}-\Lambda_{k1}\frac{ig_{jk}}{\omega_a-\epsilon_{kj}}\frac{ig_{0k}}{2\omega_a-\epsilon_{k0}}+\Lambda_{0k}\frac{ig_{j1}}{\omega_a-\epsilon_{1j}}\frac{ig_{kj}}{2\omega_a-\epsilon_{1k}}\Bigg)
\end{aligned}
\tag{A.35}
$$

The overall three-wave interaction is given by $g_2(t)(\boldsymbol{a}^{\dagger 2}|0\rangle\langle 1| + \boldsymbol{a}^2|1\rangle\langle 0|)$, with $g_2(t) = g_{2,d}\cos(\omega_p t)$. Choosing the pump frequency such that $\omega_p = |2\omega_a - \epsilon_{01}|$ yields an effective anharmonicity of magnitude $\sqrt{2}g_{2,d}/2$.

Appendix B

Fabrication procedures

B.1 Sample cleaning

Before any chemical processing, glass beakers are cleaned with acetone and methanol to remove any particulates that would contaminate the sample surface. Glassware is usually replaced on a yearly basis, and every beaker is uniquely assigned to each solvent and they are always kept in the cleanroom covered with aluminum foil.

B.1.1 TAMI solvent cleaning

This is a general solvent cleaning technique performed regularly throughout the entire device process flow. It involves the solvents: Toluene, Acetone, Methanol, Isopropanol (IPA), thus the acronym TAMI.

- Place sample in Toluene, sonicate for 2 minutes.
- Remove from Toluene while spraying with Acetone to prevent drying and transfer into beaker with Acetone. Sonicate for 2 minutes.
- Remove from Acetone while spraying with Methanol to prevent drying and transfer into beaker with Methanol. Sonicate for 2 minutes.

- Remove from Methanol while spraying with Isopropanol to prevent drying and transfer into beaker with Isopropanol. Sonicate for 2 minutes.
- Blow dry sample with nitrogen

B.1.2 NMP cleaning

This is a solvent cleaning procedure dedicated to removing any residual photoresist layer from previous lithography/etching/dicing steps. Chemical used is n N-Methyl-pyrrolidone (NMP), different trade names Nano^{TM} Remover PG, 1165 or MICROPOSIT^{TM} REMOVER 1165.

- Place sample in a clean beaker with NMP. Sonicate for 2 minutes to remove a large fraction of the photoresist layer.
- Remove sample from NMP beaker (contaminated with photoresist) to a new clean beaker with NMP. Cover the lid with aluminum foil and leave it on a hotplate at 80° C for > 1 hour.
- Remove sample from the second NMP beaker and perform TAMI cleaning.

B.2 Nb sputtering

Our samples are fabricated on a 500 µm thick C-plane sapphire substrate purchased from CrysTec GmbH. Prior to metal deposition, we clean the substrates using the TAMI procedure, in suitable glassware for 4" (100 mm) wafers. A 200 nm Nb film is sputtered onto the wafers using the AJA sputtering tool. It is important to blow dry the wafer before loading it into the loadlock The quality of the film is found to improve when heating the sample holder chuck during deposition.

The 4 inch wafer is diced into 1 inch square pieces. Dicing procedure requires coating the wafer with a protective resist layer.

B.3 Photolithography

We use photolithography to define circuit structures (such as resonators) with minimum features above 2 µm.

Clean and spin coat photoresist.

- If the chip has photoresist from the previous step (photolithography, etching or dicing), remove the resist with the NMP cleaning steps followed by TAMI solvent cleaning step.
- Before spin coating resist, it is important to check if the sample chuck can hold good vacuum. Clean the sample chuck with Isopropanol (do not use Acetone because it will destroy the O-ring) and run a trial run with a dummy sample.
- Place sample on a hotplate at 95° C for 1 minute to remove any moisture and ensure good surface adhesion.
- Spin AZ1505 at 65000 RPM for 40 seconds with a ramp rate of 10000 RPM/s. Soft bake sample on hotplate at 95° C for 1 minute. Leave it to cool down on a metal plate for 1 minute.
- Inspect sample to ensure the photoresist was uniformly coated and does not have any resist bubbles or debris.

Exposure and development. Use the Heidelberg DWL 66+ to perform direct laser writing on the substrate. The tool allows both pneumatic and optical focusing where optical focusing gives the best resolution performance. In order to use optical focusing, need to ensure the sapphire substrates have metal layers to ensure it is reflective.

- Heidelberg parameters; 2 mm write head, optical focus setting 20, intensity 70% with an additional 1% filter. The intensity value is chosen from a series of dose tests. Before running the process, check the tool ambient temperature 20°-21° C since photoresist selectivity is sensitive to temperature.

- Load substrate on the sample stage close to the center. Perform optical focus. Find the center of the chip. Bring the write head out of focus and bring it back to focus with the center. This focus setting will be used during the entire write.
- Load and render your CAD design in the Heidelberg software. Typical write time for a 25×25 mm CAD layout takes approximately 1.5 hours.
- Develop the sample in a beaker of AZ300MIF for 1 minute. Do no aggressively swirl the sample, instead gently rotate it around the beaker to detach the developed resist. Rinse sample in running DI water and blow dry with nitrogen.
- Inspect sample in UV filtered optical microscope. Hard bake at 105° C for 1 minute if the next step is metal etching.

B.4 Metal etching

The Nb metal layer is etched using reactive ion etching (RIE) in the APEX Plasma etcher. The developed photoresist is used as a mask for etching the Nb areas defined by the exposed areas of the resist. Prior to etching the sample, the tool main chamber is cleaned with an O_2 plasma followed by a trial run of the plasma etching chemistry to condition the chamber. The recipes used for etching Nb consist of two steps. The first step is an O_2 descum process to remove any residual resist in the exposed areas and around the resist side walls. Descum parameters are O_2 20 sccm, Bias power 100 W, ICP power 100W, chamber pressure 50 mTorr, process time 15 seconds. The Nb etching is done with a fluorine-based plasma with a gas mixture of SF_6 (15 sccm), CHF_3 (40 sccm) and Ar (10 sccm), with the Bias and ICP power set to 100W. The chamber pressure during the etching is set to 50 mTorr which needs to be lowered in future recipe developments in order to optimize the Nb side wall profile. With these parameters, the 200 nm Nb film can be fully etched in 6 minutes.

After the RIE step, the 1 inch sample is cleaned using the NMP cleaning procedure followed by TAMI cleaning step.

B.5 Electron beam lithography

The Josephson junction fabrication is performed with electron beam (e-beam) lithography using the ElionixELS-125. The sample is coated with a bi-layer resist MMA-PMMA in order to define resist undercuts and bridges used in a shadow evaporation step to create the junctions.

Spin coat e-beam resist.

- Spin MMA(8.5) MAA EL13 at 5000 RPM, with a 500 RPM/sec ramp rate, for 70 seconds total
- Bake at 175° C for 2 minutes
- Spin PMMA950 A3 at 4000 RPM, with a 500 RPM/sec ramp rate, for 68 seconds total
- Bake at 175° C for 30 minutes
- Cool down on a metal plate for 2 minutes

Anti-charging evaporation.

Since the sapphire substrate is insulating, an very thin anti-charge aluminum layer is deposited on the resist stack to prevent charging effects that would result in overexposing the e-beam features. Sample is mounted on a glass slide or aluminum holder with Kapton tape and loaded in the Plassys evaporator after the sample was blow off with nitrogen to remove particles. Typically we evaporate a 40 nm aluminum layer at a rate of 0.4 nm/s.

The 1 inch sample is then diced into individual 7×7 mm chips ready to be used for e-beam lithography.

E-beam exposure.

Beam parameters: 1 nA beam current 60 µm aperture, 1.15 µs/dot, 500 µm write field, 50000 dots per field. Dose factors are full clear 1.4 (PMMA + MMA) and undercut 0.25 (just MMA).

Development.

- Remove aluminum anti-charge layer in MF-319 developer for 3 minutes, followed by DI water for 1 minutes and blow dry with nitrogen
- Develop in 1:3 Methyl Isobutyl Ketone (MIBK):IPA for 50 seconds, gently swirling the device
- Dip sample in IPA for 10 seconds while swirling.
- Gently blow dry the device with nitrogen and inspect the exposed areas in the microscope and check for any residue from partial development.

B.6 Junction deposition

Mount sample on a metal piece and load it in the Plassys following the correct undercut orientation. Once the chamber and load-lock reach low 10^{-7} mbar pressures, fill the cold trap with liquid nitrogen to freeze moisture and further reduce the pressures.

Descum.

Argon ion etch to clean the exposed junction areas prior to evaporation. Ion gun parameters are anode voltage 400 V, emitter current 60 mA and acceleration voltage -80V. Etching is performed for 45 seconds for each evaporation angle.

Aluminum evaporation.

- Evaporate titanium at 0.3 nm/s for 1 minute and wait 2 minutes until chamber pressures go down to low 10^{-8} mbar.
- Evaporate 30 nm of aluminum at rate 0.4 nm/s with tilt angle 25°.
- Oxidize using a Ar:O_2 (15%:85%) gas mixture for 10 minutes at 200 mbar.
- Evaporate 50 nm of aluminum at rate 0.4 nm/s with tilt angle -25°.
- Oxidize using a Ar:O_2 (15%:85%) gas mixture for 20 minutes at 40 mbar to passivate the aluminum surface.

Liftoff.

- Remove the sample from the evaporator. Leave the sample in a cleaned beaker filled with NMP for 3 hours at 80° C.
- Prepare a second cleaned beaker with NMP. Grab the sample from the first beaker and without letting the device dry, spray with NMP to remove excess metal. Place the sample in the second NMP beaker and sonicate for 30 seconds.
- Move the sample in a third cleaned beaker with IPA and sonicate for 30 seconds. Blow dry with nitrogen.

Appendix C

Experimental setup

This section serves as a brief overview of the cryogenic and instrumentation setup used for the experiment described in Chapter 3. This is a generic setup for any type of circuit QED experiment and it serves as a reference also for the experiment done in Chapter 5.

C.1 Cryogenic setup

Once the device is packaged in a dedicated PCB, it is then mounted to the base stage of a commercial dilution refrigerator, as shown in Fig. C.1. The device is placed in a μ-metal container and an aluminum (superconducting) container in order to shield it against magnetic noise. Additionally, we shield the device against radiation which could break Cooper pairs by covering the outside of each can with my Mylar and coating the inside of the inner most (aluminum) container with Stycast.

The device is connected to coax lines that are passed through every stage of the fridge and connected to room temperature equipment. For controlling the circuit, there are two types of input lines: microwave and DC. As shown in the cryogenic setup in Fig. C.1, these two types of coax lines have different configurations of attenuators and filters. Attenuators are introduced to reduce the black body radiation from higher temperature stages. However, the levels of attenuation cannot to increased indefinitely since we need to be able to introduce enough microwave power to drive a few photons into the device ($\sim$ aW) and to be able to circulate enough current to thread a few flux quanta. Fortunately, this can be accomplished with a reasonable amount of attenuation that also prevents increasing the photon temperature of the circuit. The microwave input lines have low pass filters with a 10-12 GHz cutoff to block as much as possible any higher freq radiation which could break a Cooper pair, and thus introduce dissipation, while still allowing microwave drives to control the circuit. For flux-tunable devices, we use a DC line which is heavily low pass filtered down to a 12 kHz bandwidth to reduce flux noise. For experiments that require parametric flux modulation (Chapter 3), the DC flux bis current is combined with the ac flux drive using a bias tee thermally anchored to the base stage.

The output of the device is connected to a coax line dedicated for detecting the emitted photons from the cavities. Since this signal is very weak there, it must pass through cryogenic amplifiers anchored to various stages of the fridge. Any additional attenuation from the output port of the device to the first amplifier contributes to the increase of the noise temperature, and consequently the noise temperature of the first amplifier sets the overall signal to noise ratio (SNR) of the measured signal at room temperature [176]. Typically the first amplifier in the chain is a HEMT amplifier at the 4K stage which typically has a noise temperature of 2K, and to further increase the SNR we can take advantage of near-quantum limited amplifier made from Josephson circuits such as the traveling wave parametric amplifier [177] (TWPA) used in(Chapter 3). A set of cryogenic isolators anchored to the base stage are introduced between the device and amplifiers in order to minimize any amplifier back-action and isolate the strong microwave pump drives used for parametrically activating the gain in the Josephson amplifiers. Since there is very little attenuation between the cavity output and the higher stages of the fridge, we need to introduce the

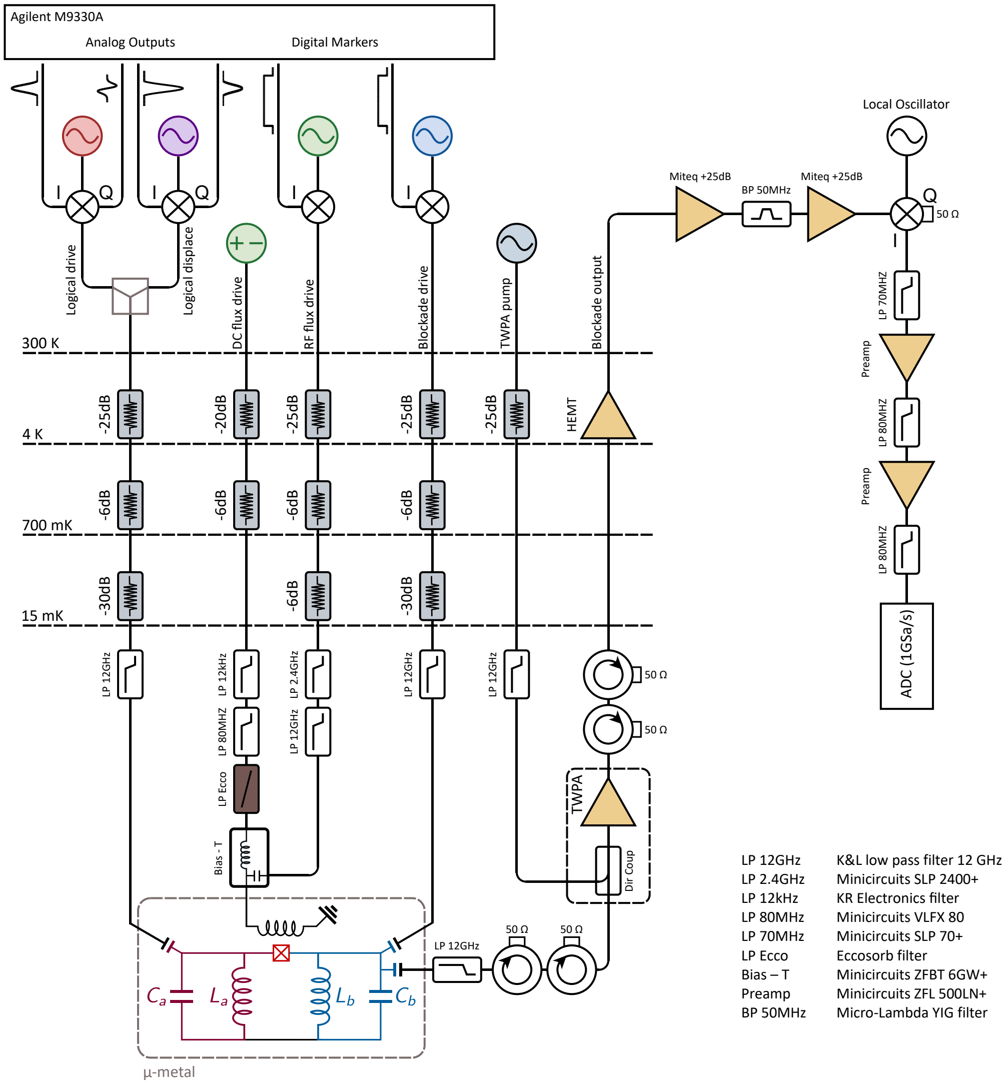

LP 12GHz	K&L low pass filter 12 GHz
LP 2.4GHz	Minicircuits SLP 2400+
LP 12kHz	KR Electronics filter
LP 80MHz	Minicircuits VLFX 80
LP 70MHz	Minicircuits SLP 70+
LP Ecco	Eccosorb filter
Bias – T	Minicircuits ZFBT 6GW+
Preamp	Minicircuits ZFL 500LN+
BP 50MHz	Micro-Lambda YIG filter

Figure C.1: **Experimental setup.** Schematic diagram of the cryogenic and instrumentation setup.

same low pass filters used for the microwave lines to block any black body radiation which can lead to dissipation and thermal photon population in the device.

C.2 Control and measurement setup

The microwave pulses used for driving qubits and cavities are generated by IQ modulation of a base-band pulses with a carrier provided by a microwave signal generator.

In some experiments we make use of dedicated vector generators (Agilent E8267D) with internal wide-band IQ mixing functionality. The base-band pulses are generated by an arbitrary waveform generator (AWG, Agilent M9330A) with a sampling rate of 1.25 GSa/s. Some waveforms, such as the readout and flux-modulation pulses, which do not require precise control over shape and can be simply implemented as a square pulse, are generated using cheaper analog signal generators (Agilent E8257D) triggered by digital marker pulses from the same AWG. The DC flux bias current is provided by a low-noise current source (YOKOGAWA GS200).

Typically all measurements involve probing the emitted field from a cavity. The signal is additionally amplified at room temperature using low-noise amplifiers (MITEQ) and in some cases a tunable narrow band (50 MHz) YIG filter is used to filter any noise outside the band of the readout frequency. The amplitude and phase of the output signal are obtained through a single-channel heterodyne measurement, using an IQ mixer (Marki IQ4509LXP) and reference oscillator (analog signal generator), to down convert the output to a $\omega_{\text{if}} = 50$ MHz signal $S(t)$. After filtering and amplifying the heterodyne signal, we digitize it using a fast ADC card (Agilent U1084A), and down convert it in software to measure the homodyne quadrature voltages $I = \sum_{nT_{\text{if}}} S(t)\cos(\omega_{\text{if}}t)$ and $Q = \sum_{nT_{\text{if}}} S(t)\sin(\omega_{\text{if}}t)$. The amplitude and phase of the readout voltage were calculated as $A = \sqrt{I^2 + Q^2}$ and $\phi = \tan^{-1}(Q/I)$ respectively. One can also directly digitize the homodyne voltage by tuning the local oscillator to the signal frequency $\omega_{\text{if}} = 0$. In this scenario the signal is at DC, making it easier to process but leaving it susceptible to 1/f noise and DC drifts.

Appendix D

Publications and Presentations

D.1 Publications

- A. Vrajitoarea, Z. Huang, P. Groszkowski, J. Koch, A.A. Houck, *Quantum control of an oscillator using a stimulated Josephson nonlinearity*, Nature Physics, **16**, 211-217 (2020)
- A. Vrajitoarea, A. C. Y. Li, Z. Huang, J. Koch, A.A. Houck, *Photon crystallization in synthetic dimensions using parametrically driven superconducting circuits*, manuscript in preparation
- A. Vrajitoarea, R. Belyansky, R. Lundgren, A. V. Gorshkov, A.A. Houck, *Ultrastrong coupling in a photonic crystal waveguide*, manuscript in preparation
- J. Raftery, A. Vrajitoarea, G. Zhang, Z. Leng, S.J. Srinivasan, A.A. Houck, *Direct digital synthesis of microwave waveforms for quantum computing*, arXiv:1703.00942[quant-ph]

D.2 Presentations

- A. Vrajitoarea and A.A. Houck, *Quantum simulation in a field-programmable cavity array*, Quantum Simulation and Computation, ICMAT-CSIC, Madrid, Spain (2019)
- A. Vrajitoarea, R. Belyansky, R. Lundgren, Y. Wang, P. Bienias, A. V. Gorshkov, A.A. Houck, *Quantum impurity in a 1D photonic crystal*, APS March Meeting, Boston, Massachusetts, USA (2019)
- A. Vrajitoarea, Z. Huang, P. Groszkowski, J. Koch, A.A. Houck, *Implementing logical oscillators by parametric two photon blockade*, Los Angeles, California, USA (2018)
- A. Vrajitoarea, J. Koch, A.A. Houck, *Proposal for cavity based superconducting qubit*, APS March Meeting, Baltimore, Maryland, USA (2016)

Bibliography

[1] R. P. Feynman. Simulating physics with computers. *International Journal of Theoretical Physics* **21**, 467–488 (1982).

[2] I. M. Georgescu, S. Ashhab, and F. Nori. Quantum simulation. *Rev. Mod. Phys.* **86**, 153 (2014).

[3] M. A. Nielsen and I. L. Chuang. Quantum computation and quantum information. *Cambridge University press,* (2000).

[4] J. I. Cirac and P. Zoller. Goals and opportunities in quantum simulation. *Nature Physics* **8**, 264–266 (2012).

[5] S. Lloyd. Universal quantum simulators. *Science* **273**, 1073–1078 (1996).

[6] R. Blatt and C. F. Roos. Quantum simulations with trapped ions. *Nat. Phys.* **8**, 277–284 (2012).

[7] T. Choi *et al.* Optimal quantum control of multimode couplings between trapped ion qubits for scalable entanglement. *Phys. Rev. Lett.* **112**, 1–5 (2014).

[8] A. Bermudez *et al.* Assessing the progress of trapped-ion processors towards fault-tolerant quantum computation. *Phys. Rev. X* **7**, 041061 (2017).

[9] I. Bloch. Ultracold quantum gases in optical lattices. *Nat. Phys.* **1**, 23–30 (2005).

[10] I. Bloch *et al.* Quantum simulations with ultracold quantum gases. *Nat. Phys.* **8**, 267–276 (2012).

[11] D. D. Awschalom *et al.* Quantum spintronics: Engineering and manipulating atom-like spins in semi- conductors. *Science* **339**, 1174–1179 (2013).

[12] J. T. Muhonen *et al.* Quantifying the quantum gate fidelity of single-atom spin qubits in silicon by randomized benchmarking. *Journal of physics. Condensed matter : an Institute of Physics journal* **27**, 154205 (2015).

[13] A. Aspuru-Guzik and P. Walther. Photonic quantum simulators. *Nat. Phys.* **8**, 285–291 (2012).

[14] M. H. Devoret and R. J. Schoelkopf. Superconducting circuits for quantum information: an outlook. *Science* **339**, 1169–1174 (2013).

[15] G. Wendin. Quantum information processing with superconducting circuits: a review. *Reports on Progress in Physics* **80**, 106001 (2017).

[16] I. Carusotto *et al.* Photonic materials in circuit quantum electrodynamics. *Nature Physics* **16**, 268–279 (2020).

[17] A. Blais *et al.* Quantum information processing and quantum optics with circuit quantum electrodynamics. *Nature Physics* **16**, 247–256 (2020).

[18] N. Ofek *et al.* Extending the lifetime of a quantum bit with error correction in superconducting circuits. *Nature* **536**, 441–445 (2016).

[19] J. Tangpanitanon and D. G. Angelakis. Many-body physics and quantum simulations with strongly interacting photons. *arXiv:1907.05030[quant-ph]*, (2019).

[20] M. J. Hartman. Quantum simulation with interacting photons. *Journal of Optics* **18**, 104005 (2016).

[21] C. Noh and D. G. Angelakis. Quantum simulations and many-body physics with light. *Rep. Prog. Phys* **80**, 016401 (2016).

[22] S. Schmidt and J. Koch. Circuit qed lattices: Towards quantum simulation with superconducting circuits. *Ann. Phys. (Amsterdam)* **525**, 395–412 (2013).

[23] A. A. Houck, H. E. Tureci, and J. Koch. On-chip quantum simulation with superconducting circuits. *Nature Physics* **8**, 292–299 (2012).

[24] I. Carusotto and C. Ciuti. Quantum fuids of light. *Rev. Mod. Phys.* **80**, 299–366 (2013).

[25] S. Haroche and J. M. Raimond. Exploring the quantum: Atoms, cavities, and photons.. *Oxford Graduate Texts*, (2013).

[26] D. E. Chang, V. Vuletic, and M. D. Lukin. Quantum nonlinear optics photon by photon.. *Nature Photonics* **8**, 685 (2014).

[27] M. J. Hartmann, F. G. S. L. Brando, and M. B. Plenio. Strongly interacting polaritons in coupled arrays of cavities. *Nature Physics* **2**, 849–855 (2006).

[28] A. D. Greentree, C. Tahan, J. H. Cole, and L. C. L. Hollenberg. Quantum phase transitions of light. *Nature Physics* **2**, 856–861 (2006).

[29] D. G. Angelakis, M. F. Santos, and B. Sougato. Photon-blockade induced mott transitions and xy spin models in coupled cavity arrays. *Phys. Rev. A* **76**, 031805 (2007).

[30] J. Cho, D. G. Angelakis, and S. Bose. Fractional quantum hall state in coupled cavities. *Phys. Rev. Lett.* **101**, 246809 (2008).

[31] A. Petrescu, A. A. Houck, and K. LeHur. Anomalous hall effects of light and chiral edge modes on the kagome lattice. *Phys. Rev. A* **86**, 053804 (2012).

[32] B. M. Anderson *et al.* Engineering topological many-body materials in microwave cavity arrays. *Phys. Rev. X* **6**, 041043 (2016).

[33] M. J. Hartman *et al.* Effective spin systems in coupled microcavities. *Phys. Rev. Lett.* **99**, 160501 (2007).

[34] A. Kay and D. G. Angelakis. Reproducing spin lattice models in strongly coupled atom-cavity systems. *Europhysics Letters)* **84**, 20001 (2008).

[35] P. B. Li *et al.* Generation of ising interaction and cluster states in a one-dimensional coupled resonator waveguide. *The European Physical Journal D* **55**, 205 (2009).

[36] S. Sarkar. Quantum field theoretical study of an effective spin model in coupled optical cavity arrays. *Physica B: Condensed Matter* **407**, 44–48 (2012).

[37] D. G. Angelakis *et al.* Luttinger liquid of photons and spin-charge separation in hollow-core fibers. *Phys. Rev. Lett.* **106**, 1–4 (2011).

[38] D. Gerace *et al.* The quantum-optical josephson interferometer.. *Nature Physics* **5**, 281–284 (2009).

[39] I. Carusotto *et al.* Fermionized photons in an array of driven dissipative nonlinear cavities. *Phys. Rev. Lett.* **103**, 033601 (2009).

[40] M. J. Hartmann. Polariton crystallization in driven arrays of lossy nonlinear resonators. *Phys. Rev. Lett.* **104**, 113601 (2010).

[41] R. Umucalilar and I. Carusotto. Fractional quantum hall states of photons in an array of dissipative coupled cavities. *Phys. Rev. Lett.* **108**, 206809 (2012).

[42] E. Kapit *et al.* Induced self-stabilization in fractional quantum hall states of light. *Phys. Rev. X* **4**, 031039 (2014).

[43] M. Hafezi *et al.* Chemical potential for light by parametric coupling. *Phys. Rev. B* **92**, 174305 (2015).

[44] J. Lebreuilly *et al.* Towards strongly correlated photons in arrays of dissipative nonlinear cavities under a frequencydependent incoherent pumping. *C. R. Phys.* **17**, 836–860 (2016).

[45] R. Ma *et al.* Autonomous stabilizer for incompressible photon fuids and solids. *Phys. Rev. A* **95**, 043811 (2017).

[46] J. Raftery *et al.* Observation of a dissipation-induced classical to quantum transition.. *Phys. Rev. X* **4**, 031043 (2014).

[47] S. Hacohen-Gourgy *et al.* Cooling and autonomous feedback in a bose-hubbard chain with attractive interactions. *Phys. Rev. Lett* **115**, 240501 (2015).

[48] P. Roushan *et al.* Chiral ground-state currents of interacting photons in a synthetic magnetic field. *Nature Physics* **13**, 146151 (2017).

[49] M. Fitzpatrick *et al.* Observation of a dissipative phase transition in a one-dimensional circuit qed lattice. *Phys. Rev. X* **7**, 011016 (2017).

[50] R. Ma *et al.* A dissipatively stabilized mott insulator of photons. *Nature* **566**, 51–57 (2019).

[51] P. Roushan *et al.* Spectroscopic signatures of localization with interacting photons in superconducting qubits. *Science* **358**, 1175–1179 (2017).

[52] X. Gu, A. F. Kockum, A. Miranowicz, Y. Liu, and F. Nori. Microwave photonics with superconducting quantum circuits. *Physics Reports* **718-719**, 1–102 (2017).

[53] P. Krantz *et al.* A quantum engineer's guide to superconducting qubits. *Applied Physics Reviews* **6**, 021318 (2019).

[54] M. Kjaergaard *et al.* Superconducting qubits: Current state of play. *Annual Review of Condensed Matter Physics* **11**, 369–395 (2019).

[55] B. Yurke and D. J. S. Quantum network theory. *Phys. Rev. A* **29**, 1419 (1984).

[56] M. H. Devoret. Quantum fluctuations in electrical circuits. *Les Houches, Session LXIII*, (1995).

[57] U. Vool and D. M. H. Introduction to quantum electromagnetic circuits.. *IJCTA - Special Issue on Quantum Circuits* **45**, 897–934 (2017).

[58] S. M. Girvin. Circuit qed: Superconducting qubits coupled to microwave photons.. *Les Houches Session XCVI*, 112–255 (2011).

[59] M. Tinkham. Introduction to superconductivity. *Dover Publications Inc.*, (1996).

[60] J. Koch *et al.* Charge-insensitive qubit design derived from the cooper pair box. *Phys. Rev. A* **76**, 042319 (2007).

[61] I. Chiorescu *et al.* Coherent quantum dynamics of a superconducting flux qubit. *Science* **299**, 1869–1871 (2003).

[62] F. Yan *et al.* The flux qubit revisited to enhance coherence and reproducibility. *Nat. Comm.* **7**, 12964 (2016).

[63] V. E. Manucharyan *et al.* Fluxonium: Single cooper-pair circuit free of charge offsets. *Science* **326**, 113–116 (2009).

[64] L. B. Nguyen *et al.* High-coherence fluxonium qubit. *Phys. Rev. X* **9**, 041041 (2019).

[65] H. Zhang *et al.* Universal fast flux control of a coherent, low-frequency qubit. *https://arxiv.org/abs/2002.10653*, (2020).

[66] D. Braak. Integrability of the rabi model. *Phys. Rev. Lett.* **107**, 100401 (2011).

[67] E. T. Jaynes and F. W. Cummings. Comparison of quantum and semiclassical radiation theories with application to the beam maser. *Proc. IEEE* **51**, 89 (1963).

[68] C. Ciuti, G. Bastard, and I. Carusotto. Quantum vacuum properties of the intersubband cavity polariton field. *Phys. Rev. B* **72**, 115303 (2005).

[69] P. Forn-Diaz *et al.* Ultrastrong coupling regimes of light-matter interaction. *Rev. Mod. Phys.* **91**, 025005 (2019).

[70] M. Devoret, S. Girvin, and R. Schoelkopf. Circuitqed: How strong can the coupling between a josephson junction atom and a transmission line resonator be?. *Ann. Phys.* **16**, 767 (2007).

[71] N. A. Masluk *et al.* Microwave characterization of josephson junction arrays: Implementing a low loss superinductance. *New J. Phys.* **109**, 137002 (2012).

[72] C. K. Andersen and A. Blais. Ultrastrong coupling dynamics with a transmon qubit. *New J. Phys.* **19**, 023022 (2017).

[73] S. J. Bosman *et al.* Multi-mode ultra-strong coupling in circuit quantum electrodynamics. *npj Quant. Info.* **3**, 46 (2017).

[74] V. E. Manucharyan *et al.* Resilience of the quantum rabi model in circuit qed. *J. Phys. A: Math. Theor.* **50**, 294001 (2017).

[75] T. Niemczyk *et al.* Circuit quantum electrodynamics in the ultrastrong-coupling regime. *Nature Physics* **6**, 772 (2010).

[76] P. Forn-Diaz *et al.* Observation of the bloch-siegert shift in a qubit-oscillator system in the ultrastrong coupling regime. *Phys. Rev. Lett.* **105**, 237001 (2010).

[77] F. Yoshihara *et al.* Superconducting qubitoscillator circuit beyond the ultrastrong-coupling regime. *Nature Physics* **13**, 44 (2017).

[78] P. Forn-Diaz *et al.* Ultrastrong coupling of a single artificial atom to an electromagnetic continuum in the nonperturbative regime. *Nature Physics* **13**, 39–43 (2017).

[79] D. I. Schuster. Circuit quantum electrodynamics. *PhD thesis - Yale*, (2007).

[80] A. Blais *et al.* Cavity quantum electrodynamics for superconducting electrical circuits: An architecture for quantum computation. *Phys. Rev. A* **69**, 062320 (2004).

[81] J. Clarke, A. N. Cleland, M. H. Devoret, D. Esteve, and J. M. Martinis. Quantum mechanics of a macroscopic variable: the phase difference of a josephson junction. *Science* **239**, 992–997 (1988).

[82] M. Reagor *et al.* Quantum memory with millisecond coherence in circuit qed. *Phys. Rev. B* **94**, 014506 (2016).

[83] M. Mirrahimi *et al.* Dynamically protected cat-qubits: a new paradigm for universal quantum computation. *New J. Phys.* **16**, 045014 (2014).

[84] R. K. Naik *et al.* Random access quantum information processors using multimode circuit quantum electrodynamics. *Nat. Comm.* **8**, 1904 (2017).

[85] A. Vrajitoarea, Z. Huang, P. Groszkowski, J. Koch, and A. A. Houck. Quantum control of an oscillator using a stimulated josephson nonlinearity. *Nature Physics* **16**, 211–217 (2020).

[86] Z. Leghtas *et al.* Confining the state of light to a quantum manifold by engineered two-photon loss. *Science* **347**, 853–857 (2015).

[87] S. Touzard *et al.* Coherent oscillations inside a quantum manifold stabilized by dissipation. *Phys. Rev. X* **8**, 021005 (2018).

[88] L. Bretheau, P. Campagne-Ibarcq, E. Flurin, F. Mallet, and B. Huard. Quantum dynamics of an electromagnetic mode that cannot contain n photons. *Science* **348**, 776–779 (2015).

[89] P. Bertet, C. J. P. M. Harmans, and J. E. Mooij. Parametric coupling for superconducting qubits. *Phys. Rev. B* **73**, 064512 (2006).

[90] A. O. Niskanen *et al.* Quantum coherent tunable coupling of superconducting qubits. *Science* **8**, 021005 (2018).

[91] D. C. McKay *et al.* Universal gate for fixed-frequency qubits via a tunable bus. *Phys. Rev. Applied* **6**, 064007 (2016).

[92] M. Reagor *et al.* Demonstration of universal parametric entangling gates on a multi-qubit lattice. *Science Advances* **4**, (2018).

[93] E. Zakka-Bajjani *et al.* Quantum superposition of a single microwave photon in two different colour states. *Nature Physics* **7**, 599603 (2011).

[94] Y. Lu *et al.* Universal stabilization of a parametrically coupled qubit. *Phys. Rev. Lett.* **119**, 150502 (2017).

[95] N. Bergeal *et al.* Phase-preserving amplification near the quantum limit with a josephson ring modulator. *Nature* **465**, 64–68 (2010).

[96] M. A. Castellanos-Beltran, K. D. Irwin, G. C. Hilton, L. R. Vale, and K. W. Lehnert. Amplification and squeezing of quantum noise with a tunable josephson metamaterial. *Nature Physics* **4**, 929–931 (2008).

[97] T. Yamamoto *et al.* Flux-driven josephson parametric amplifier. *Appl. Phys. Lett.* **93**, 042510 (2008).

[98] F. Lecocq *et al.* Nonreciprocal microwave signal processing with a field-programmable josephson amplifier. *Phys. Rev. Applied* **7**, 024028 (2017).

[99] N. E. Frattini *et al.* 3-wave mixing josephson dipole element. *Appl. Rev. Lett.* **110**, 222603 (2017).

[100] U. Vool *et al.* Driving forbidden transitions in the fluxonium artificial atom. *Phys. Rev. Applied* **9**, 054046 (2018).

[101] D. Markovic *et al.* Demonstration of an effective ultrastrong coupling between two oscillators. *Phys. Rev. Lett.* **121**, 040505 (2018).

[102] V. V. Sivak *et al.* Kerr-free three-wave mixing in superconducting quantum circuits. *Phys. Rev. Applied* **11**, 054060 (2019).

[103] E. T. Holland *et al.* Single-photon-resolved cross-kerr interaction for autonomous stabilization of photon-number states. *Phys. Rev. Lett.* **115**, 180501 (2015).

[104] D. I. Schuster *et al.* Resolving photon number states in a superconducting circuit. *Nature* **445**, 515–518 (2007).

[105] L. S. Bishop *et al.* Nonlinear response of the vacuum rabi resonance. *Nature Physics* **5**, 105–109 (2009).

[106] M. Hofheinz *et al.* Synthesizing arbitrary quantum states in a superconducting resonator. *Nature* **459**, 546–549 (2009).

[107] G. Kirchmair *et al.* Observation of quantum state collapse and revival due to the single-photon kerr effect. *Nature* **495**, 205–209 (2013).

[108] Y. Shalibo *et al.* Direct wigner tomography of a superconducting anharmonic oscillator. *Phys. Rev. Lett.* **110**, 100404 (2013).

[109] J. Wenner *et al.* Surface loss simulations of superconducting coplanar waveguide resonators. *Appl. Rev. Lett.* **99**, 113513 (2011).

[110] C. Wang *et al.* Surface participation and dielectric loss in superconducting qubits. *Appl. Rev. Lett.* **107**, 162601 (2015).

[111] M. Reagor *et al.* Reaching 10ms single photon lifetimes for superconducting aluminum cavities. *Appl. Rev. Lett.* **102**, 192604 (2013).

[112] G. Ithier *et al.* Decoherence in a superconducting quantum bit circuit. *Phys. Rev. B* **72**, 134519 (2005).

[113] A. Shnirman *et al.* Noise and decoherence in quantum two-level systems. *Physica Scripta* **2002**, 147 (2002).

[114] P. Groszkowski *et al.* Coherence properties of the 0-π qubit. *New Journal of Physics* **20**, 043053 (2018).

[115] V. Manucharyan. Superinductance. *PhD thesis - Yale*, (2012).

[116] Y. H. Lin *et al.* Demonstration of protection of a superconducting qubit from energy decay. *Phys. Rev. Lett.* **120**, 150503 (2018).

[117] M. D. Hutchings *et al.* Tunable superconducting qubits with flux-independent coherence. *Phys. Rev. Applied* **8**, 044003 (2017).

[118] D. J. Van Harlingen *et al.* Decoherence in josephson-junction qubits due to critical-current fluctuations. *Phys. Rev. B* **70**, 064517 (2004).

[119] J. Koch *et al.* Charging effects in the inductively shunted josephson junction. *Phys. Rev. Lett.* **103**, 217004 (2009).

[120] A. Romanenko *et al.* Three-dimensional superconducting resonators at $t < 20$ mk with the photon lifetime up to $\tau = 2$ seconds. *https://arxiv.org/abs/1810.03703*, (2018).

[121] I. M. Pop *et al.* Coherent suppression of electromagnetic dissipation due to superconducting quasiparticles. *Nature* **508**, 369–372 (2014).

[122] B. Peropadre *et al.* Tunable coupling engineering between superconducting resonators: From sidebands to effective gauge fields.. *Phys. Rev. B* **87**, 134504 (2013).

[123] M. C. o. Collodo. Observation of the crossover from photon ordering to delocalization in tunably coupled resonators.. *Phys. Rev. Lett.* **122**, 183601 (2019).

[124] R. Lescanne *et al.* Exponential suppression of bit-flips in a qubit encoded in an oscillator.. *Nature Physics* **16**, 509–513 (2020).

[125] N. R. A. Lee *et al.* Electric fields for light: Propagation of microwave photons along a synthetic dimension.. *arXiv:1908.10329 [quant-ph]*, (2020).

[126] J. Raftery *et al.* Direct digital synthesis of microwave waveforms for quantum computing.. *arXiv:1703.00942 [quant-ph]*, (2017).

[127] H. J. Carmichael. Statistical methods in quantum optics 1: Master equations and fokker-planck equations. *Physics and Astronomy Online Library Springer*, (1999).

[128] U. Weiss. Quantum dissipative systems.. *World Scientific*, (2012).

[129] A. J. Daley. Quantum trajectories and open many-body quantum systems.. *Advances in Physics* **63**, 77–149 (2014).

[130] J. R. Johansson *et al.* Qutip: An open-source python framework for the dynamics of open quantum systems.. *Comput. Phys. Commun.* **183**, 1760 (2012).

[131] K. M. Birnbaum *et al.* Photon blockade in an optical cavity with one trapped atom.. *Nature* **436**, 87–90 (2005).

[132] I. Schuster *et al.* Nonlinear spectroscopy of photons bound to one atom.. *Nature Physics* **4**, 382–385 (2008).

[133] D. E. Chang *et al.* Crystallization of strongly interacting photons in a nonlinear optical fibre.. *Nature Physics* **4**, 884–889 (2008).

[134] A. Abragam *et al.* The principles of nuclear magnetism.. *Oxford University Press*, (1961).

[135] M. D. Girardeau. Relationship between systems of impenetrable bosons and fermions in one dimension.. *Math. Phys. (N.Y.)* **1**, 516 (1960).

[136] T. Grujic *et al.* Non-equilibrium many-body effects in driven nonlinear resonator arrays.. *New J. Phys.* **14**, 103025 (2012).

[137] M. Mancini *et al.* Observation of chiral edge states with neutral fermions in synthetic hall ribbons.. *Science* **349**, 1510 (2015).

[138] B. K. Stuhl *et al.* Visualizing edge states with an atomic bose gas in the quantum hall regime.. *Science* **349**, 1514 (2015).

[139] L. F. Livi *et al.* Synthetic dimensions and spin-orbit coupling with an optical clock transition.. *Phys. Rev. Lett.* **117**, 220401 (2016).

[140] E. J. Meier *et al.* Observation of the topological soliton state in the suschriefferheeger model.. *Nat. Comm.* **7**, 13986 (2016).

[141] F. A. An *et al.* Direct observation of chiral currents and magnetic reflection in atomic flux lattices.. *Science* **3**, 4 (2017).

[142] D. Xie *et al.* Topological characterizations of an extended suschriefferheeger model.. *npj Quantum Information* **5**, 55 (2019).

[143] A. Regensburger *et al.* Paritytime synthetic photonic lattices.. *Nature* **488**, 167171 (2012).

[144] E. Lustig *et al.* Photonic topological insulator in synthetic dimensions.. *Nature* **567**, 356360 (2019).

[145] B. A. Bell *et al.* Spectral photonic lattices with complex long-range coupling.. *Optica* **4**, 1433–1436 (2017).

[146] A. Dutt *et al.* A single photonic cavity with two independent physical synthetic dimensions.. *Science* **367**, 59–64 (2020).

[147] D. J. Egger and F. K. Wilhelm. Multimode circuit quantum electrodynamics with hybrid metamaterial transmission lines.. *Phys. Rev. Lett.* **111**, 163601 (2013).

[148] J. J. Garcia-Ripoll *et al.* Quantum simulation of anderson and kondo lattices with superconducting qubits. *Phys. Rev. B* **77**, 024522 (2008).

[149] K. Le Hur *et al.* Kondo resonance of a microwave photon. *Phys. Rev. B* **85**, 140506 (2012).

[150] M. Goldstein *et al.* Inelastic microwave photon scattering offa quantum impurity in a josephson-junction array.. *Phys. Rev. Lett.* **110**, 017002 (2013).

[151] N. Gheeraert *et al.* Particle production in ultrastrongcoupling waveguide qed. *Phys. Rev. A* **98**, 043816 (2018).

[152] J. P. Martinez *et al.* A tunable josephson platform to explore many-body quantum optics in circuit-qed. *npj Quantum Information* **5**, 19 (2019).

[153] R. Kuzmin *et al.* Superstrong coupling in circuit quantum electrodynamics. *npj Quantum Information* **5**, 20 (2019).

[154] G. Calajo *et al.* Atom-field dressed states in slow-light waveguide qed giuseppe.. *Phys. Rev. A* **93**, 033833 (2016).

[155] Y. Liu and A. A. Houck. Quantum electrodynamics near a photonic bandgap.. *Nature Physics.* **13**, 48–52 (2017).

[156] N. M. Sundaresan *et al.* Interacting qubit-photon bound states with superconducting circuits.. *Phys. Rev. X* **9**, 011021 (2019).

[157] E. Sanchez-Burillo *et al.* Scattering in the ultrastrong regime: Nonlinear optics with one photon.. *Phys. Rev. Lett.* **113**, 263604 (2014).

[158] W. C. Smith *et al.* Quantization of inductively shunted superconducting circuits.. *Phys. Rev. B* **94**, 144507 (2016).

[159] A. J. Leggett *et al.* Dynamics of the dissipative two-state system.. *Rev. Mod. Phys.* **65**, 725 (1995).

[160] K. Le Hur. Kondo resonance of a microwave photon. phys.. *Phys. Rev. B* **85**, 140506(R) (2012).

[161] B. Peropadre *et al.* Nonequilibrium and nonperturbative dynamics of ultrastrong coupling in open lines.. *Phys. Rev. Lett.* **111**, 243602 (2013).

[162] O. Astafiev *et al.* Resonance fluorescence of a single artificial atom.. *Science* **327**, 840–843 (2010).

[163] I. C. Hoi *et al.* Generation ofnonclassical microwave states using an artificial atom in 1d open space.. *Phys. Rev. Lett.* **108**, 263601 (2012).

[164] M. D. Reed. Entanglement and quantum error correction with superconducting qubits. *PhD thesis - Yale*, (2013).

[165] P. Forn-Diaz. Microwave quantum optics with superconducting quantum circuits. *Lecture notes QIC 890/891*, (2016).

[166] L. Magazzu *et al.* Probing the strongly driven spin-boson model in a superconducting quantum circuit.. *Nat. Comm.* **9**, 1403 (2018).

[167] G. Diaz-Camacho *et al.* Dynamical polaron ansatz: a theoretical tool for the ultra-strong coupling regime of circuit qed.. *Phys. Rev. A* **93**, 043843 (2016).

[168] J. M. Zhang and R. X. Dong. Exact diagonalization: the bose hubbard model as an example.. *European Journal of Physics* **31**, (2010).

[169] C. Eichler *et al.* Characterizing quantum microwave radiation and its entanglement with superconducting qubits using linear detectors.. *Phys. Rev. A* **86**, 032106 (2012).

[170] M. Hillery and M. S. Zubairy. Multimode circuit quantum electrodynamics with hybrid metamaterial transmission lines.. *Phys. Rev. Lett.* **95**, 050503 (2006).

[171] S. Wolk *et al.* Unified approach to entanglement criteria using the cauchy-schwarz and hlder inequalities.. *Phys. Rev. A* **90**, 022315 (2014).

[172] A. H. Castro Neto *et al.* Quantum magnetic impurities in magnetically ordered systems. *Phys. Rev. Lett.* **91**, 096401 (2003).

[173] D. V. Khveshchenko *et al.* Quantum impurity models of noisy qubits. *Phys. Rev. B* **69**, 153311 (2004).

[174] E. Novais *et al.* Frustration of decoherence in open quantum systems. *Phys. Rev. B* **72**, 014417 (2005).

[175] E. Magesan *et al.* Effective hamiltonian models of the cross-resonance gate.. *Phys. Rev. A* **101**, 052308 (2020).

[176] A. A. Clerk *et al.* Introduction to quantum noise, measurement, and amplification.. *Rev. Mod. Phys.* **84**, 1155 (2010).

[177] C. Macklin *et al.* A near-quantum-limited josephson traveling-wave parametric amplifier.. *Science* **350**, 307–310 (2015).